High Temperature Electrochemical Studies on Nickel: Glycerol and Nickel Electro-oxidation

by

Tory Borsboom-Hanson
B.Sc., University of Victoria, 2016

A Dissertation Submitted in Partial Fulfillment of the
Requirements for the Degree of

Doctor of Philosophy

in the Department of Chemistry

High Temperature Electrochemical Studies on Nickel: Glycerol and Nickel Electro-oxidation

by

Tory Borsboom-Hanson
B.Sc., University of Victoria, 2016

Supervisory Committee

Dr. David A. Harrington, Supervisor (Department of Chemistry)

Dr. Matthew Moffitt, Departmental Member (Department of Chemistry)

Dr. Nedjib Djilali, Outside Member (Department of Mechanical Engineering)

Supervisory Committee

Dr. David A. Harrington, Supervisor (Department of Chemistry)

Dr. Matthew Moffitt, Departmental Member (Department of Chemistry)

Dr. Nedjib Djilali, Outside Member (Department of Mechanical Engineering)

Abstract

In this dissertation electrochemical nickel oxide formation in alkaline solution and the electro-oxidation of glycerol on polycrystalline electrodes are studied as a function of temperature. This is done using electrochemical impedance spectroscopy (EIS), Tafel analysis, cyclic voltammetry, chronoamperometry, and chronopotentiometry among other techniques. Additionally, in order to facilitate the study of aqueous alkaline systems beyond the normal boiling point of water, an electrochemical cell was designed utilizing a self-pressurizing autoclave. This allowed for the study of aqueous alkaline systems up to 140 °C.

Product analysis of glycerol electro-oxidation on nickel was performed at various temperatures using HPLC. A reaction pathway for the organic products was determined. At sufficiently high temperatures a polymer was discovered. This polymer product was characterized by DLS, DSC, CP-MAS NMR, and ATR-IR and determined to likely be a pseudo-polysaccharide. DSC analysis suggests that the polymer exists as three distinct structures, and DLS analysis suggests that the polymer exists in three different size distributions. The lack of a glass transition temperature in the DSC spectrum indicates that it is likely thoroughly cross-linked.

The aging process of α-$Ni(OH)_2$ to β-$Ni(OH)_2$ was studied as a function of temperature using cyclic voltammetry and dynamic EIS. This lead to the observation that β-$Ni(OH)_2$ does not appear to form on the oxide surface at 100 °C and above. A methodology was developed for preferentially stabilizing either β-NiOOH or γ-NiOOH on the electrode surface. This methodology was used to determine that β-NiOOH is the better oxygen evolution catalyst of the two oxide phases. The reversible potential of $Ni(OH)_2$ oxidation was observed to have a shift of -1.14 mV K^{-1}, and this data was used in a thermodynamic analysis to identify the nickel species involved in the

reaction. Based on data from the literature the oxidation of NiO or $Ni(OH)_2$ to NiO_2 appears to best match the observed data.

Mechanistic analysis was performed for glycerol on nickel in alkaline solution using a combination of Tafel analysis, cyclic voltammetry, AC voltammetry, and EIS. This study indicates that glycerol oxidation behaves differently on γ-NiOOH and β-NiOOH, perhaps explaining the discrepancy between various pieces of data found in the literature. Tafel analysis led to the observation that there appear to be two different glycerol oxidation regimes. Below 80 °C, $\alpha = 0.5$, indicating that the rate determining step is an electron transfer step with no pre-equilibrium electron transfers. At 80 °C and above $\alpha = 1$, indicating that the rate determining step has no electron transfer and one pre-equilibrium electron transfer. This was determined to be caused by the transition of the underlying nickel oxide phase from γ-NiOOH to β-NiOOH because the change is retained upon cooling. Additionally, EIS showed two semicircles which indicates the presence of one kinetically significant adsorbed intermediate. These observations were incorporated into a detailed proposed reaction mechanism.

Table of Contents

List of Tables

List of Figures

Nomenclature

Symbol	Meaning	Units
a	Activity	Unitless
C	Capacitance	F cm^{-2}
C_{dl}	Double Layer Capacitance	F cm^{-2}
$C_{dl,eff}$	Effective Double Layer Capacitance of CPE	F cm^{-2}
C_2	Capacitance of Nest Voigt Element	F cm^{-2}
C	Concentration	M
E	Applied Potential	V
$\tilde{E}$	Applied Potential Phasor	V
E_r	Reversible Potential	V
E°	Standard Potential	V
E_{ac}	AC Potential	V
E_{dc}	DC Potential	V
F	Faraday's Constant	C mol^{-1}
f	Fugacity	bar
f	Frequency	Hz
G°	Standard Gibbs Energy	kJ mol^{-1}
H°	Standard Enthalpy	kJ mol^{-1}
I	Current	A
j	Current Density	A cm^{-2}
$\tilde{j}$	Current Density Phasor	A cm^{-2}
j_{ac}	AC Current Density	A cm^{-2}
j_{dc}	DC Current Density	A cm^{-2}
j_{ss}	Steady State Current Density	A cm^{-2}
j_0	Exchange Current Density	A cm^{-2}
n	Number of Electrons	Unitless
k	Rate Constant	s^{-1}
k^{eq}	Equilibrium Rate Constant	s^{-1}
k	Number of Fitting Parameters	Unitless
L	Inductance	H cm^2
L_{ad}	Adsorption Inductance	H cm^2
$\widehat{L}$	Likelihood Estimator	Unitless
p	Partial Pressure	bar

Symbol	Meaning	Units
p°	Standard Pressure	bar
Q	Charge	C
Q	Constant Phase Element Coefficient	S s^{α} cm^{-2}
R	Universal Gas Constant	J mol^{-1} K^{-1}
R	Resistance	Ω cm^2
R_s	Solution Resistance	Ω cm^2
R_{ct}	Charge Transfer Resistance	Ω cm^2
R_{ad}	Adsorption Resistance	Ω cm^2
R_2	Resistance of Nested Voigt Element	Ω cm^2
R_p	Polarization Resistance	Ω cm^2
R_0	Impedance Determined Resistance	Ω cm^2
R_{DC}	CV Determined Polarization Resistance	Ω cm^2
S°	Standard Entropy	J mol^{-1} K^{-1}
S_f°	Standard Entropy of Formation	J mol^{-1} K^{-1}
s	Sweep Rate	mV s^{-1}
T	Temperature	K
t	Time	s
V	Volume	L
Y	Admittance	S cm^{-2}
Z	Impedance	Ω cm^2
α	Charge Transfer Coefficient	Unitless
α	Constant Phase Element Exponent	Unitless
γ	Fugacity Coefficient	Unitless
ϵ	Permittivity	F m^{-1}
η	Overpotential	V
π	Pi	Unitless
σ	Charge Density	C cm^{-2}
σ_{mono}	Charge Density of a Monolayer	C cm^{-2}
τ	Time Constant	s
τ_{cell}	Cell Time Constant	s
τ_{dl}	Double Layer Time Constant	s
τ_f	Faradaic Time Constant	s
τ_{sys}	System Time Constant	s
ϕ	Phase Angle	rad

Symbol	Meaning	Units
ω	Angular Frequency	rad s^{-1}

Acronym	Meaning
AC	Alternating Current
ATR-IR	Attenuated Total Reflectance Infrared
CE	Counter Electrode
CP-MAS	Cross Polarization Magic Angle Spinning
CS1	Casella Mechanism Number 1
CS2	Casella Mechanism Number 2
DC	Direct Current
DSC	Differential Scanning Calorimetry
DLS	Dynamic Light Scattering
dEIS	Dynamic Electrochemical Impedance Spectroscopy
EC	Equivalent Circuit
ECSA	Electrochemical Surface Area
EIS	Electrochemical Impedance Spectroscopy
EQCM	Electrochemical Quartz Crystal Microbalance
HPLC	High-Performance Liquid Chromatrography
KK	Kramers-Kronig
NMR	Nuclear Magnetic Resonance
pEIS	Potentiostatic Electrochemical Impedance Spectroscopy
RDS	Rate Determining Step
RE	Reference Electrode
RHE	Reversible Hydrogen Electrode
WE	Working Electrode

Acknowledgements

This work was financially supported by the Natural Sciences and Engineering Research Council of Canada through its Discovery Frontiers program (Engineered Nickel Catalysts for Electrochemical Clean Energy project (Ni Electro Can) administered from Queen's University), Discovery Grants program and CREATE program (Materials for Enhanced Energy Technologies (MEET) project), and by the Research Council of Norway through its International Partnerships Program (Canada-Norway Partnership in Electrochemical Energy Technologies (CANOPENER) project). Thank you for your support.

I would also like to thank Jeremy Wulff, Austin Burman, and Liam MacFarlane for their help in characterizing and understanding the polymer discovered in this work. I would have been lost without your help.

On a more personal note, a special thanks to my supervisor and mentor David A. Harrington for taking me on as a student and guiding me for the past four years. The graduate school experience you gave me was far more than the sum of its parts. To Thomas Holm, your friendship and guidance helped more than you can know both personally and professionally. To my lab mates Tianyu, Natalie, and Victor, the camaraderie we shared made the bad days better. Thank you for being my sounding board whenever I was stuck or just plain blind. To the kind folks at my favorite pub, Sans Campari, thank you for helping me keep my head on straight when the world felt like it was on top of me. To all the people who supported and encouraged me, this one's for you. To all the people who said I'd never make it, I couldn't have done this without you.

You are not some disinterested bystander. Exert yourself.
- Epictetus

Chapter 1

Introduction

1.1 Objectives

This dissertation presents a high temperature electrochemical study on nickel and nickel oxides for the application of glycerol valorization. Valorization is the term coined for converting one thing to another thing of higher value. By learning more about the nickel oxide phases and the glycerol oxidation mechanism it is hoped that they may be better applied to the purpose of glycerol valorization in the future. By tuning glycerol oxidation product selectivity to yield higher value products biodiesel synthesis can be made even more lucrative, drawing a larger market for green energy. Additionally, work done on the nickel oxide phases provides perspective that has previously been absent from the literature.

Electrochemistry is performed using two and three-electrode electrochemical cell setups built inside a self-pressurizing autoclave. Aqueous alkaline solutions are used and the autoclave allows for the cell to be heated beyond the normal boiling point of the electrolyte. To perform the high temperature experiments, earlier high temperature methodology developed in the Harrington group [1] was modified to enable use in concentrated alkaline solutions up to 140 °C, beyond the typical evaporation temperature for aqueous solutions. This was done using a self-pressurizing autoclave. The developed methodology and equipment are fully described in Section 2.2.

High temperature aqueous electrochemistry was chosen as the major focus for this dissertation because temperatures beyond the normal boiling point of water remain largely unexplored. A small body of work exists exploring the effect of

supercritical conditions on electrochemical systems [2–4], and the corrosion literature makes thorough use of high temperature studies to study thick film formation and other processes under industrial conditions [5–7]. Additionally, high temperatures have been previously shown to have mechanistic effects for the oxidation of organics on platinum [1, 8]. More general studies have also been performed exploring the effects of temperature on reaction thermodynamics [9]. However, there is little mechanistic and electrocatalytic work, and high temperatures represent a broad opportunity for study.

Chapter 3 describes high temperature glycerol oxidation product analysis and selectivity studies, with a focus on maximizing product yields. Glycerol oxidation product selectivity analysis was done quantitatively using standard HPLC methodologies [10, 11]. This, along with literature comparisons, allows for a reaction pathway to be determined. High temperature oxidation of organics has been shown to alter product selectivities [1, 8], and the autoclave setup allowed for the study of reaction conditions that had not yet been explored. Upon discovering that a polymer is formed under certain conditions this project changed course to investigate the polymer more thoroughly. The likely structure of the polymer and the mechanism by which it forms are presented.

The focus of the work in Chapter 4 was to study the interconversion of the various nickel oxide phases, alongside the initial steps of their formation, as a function of temperature. The basis of this work is a mechanistic analysis on smooth polycrystalline nickel electrodes, and not on alloy or custom catalyst development. There have been many literature studies on bulk nickel oxide electrodes [12–19]. These studies have done an excellent job characterizing bulk nickel oxide electrodes using various techniques such as X-Ray Diffraction, and Electrochemical Quartz Crystal Microbalance analysis. Work in this Chapter seeks to take the literature understanding of the bulk oxide phases and apply that knowledge to study the thin film growth of the various oxide phases from a metallic nickel electrode, focusing largely on the effect temperature has on the conversion of α-$Ni(OH)_2$ to β-$Ni(OH)_2$ as well as the effect on the oxide phases caused by potential cycling to steady state through different potential regions. A study involving the aging of nickel electrodes in alkaline solution was performed to stabilize specific active oxide phases on the surface, and mechanistic information is determined for their formation. Thermodynamic analysis was performed in order to determine the source of a shift in the reversible potentials of these active phases as a function of temperature. Cyclic voltammetry

and dynamic electrochemical impedance spectroscopy was then used to examine the passive oxide phases that exist on the electrode surface. It was also discovered that specific phases of nickel oxide cease to form beyond 100 °C.

Chapter 5 combines insights acquired from the previous two chapters, and uses these to perform a mechanistic analysis on the high temperature oxidation of glycerol on nickel. High temperatures have been previously shown to have mechanistic effects for the oxidation of organics on platinum [1, 8], and this work set out to determine if similar effects could be observed in the glycerol/nickel system. The study uses knowledge of surface species obtained from literature [20], alongside knowledge of solution state species determined in Chapter 3 to achieve this. The standard mechanistic analysis in literature for the oxidation of organics on nickel oxide electrodes involves the Fleischmann mechanism [16, 21, 22], and makes a bold assumption that many monolayers of NiOOH are reduced to $Ni(OH)_2$ by the glycerol substrate. The work in this chapter challenges that model by performing a ground up mechanistic analysis using an alternative mechanism from the literature that ultimately better describes the observed data.

1.2 Literature and Background

1.2.1 Glycerol

Glycerol is a byproduct of biodiesel synthesis, making up approximately 10 wt.% of the biodiesel synthesis products [23]. The demand for biodiesel has grown substantially in recent years, with an estimated demand of approximately 20 billion gallons worldwide in 2020 [24]. With such a high demand for biodiesel, a vast amount of glycerol is created. However, the world has little use for glycerol in these quantities. Due to the glut of glycerol available and its low cost, the valorization of glycerol has become a topic of some interest [23, 25–29]. These studies have resulted in the production of various chemicals [23, 30–32] including many small acids, alcohols, and hydrogen.

Glycerol fuel cells represent a promising avenue of study [33, 34]. Glycerol oxidation is performed at the anode of an electrochemical cell, while water reduction to hydrogen is performed at the cathode. The result is that glycerol valorization and hydrogen production are performed simultaneously. Because glycerol does not readily reduce and hydrogen can be collected in the gas phase no conductive membrane is

needed to separate the anode and cathode chambers.

1.2.1.1 Glycerol oxidation on noble metals

Noble metals have long been the predominant catalysts used for glycerol valorization due to their high activities. While the processes that result in these high activities are of scientific interest, nickel has more recently been sought after due to its inexpensive nature. This makes nickel more industrially viable. Nevertheless it is useful to look at some of the noble metal literature to understand the state of the field.

There are two pathways that glycerol can take to undergo electrooxidation, either through the adsorption of an oxygen atom or through the adsorption of a carbon atom to the electrode surface (Fig. 1.1) [35]. This occurs through the coordination of a lone pair of electrons at the specified atom to the metal surface. These pathways result in the formation of different products [36]. Catalysts can then be tuned in an attempt to promote selectivity for specific reaction pathways, and therefore different products.

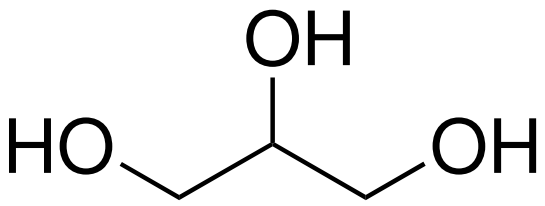

Figure 1.1: The chemical structure of glycerol.

Platinum is known to be the most active noble metal for glycerol oxidation. This is owing to its ability to efficiently deprotonate OH groups, which is favorable for the O adsorption pathway [37]. Since the O adsorption pathway requires the deprotonation of OH groups its rate is increased by the presence of alkaline solution [38]. Of the two oxidation pathways available on platinum the C adsorption pathway occurs at a lower potential than the O adsorption pathway [35]. After the initial deprotonation and adsorption of glycerol to the platinum surface, a second deprotonation results in the formation of either glyceraldehyde or dihydroxyacetone [39]. These species can interconvert in alkaline solution, and further react to form glyceric acid [40].

Palladium has a similar C adsorption pathway to platinum for glycerol oxidation [41]. Palladium does not, however, offer the ability to efficiently deprotonate OH groups. This requires a more alkaline electrolyte in order to quickly deprotonate the

OH groups [42]. Simultaneously, OH adsorbed to the metal surface from solution can inhibit glycerol oxidation activity [43]. It appears that the palladium requires free Pd sites next to OH adsorbed sites in order for glycerol oxidation to occur [44]. The ability of palladium to cleave C-C bonds is also reduced compared to Pt and Au [45, 46]. This is owed to the necessity of neighboring C atoms to be adsorbed to the palladium surface before C-C cleavage can occur [47]. So while palladium may require more tuning with regards to pH in order to optimize its reaction, it offers opportunities in determining glycerol oxidation methods that select for products wherein no C-C bonds have been cleaved.

For gold, it has been shown that deprotonation is the rate determining step for glycerol oxidation [48, 49], and while a high degree of deprotonation is favorable for Pd and Pt reaction rates this step only appears to be rate determining for gold. Computational studies have shown that adsorption of OH to the gold surface lowers the activation barrier of both C and O pathway deprotonation [50], conversely to what was discovered for Pd. On gold, OH deprotonates at a lower potential than CH for glycerol oxidation [50], and this may actually apply to Pd as well [51]. Of note, is that for gold electrodes it appears that glycerol can undergo the full oxidation mechanism on sites that have adsorbed OH [52–54].

Since noble metals aren't the focus of this work, this brief overview provides background context for a more in-depth look of the glycerol oxidation literature pertaining specifically to nickel and nickel oxides.

1.2.1.2 Glycerol oxidation on nickel oxides

Nickel has been shown to have a reasonable glycerol oxidation activity with respect to the noble metals [55]. It is for this reason, alongside its low cost and high availability, that glycerol oxidation on nickel has become a sought after process recently [14, 15, 20, 27, 28, 56–58].

Previous studies utilizing nickel electrodes for glycerol oxidation have found that NiOOH is the active oxide phase on the electrode surface for oxidation processes [59–68]. With specific regard to glycerol oxidation, the nature of the effect of the β-NiOOH and γ-NiOOH phases has gone relatively unexplored. Due to the necessity of some phase of NiOOH to be formed on the surface before glycerol oxidation can occur, the oxidation of glycerol on nickel occurs at relatively high potentials (> 1.3 V) compared to the noble metals (> 0.5 V for Pt) [14, 15, 56, 57]. NiOOH does appear

to be selective toward oxidizing glycerol and glycerol oxidation intermediates when compared to the OH adsorption pathway, a feature not seen in the noble metals [69]. This affinity also appears to have the effect of shifting oxygen evolution to higher potentials when glycerol is present in solution [70].

By performing long term oxidations at 1.6 V at room temperature on alkaline glycerol solutions using nickel electrodes the major product detected when performing HPLC has been found to be formate with glycerate, glycolate, tartronate, oxalate, and carbonate making up the more minor products [70]. Performing similar experiments at 1.9 V appears to not have a significant effect on product selectivity, save for the fact that more carbonate appears to be formed [10]. A noteworthy observation is that nickel appears to have affinity for oxidizing glycerol to carbonate in alkaline solution [71].

Glyceraldehyde has been shown, using in-situ spectroscopic techniques, to be the major product formed at the electrode surface during glycerol oxidation on nickel [20, 27, 28, 58]. Glyceraldehyde is not detected by HPLC however, because subsequent product speciation occurs through further oxidation of product species in solution. This either occurs by further oxidation at the electrode or by a redox reaction with OH^- ions in the solution itself [10, 69, 70].

Of note is that one of the more common reaction products seen for glycerol electrooxidation on noble metal catalysts is lactic acid [72], which appears to be absent from the nickel metal glycerol oxidation literature. Lactic acid can also be seen to form when noble metal catalysts are mixed with alkaline glycerol solutions and raised to high temperatures with no electrochemistry being involved [29, 73–75]. This missing product is relevant to the work performed later in this dissertation.

A rudimentary reaction pathway for the glycerol electrooxidation process on nickel is suggested by Oliveira et al [69]. It is flawed in that it neglects some of the reactivity that oxidation products can undergo in aqueous alkaline solution. Given their reaction pathway, one would expect significantly more oxalic acid to appear in solution, however two pathways exist for oxalic acid to be converted into formic acid in an aqueous akaline glycerol solution. First, computational studies suggest that unimolecular decomposition can occur [76]. Second, there is a notable means by which oxalic acid can react with glycerol directly to form oxalic acid [77]. These pathways account for the lack of a significant amount of oxalic acid as a reaction product in product selectivity studies.

NiOOH has been studied mechanistically for general electrochemical oxidation

alcohols for some time, with the Fleischmann mechanism (Eqn. 1.1) being the generally accepted mechanism by which oxidation occurs [21, 22, 78]. This explains the potential independent nature often seen for the oxidation of alcohols on nickel.

$$\begin{aligned} \mathrm{Ni(OH)_2 + OH^- &\longrightarrow NiOOH + H_2O + e^-} \\ \mathrm{2\,NiOOH + RCH_2OH &\xrightarrow{RDS} 2\,Ni(OH)_2 + RCHO} \end{aligned} \tag{1.1}$$

Other mechanisms have been suggested more recently in the literature, but haven't received much attention [79–81]. One of the notable alternatives is the Casella mechanism [79]:

$$\begin{aligned} \mathrm{Ni(OH)_2 + OH^-} &\longrightarrow \mathrm{NiOOH + H_2O + e^-} \\ \mathrm{NiOOH + RCH_2OH} &\longrightarrow \mathrm{NiOOH(RCH_2OH)(ads)} \\ \mathrm{NiOOH(RCH_2OH)(ads) + NiOOH} &\longrightarrow \mathrm{NiOOH(RCH_2O)(ads) + Ni(OH)_2} \\ \mathrm{NiOOH(RCH_2O)(ads) + NiOOH} &\longrightarrow \mathrm{NiOOH(RCHO)(ads) + Ni(OH)_2} \\ \mathrm{NiOOH(RCHO)(ads)} &\longrightarrow \mathrm{NiOOH + RCHO} \end{aligned} \tag{1.2}$$

This mechanism incorporates the existence of adsorbed intermediates, something that the original Fleischmann mechanism notably lacks.

The Fleischmann and Casella mechanisms are examples of what the literature calls indirect mechanisms, where an organic substrate is not oxidized directly, but where $Ni(OH)_2$ is first oxidized to NiOOH. This NiOOH then undergoes a redox reaction with the substrate, oxidizing the organic substrate while the nickel is reduced back to $Ni(OH)_2$. The Fleischmann mechanism has received some criticisms, however, in that the reaction rate can be shown to be exponentially potential dependent in some scenarios and the cathodic peak shown for NiOOH reduction can often still be seen when alcohols are present [80, 82]. The Fleischmann mechanism predicts fails to account for both of these facts. A direct mechanism has also been proposed where, during charging, alcohols are drawn within the oxide film alongside OH^- ions and are then directly oxidized in this highly charged environment [83]. This has also been called into question, however, as the amount of OH^- ions entering the electrode is not sufficient to explain the amount of organic substrate being oxidized [84].

1.2.2 Nickel and Nickel Oxides

Nickel and its various oxide phases are important materials in chemistry and engineering owing to their applications in energy storage [85]. Nickel is used in the cathodes of many varieties of batteries [86] due to the ability of nickel hydroxides to intercalate many ions allowing for dense energy storage [87, 88]. Energy is stored in the material by intercalating ions, and so by intercalating a large number of ions in a small space a high energy storage density is obtained. Batteries made of nickel-based materials also offer good long term stability and are rather inexpensive compared to some alternative means of energy storage [89, 90].

Nickel oxidizes readily in alkaline solution, but the process is not simple. There are four common phases of nickel oxide that exist and their interconversion is complicated (Fig. 1.2)[91]. All four phases of nickel oxide are studied in this work, with a special interest in the NiOOH phases. Both phases of $Ni(OH)_2$ are passive oxide layers and do not facilitate the oxidation of any organic feedstock.

Not shown in Fig. 1.2a is a very thin layer of NiO, which has been shown to exist on the electrode in a thin layer between the $Ni(OH)_2$ phase and the pure nickel metal (Fig. 1.3) [92, 93]. The NiO phase is a poor conductor and as it grows can be expected to inhibit some electrochemical reactions [94]. This phase grows at potentials above 0.5 V, and appears to undergo accelerated growth at potentials in which NiOOH is formed. Burke has suggested that this is due to the formation of a bridged (Ni-O-Ni) oxygen species from oxygen species trapped in the oxide surface during the cathodic portion of a CV [95]. The NiO layer formed appears to be quite stable, not undergoing much interconversion [93]. As the nickel electrode is continuously cycled, steady growth of the NiO phase eventually begins to inhibit NiOOH growth by reducing the total oxidative current passed during a sweep. NiO growth continues until the thickness of the resistive NiO layer begins to significantly slow the processes by which NiO can be formed [93, 96–100].

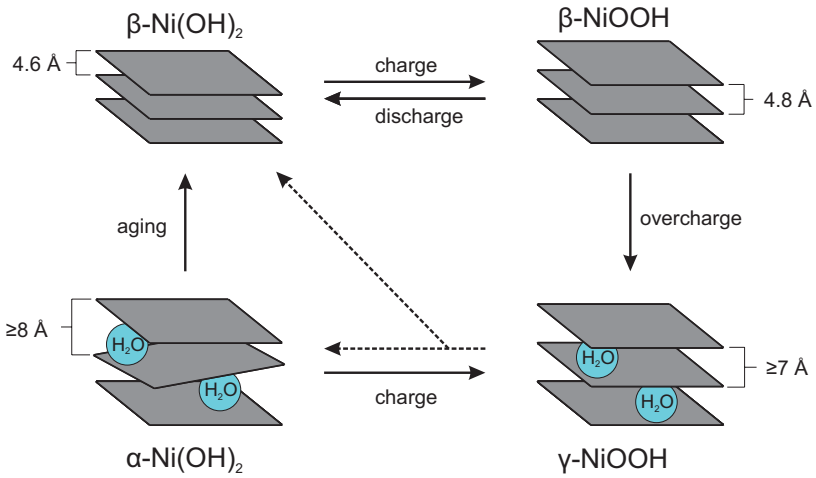

(a) The Bode diagram for nickel oxide phases. The dotted lines indicate transitions that occur simultaneously. While the α-Ni(OH)$_2$ to β-Ni(OH)$_2$ is labelled as an aging transition there does appear to be some potential driven effect on its rate. The transition itself, however, requires no charge transfer to proceed [91, 101].

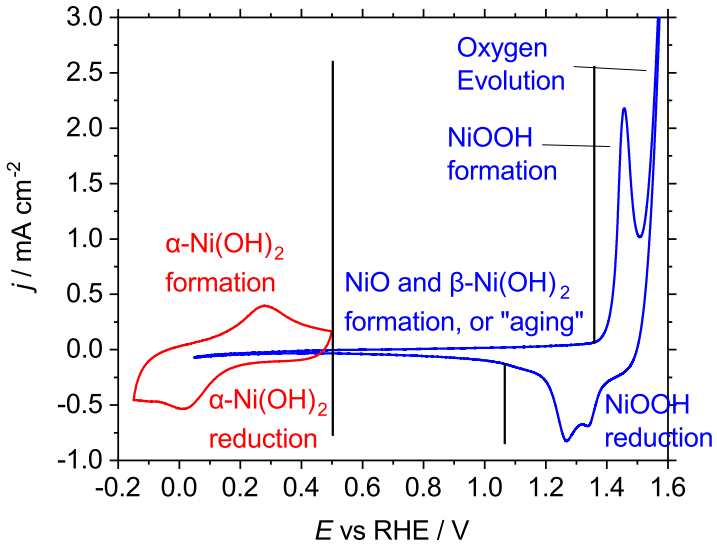

(b) Two CVs for polycrystalline nickel highlighting different nickel oxide phases. Done in 0.5 M NaOH with sweep rate = 100 mV s^{-1}. The red CV is on a freshly electropolished surface from -0.15 V to 0.45 V vs RHE, this highlights the oxidation and reduction of the α-Ni(OH)$_2$ phase from pure Ni. The blue CV is on an aged electrode, having been cycled for several hours, and is from 0.05 V to 1.6 V vs RHE. This highlights the NiOOH formation and reduction from NiO and β-Ni(OH)$_2$, as well as the somewhat irreducible nature of the NiO and β-Ni(OH)$_2$ phases.

Figure 1.2: The Bode diagram for nickel and example Ni CVs.

The relationship between α-$Ni(OH)_2$ and β-$Ni(OH)_2$ is one of crystallinity [18, 98, 102–104]. The α-$Ni(OH)_2$ phase is amorphous, heavily intercalated with ions and water. It readily ages into the more crystalline β-$Ni(OH)_2$ when exposed to alkaline solution. This is not a faradaic reaction but is still sped up by increased potential. Electron microscopy suggests that this occurs through a dissolution-precipitation mechanism [105]. This fact has been used to develop electrochemical β-$Ni(OH)_2$ synthesis techniques [106]. The increased crystallinity of β-$Ni(OH)_2$ makes it very stable, so a transition back to α-$Ni(OH)_2$ is unlikely without holding at sufficiently negative potentials for large durations [107, 108].

By increasing the electrode potential the $Ni(OH)_2$ phases are oxidized further, with α-$Ni(OH)_2$ becoming γ-NiOOH, and β-$Ni(OH)_2$ becoming β-NiOOH which is the active species for the oxidation of organics [10, 20–22, 58, 79, 109]. This occurs through the diffusion of protons and hydroxide groups through galleries in the nickel oxide surface (Fig. 1.4). This was proven by performing in-situ AFM during the cycling of nickel hydroxide films, through the mathematical modeling of charge accumulation in the oxide matrix during oxidation, and by various Electrochemical Quartz Crystal Microbalance (EQCM) studies [19, 93, 96, 110–115]. Proton diffusion occurs alongside propagation of OH^- through the oxide structure [19, 93, 95, 114–118] during the charging process, allowing for charge to pass through the oxide layer (Fig. 1.3). This also results in a slow, but steady increase to the overall surface area of the electrode as an experiment continues at high potentials. Additionally, in this work it is proven (Section 5.3.2) that the bulk of the oxide is electroactive. This is facilitated by the galleries in the nickel oxide surface (Fig. 1.4).

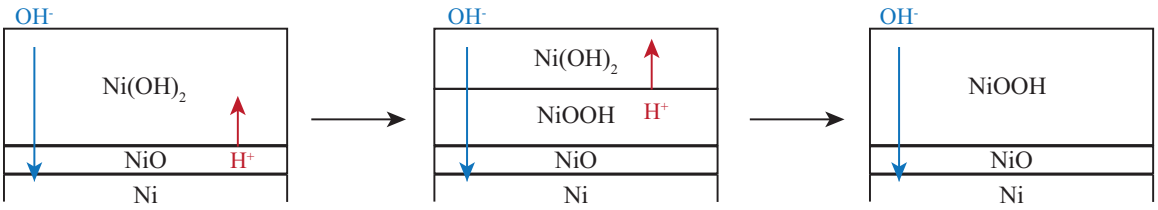

Figure 1.3: $Ni(OH)_2$ oxidation to NiOOH by proton diffusion and propagation of OH^- through the oxide phase. The red arrow denotes the direction of proton diffusion. The blue arrow denotes the direction of hydroxide propagation.

The means by which OH^- ions propagate through the oxide surface is somewhat controversial in the literature. EQCM and Probe Beam Deflection (PBD) experiments

have shown that OH^- ions appears to enter the oxide layer during oxidation [19, 114, 115]. This likely occurs through the galleries in the oxide after the protons have diffused out of the oxide layer. Voltammetric evidence has suggested that the thickening of the NiOOH layer occurs via a simple insertion mechanism [119] during an anodic sweep, alongside the electroreduction of various oxygen species in solution (OH^-, H_2O) [93, 95, 119] during a cathodic sweep. This mechanism does not explain how charge can continue to move through the circuit long after the diffusion of protons out of the oxide layer has completed, and the layer has been filled with OH^- ions. It has been suggested that OH^- ions may be able to move through the NiOOH layer via a place exchange mechanism [93, 95], allowing the transport of OH^- ions into the layered structure. This place exchange mechanism also appears to be possible at the NiO/NiOOH interface. This process could be responsible for the continuation of charge flow during long term anodic holds.

A common method of attempting to tune product selectivity and increase oxidation activity on metal electrodes is through alloying the selected metal with other metals and forming the electrodes into complex nanostructures [27, 109, 120–125]. This is often quite effective for short term studies, but in the long term this has been shown to be a somewhat fruitless endeavor due to the tendency for the nickel oxide phases to grow to the extent that alloying particles are often hidden and nanostructures are often destroyed [123].

β-NiOOH can overcharge to γ-NiOOH at sufficiently high potentials [68]. This is because in addition to the difference between the NiOOH phases being one of crystallinity, with γ-NiOOH being amorphous with a high degree of intercalation and β-NiOOH being crystalline, there is a difference in oxidation state between the nickel atoms. It appears that nickel atoms in the γ-NiOOH phase have an oxidation state between 3.3 and 3.7 and atoms in the β-NiOOH phase have an oxidation state between 2.7 and 3.0 [126]. The reason these phases can exist in non-discrete oxidation states is that while they are often discussed as though they are discrete phases for simplicity they actually exist in non-stoichiometric continuums [63, 127–129]. The reason for these non-stoichiometric phases is likely due to the ability of the nickel oxide phases to uptake various ions from solution, resulting in very complex localized chemistry. For this reason specific stoichiometries are typically not specified, and instead the phases are referred to using broader terms that acknowledge their respective average oxidation states and structural order. The oxidation states of the phases are then given as an average over the atoms in the phase, and that for the γ-NiOOH phase

the possibility of a Ni^{IV} state exists.

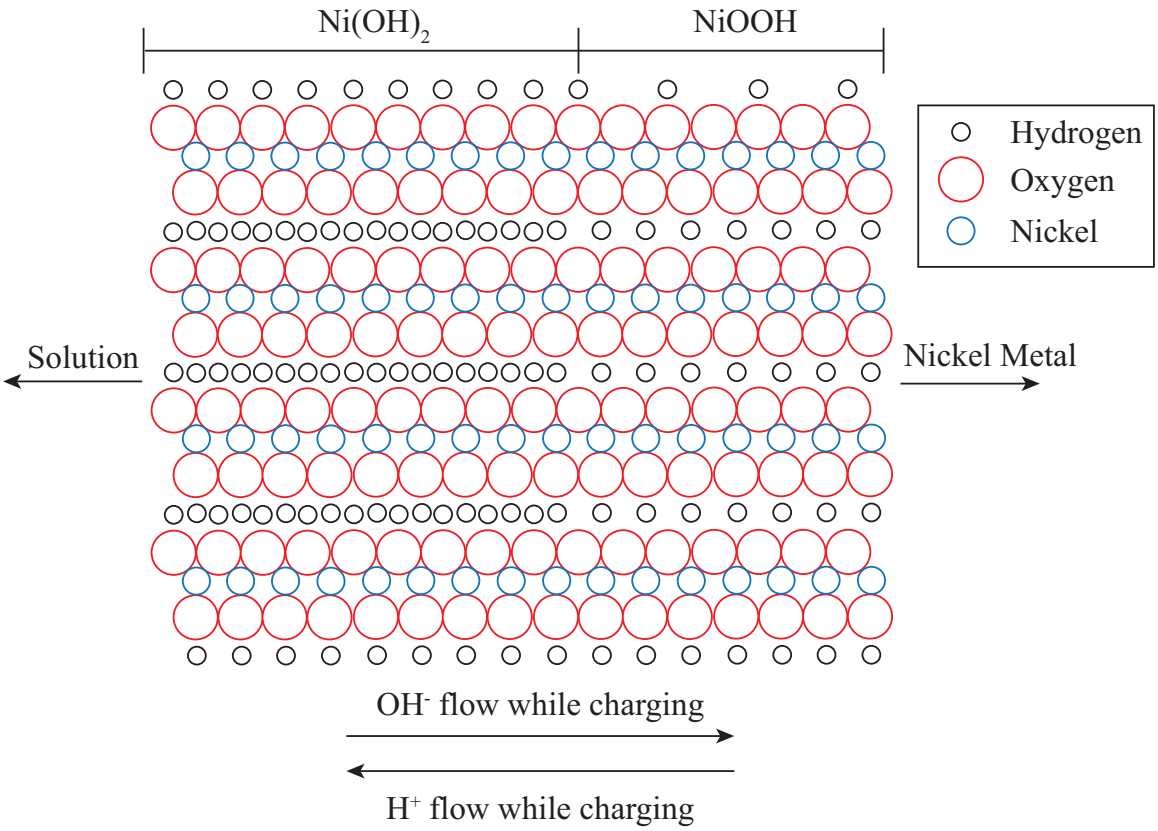

Figure 1.4: NiOOH formation by proton diffusion through galleries. An ideal β-$Ni(OH)_2$/β-NiOOH matrix is shown. Not shown is the simultaneous diffusion of hydroxide ions through the galleries.

There is some debate in the literature as to which phase of NiOOH has higher oxygen evolution activity. Godwin showed that by ageing a nickel electrode in alkaline solution by cyclic voltammetry its oxygen evolution activity increases [129]. In the potential region Godwin performed his cycling, 0.545 V to 1.555 V, this should result in the formation of β-NiOOH on the surface. Lu performed ellipsometry tests during potential cycling and holds that suggested this is due to a higher density of Ni^{3+} sites on the surface for the β-NiOOH phase, and that potentials higher than 1.56 V cause the formation of inactive Ni^{4+} sites on the oxide surface [127]. Performing a computational study, Li determined that β-NiOOH has a lower overpotential than γ-NiOOH by 0.06V. Conversely, Klaus and Trotochaud have developed methods by which Fe can be thoroughly excluded from electrolyte solution [68, 126]. Their evidence suggests that γ-NiOOH is more active for oxygen evolution in its native

state, however β-NiOOH traps Fe from solution in its surface sites, causing enhanced catalytic activity. Similarly, Gao found that synthesized α-$Ni(OH)_2$ nanocrystals offered higher oxygen evolution activity than β-$Ni(OH)_2$ [122]. These phases should oxidize to γ-NiOOH and β-NiOOH respectively, indicating that their γ-NiOOH had a higher activity. More recently Bediako determined using in-situ X-ray absorption spectroscopy that γ-NiOOH is the more active phase for oxygen evolution, and that Ni^{4+} is more active than Ni^{3+} in complete opposition of the findings presented by Lu.

Oxygen evolution is expected to occur in a potential region close to NiOOH formation as this is the active nickel oxide phase for that reaction. This can cause the formation of trapped oxygen gas within the NiOOH as trapped water is oxidized. Additionally, within the NiOOH matrix at these potentials the deprotonation of OH^- can occur, resulting in trapped oxide ions within the NiOOH layer [93, 100]. Finally, some terminal nickel hydroxide groups from $Ni(OH)_2$ are deprotonated to NiO^- [62, 95] (Fig. 1.5).

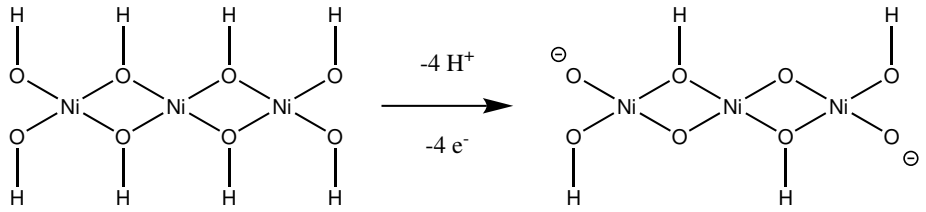

Figure 1.5: Formation of terminal oxide ions in NiOOH matrix.

Before being placed in solution a thin layer of NiO exists, approximately 5.4 Å thick, beneath the hydroxide phases. During the cathodic sweep the various trapped oxygen species then react at the NiO surface, causing the accelerated formation of NiO [93, 95]. After cycling at 50 mVs^{-1} for 90 min this layer was found to be 15.8 Å on a Ni (111) single crystal, according to synchrotron X-ray scattering experiments [92, 93]. NiO is a poor conductor [94] and as a result its resistance increases significantly as it gets thicker.

1.2.3 High Temperature Electrochemistry

Due to the experimental challenges associated with high temperature electrochemistry, it is relatively unexplored when compared to experiments performed at room temperature [9]. Reference electrode (RE) stability can become a problem at high temperatures making novel reference electrodes necessary [130, 131].

Heating electrolyte beyond its boiling point requires the use of special equipment such as an autoclave, like the one used in this work, or a more complex high-temperature high-pressure system [1, 132, 133].

There are many reasons for wanting to perform electrochemistry at high temperatures. Electrolytes used in electrochemistry have properties that change with temperature [134, 135], allowing for processes to occur faster and with less resistance. Mechanistic changes have been shown to occur at sufficiently high temperatures [8, 131]. Temperature also has a significant effect on mass transport phenomena and the activation energies of processes [136–138]. High temperatures have been very successfully employed in water electrolysis for hydrogen production [139–141]. Perhaps the most industrially relevant advantage to high temperature electrochemistry is the increased thermal efficiency for electrocatalytic reactions [142–145]. For these reasons high temperature electrochemistry is an industrially relevant process.

Some experiments have been performed on nickel at increased temperatures, with Alsabet et al. [56] having performed cyclic voltammetry up to 40 °C and MacDonald et al. [146] having done cyclic voltammetry up to 100 °C. The high temperature work was not a focal point in Alsabet's work, with the only observation being that there appears to be an increased rate of aging from γ-NiOOH to β-NiOOH. MacDonald found that the rate of oxygen evolution is significantly increased with temperature, and that the onset potential of oxygen evolution appears to be lower. They fail to account for the increased oxide bulk on the electrode, however. There have also been corrosion experiments performed on nickel to temperatures as high as 1400 °C [147], but these experiments focus largely on structural changes in bulk oxides and rates of oxidation and so don't really apply to the work done in the regime presented in this dissertation.

Chapter 2

Methods

Before getting into any specifics, it is necessary to highlight one very important point. Electrical current is typically denoted with the symbol I and has units in A. In this work all current will be normalized by surface area. To depict this the symbol j will be used, and the units will be given as A cm^{-2}. This normalization also goes for resistors, capacitors, and inductors which will be given units of Ω cm^2, F cm^{-2}, and H cm^2 respectively.

Additionally, for ease of reading all potentials are given versus the reversible hydrogen electrode (RHE) regardless of the actual reference electrode used. In cases where a Hg/HgO reference electrode was used, conversion to potential vs RHE was performed:

$$\begin{aligned} E_{RHE} &= E_{Hg/HgO} + E^{\circ}_{Hg/HgO} + 0.059\,pH \\ E_{RHE} &= E_{Hg/HgO} + 0.906V \end{aligned} \tag{2.1}$$

2.1 Tafel Slope Analysis and Charge Transfer Coefficients

The Tafel equation can be used to relate the rate of an electrochemical reaction to its overpotential. It can be written as follows

$$\begin{aligned} j &= j_0 \exp\left(\frac{\alpha F \eta}{RT}\right) \\ \ln j &= \ln j_0 + \left(\frac{\alpha F \eta}{RT}\right) \end{aligned} \tag{2.2}$$

where j is current density, j_0 is the exchange current density, α is the charge transfer coefficient, F is Faraday's constant, η is the overpotential, R is the universal gas constant, and T is the absolute temperature.

Given the logarithmic form of equation 2.2 it is seen that a plot of $\ln j$ vs η should be linear with slope $\alpha F R^{-1} T^{-1}$ (Fig. 2.1). In theory this experiment needs to be done at steady state to produce reliable results, but in practice it can be determined using cyclic voltammetry so long as the sweep rate is slow enough [8, 148]. The steady state of a system is essentially an equilibrium at non-ground state. By continuously applying a constant amount of energy it can be forced to maintain a consistent state at a higher energy than the equilibrium ground state. This higher energy state is called a steady state.

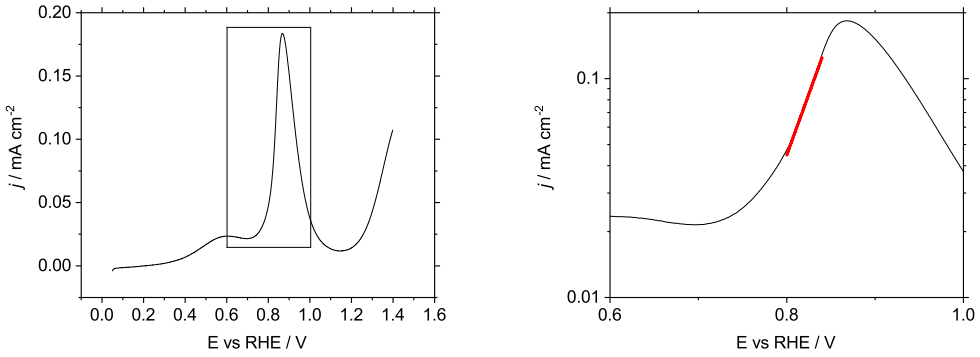

(a) (b)

Figure 2.1: Anodic portion of CV of formic acid oxidation on platinum, Tafel plot example. (a) Full anodic sweep, highlighting expanded area shown in b. (b) Focus on the oxidation peak with a logarithmic y-axis. It should be noted here that the plot has a log10 axis for easy viewing, however ln is required for the equation to function appropriately. The sweep rate is 20 mV s^{-1}. The slope of the fit is 9.145.

As seen in the above figure, the Tafel slope for the oxidation of formic acid on platinum at room temperature can be extracted. From there it follows that

$$\begin{aligned} \alpha &= \frac{RT}{F}\frac{\mathrm{d}\ln j}{\mathrm{d}\,\eta} \\ \alpha &= 0.63 \end{aligned} \tag{2.3}$$

The α value obtained from this type of analysis is a diagnostic tool that can be used to determine more information about the mechanism of the oxidation and its rate determining step (RDS). Values close to 0.5 as here are consistent with the first step as a rate-determining electron transfer step.

2.2 High Temperature Electrochemical Equipment

High temperature electrochemical experiments were carried out using a self-pressurizing autoclave (Buchi Glas Uster, Miniclave), the design of which was adapted from previous work in the Harrington and Seland groups [1, 8] (Fig. 2.2).

Figure 2.2: Autoclave setup. The self-pressurizing autoclave setup used for high temperature electrochemical experiments. The first panel shows the assembled autoclave with the digital temperature probe used for calibrating the internal temperature. The second panel shows the electrode assembly. Heat-shrink teflon tubing is used to allow only a small portion of the nickel wire to be exposed to solution. The remainder of the assembly prevents any steel pieces from being exposed to solution, while also keeping the autoclave pressurized. The third panel shows the cell interior, a teflon sleeve of single piece construction. The fourth panel shows the ramping hotplate with an insulated beaker on top. The beaker is filled with silicone oil and a temperature probe is placed inside.

To facilitate the use of alkaline electrolytes in the autoclave many of the components were switched for alkaline inert counterparts. (Fig. 2.2). The nickel wire in the autoclave was wrapped in heat-shrink teflon tubing (Zeus, Inc.) as well in order to limit the electrochemically available surface area of the electrode to a more consistent area.

This whole autoclave setup was then lowered into a large beaker of silicone oil, wrapped in insulation, and set on top of a programmable hotplate (Torrey Pines Scientific, HP61 Programmable Hotplate). The internal temperatures of the autoclave were calibrated against the hotplate set temperatures using a digital temperature probe (VWR, Dual Channel Thermometer) inserted through the top of the autoclave in a glass sheath (Fig. 2.3). This glass sheath and temperature probe were not present during actual experimentation.

Many alkaline exchange membranes were tested, but unfortunately due to instability of the membranes tested in the conditions of the long term (>48 hr)

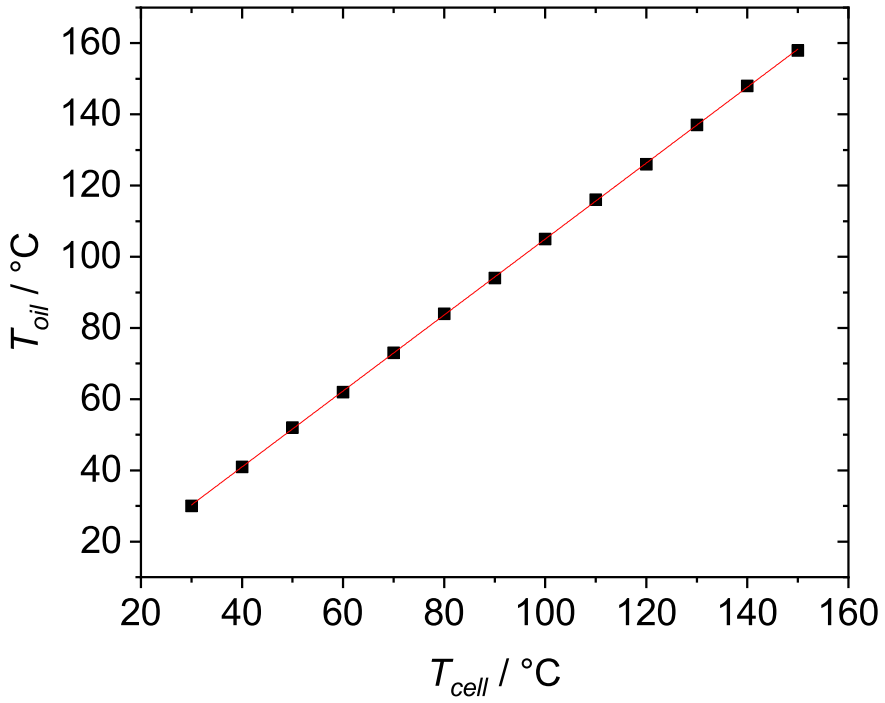

Figure 2.3: Oil bath temperature calibration curve. The formula for the line is $T_{oil} = -1.7 \pm 0.2\ ^{\circ}\mathrm{C} + 1.067 \pm 0.002\ ^{\circ}\mathrm{C}\ ^{\circ}\mathrm{C}^{-1} \times T_{cell}$ with $\mathrm{R}^2 = 0.999$.

experiments a glass frit had to be used in order to separate electrode compartments. In two-electrode product analysis experiments this was placed between the working and counter electrodes to prevent the reduction of oxidation products, as well as to concentrate the oxidation products in a smaller volume for HPLC analysis. In three-electrode mechanistic and kinetic experiments it was placed around the reference electrode to prevent any compound in solution from affecting its stability. While glass is not totally alkaline inert, this does not appear to have affected the results of the long term experiments.

2.3 Electrochemical Impedance Spectroscopy

Electrochemical Impedance Spectroscopy (EIS) is a useful electrochemical tool when it comes to attempting to determine the mechanism or kinetics of an electrochemical process. Applying alternating current (AC) potentials of various frequencies causes

different processes in electrochemical systems to respond in different ways. By looking at the current response to the applied electrochemical signal information can be gathered on what is occurring in the electrochemical system tested. It should be noted that a system at steady state is necessary in order to get usable data.

In order to best interpret the data gathered via EIS the system is modeled as an electrical circuit. There are many methods of determining which equivalent circuit (EC) to use for modeling the data. One method is to start with the most basic possible EC and attempt to fit the data to that model, then sequentially add components to the equivalent circuit in some logical fashion. As each new element is added the data is fit to the new EC and the new EC is tested for statistical significance using the F-Test [149] or the Akaike Information Criterion [150]. In another method a mechanism is determined for whatever process is being studied, an EC is derived from that mechanism, and the data is fitted to said EC. There is also a hybrid process by which an EC and possible mechanism can be determined simultaneously [151]. In this work the first method is used.

When the potential is applied it is defined as two separate components

$$E = E_{ac} + E_{dc} = |E| \sin(\omega t) + E_{dc} \tag{2.4}$$

E_{dc} is the constant direct current (DC) potential on which the periodic AC potential is superimposed and at which the impedance of the system is measured. $|E|$ is the amplitude of the AC potential, and ω is the angular frequency of the perturbation. Given the above, the current response expected from the circuit should be

$$j = j_{ac} + j_{dc} = |j| \sin(\omega t + \phi) + j_{dc} \tag{2.5}$$

where ϕ is the phase shift between the potential exciting and the current response. Because the potential is defined as having zero phase ϕ does not exist in Eq. (2.4), so by representing the AC components of the above equations as complex numbers (phasors) the following is shown

$$\tilde{E} = |E| \exp(i\phi) = |E| \exp(0) = |E| \tag{2.6}$$

$$\tilde{j} = |j| \exp(i\phi) \tag{2.7}$$

Finally, the impedance of a system is defined as the ratio of the current response

phasor to the potential excitation phasor:

$$Z = \frac{\tilde{E}}{\tilde{j}} = \frac{|E|}{|j|\exp(i\phi)} = |Z|\exp(-i\phi) \tag{2.8}$$

So the magnitude of the impedance, $|Z|$, and the phase difference between the current and potential, ϕ, are a function of the angular frequency applied to the system. This impedance experiment can then be run at different DC potentials, E_{dc}, allowing it to be used to explore many different processes at the electrode.

2.3.1 Dynamic Electrochemical Impedance Spectroscopy

Dynamic Electrochemical Impedance Spectroscopy (dEIS) is a special type of EIS experiment wherein a multisine waveform of non-interfering AC potentials [152, 153] is used in order to gather EIS data at many frequencies simultaneously. This waveform consists of many sinusoidal waveforms overlapped, with frequencies carefully chosen such that they do not occupy any harmonics of the base frequency. The multisine waveform used here contains 13 frequencies per decade, with each decade having frequencies 10 times higher than the previous decade. Amplitudes decrease by a factor of 2 for every decade increase in frequency; this gives low frequencies higher amplitudes than high frequencies in order to combat issues with noise observed in the lower frequency measurements. This allows for the DC potential to be swept slowly in such a way that a pseudo-steady state is maintained throughout the experiment. In doing so EIS can be used to study a changing system.

2.3.1.1 Instrumentation

To accomplish the addition of the AC and DC signals an HB-111 analog DC function generator is used in order to generate a sweeping DC waveform, and a Keithley 3116 digital-to-analog converter to generate the multisine AC waveform. To maintain a high level of fidelity in the AC signal it is generated at 10 V amplitude using the Keithley 3116 and divided down using a Stanford Research Systems SIM983 Scaling Amp set to x0.01. The AC signal is then added to the DC signal using a Stanford Research Systems SIM980 Summing Amp and the result is applied to the cell using the Gamry Reference 600 Potentiostat. Current information is sent directly from the potentiostat to Keithley 3116 channel ADC0. Potential information is first sent to a Stanford Research Systems SIM980 Summing Amp where the DC potential is

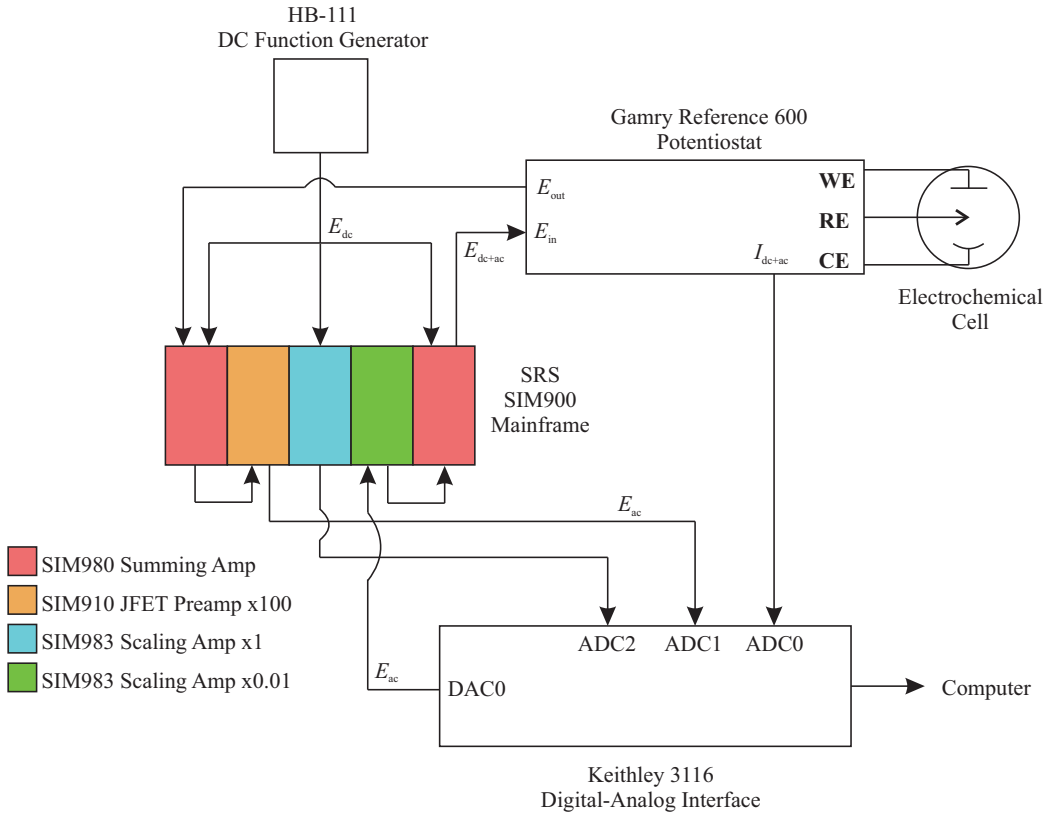

Figure 2.4: dEIS instrumentation setup [154].

subtracted. The remaining AC potential is then scaled back up using a Stanford Research Systems SIM910 JFET Preamp set to x100. This AC signal is then sent to Keithley 3116 channel ADC2. Lastly, the DC potential is sent from the HB-111 through a Stanford Research Systems SIM983 Scaling Amp set to x1, and the directly to Keithley channel ADC1. The purpose of the Stanford Research Systems SIM983 module is to buffer the Keithley from the HB-111 due to the high output impedance of the HB-111. All signal addition is done using analog circuitry to minimize signal degradation, and the sampling strategy is described in the literature [154].

2.3.2 Equivalent Circuits

There are three common circuit elements used in the making of an equivalent circuit: resistors, capacitors, and inductors (Fig. 2.5). Elements may be combined in series or in parallel to represent different processes, and each element has a different impedance.

Figure 2.5: Common passive circuit elements. The common elements used to build equivalent circuits.

2.3.2.1 Resistors

The impedance of a differential resistor is derived starting with the differential form of Ohm's Law and substituting in Eq. (2.4) and (2.5).

$$\begin{aligned} R &= \frac{\mathrm{d}\,E}{\mathrm{d}\,j} \\ &= \frac{\mathrm{d}\,|E|\sin(\omega t)}{\mathrm{d}\,|j|\sin(\omega t)} \\ &= \frac{\omega|E|\cos(\omega t)\,\mathrm{d}\,t}{\omega|j|\cos(\omega t)\,\mathrm{d}\,t} \\ &= \frac{|E|\sin(\omega t+\pi/2)\,\mathrm{d}\,t}{|j|\sin(\omega t+\pi/2)\,\mathrm{d}\,t} \end{aligned} \tag{2.9}$$

Lastly, converting to phasors and using Eq. (2.8) determines the impedance of the resistor.

$$Z = \frac{\tilde{E}}{\tilde{j}} = \frac{\omega|E|\exp(i\pi/2)\,\mathrm{d}\,t}{\omega|j|\exp(i\pi/2)\,\mathrm{d}\,t} = \frac{|E|}{|j|} = R \tag{2.10}$$

Here it is seen that the impedance of a resistor is wholly real, with no phase difference between excitation and response.

2.3.2.2 Capacitors

For a capacitor the following relation exists:

$$j = C\frac{\mathrm{d}\,E}{\mathrm{d}\,t} \tag{2.11}$$

Where C is capacitance. By combining Eq. (2.4) with this equation and switching to complex notation the following relation is shown:

$$
\begin{aligned}
j &= C\frac{\mathrm{d}\,|E|\sin(\omega t)}{\mathrm{d}\,t} \\
&= \omega C|E|\cos(\omega t) \\
&= \omega C|E|\sin(\omega t + \pi/2) \\
\tilde{j} &= i\omega C\tilde{E} \\
\frac{\tilde{E}}{\tilde{j}} &= Z = \frac{1}{i\omega C}
\end{aligned}
\tag{2.12}
$$

This shows that a capacitor has a $\pi/2$ phase shift, and the impedance is inversely proportional to ω. Therefore the impedance of a capacitor approaches zero as applied frequencies approach infinity and it acts like a wire, and its impedance approaches infinity as applied frequencies approach zero thereby acting as an open circuit.

2.3.2.3 Inductors

Inductors share a similar relationship to capacitors as seen in Eq. (2.11):

$$E = L\frac{\mathrm{d}\,j}{\mathrm{d}\,t} \tag{2.13}$$

Where L is inductance. Following the same procedure as for the capacitor results in the following:

$$
\begin{aligned}
E &= L\frac{\mathrm{d}\,|j|\sin(\omega t)}{\mathrm{d}\,t} \\
&= \omega L|j|\cos(\omega t) \\
&= \omega L|j|\sin(\omega t + \pi/2) \\
\tilde{E} &= i\omega L\tilde{j} \\
\frac{\tilde{E}}{\tilde{j}} &= Z = i\omega L
\end{aligned}
\tag{2.14}
$$

This shows that the inductor provides a $-\pi/2$ phase shift to the impedance, as well as being proportional to ω. The inductor behaves essentially inversely to the capacitor, having an impedance that goes to infinity at infinite frequencies like an open circuit, and going to zero at low frequencies like a wire.

2.3.2.4 Combining impedances and building circuits

Now that some circuit elements have been defined along with their impedances they can be used to build ECs to represent electrochemical systems.

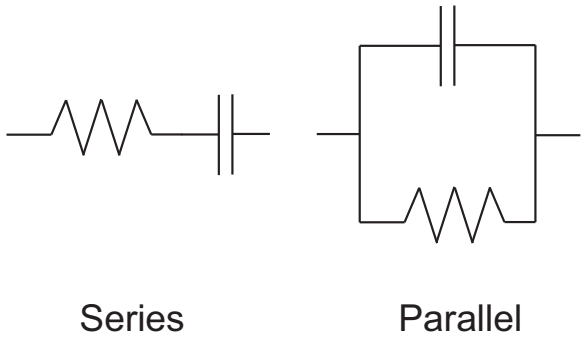

Figure 2.6: Series and parallel circuit elements.

Figure 2.6 shows the different ways circuit elements can be combined and the rules for mathematically combining impedances are quite simple. For the series combination they are simply additive:

$$Z = R + \frac{1}{i\omega C} \tag{2.15}$$

For the parallel combination the reciprocals of the impedances are additive:

$$\begin{aligned} \frac{1}{Z} &= \frac{1}{R} + i\omega C \\ Z &= \frac{1}{\frac{1}{R} + i\omega C} \end{aligned} \tag{2.16}$$

For any electrochemical cell there are at least two elements. The first is solution resistance, denoted R_s, which represents the resistance of the solution between the working electrode and the reference electrode. The second is double-layer capacitance, denoted C_{dl}, which represents the formation of a double layer at the electrode surface and its subsequent charging.

Just to briefly illustrate, a double layer is formed at an electrode surface as charge gathers in the electrode surface. This causes opposing charges, in the form of ions in the electrolyte, to gather near the electrode surface. These two planes of charges are often separated by a layer of solvent molecules that are trapped on the electrode surface, causing a separation of charge much like one would see in a parallel plate

capacitor (Fig. 2.7).

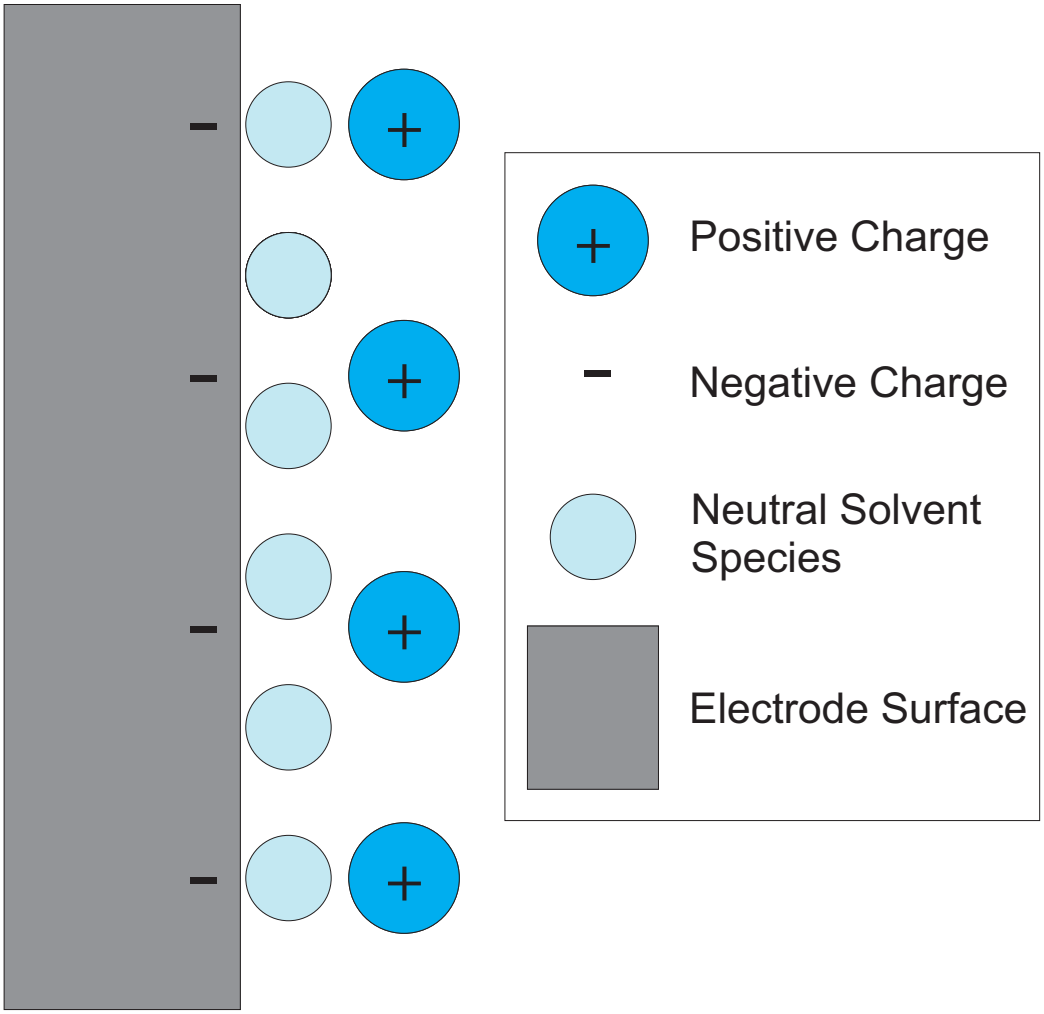

Figure 2.7: Formation of a double layer.

These two values can be used to define τ_{cell}, the time constant of the electrochemical cell:

$$\tau_{cell} = R_s C_{dl} \tag{2.17}$$

This value represents the fastest rate that the potential applied to the cell can change, which means that processes faster than this cannot be studied by EIS.

In order to convey what it is that EIS can do, a system with one measurable faradaic process can be explored. This is commonly represented using a simple circuit (Fig. 2.8).

In the single time constant circuit (Fig. 2.8) charge transfer resistance is introduced, R_{ct}, that represents the resistance involved in the faradaic process of

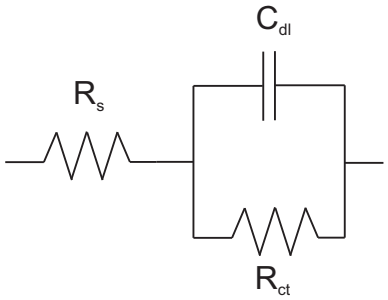

Figure 2.8: A single time constant circuit. This circuit represents an electrochemical cell with one faradaic step.

transferring charge between the electrode and a species in solution. This is the resistance involved in transferring electrons during faradaic processes that takes place at the electrode and is defined as follows:

$$R_{ct}^{-1} = \left(\frac{\partial j_F}{\partial E} \right)_{\theta_i, C_i} \tag{2.18}$$

where j_F is the Faradaic current density, E is potential, and θ_i and C_i are the reactant coverages and concentrations at the electrode interface. Because the transfer of electrons must occur across the double layer it is placed parallel to C_{dl} in the circuit. The time constant of these parallel components is given by:

$$\tau_f = R_{ct} C_{dl} \tag{2.19}$$

This data is commonly presented in Nyquist and Bode plots and some simulated single time constant circuit data is shown in Fig. 2.9. The Nyquist plot shows the real and imaginary parts of the impedance as a function of frequency, and the Bode plot shows both the magnitude and the phase of the impedance as a function of frequency. The single semicircle in the Nyquist plot is indicative of the parallel combination of R_{ct} and C_{dl} in the single time constant circuit, and conveys the existence of a single time constant in the system. The high frequency intercept on the left of the real axis gives the value of R_s, the diameter of the semicircle gives R_{ct}, the reciprocal of the frequency at the top of the semicircle gives τ_f, and through these values C_{dl} can be determined. Lastly the low frequency intercept on the right of the real axis gives the polarization resistance, R_p, which is the differential resistance experienced by DC current applied to the cell. That is to say the slope of the steady state polarization curve is governed by this value (Eq. 2.20). On the Bode plot much of

the same information can be seen, with the magnitude of the impedance at high and low frequencies giving R_s and R_p respectively as well as the middle portion having a slope of -1 indicating the presence of a capacitor. The Bode plot also gives the time constants of the system by the reciprocals of the angular frequencies at which there are inflection points in the magnitude plot, or peaks in the phase plot.

Since the steady state polarization curve can also be used to acquire R_p

$$\frac{1}{R_p} = \frac{\mathrm{d}\, j_{ss}}{\mathrm{d}\, E} \tag{2.20}$$

this can be a good method of validating impedance data. If the values of the two methods agree within a reasonable degree then all of the kinetic data for the system has been captured in the impedance experiment. If the two values do not match then it is likely that something else is going on that was undetected by the impedance experiment.

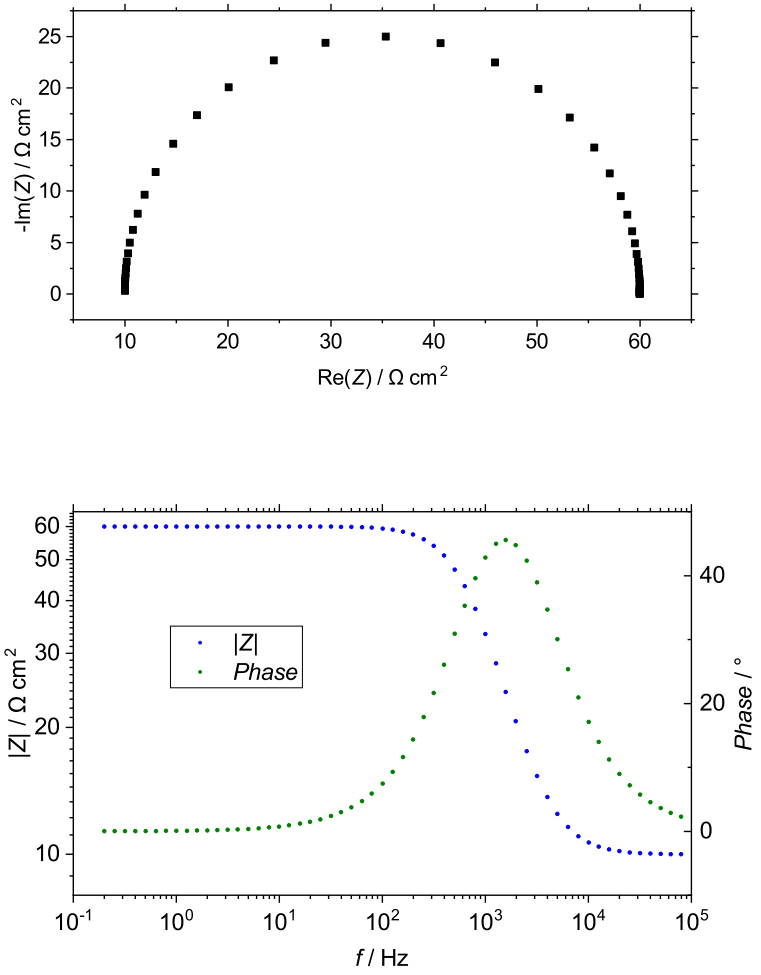

Figure 2.9: Nyquist and Bode plot examples. The top plot is the Nyquist plot, the bottom is the Bode plot. The axes on the Nyquist plot must be forced to 1:1 X:Y proportions, and the $|Z|$ and Frequency axes on the Bode plot are in log scale. These plots were simulated on the circuit shown in Fig. 2.8 using the following parameters: $R_s = 10\ \Omega\ \text{cm}^2, R_{ct} = 50\ \Omega\ \text{cm}^2, C_{dl} = 5 \times 10^{-5}\ \text{F cm}^2$.

In this work some systems are explored that have two faradaic time constants, and for those systems one of two circuits are used (Fig. 2.10). The implementation and interpretation of these will be discussed in section 5.2.

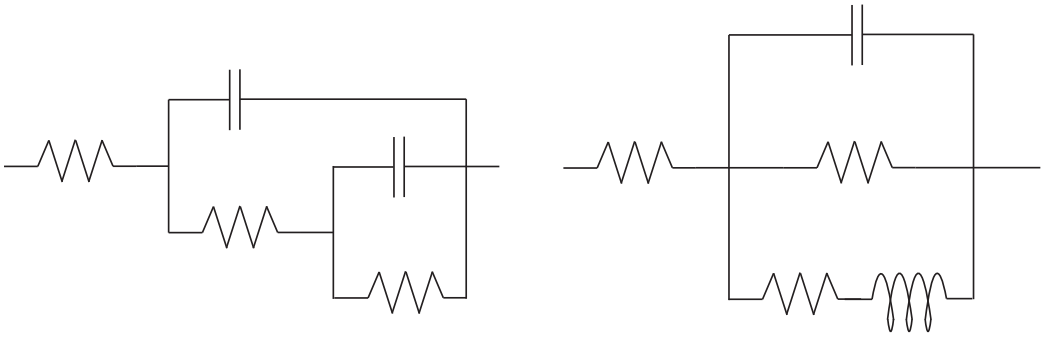

Figure 2.10: ECs with two time constants. The left uses two parallel RC combinations to achieve this, while the right uses one parallel RC and one series RL.

2.3.2.5 System time constants

The impedance for a simple one time constant circuit (Fig. 2.11) can be written simply as

$$Z = R_s + \frac{1}{i\omega C_{dl} + R_{ct}^{-1}} \tag{2.21}$$

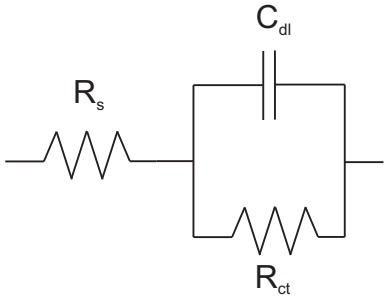

Figure 2.11: A single time constant circuit. This circuit represents an electrochemical cell with one faradaic step.

Because impedance experiments are performed by controlling potential and measuring current, the transfer function is admittance by definition

$$\begin{aligned}\text{Transfer Function} &= \frac{Output}{Input} = \frac{Current}{Potential} \\ Y = \frac{Current}{Potential} &= \frac{1}{Z} = \frac{1}{R_s + \dfrac{1}{i\omega C_{dl} + \dfrac{1}{R_{ct}}}} \\ &= \frac{R_{ct}C_{dl}i\omega + 1}{R_{ct}R_sC_{dl}i\omega + R_{ct} + R_s}\end{aligned} \tag{2.22}$$

In this form the poles and zeroes of the transfer function become clear.

$$Y = \frac{R_{ct}C_{dl}i\omega + 1}{i\omega + \dfrac{R_{ct} + R_s}{R_{ct}R_sC_{dl}}} \tag{2.23}$$

The poles are found at frequencies where $i\omega$ makes the denominator become zero. The system time constants are then the negative of the reciprocals of the poles for the transfer function.

$$\begin{aligned}pole &= -\frac{R_{ct} + R_s}{R_{ct}R_sC_{dl}} \\ \tau_{sys} &= \frac{R_{ct}R_sC_{dl}}{R_{ct} + R_s}\end{aligned} \tag{2.24}$$

2.3.2.6 Constant Phase Element

The constant phase element is an element that pertains to electrochemistry directly. Impedance spectroscopy is often performed on electronic circuits, and in these circuits capacitors of a more ideal nature are used. This results in a near perfect semicircle in the Nyquist plot of the resulting data (Fig 2.9). When performing the same experiment on an electrochemical system the double layer (Fig. 2.7) is found to be considerably less ideal. As a result a typical one time constant circuit has a broadened semi-circle. This represents the fact that there isn't one time constant associated with charging the double layer. Instead there are many time constants of similar values superimposed on top of each other, resulting in the broadening of the semicircle in the Nyquist plot. In order to accommodate this feature, a small alteration is made

to the impedance formula for a capacitor in the form of an exponent, α, and by changing the capacitance value C to Q to represent the fact that these values are not interchangeable:

$$Z = \frac{1}{(i\omega)^{\alpha}Q} \tag{2.25}$$

α is related to the angle of the semicircle at the intercept, called the phase:

$$\text{Phase} = 90^{\circ} \times \alpha \tag{2.26}$$

The α value must be between 1 and 0, and when the α value is determined to be 1 the CPE impedance relationship can be shown to be identical to the one for capacitance:

$$Z_{CPE} = \frac{1}{(i\omega)^{1}Q} = Z_C = \frac{1}{i\omega C} \tag{2.27}$$

2.3.2.7 Equivalent circuits and their kinetic interpretation

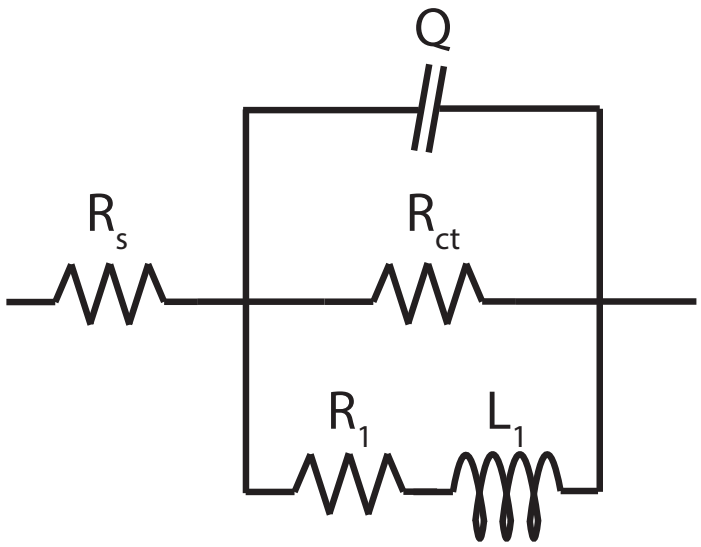

Figure 2.12: Two time constant inductive circuit. This circuit is often used to describe a charge transfer process with one adsorption step.

For many equivalent circuits the impedance expression is too complex to directly draw conclusions about the kinetics of a system, however some equivalent circuits lend themselves well to this application. For example, the two time constant inductive circuit (Fig. 2.12) is often used to describe a charge transfer process

with one adsorption step and fast mass transport. It is shown in the literature [148, 149, 151, 155] that this circuit pertains directly to the kinetic and mechanistic information of a single adsorption mechanism using the following equations:

$$\begin{aligned} Z^{-1} = Y &= R_{ct}^{-1} + \frac{L_1^{-1}}{(i\omega)^{\alpha} Q + R_1 L_1^{-1}} \\ R_{ct}^{-1} &= F\left(\frac{\partial\, r_e}{\partial\, E}\right)_{\theta} \\ L_1^{-1} &= \frac{F}{\Gamma_m}\left(\frac{\partial\, r_e}{\partial\, \theta}\right)_E \left(\frac{\partial\, r_\theta}{\partial\, E}\right)_E \\ R_1 L_1^{-1} = \tau^{-1} &= -\frac{1}{\Gamma_m}\left(\frac{\partial\, r_\theta}{\partial\, \theta}\right)_E \end{aligned} \tag{2.28}$$

where Z is impedance, Y is admittance defined as the reciprocal of the impedance, r_e is the rate of electron transfer, E is the potential, θ is the percent adsorbate coverage, Γ_m is the surface concentration of oxidation sites in mol cm^{-2}, r_θ is the net rate of production of the adsorbed species in mol cm^{-2} s^{-1} , and τ is the time constant of the R_1L_1 resistor inductor series branch.

More often, however, there is little direct physical meaning to the values of the circuit elements as processes can be coupled in very complex ways. For processes that fit these more complex circuits qualitative information can still be inferred from the circuit of best fit. The number and type of elements can be used to validate mechanisms, with an increasing number of time constants indicating the existence of more kinetically significant adsorbed species. The more exotic Warburg element can also present information about mass transport effects in the system.

In this work the more qualitative approach is used, even for processes wherein the inductive ladder circuit (Fig. 2.12) is found to be the circuit of best fit. This is because the Γ_m parameter is not a fixed constant due to the nature of the nickel oxide phases that continually grow on the electrode surface (Section 1.2.2) and so the concentration of surface oxidation sites is continually changing. This makes a quantitative mechanistic analysis considerably more challenging.

2.4 Determination of Electrochemical Surface Area of Nickel

While some metals may look flat, even a very well polished piece of metal is not perfectly flat. Roughness exists at a nanoscopic level on most metal surfaces, causing the surface area available for electrochemical reactions to be larger than the geometric surface area acquired from simply measuring the electrode with a ruler. This area is called the Electrochemical Surface Area (ECSA).

In order to determine the ECSA of the nickel electrodes a modified version of a literature procedure [102] is used. The procedure uses the oxidation of nickel metal to the somewhat amorphous α-$Ni(OH)_2$ and the known charge of an ideal monolayer, 514 $\mu C\ cm^{-2}$, to determine the electrochemically available surface area of the electrode.

One issue with this method, however, is that nickel metal reorganizes from α-$Ni(OH)_2$ to the far more stable and crystalline β-$Ni(OH)_2$ form rapidly when exposed to alkaline solution. This also occurs slowly over time in open atmosphere [92]. Once the nickel metal has reached the β-$Ni(OH)_2$ phase it is impractical to get it to reduce back to the α-$Ni(OH)_2$ or nickel metal phases [85, 91, 92, 101, 126](Fig. 1.2b reproduced for convenience here as Fig. 2.13). In order to get a realistic measure of the charge used to form a monolayer of α-$Ni(OH)_2$ the electrode must be polished in order to expose the nickel metal surface. In this work electropolishing to achieve the removal of the β-$Ni(OH)_2$ layer (Sec. 2.4.1) (Fig. 2.14) is employed. It should be noted, however, that given a long enough potential hold at sufficiently negative potentials some of the β-$Ni(OH)_2$ layer can be reduced to metallic nickel [107, 108].

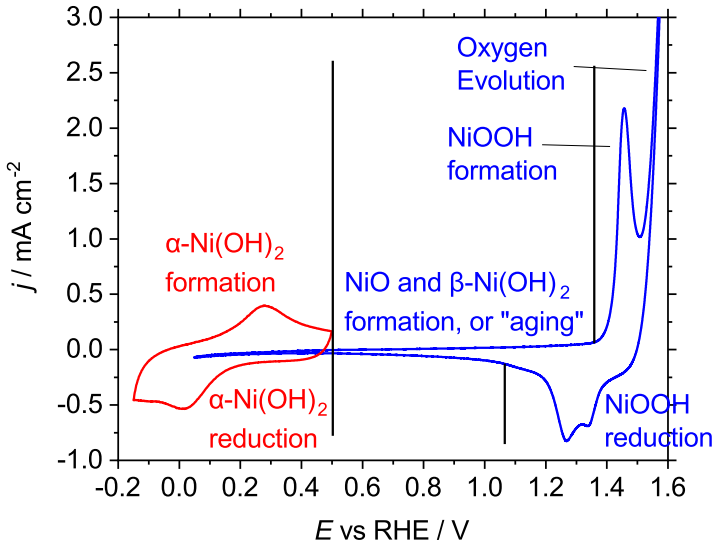

Figure 2.13: Two CVs for polycrystalline nickel highlighting different nickel oxide phases. Done in 0.5 M NaOH with sweep rate = 100 mV s^{-1}. The red CV is on a freshly electropolished surface from -0.15 V to 0.45 V vs RHE, this highlights the oxidation and reduction of the α-$Ni(OH)_2$ phase from pure Ni. The blue CV is on an aged electrode, having been cycled for several hours, and is from 0.05 V to 1.6 V vs RHE. This highlights the NiOOH formation and reduction from NiO and β-$Ni(OH)_2$, as well as the irreducible nature of the NiO and β-$Ni(OH)_2$ phases.

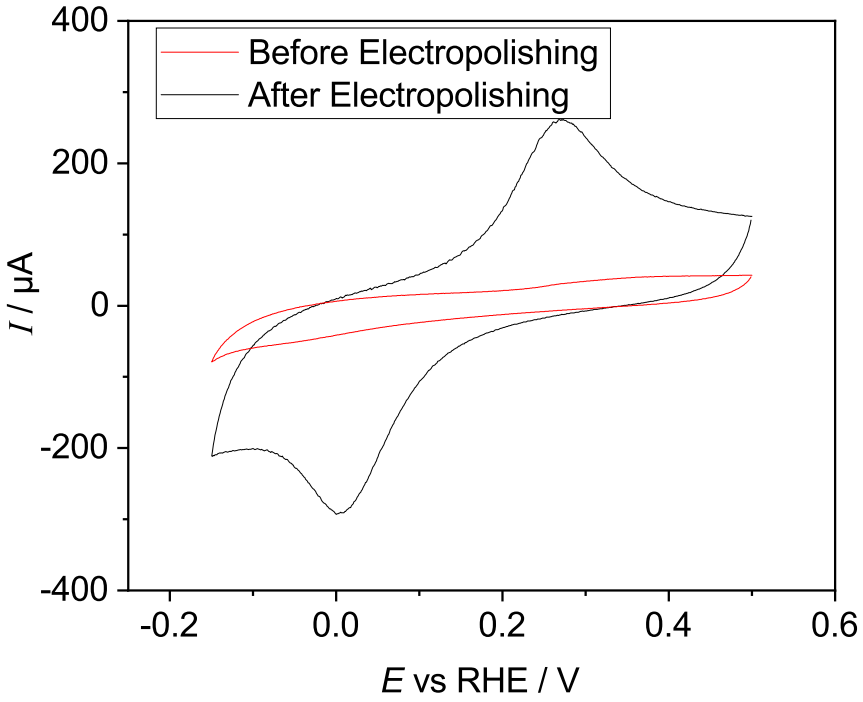

Figure 2.14: α-Ni(OH)$_2$ CV before and after polishing. Sweep rate = 100 mV s^{-1}.

After polishing, the electrode is removed from the electropolishing solution and rinsed thoroughly using Milli-Q water (18 MΩ cm). The electrode is then placed in a typical three-electrode system with argon purged 0.5 M KOH (Sigma, 99.99%) as the electrolyte. Care must be taken when transferring the electrode from the electropolishing solution, through the washing process, and into the KOH. Ideally, this process should take no more than ≈15 s. Special care must also be taken to ensure that potential control is maintained on the electrode from the moment it enters solution, otherwise the β-Ni(OH)$_2$ layer forms and electropolishing must be performed once more.

Once the electrode is in solution it is held at a potential of -0.2 V for 200 s and then at 0 V for 400 s. The first potential hold is performed in order to reduce any small amount of oxide or contaminant that may be on the surface, and the second potential hold is performed to oxidize any nickel hydride or trapped hydrogen gas that may have formed in the previous step. This ensures the α-Ni(OH)$_2$ formation takes place on a pristine Ni surface.

Cyclic voltammetry (CV) is then performed from -0.15 V to 0.45 V at a scan rate of 100 mV s^{-1}. This results in a clean CV of the α-$Ni(OH)_2$ peak (Fig. 2.14). The ECSA of the electrode can then be determined as follows using the charge density of α-$Ni(OH)_2$ formation for the second cycle

$$\begin{aligned} ECSA &= \frac{Q}{\sigma_{mono}} \\ &= \frac{\frac{Area_{Ox}}{s}}{514\ \mu C\ cm^{-2}} \end{aligned} \tag{2.29}$$

Where Q is the total charge passed during the oxidation process, $Area_{Ox}$ is the area under the oxidation peak, s is the sweep rate in V s^{-1}, and σ_{mono} is the charge density associated with forming a monolayer of α-$Ni(OH)_2$ [102]. The Q value for this procedure is typically acquired directly from the Gamry Echem Analyst integrate function by integrating all oxidative current for the second cycle, including the oxidative current on the reverse sweep.

Before integrating, a baseline correction is performed on the CV. A fixed current value is added to the whole CV so that integrating the entire CV gives 0 Ccm^{-2}. This method makes the assumption that capacitive charge is negligible, and that all oxidative and reductive charge after the baseline correction goes toward creating and subsequently reducing the α-$Ni(OH)_2$ layer implying that hydrogen evolution is a negligible reaction in these conditions. These assumptions are also made in the literature method on which this modified method is based [102]. The need for a baseline correction is likely due to trace amounts of oxygen gas dissolved in solution. The surface area determined by this method is used to normalize all relevant data (Section 2).

Lastly, it should be noted that while this method is the accepted method from literature it involves some inherently flawed assumptions. The value of 514 $\mu C\ cm^{-2}$ used in literature is actually based on a perfectly stoichiometric monolayer of OH^- being adsorbed onto Ni(100) to make α-$Ni(OH)_2$ [156, 157]. This fails to take into account two major factors.

First, the oxide undergoes an expansion as it is formed leaving fewer sites for reaction to take place. Nickel metal has a close packed face centered cubic structure, whereas $Ni(OH)_2$ has an expanded and layered structure (Fig. 2.15).

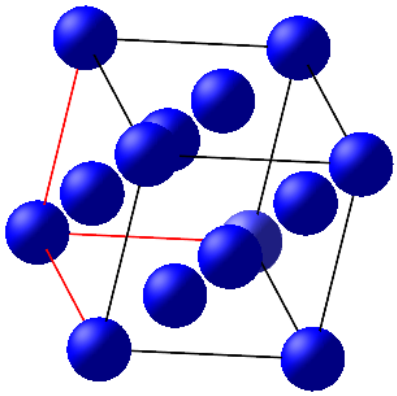

(a) The crystalline nickel unit cell. Nickel has a face centered cubic crystal structure.

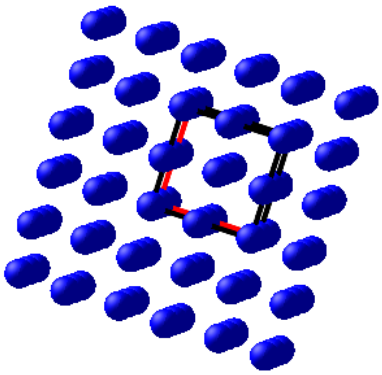

(b) A small nickel crystal cluster. This illustrates the close packing and structural difference from $Ni(OH)_2$.

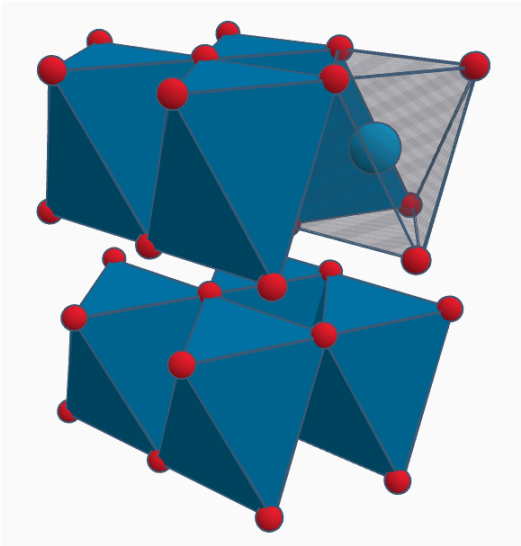

(c) An idealized $Ni(OH)_2$ structure. Nickel atoms (blue) appear at the center of oxygen octahedra (red) . The H atoms occupy the interlayer space but are not pictured for clarity.

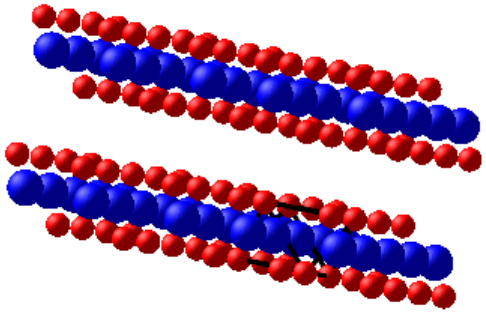

(d) A $Ni(OH)_2$ cluster. This illustrates the layered nature of the $Ni(OH)_2$.

Figure 2.15: Crystal structures of nickel metal and $Ni(OH)_2$. The distance between Ni atoms on a Ni(111) surface is 2.49 Å and the distance between Ni atoms in a layer of $Ni(OH)_2$ is 3.13 Åfor scale.

Second, the nickel used in this work is polycrystalline as opposed to a (111) crystalline surface. Ignoring the problems with the expansion of the oxide, the

amount of the surface occupied by each of Ni(100), Ni(110), Ni(111), and any facet contributions where these layers meet should be determined and the charge density associated with each surface should be used in proportion with their representation on the surface. Unfortunately at this point that is not practical, and even if it were the oxide expansion would convolute the issue even further.

2.4.1 Electropolishing

To electropolish the electrode a solution of 50% v/v phosphoric acid (ACS, Reagent Grade) in Milli-Q water (18 MΩ cm) is made, and the nickel electrode is used as the working electrode (WE) in a standard two-electrode system. A current density of $\approx$ 1 mA cm^{-2} is used to oxidize the electrode for 10 seconds. To determine the current required to achieve this current density the approximate geometric surface area of the electrode is used.

Chapter 3

Product Analysis of High Temperature Electrochemical Oxidation of Glycerol on Nickel

3.1 Introduction

In this chapter the self-pressurizing autoclave is used alongside a two-electrode electrochemical cell. This cell is used to perform glycerol electro-oxidation. Nickel foil electrodes are used to offer large surface areas in order to maximize the concentration of oxidation products formed. Alkaline glycerol solution is placed within the cell and current is passed for 48 h at various temperatures. The resulting solution is then analyzed via HPLC in order to determine the products of glycerol electro-oxidation and their relative selectivities. During the course of this project a polymer product was discovered. This polymer product was then characterized using various techniques including Attenuated Total Reflectance Infrared Spectroscopy, Nuclear Magnetic Resonance Spectroscopy, Dynamic Light Scattering, and Differential Scanning Calorimetry. No reference electrode (RE) was used in this experiment due to the instability of the reversible hydrogen electrode (RHE) at temperatures greater than 100 °C over long periods of time (>30 hrs). By designing the cell without a reference electrode higher temperatures were able to be probed during the long term oxidation, allowing the exploration of temperatures as high as 140 °C. This came at the cost of kinetic information, but ultimately facilitated the discovery of a novel polymer synthesis.

Converting glycerol to value added products has been a topic of significant interest [10, 11, 23, 26–30, 69, 72, 73, 77, 79, 158–161]. Many of these studies involve the use of complex nanostructured catalysts, or expensive noble metals [23, 27–29, 72, 73, 159, 160], often with some success. In order to make these processes more industrially viable, lower cost catalysts are desired.

Nickel based catalysts have been shown to be effective at oxidizing organics [21, 22, 79, 162–164], and given the low cost of nickel it is very viable to use on an industrial scale. Using polycrystalline nickel foils also avoids the stability issues associated with nickel nanostructures such as corrosion [123]. For these reasons nickel proves a strong candidate as an industrial electrocatalyst.

Product analysis of glycerol electro-oxidation has been performed before [10, 11, 27]. An exploration of this process at high temperatures is a novel idea, however. High temperature electrochemistry has been shown to exhibit many interesting behaviors [1, 8, 9, 131, 136–138, 148].

These factors combine to make the study of high temperature glycerol oxidation using simple nickel electrodes an obvious choice.

3.2 Experimental

3.2.1 Electrochemistry

Before any electrochemistry took place all labware was soaked in 80 °C concentrated sulfuric acid (Sigma, 95%) for 2 hr, and rinsed thoroughly with Milli-Q water. Electrochemistry was performed using a Gamry Reference 600 potentiostat. The surface area of the working electrode (WE) was determined using the method described in section 2.4 of this document.

For this experiment all cell design was geared towards maximizing product yield, and kinetic information was allowed to fall to the wayside. To this end a typical two-electrode electrochemical cell was built within the autoclave. The working electrode (WE) and counter electrode (CE) were 99.999% polycrystalline nickel wires (Alfa Aesar, Puratronic) with a $\geq$99.9% nickel foil (Sigma Aldrich) spot welded onto the end of the nickel wire in order to facilitate higher current densities. The WE was then lowered into a small glass chamber, the purpose of which was to prevent the diffusion of products into the bulk solution and to separate them from the counter electrode. This both served to concentrate the products as well as prevent them from

being reduced at the counter electrode.

All long term glycerol oxidation experiments were performed in 30 mL solutions of 0.1 M potassium hydroxide (KOH) (Sigma, 99.99%) and 0.1 M glycerol (Anachemia, ACS Grade). These solutions were purged with argon for 10 min after being transferred to the self-pressurizing autoclave. Once this purge was complete the autoclave was sealed shut. Current was held at 0 mA cm^{-2} during heating, and once temperature was reached current was held at 1 mA cm^{-2} for 48 h.

3.2.2 High-Performance Liquid Chromatography

The HPLC methodology used was modified from previous work [10]. The process was performed on an Agilent 1200 series HPLC system. Separation of the various alcohols was accomplished using an Aminex HPX-87H ion exclusion column held at 70 °C. This column separates compounds based on pK_a, with more acidic compounds moving through the column faster than less acidic ones. Sterics also play a factor in the separation, with smaller compounds spending a longer time on the column than larger ones. Elution was isocratic using a solution of 5 mM Sulfuric Acid at 0.500 mL/min. Injection volume was 20 μL and compound detection was performed using a UV-Vis detector analyzing absorbance at 210 nm.

Peak assignments and quantitative compound concentrations were determined by comparing the retention times and peak areas with those of standards of known concentration (Fig. 3.2). Calibration curves of all relevant compounds were created in order to facilitate this (Fig. 3.1). All solutions for calibration curves were made using HPLC grade chemicals from Sigma Aldrich.

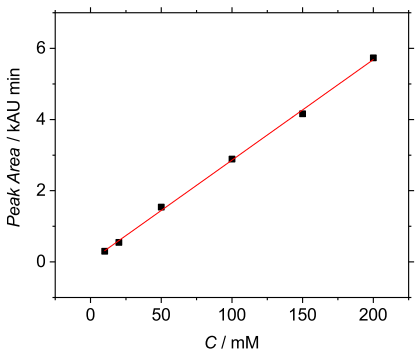

(a) Formic acid

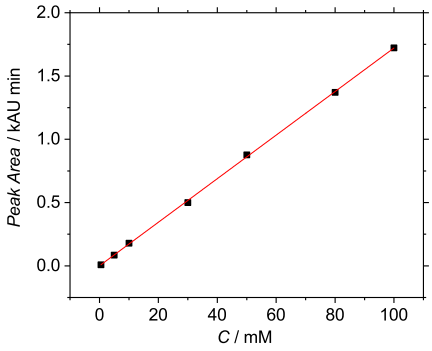

(b) Glyceric Acid

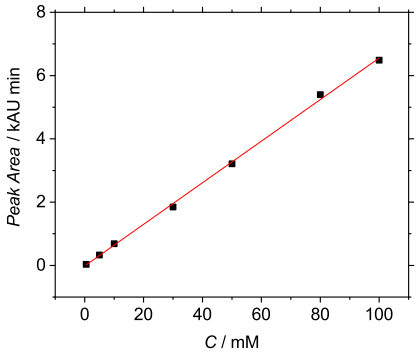

(c) Glycolic Acid

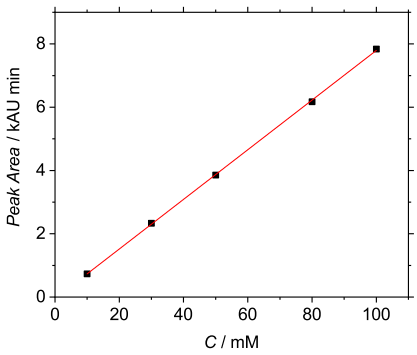

(d) Lactic Acid

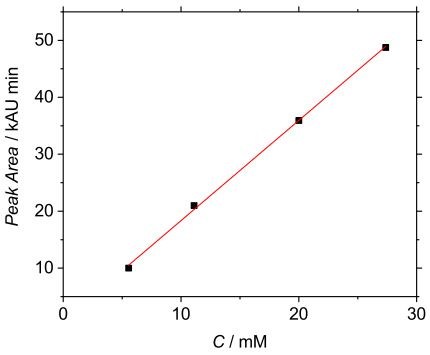

(e) Oxalic Acid

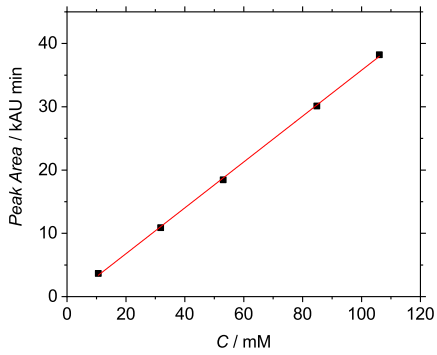

(f) Tartronic Acid

Figure 3.1: HPLC calibration curves.

Compound	Slope / kAU min mM^{-1}	Intercept / kAU min	R^2
Formic Acid	$2.826 \times 10^{-2} \pm 5 \times 10^{-4}$	$3 \times 10^{-2} \pm 5 \times 10^{-2}$	0.99851
Glyceric Acid	$1.72 \times 10^{-2} \pm 1 \times 10^{-4}$	$3 \times 10^{-4} \pm 6 \times 10^{-3}$	0.99971
Glycolic Acid	$6.6 \times 10^{-2} \pm 1 \times 10^{-3}$	$-2 \times 10^{-2} \pm 5 \times 10^{-2}$	0.99859
Lactic Acid	$7.85 \times 10^{-2} \pm 6 \times 10^{-4}$	$-5 \times 10^{-2} \pm 4 \times 10^{-2}$	0.99977
Oxalic Acid	$1.76 \pm 4 \times 10^{-2}$	$7 \times 10^{-1} \pm 7 \times 10^{-1}$	0.99872
Tartronic Acid	$3.62 \times 10^{-1} \pm 4 \times 10^{-3}$	$-5 \times 10^{-1} \pm 3 \times 10^{-1}$	0.99954

Table 3.1: Calibration curve data for HPLC standards. All fits were performed in OriginPro 2018 using the Linear Fit algorithm. Slope and Intercept refer to the slope and intercept of a $y = mx + b$ line equation.

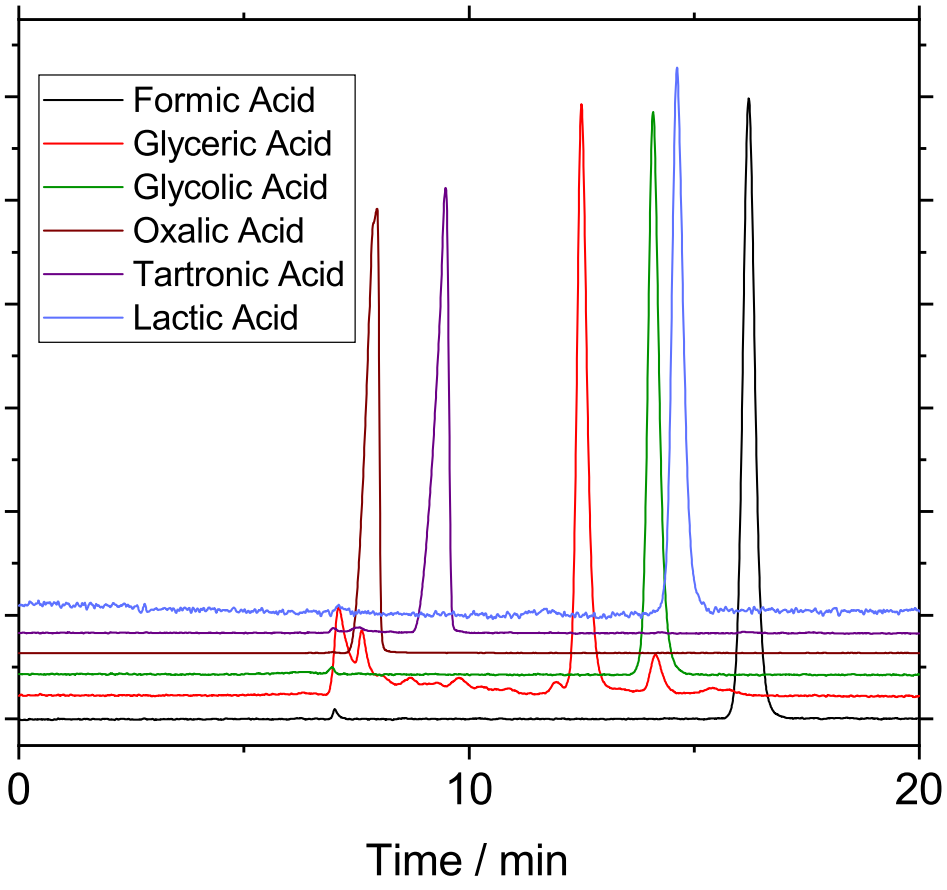

Figure 3.2: HPLC traces of individual HPLC standards. Glyceric acid can be seen to have dissociated due to the alkaline solution used to make the standard.

3.2.3 Attenuated Total Reflectance Infrared Spectroscopy and Solid State Nuclear Magnetic Resonance

Attenuated total reflectance infrared (ATR-IR) spectroscopy was performed using a Perkin Elmer Spectrum Two FT-IR Spectrometer. A background scan of ambient air was taken, solid sample was placed on the detector, and the sample was pressed so that the system force gauge read 100.

Solid state nuclear magnetic resonance (NMR) was performed on a Bruker Avance III 400 using a 2.5 mm probe. 10 mg of sample was used in the collection of NMR data. Experiments include ^{1}H NMR and ^{1}H-^{13}C cross polarization magic angle spinning (CP-MAS) NMR.

3.2.4 Dynamic Light Scattering

Dynamic Light Scattering (DLS) was performed using a Zetasizer Ultra. Polymer samples were prepared in a 10 mM KNO_3 solution. Solution was made up with Milli-Q water and passed through a 0.2 μm cellulose acetate sterile syringe filter. The polymer was added after filtration so that no filtering of the polymer was performed. KNO_3 was used to screen electrostatic interactions between polymer particles to prevent aggregation. A measured amount of polymer was placed in a vial and KNO_3 solution was added. This vial was then sonicated for 2 hours at 40 °C. Samples were tested at both 0.25 mg mL^{-1} and 2 mg mL^{-1}.

3.2.5 Differential Scanning Calorimetry

Differential Scanning Calorimetry (DSC) was performed using a TAInstruments DSC25. 3 mg was the minimum sample size used. All temperature ramping was performed at 10 °C min^{-1}. High purity Nitrogen (PraxAir, 99.998%) was used to continuously purge the test chamber.

3.3 Results and Discussion

3.3.1 Effects of temperature on the electro-oxidation pathway

An ideal and complete oxidation of glycerol to CO_2 is a 14 electron process

$$C_3H_8O_3 + 3\,H_2O \longrightarrow 3\,CO_2 + 14\,H^+ + 14\,e^- \tag{3.1}$$

but in practice several products are seen when performing glycerol oxidation on nickel in alkaline solutions including oxalic acid, tartronic acid, glyceric acid, glycolic acid, formic acid, and lactic acid (Fig. 3.3, Table 3.2) [10, 29, 69, 72]. Unfortunately, due to the necessity of a self-pressurized autoclave, aliquots for the high temperature processes can only be taken after the oxidation has completed and the cell has been cooled to room temperature.

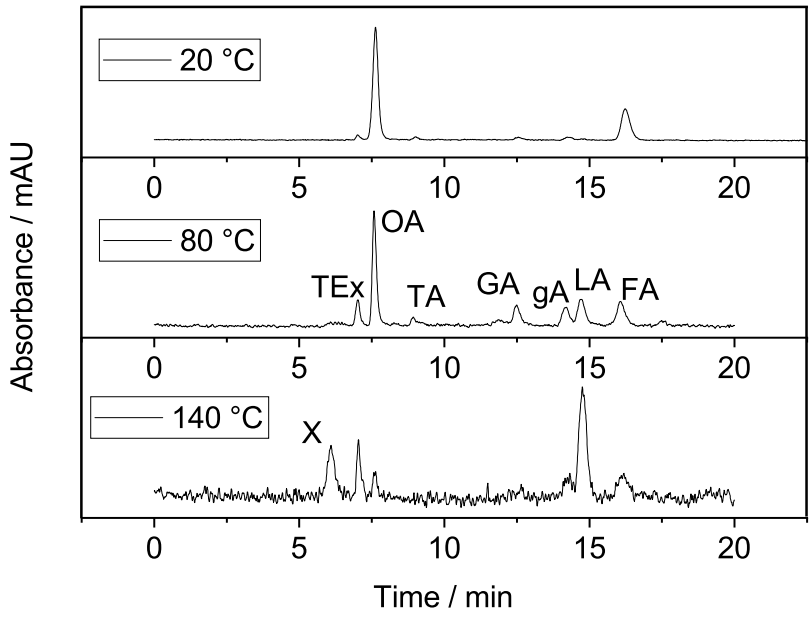

Figure 3.3: HPLC spectra highlighting product selectivity of glycerol oxidation at various temperatures. All trials were run at 1 mA cm^{-2} for 48 h.
FA = Formic Acid, LA = Lactic Acid, gA = Glycolic Acid,
GA = Glyceric Acid, TA = Tartronic Acid, OA = Oxalic Acid,
TEx = Total Exclusion Peak, X = Polymer Product

	Product Percentage at RT	Product Percentage at 80 °C	Product Percentage at 140 °C
Oxalic Acid	4.8	0.4	-2.6
Tartronic Acid	4.4	7.1	0.0
Glyceric Acid	4.9	11.9	2.7
Glycolic Acid	0.4	10.7	-1.9
Lactic Acid	0.0	20.5	50.6
Formic Acid	85.6	49.4	56.6

Table 3.2: Product selectivity of glycerol oxidation at various temperatures. Product concentrations were determined after 48 h oxidations. Negative values at 140 °C are due to a very small amount of product being in solution due to the formation of a polymer. This polymer appears to be a new discovery and is not discussed in the literature. Values for the 140 °C oxidation neglect the presence of the polymer product, as their composition is unknown. These factors make the error for the 140 °C trial very high.

Combining HPLC results and data from the literature a glycerol oxidation pathway emerges (Fig. 3.4).

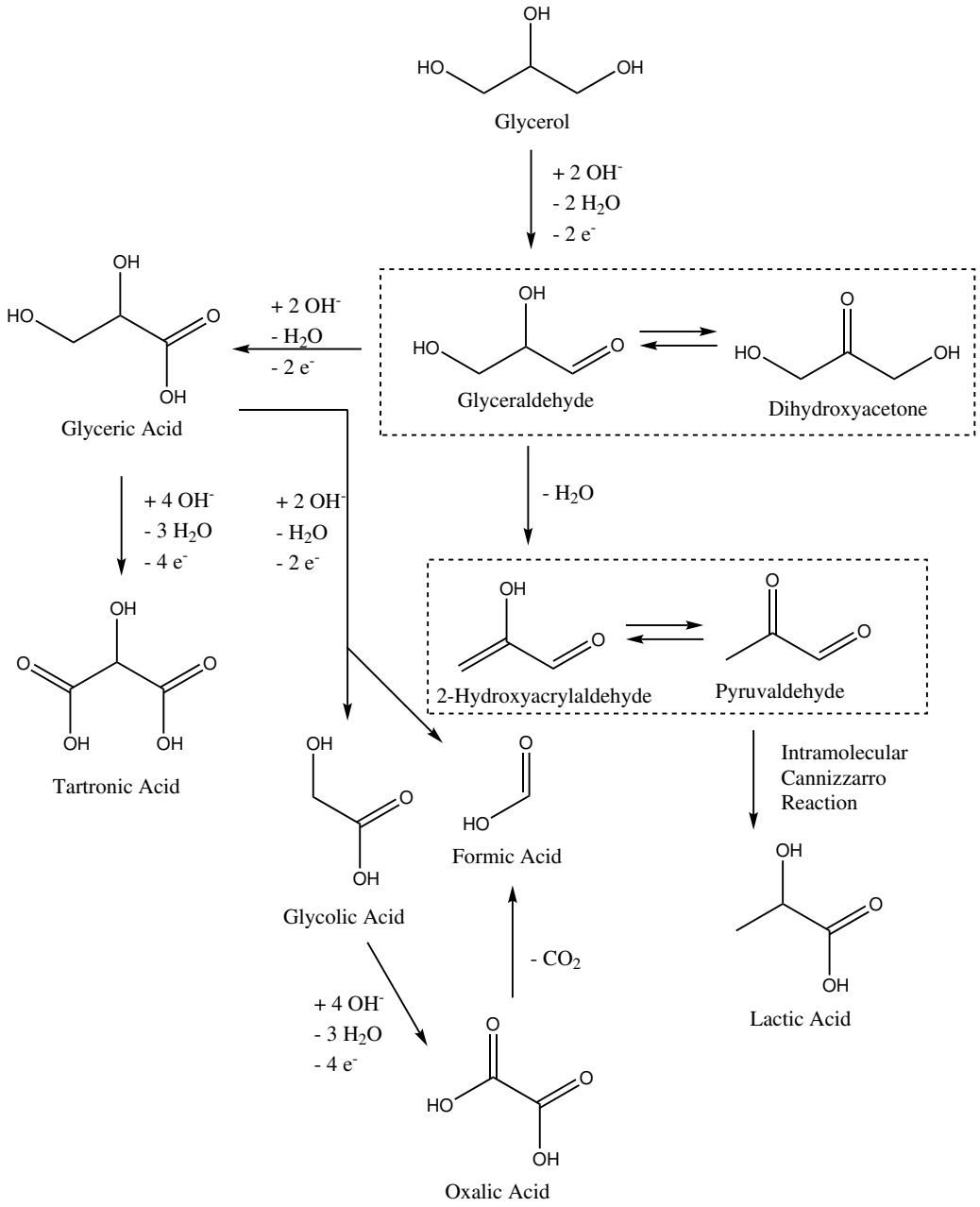

Figure 3.4: A likely glycerol oxidation pathway based on literature and HPLC findings [10, 20, 29, 69, 69, 70, 72–77, 165–167]. Note that the focus of this pathway is to describe the means by which HPLC identified products are formed.

Glyceraldehyde is prevalent in this pathway and while it has been shown previously that glyceraldehyde is one of the main products seen at the electrode surface upon oxidizing glycerol along with some unidentified carboxylate species, likely glyceric

acid [10, 20, 27], the HPLC data shows no trace of glyceraldehyde. This is because glyceraldehyde is very unstable in alkaline solution (Fig. 3.5).

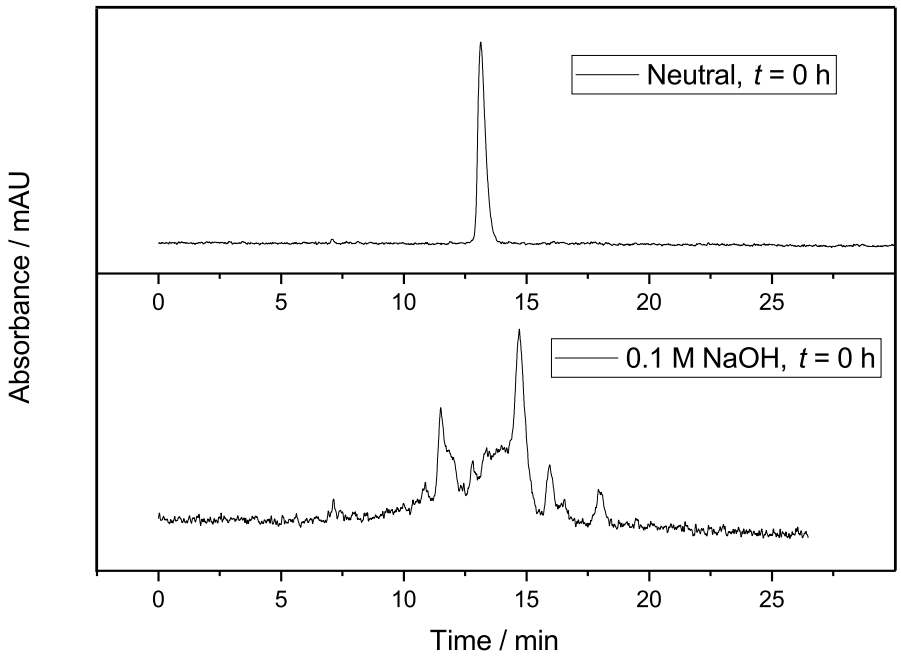

Figure 3.5: HPLC Spectra highlighting glyceraldehyde instability in alkaline solution. Neutral solution is 0.266 M glyceraldehyde in Milli-Q water. Basic solution is 5.33 mM glyceraldehyde in 0.1 M NaOH. Both HPLC spectra were taken quite shortly after having made the solutions.

The suggested pathway also highlights the nature of the concentration dependence of lactic acid on temperature. Glycerol is oxidized to glyceraldehyde, which is then further oxidized to glyceric acid. However there is also a competing, non-electrochemical pathway where glyceraldehyde is dehydrated to 2-hydroxyacrylaldehyde and continues to react, finally reaching lactic acid. As the temperature of the reaction vessel increases this dehydration becomes faster, until eventually the lactic acid pathway is in competition with the glyceric acid pathway.

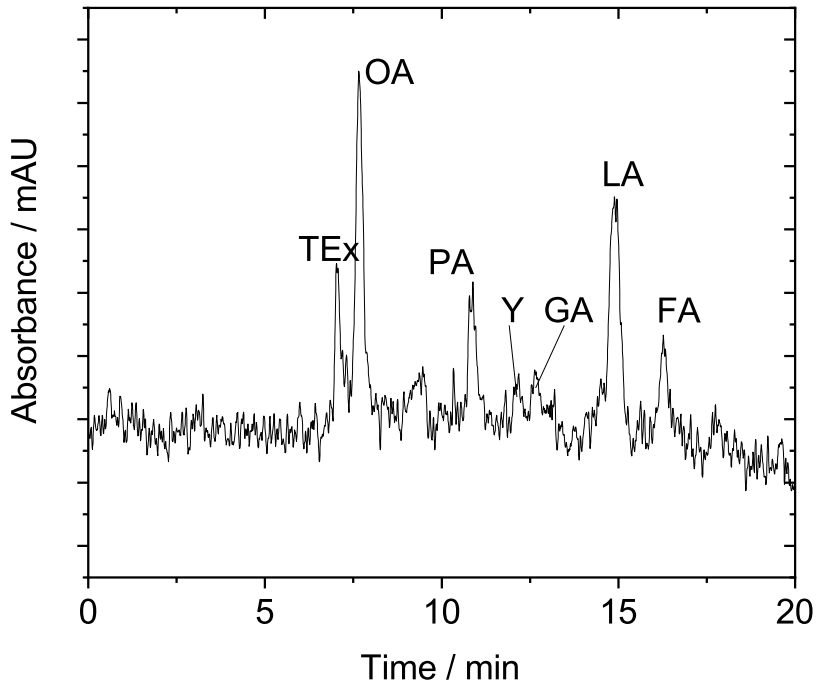

Figure 3.6: HPLC Spectra highlighting glyceraldehyde speciation in alkaline solution at high temperatures. Solution is 5.33 mM glyceraldehyde in 0.1 M NaOH. Solution has been heated at 140 °C for 48 h. No electrochemistry has been done.
FA = Formic Acid, LA = Lactic Acid GA = Glyceric Acid,
Y = Unknown Species, OA = Oxalic Acid, PA = Pyruvic Acid,
TEx = Total Exclusion Peak

This can be shown using a control test where 5.33 mM of glyceraldehyde was heated at 140 °C in 0.1M NaOH solution for 48 h (Fig. 3.6). The presence of formic acid, glyceric acid, and oxalic acid in this reaction mixture indicates that the glyceric acid pathway is not a strictly electrochemical pathway at these temperatures. Additionally, the presence of lactic acid and pyruvic acid is indicative of the lactic acid pathway. It is likely that the pyruvaldehyde in solution is unstable much like glyceraldehyde, and reacts to form pyruvic acid. The fact that this is not seen in electrochemical trials suggests that the applied potential has some affect on preventing the buildup of pyruvaldehyde. Alternatively, the presence of pyruvaldehyde could also be a function of a large amount of glyceraldehyde existing in solution at once, as opposed to small amount being made over time at the electrode. Of note here

is that while a true and total carbon balance cannot be performed on this data due to the existence of an unknown species, Y, 4.52 mM of lactic acid has been made. This is quite a high selectivity, containing 84.8% of the carbon atoms contained in the original 5.33 mM glyceraldehyde solution.

3.3.2 High temperature glycerol electro-oxidation polymer product analysis

Having identified the likely oxidation pathways and all the major products of the glycerol oxidation, it is now important to address the formation of a polymer during the 140 °C glycerol oxidation trial, which was mentioned briefly in Fig. 3.3 and Table 3.2. This polymer appears to be a new discovery, and is not discussed in the literature. The polymer appeared as a cloudy white suspension in solution, and was separated from solution by centrifugation at 18000 g in 1.5 mL Eppendorf centrifuge tubes. The polymer synthesis was reproducible with a yield of 4-6 mg. The remaining supernatant solution was passed through a syringe filter (VWR, 0.2 μm, cellulose acetate) and tested by HPLC resulting in the 140 °C HPLC spectrum in Fig. 3.3. The peak in the figure labeled X is likely caused by polymers chains that managed to pass through the syringe filter. This is possible because while the polymer chains may be large, when solvated they typically curl into small "hairy spheres." This can facilitate the passing of large polymer molecule through small-pore filters.

Control experiments were performed in order to prove the necessity of an electrochemical driving force for polymer formation. The first type of control experiment was done using the same conditions, but with a piece of nickel foil placed in solution and no potential control. The second type of control experiment used a piece of nickel foil in solution with conditions kept consistent, but this time used a solution of 5 mM glyceraldehyde as the starting solution. This solution was chosen because of the glyceraldehyde speciation shown previously (Fig. 3.6). No polymer product was formed in either case, confirming that the polymerization process is electrochemically driven.

In an attempt to simplify the reaction vessel design the experiment was also performed using a larger volume, 100 mL instead of 30 mL, in the reaction vessel with all other conditions kept the same. In this experiment no polymer formed, suggesting that there is a critical concentration of alcohols that must be achieved before polymerization can occur. Further evidence of this is suggested by the

chronopotentiometry results discussed in Section 3.3.2.4).

The polymer does not dissolve easily suspend or dissolve in THF, DMSO, or water despite heating and sonication. By placing a small amount of polymer (<2 mg) in a solution of 10 mM KNO_3 and sonicating at 40 °C for 2 hours a suspension was formed, though some small amount of unsuspended polymer remained at the bottom of the sample vial. This solution was used to perform DLS. The difficulty dissolving the polymer in solution limits the techniques available for polymer analysis as many of them require a solution state. Large polymer chains are more energetically demanding to solvate, even more so when they are cross-linked as this prevents the polymer chains from fanning out in solution thereby reducing the surface area available for solvation to occur. This indicates the polymer is likely quite large and cross-linked. The presence of compounds with three or more functional groups in the reaction mixture make this a possibility [168].

3.3.2.1 Dynamic Light Scattering Analysis

Dynamic light scattering (DLS) was performed on the polymer sample (Fig. 3.7) to determine the solvated size of the polymer in solution. Correlograms collected by ZS Xplorer were processed in ZS Xplorer using the cumulant method [169] to obtain size/intensity plots. The polydispersity index as determined by the cumulant method was 18.23. Intensity in the DLS spectrum is determined by the number of photons counted at the detector caused by scattering of light off polymer particles. Because larger particles scatter more light the intensity plot inherently skews towards larger particles.

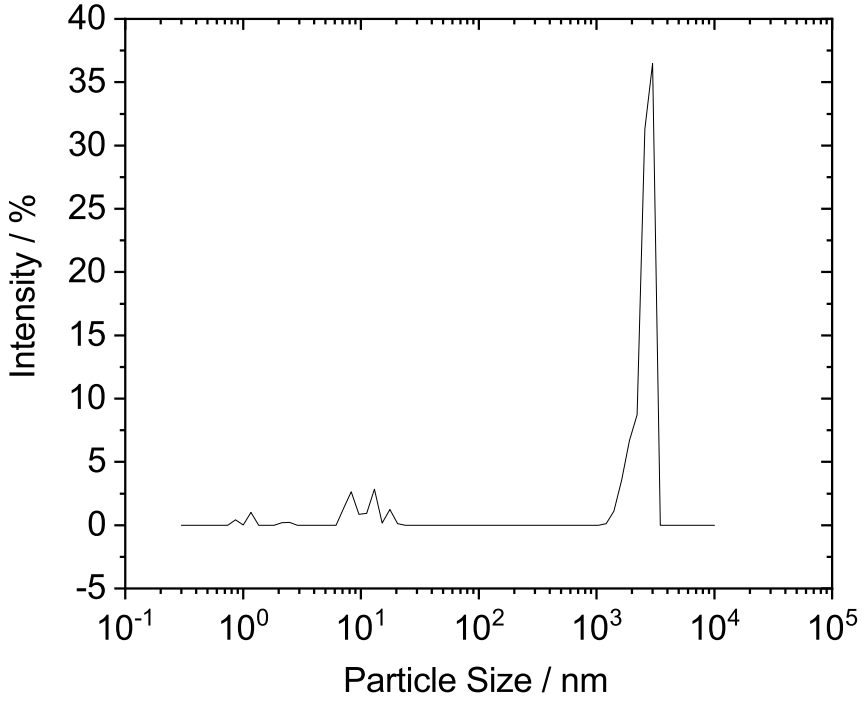

Figure 3.7: DLS results for polymer samples. Three separate polymer samples were made by performing the 140 °C glycerol oxidation procedure (Section 3.2.1). Each of these samples were suspended in a 10 mM KNO_3 in Milli-Q water solution and DLS was performed. Four runs were performed on three different samples, and the intensity distributions of all twelve runs were averaged to give the resulting DLS trace. Two samples were run at 0.25 mg mL^{-1} and the third was run at 2 mg mL^{-1}, however the results appear unnaffected by this. Peaks appear at 2990 nm, 17.66 nm, 13.06 nm, 8.302 nm, 2.134nm, 1.167 nm, and 0.863 nm. There appear to be three discrete size populations: 0.5 nm to 2 nm, 6 nm to 24 nm, and 1040 nm to 4040 nm.

Particle Size / nm	Mean Size / nm	Standard Deviation / nm
0.5 to 2	1.353	0.5388
6 to 24	11.25	3.443
1040 to 4040	2604	416.6

Table 3.3: Polymer sample DLS size data.

3.3.2.2 Differential Scanning Calorimetry Analysis

DSC was performed (Fig. 3.8) according to the method established previously (Section 3.2.5). The initial run was performed from 40 °C to 400 °C, cooled to -40 °C, then heated back to 400 °C. This revealed three separate endothermic transitions found at 139 °C, 167 °C, and 216 °C, and one broad exothermic feature above 250 °C. No features were observed during the cooling process, nor were any features observed on the subsequent heating. This indicates that some sort of thermal degradation took place that destroyed the polymer.

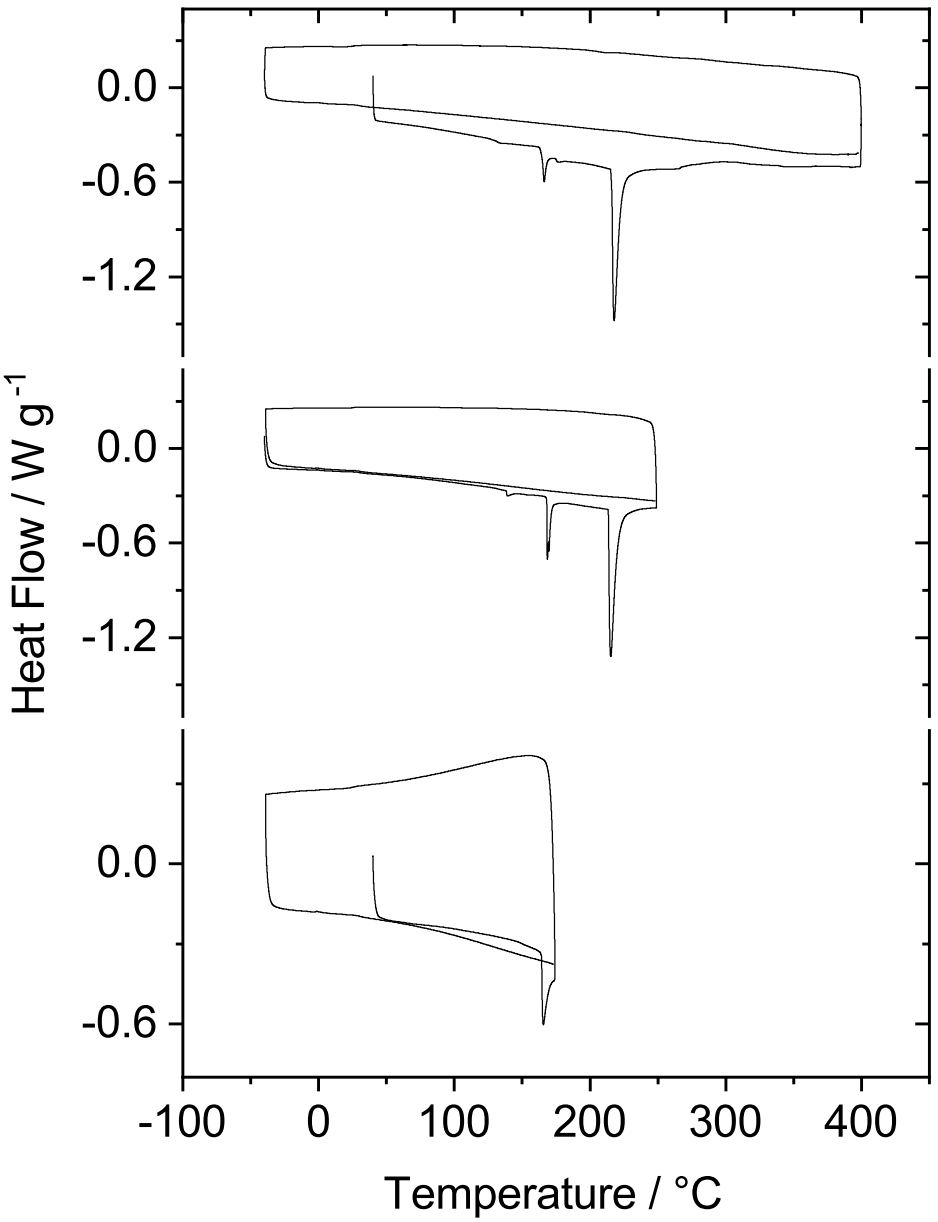

Figure 3.8: DSC results for polymer samples. Trials were run using a minimum 3 mg with ramping set at 10 °C min^{-1}.

Another trial was performed starting from -40 °C to 250 °C. The starting temperature was chosen as it allows the observation of transitions below 40 °C without having to worry about thermal degradation. The upper temperature limit was chosen

to avoid the exothermic transition occurring at approximately 300 °C. Subsequent cooling and heating again showed no features, indicating that the peak at 216 °C was due to thermal degradation. This likely means that the exothermic feature above 250 °C on the first trial is due to the measurement of minor fluctuations in heat flow between the sample cup and the reference after total thermal degradation of the sample had occurred.

In order to determine the nature of the peaks at 139 °C and 167 °C, another trial was performed. This trial was heated to 175 °C from a starting point of 40 °C. Once again subsequent heating and cooling showed no features, indicating that the peak at 167 °C was also thermal degradation. No features were seen at 139 °C as had been seen previously.

The DLS and DSC data taken together describe a sample containing polymer of three distinct populations, each with no visible glass transition temperature, crystallization temperature, or melting temperature. That is to say, it appears that each of the three endothermic peaks is caused by thermal degradation. The absence of the peak at 139 °C in the 175 °C temperature trial is explained by the relatively low abundance of the smallest size population found in DLS. The data also supports the notion of a thoroughly cross-linked polymer, as the glass transition temperature of a polymer correlates with its degree of cross-linking. A sufficiently cross-linked polymer can show no glass transition temperature at all [170, 171]. If no glass transition occurs then no crystallization or subsequent melting can occur, which explains the lack of features present.

The temperature at which thermal degradation occurs for a polymer is dependent on the types of reactions involved in the degradation process, and the relevant bond energies in those reactions [172]. Additionally, DSC peaks can be integrated to determine the amount of polymer responsible for each peak (Table 3.4). Without knowing the exact structure and relevant degradation reactions responsible for the peaks its impossible to draw a direct comparison between them, however a qualitative assessment can be made. Integration was performed using Origin. The settings used were as follows: baseline was set using the second derivative at full plot range; the smoothing of which was an adjacent averaging with window size 1, threshold 0.05, and maximum anchor points set to 8. Integration was performed on the 400 °C trial.

Degradation Temperature / °C	Peak Area / W g^{-1} °C
139	0.14
167	0.42
216	5.6

Table 3.4: Processed DSC integration data.

The overall trend in population distribution determined by DSC agrees rather well with the distribution determined by DLS. No absolute value can be determined for the distributions generated by either experiment, however there does appear to be three distinct polymer structures and three distinct polymer size populations. It is possible that three similar but separate polymer structures are being synthesized simultaneously, with each structure having a distinct equilibrium size.

3.3.2.3 Infrared Spectroscopy and Nuclear Magnetic Resonance Analysis

Solid state methods described in section 3.2.3 were used to collect ATR-IR spectra (Fig. 3.9). Four notable peaks were observed, including a peak at 3300 cm^{-1} indicating the presence of O−H stretching, a peak at 1633 cm^{-1} indicating the presence of either C=C stretching or heavily conjugated C=O stretching, a peak at 1004 cm^{-1} indicating the presence of C−O stretching, and a peak at 651 cm^{-1} indicating the presence of C=C bending.

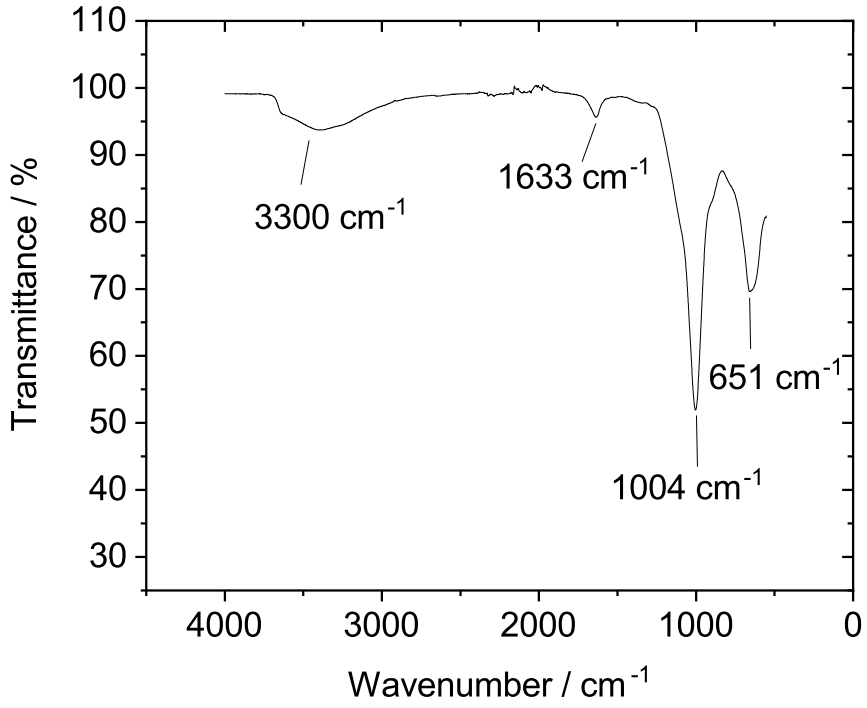

Figure 3.9: Polymer ATR-IR spectrum. Spectrum was taken on solid state sample with an air background.

The identity of the peak at 1633 cm^{-1} in the ATR-IR can be confirmed using NMR spectroscopy. ^{1}H-^{13}C CP-MAS NMR analysis (Fig. 3.10b) shows the presence of C−O bonds (Table 3.6). Due to the poor signal-to-noise ratio caused by the small sample sizes, the C=C peak in the ^{1}H-^{13}C CP-MAS appears difficult to read. The possible peak location has been highlighted, but its differentiation from the baseline cannot be guaranteed. That said, there appears to be no carbonyl peaks present in the ^{1}H-^{13}C CP-MAS spectrum. These would typically be found above 160 ppm.

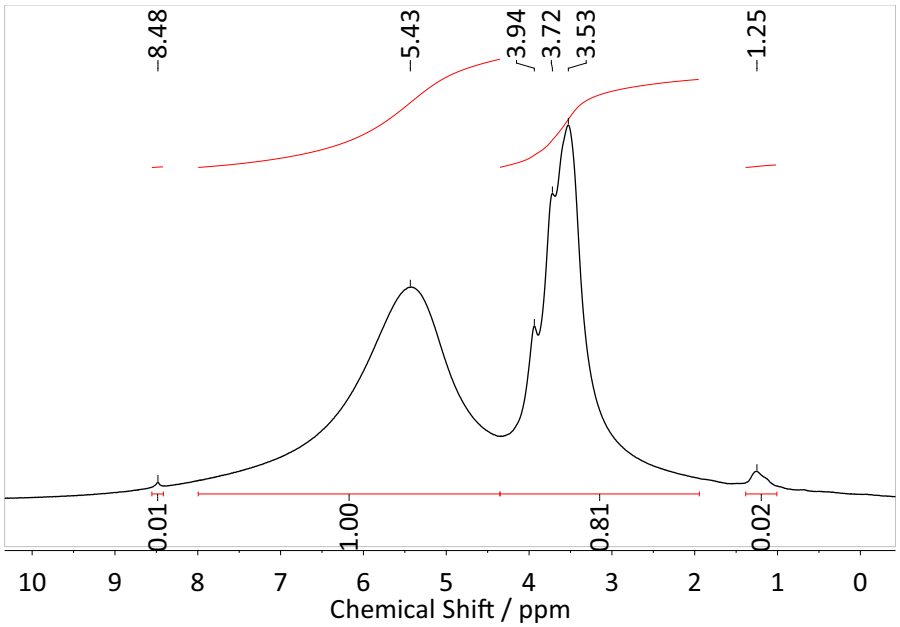

(a) ^{1}H NMR

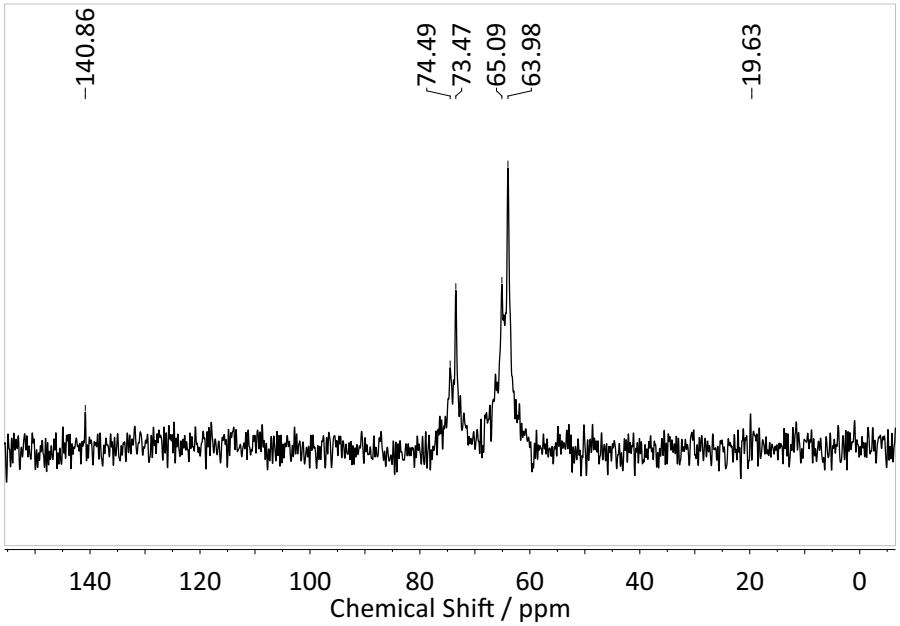

(b) ^{1}H-^{13}C CP-MAS NMR

Figure 3.10: Polymer NMR spectra. (a) ^{1}H NMR, (b) ^{1}H-^{13}C CP-MAS NMR. Peak broadening occurs in the ^{1}H NMR spectrum due to anisotropic interactions caused by the fixed bond orientation involved in solid state NMR. The low signal-to-noise ratio in the ^{1}H-^{13}C CP-MAS NMR is caused by the small sample size.

Chemical Shift / ppm	Assignment	Relative Integration
1.25	C−C−**H**	0.02
3.53	O−C−**H**	
3.72	O−C−**H**	0.81
3.94	O−C−**H**	
5.43	O−C−**H**, anomeric	1
8.48	C=C−**H**, α or β to O	0.01

Table 3.5: ^{1}H NMR Polymer Peak Assignments

Chemical Shift / ppm	Assignment
19.63	Possible Alkyl **C**−R_3 Peak
63.98	**C**−O
65.09	**C**−O
73.47	**C**−O
74.49	**C**−O
140.86	Possible **C**=C Peak

Table 3.6: ^{1}H-^{13}C CP-MAS NMR Polymer Peak Assignment

3.3.2.4 Chronopotentiometry Analysis

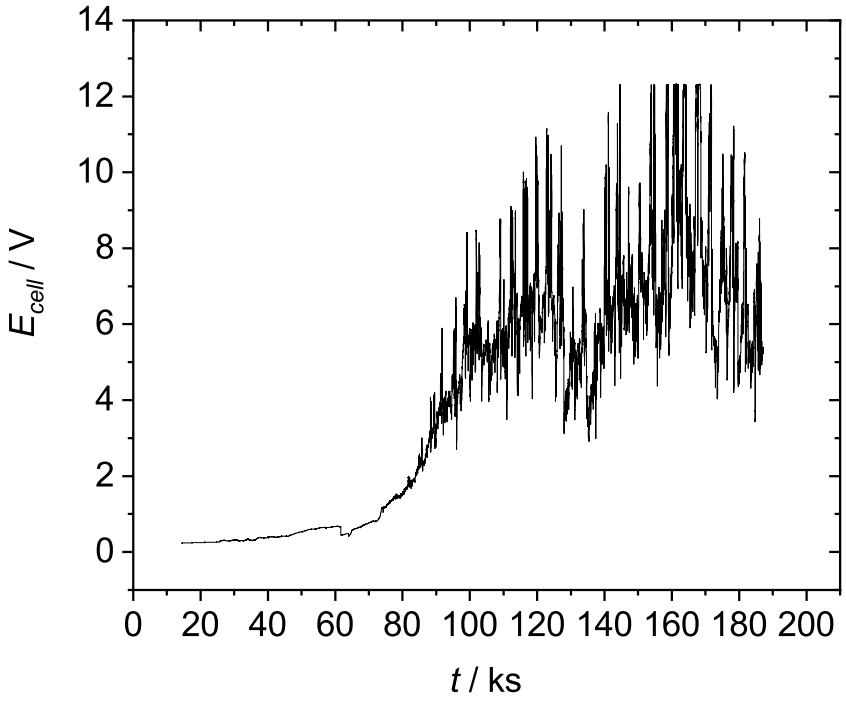

Figure 3.11: Polymer synthesis chronopotentiometry experiment. During heating, current was held at 0 mA cm^{-2}. Once 140 °C was reached, current was held at 1 mA cm^{-2}. The 1 mA cm^{-2} hold was performed for 48 h and is shown here. This experiment was performed using a two-electrode setup, with the counter electrode used as a pseudo reference electrode.

The CE will evolve hydrogen during the oxidation, acting as a pseudoreference electrode during the long term oxidation process. This pseudoreference may experience some drift due to the nature of the two-electrode setup, but most of the cell potential change will be at the working electrode. There is a large potential increase observed starting at 80 ks in the chronopotentiometry experiment during polymer synthesis. This effect is due to bulky polymer chains blocking the electrode surface. Electrochemical activity is required for polymer synthesis to occur which indicates that the formation of the polymer occurs at or near the electrode surface. It also shows that a critical concentration of products must be synthesized before polymerization occurs given that the potential increase begins at 80 ks.

3.3.2.5 Polymer Synthesis Mechanism and Structure Proposal

In Fig. 3.4 a likely chemical path is described for the formation of products identified by HPLC. It is important to understand that these do not make up all compounds present in solution, especially at high temperatures. There are likely many transient species in solution that exist only at high temperatures (Fig. 3.12).

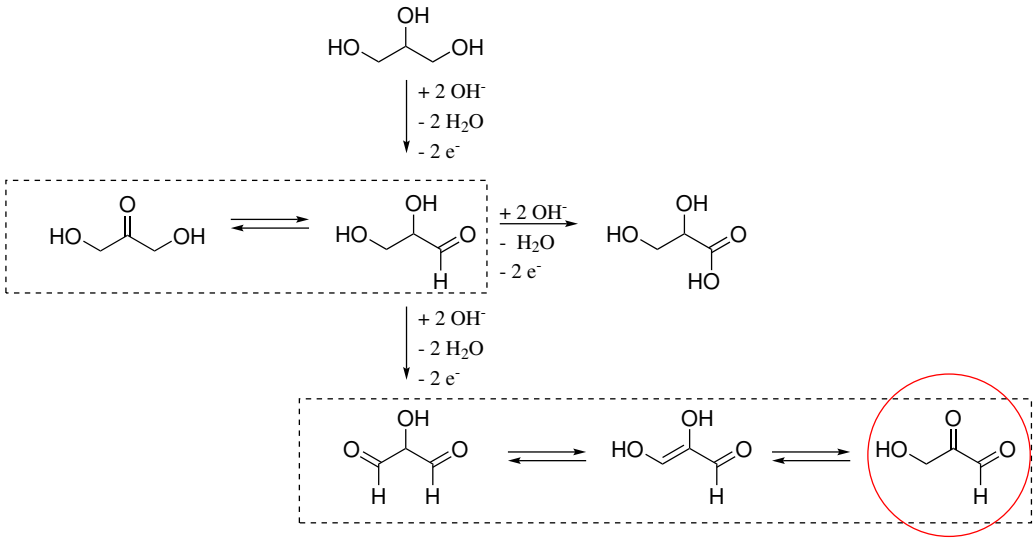

Figure 3.12: Some likely three carbon transient species in solution. The compound circled in red is a particularly strong aldol reaction candidate. This list is not exhaustive

The presence of aldehyde groups in solution in this and similar systems has been noted in the literature [20, 27, 28, 58]. These groups are known to undergo aldol reactions under alkaline conditions. An aldol reaction involves the joining of two compounds, each with a carbonyl group. Here aldehyde groups provide the reactivity, with the resulting product containing a carbon backbone and retaining a single aldehyde group (Fig. 3.13).

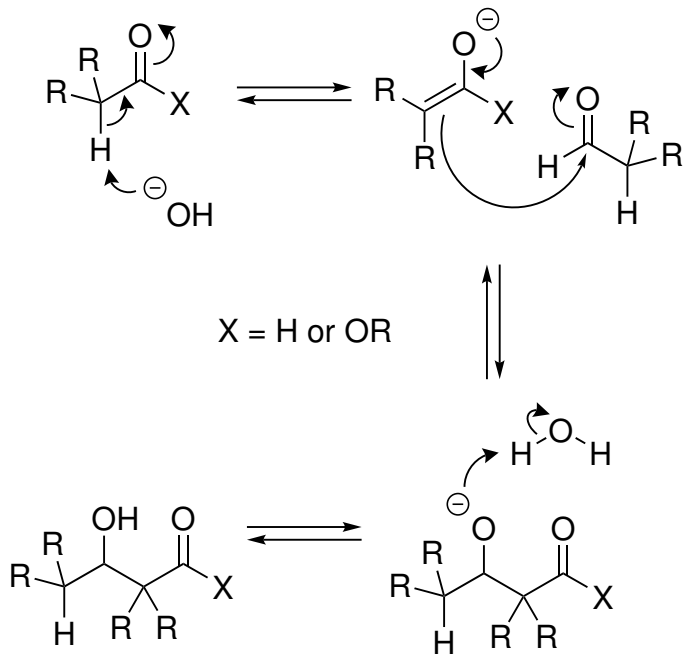

Figure 3.13: Aldol reaction mechanism. The resulting product has a carbon backbone and retains an aldehyde group through which subsequent aldol reactions can take place.

Other mechanisms considered for the polymerization reactions include esterifications, conjugate additions, and hemi-acetal formations. Each of these was found to be unlikely in alkaline solutions, given the constituent compounds present in solution (Fig. 3.14).

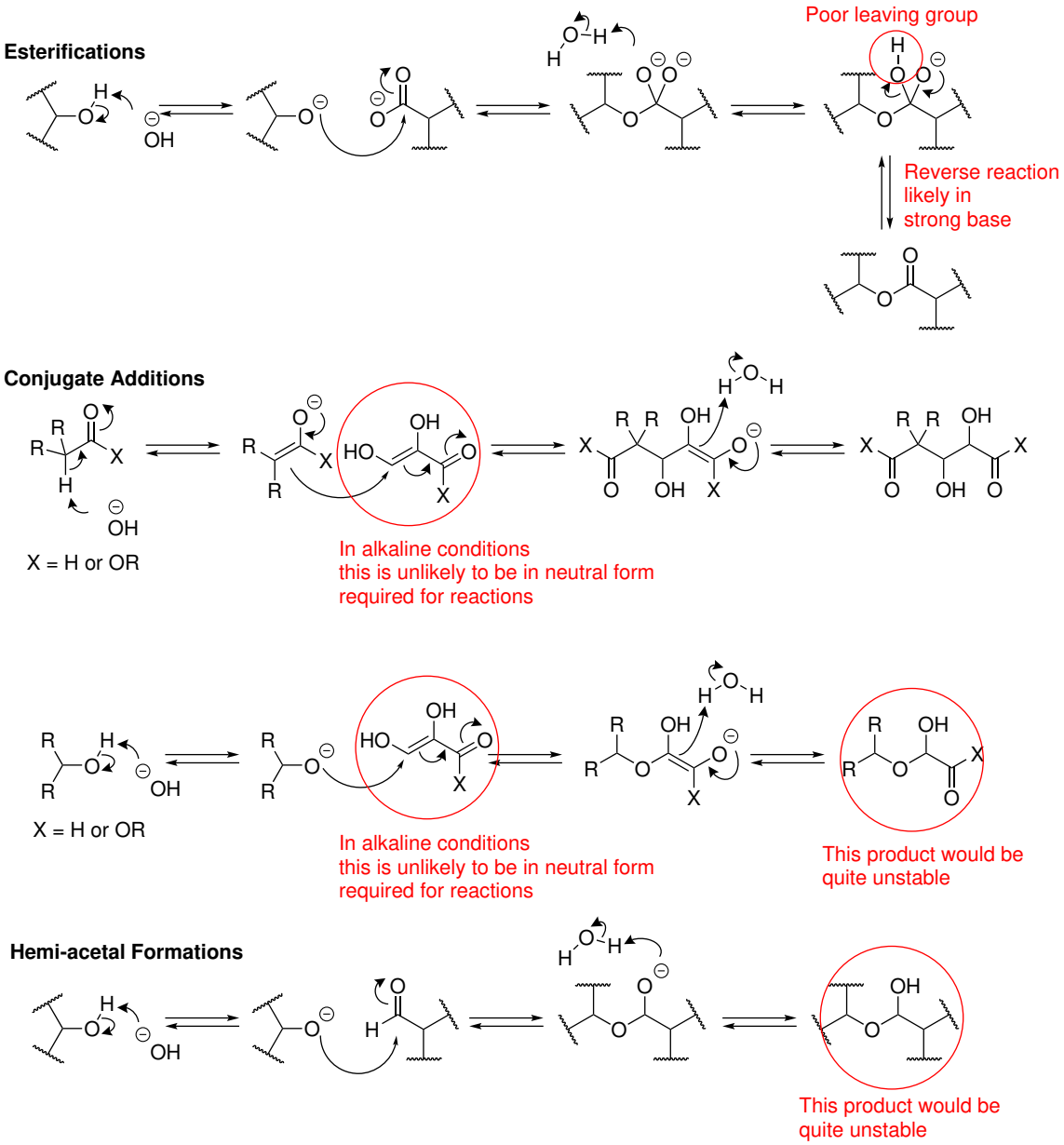

Figure 3.14: Polymerization reactions considered. Problems with each mechanism given the current reaction conditions are shown in red.

Elimination reactions can also be shown to be uncommon given the reaction conditions and constituent polymer compounds (Fig. 3.15). This makes them unlikely candidates for polymer synthesis.

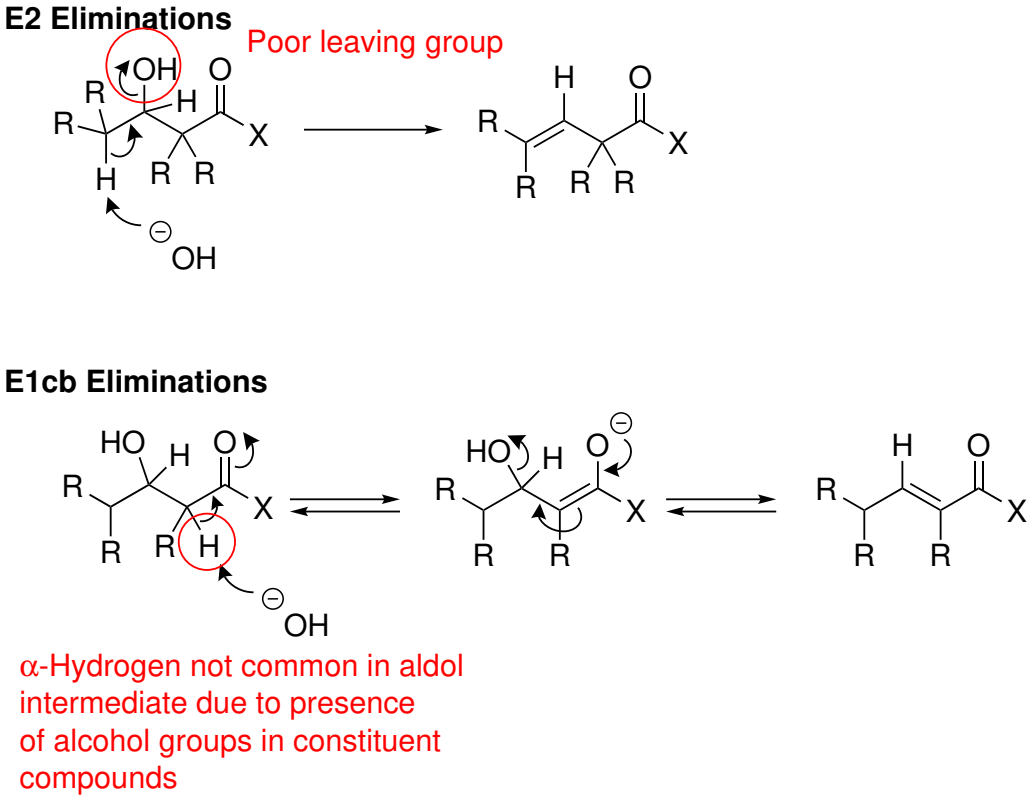

Figure 3.15: Elimination mechanisms considered. Problems with each mechanism given the current reaction conditions are shown in red.

Given this analysis a likely polymer synthesis mechanism begins to emerge (Fig. 3.16). This pathway is based on catalyst mediated carbohydrate syntheses found in the literature [173–175], and subsequent polysaccharide syntheses from various constituent carbohydrates [176]. The result is a polymer that is similar to a polysaccharide and appears to be up to 4 µm in size.

The large potential increase seen in the chronopotentiometry suggests that the polymer is formed at the electrode surface, perhaps as a sort of film, before detaching from the surface so that more may be created. This behavior would describe the noisy jumps in potential seen in the chronopotentiometry after 80 ks (Fig. 3.11). Aldehyde species can be found at the electrode surface under these reaction conditions based on PM-IRRAS studies performed on similar systems, albeit at room temperature [20, 27, 28]. These are the monomers for the polymerization reaction. The fact that the potential only begins to increase at approximately 80 ks indicates that some critical concentration of products is required before polymerization occurs. This is

likely due to many simultaneous chemical equilibria present in the system, and the necessary buildup of some specific intermediate compounds in solution.

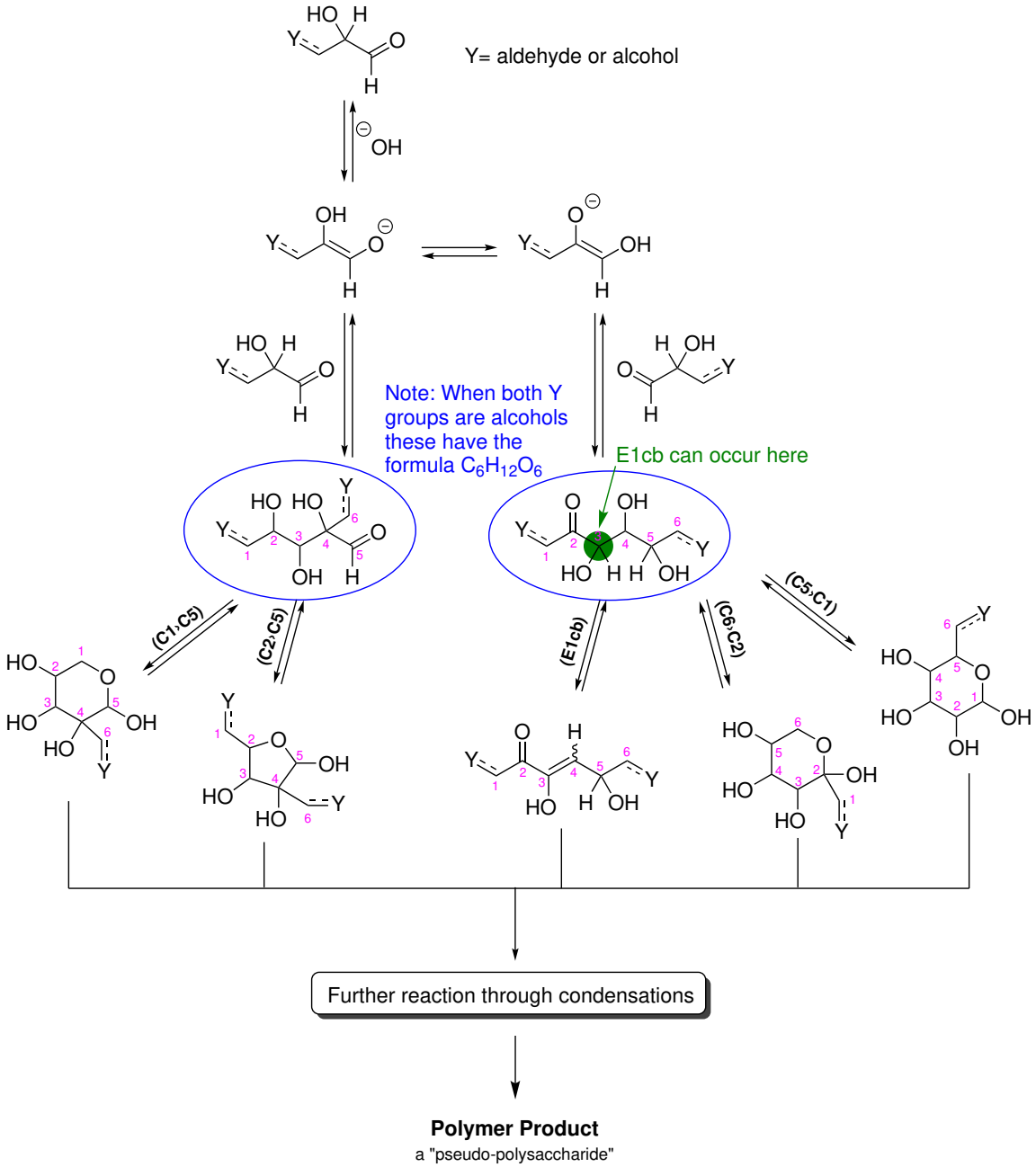

Figure 3.16: Proposed polymer product synthesis pathway. Given this mechanism it appears that the polymer product is some variety of pseudo-polysaccharide.

3.4 Conclusions

HPLC Analysis was successfully performed on glycerol oxidation products created at 20 °C, 80 °C, and 140 °C. Using standard calibration curves the product selectivity of the oxidation processes were determined and, combined with the results of similar experiments in the literature, a likely reaction pathway was determined to describe the results observed.

The experiment performed at 140 °C resulted in the formation of a polymer. Analysis using DLS and DSC determined that the polymer likely has a highly cross-linked structure. Additionally, it appears that the polymer may exist in three similar but distinct structures, each with their own equilibrium size distribution. ATR-IR and NMR indicate that the polymer contains many ether bonds and some small amount of alkenes. No carbonyl groups were detected, ruling out polyester as a structural candidate. Subsequent analysis of chronopotentiometry results suggest that the polymer forms as a loose film at the surface of the electrode. A thorough consideration of oxidation intermediates in solution and the reactions available to them indicate that the polymer is likely a pseudo-polysaccharide, with the monomer units being various aldehyde species.

Chapter 4

A Study of the Phases of Nickel Oxide as a Function of Temperature

4.1 Introduction

This chapter explores the different phases of nickel oxide and their interconversion using various electrochemical techniques including cyclic voltammetry, EIS, and various potential holds. Performing these techniques at high temperatures allows for some insights that would otherwise not have been possible to attain. Additionally, room temperature aging experiments using cyclic voltammetry are successfully employed in the study of the NiO layer.

Since this work focuses on thin films of nickel oxide and the interconversion between them at non-standard conditions, the typical techniques used to characterize oxides were not employed. Techniques such as X-Ray Diffraction are meant for use on bulk oxide phases and don't work for thin films. Surface X-Ray Diffraction could arguably be used, but this would have to be done in-situ during the electrochemical tests and the development of a high-temperature cell that an accommodate X-Ray analysis was the scope of this project. Additionally, no information would be gained from performing these techniques on the electrodes after the electrochemical experiments as their interesting features would not be retained on cooling.

Unlike Chapter 3 which was focused on product identification and therefore has experimental conditions that were optimized for product yield, this chapter focuses

on kinetics. Due to the shift in focus the experimental conditions for this work are significantly different than the previous chapter to facilitate the collection of time dependent data. These were not used in the previous chapter as conditions that facilitate time dependent studies typically do not have a high product yield. Because the autoclave is a sealed system, time dependent studies of the oxidation process are impractical using non-electrochemical techniques. Dr Tianyu Li, also from the Harrington group, performed a room temperature analysis of this system using a microfluidic electrochemical cell that allowed for simultaneous collection of Raman spectra alongside electrochemical experiments. The requirements of a material that is temperature resistant, but also Raman inactive make this experiment quite difficult at high temperatures. For this reason, this chapter relies on time dependent electrochemical techniques such as EIS to perform the relevant analyses.

The Bode diagram for nickel oxide phases (Fig. 1.2a) [91] showcases the four most common oxide phases, how they interconvert, and the existence of intercalated water in the α and γ phases that make them amorphous. This is a good overall representation of the nickel oxide system, with the addition of a thin layer of NiO that appears to sit between the metallic nickel and nickel hydroxide phases.

Due to the ability of nickel oxides to continuously pass current by the mechanisms described previously (Section 1.2.2) they are not limited to some small number of monolayers, but can grow to be many hundreds of layers thick [95, 99]. The ability to intercalate many ions in this way also gives them very high charge densities [113, 177, 178]. Studying the formation of these phases and how they interconvert could yield industrially relevant results with respect to energy storage devices.

4.2 Experimental

4.2.1 Experimental Setup

The electronic dEIS equipment was setup as in Section 2.3.

Polycrystalline 99.999% nickel wire (Alfa Aesar, Puratronic) was sealed in heat-shrink teflon tubing for use as WE and CE in a teflon electrochemical cell. A mercury/mercury oxide reference electrode (Pine Research, RREF0038) was placed in the cell for use as a RE for initial room temperature experiments, but here are

reported vs RHE.

$$\begin{aligned} E_{RHE} &= E_{Hg/HgO} + E^{\circ}_{Hg/HgO} + 0.059\,pH \\ E_{RHE} &= E_{Hg/HgO} + 0.906V \end{aligned} \tag{4.1}$$

High temperature experiments were performed using an RHE as the RE. Current densities are reported using the ECSA determined by the method described previously (Section 2.4). The cell was washed by soaking in 80 °C sulfuric acid (Sigma, ACS Reagent) for minimum 2 hours before being rinsed several times in Milli-Q water. The electrodes were rinsed in 80 °C sulfuric acid then Milli-Q water.

A solution of 99.99% 0.1 M KOH (Sigma, Semiconductor Grade) was made up in Milli-Q water and purged with Ar for 10 minutes, with slow continual bubbling continuing during initial experiments. In the event the autoclave was used, the autoclave was sealed immediately after the 10 minute Ar purge. Unless otherwise specified, all dynamic impedance experiments were carried out with a sweep rate of 5 mV s^{-1} and with frequencies ranging from 1 Hz to 13 kHz. Similarly, all potentiostatic impedance experiments were performed using frequencies ranging from 0.1 Hz to 100 kHz, taking approximately 3 minutes for acquisition to occur.

While ramping the temperature between experiments CVs were performed from -0.2 V to 0.45 V at 100 mV s^{-1} in an attempt to prevent the build-up of any excess nickel oxide on the electrode surface. This was done to keep the surface consistent between runs of the experiment.

4.2.2 Impedance Data Validation

4.2.2.1 Kramers-Kronig Test

Because AC potential excitations are being applied and the AC current response is being measured, systems must be steady-state on the time scale of the measurement [154]. What follows is a means of testing for this condition.

Valid impedance data has a special property, in that if the real part of the impedance is known at every frequency the imaginary part of the impedance at any frequency can be determined and vice versa. The equations that are used to perform

this feat are called the KK transforms, here shown in the admittance form:

$$\begin{aligned} \mathrm{Im}(Y(\omega)) &= \frac{2\omega}{\pi}\int_0^\infty \frac{\mathrm{Re}(Y(x)) - \mathrm{Re}(Y(\omega))}{x^2-\omega^2}dx \\ \mathrm{Re}(Y(\omega)) &= \mathrm{Re}(Y(\infty)) - \frac{2\omega}{\pi}\int_0^\infty \frac{x\,\mathrm{Im}(Y(x)) - \omega\,\mathrm{Im}(Y(\omega))}{x^2-\omega^2}dx \end{aligned} \tag{4.2}$$

Instead of evaluating these integrals an EC can be fit that obeys Eqs. 4.2. For this reason the Kramers-Kronig (KK) test was developed [179]. In short the KK test uses an EC with some large but finite number of time constants and attempts to see if the data can fit to that. For data validation in this work 7 time constants per frequency decade were used.

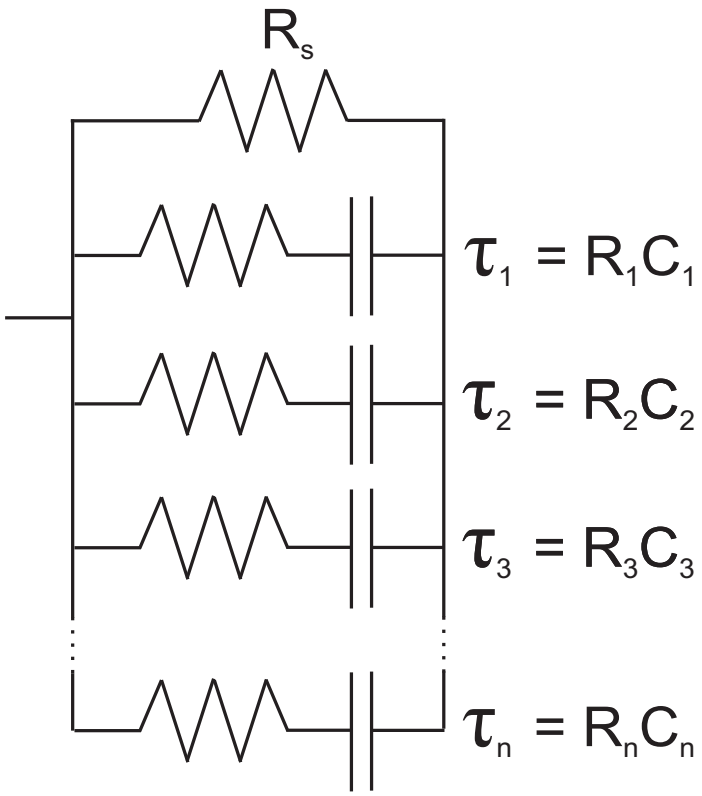

Figure 4.1: The KK test circuit. It contains a large but finite number of time constants, τ. Here it is shown in the admittance form.

The idea is that any valid data set should be able to be fit by a circuit that has so many degrees of freedom.

Once the data is fit using the large number of time constants, the residuals can then be used to check for consistency within our impedance data. A residual plot is

generated using the relative differences between the data and this new model, plotted against frequency.

$$\begin{aligned} \Delta\,\mathrm{Re}(Y(\omega)) &= \frac{\mathrm{Re}(Y(\omega))_{data} - \mathrm{Re}(Y(\omega))_{model}}{|Y(\omega)_{model}|} \\ \Delta\,\mathrm{Im}(Y(\omega)) &= \frac{\mathrm{Im}(Y(\omega))_{data} - \mathrm{Im}(Y(\omega))_{model}}{|Y(\omega)_{model}|} \end{aligned} \tag{4.3}$$

Data that is KK test compliant should have only a noise distribution around the x-axis of this plot; clear lines around the frequency axis indicate systematic corruption in the data.

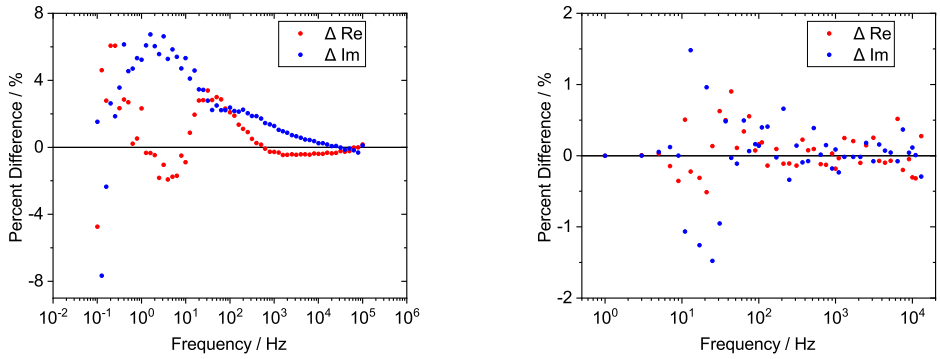

(a) Fails KK test

(b) Passes KK test

Figure 4.2: KK test example plots, showing a KK test failure and a KK test pass.

A small trend in the magnitude of the errors is sometimes seen (Fig. 4.2), typically less than 1%, however this is typically a fitting error and does not necessarily indicate a drift in the system.

4.2.2.2 Polarization Resistance Comparison

After KK testing was performed on the dEIS data, equivalent circuits were identified for the tested potential range. The impedance for these circuits was then extrapolated to a frequency of 0 Hz. An example, for a simple circuit is

$$\begin{aligned} Z &= R_s + \frac{1}{i\omega C_{dl} + \frac{1}{R_{ct}}} \\ Z(\omega = 0) &= R_s + R_{ct} = R_0 \end{aligned} \tag{4.4}$$

and as is typical, extrapolating to 0 Hz gives a single differential resistance value. This differential resistance is denoted R_0.

This resistance should coincide with the differential resistance obtained by taking the reciprocal of the derivative of the corresponding CV, denoted R_{DC}.

$$\frac{\mathrm{d}\, j}{\mathrm{d}\, E} = \frac{1}{R_{DC}} \tag{4.5}$$

By comparing these two estimates of the polarization resistance over the potential range tested it can be determined whether or not a large enough frequency range was used to capture all processes present in the system. The precision with which the values must correlate is poorly defined, and so a qualitative assessment must be made (Fig. 4.3).

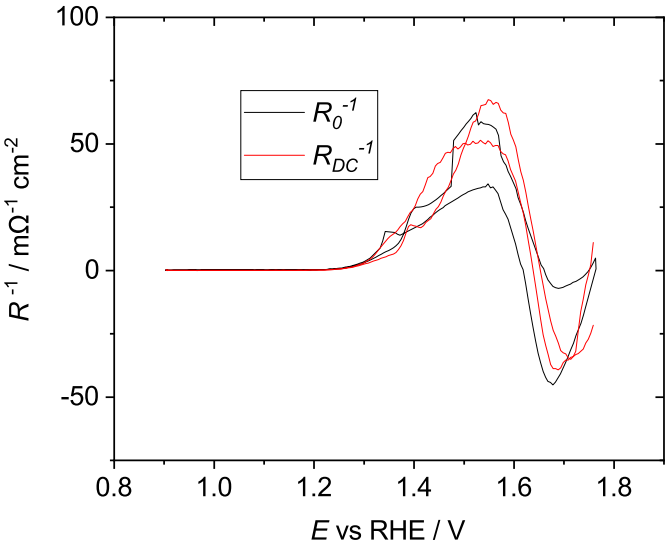

(a)

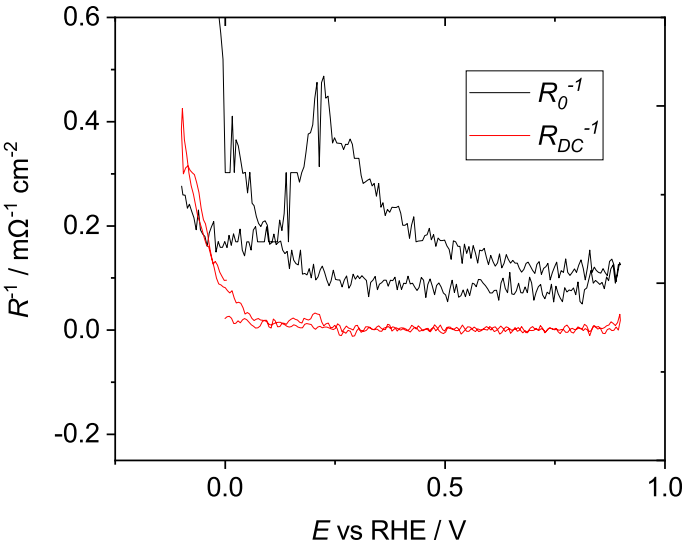

(b)

Figure 4.3: Two example polarization resistance comparisons. (a) is considered a pass of the differential resistance test here, and (b) is considered a fail. Here the reciprocals of the polarization resistances are plotted.

If the two differential resistances do not maintain similar values, or have different trends (Fig. 4.3a), it is an indication that processes are occurring at unmeasured

lower frequencies that are not being detected by the impedance experiment.

4.2.3 Electrochemical Impedance Spectrum Fitting

Potentiostatic EIS spectra (pEIS) experiments performed on this system used a 10 mV rms AC voltage with data collected from 100 kHz to 10 mHz at 10 points per frequency decade. The resulting spectra for this system were found to be quite complicated. Initially it was thought that there may have been too much drift in the system for the data to be valid, but many spectra passed the KK test to the standard set. Several equivalent circuits (ECs) were then fitted to the data (Fig. 4.4). These circuits were built by sequentially adding single fitting parameters to a nested Voigt element circuit. This was repeated until the statistical analysis performed agreed that the new fitting elements did not comprise a better model for the data (Section 2.3). Due to the complex nature of the data both AIC [150] and F-Test [180] analyses were performed to determine the circuit of best fit, and were found to be in agreement.

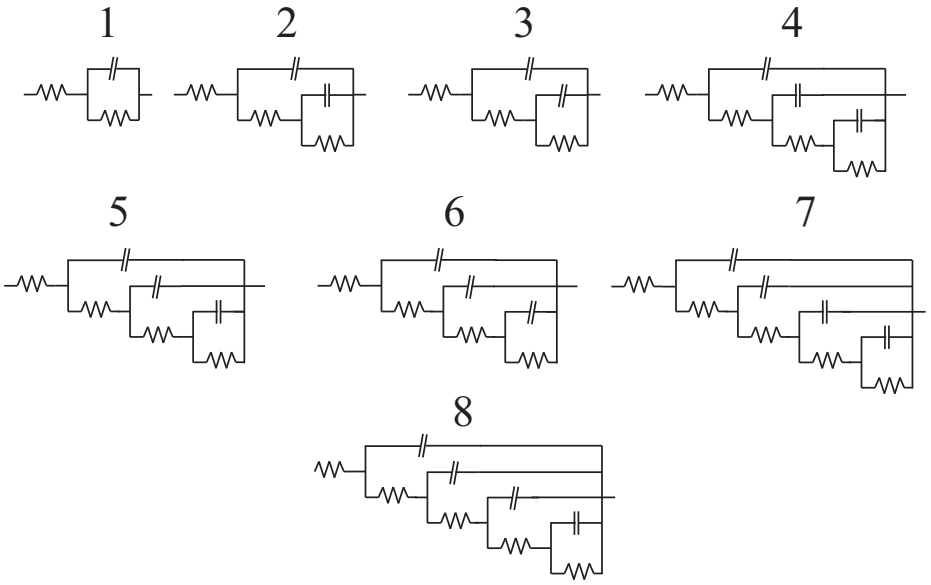

Figure 4.4: The eight equivalent circuits fitted to the $Ni(OH)_2$ pEIS data. Circuits were built by sequentially adding single fitting elements to a nested Voigt element circuit.

Based on ECs determined for the pEIS experiments similar ECs were fit to the dEIS data (Fig. 4.5). Due to the limitations caused by sweeping during an EIS experiment the frequency range used for this experiment was 13 kHz to 1 Hz, and

as a result not all processes present were detectable by dEIS. This resulted in fewer valid ECs for the fitted data.

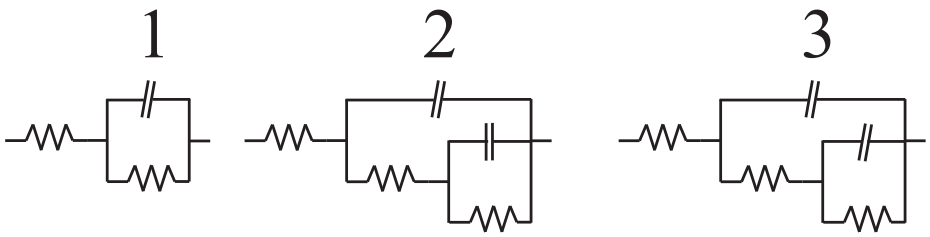

Figure 4.5: The three equivalent circuits fitted to the $Ni(OH)_2$ pEIS data. Circuits were built by sequentially adding single fitting parameters to a nested Voigt element circuit.

Both dEIS and pEIS spectra were fitted to equivalent circuits using Maple software developed by the Harrington group [150]. The script uses a non-linear least squares fitting algorithm, fitting the theoretical expressions of the ECs to the empirically collected impedance data.

The script also provides an Akaike Information Criterion (AIC) value for each fit. AIC is a method of comparing different models in order to determine the one with the best least squares fit without too many parameters. The classic problem in determining the EC of best fit for impedance data is whether or not adding additional parameters provides a better fit with any statistical significance. AIC solves this issue.

$$AIC = -2\ln\widehat{L} + 2k \tag{4.6}$$

The likelihood estimator, $\widehat{L}$, gets larger given a smaller residual sum of squares. This makes the first term more negative given a better fit. The value k is the number of parameters present in the model plus one to accommodate an estimate of the variance in the fitted parameters, therefore a simpler model makes the second term more negative. In this way AIC makes a compromise between goodness-of-fit and model simplicity with the most negative AIC value denoting the EC of best fit. It should be noted that while AIC values generated by fitting different models to a single data-set can be compared, they are data-set dependent and so cannot be used to compare fit quality between different data sets.

In cases where a circuit was determined to be the best fit but a parameter had a percent standard error larger than 50% the fit was assumed to be erroneous and the next best fit was chosen. Percent standard error is calculated as $\frac{1}{t}$ where t is the

test value determined via a Student t-test at a given confidence level for a specified number of degrees of freedom. For any value in degrees of freedom over 40, at the 95% confidence level, the t value is approximately 2. From here the standard error is found to be $\frac{1}{2} = 50\%$. This indicates that a standard error of less than 50% passes a student t-test at the 95% confidence interval. This remains true so long as the degrees of freedom remain larger than 40. These are given by

$$DOF = 2 \times number\ of\ frequencies - number\ of\ fitted\ parameters \tag{4.7}$$

4.2.4 AC Voltammetry

By applying an AC potential excitation and observing the current response the admittance of a system can be measured at a fixed frequency. This is performed by measuring the impedance (Section 2.3.1) and converting it to admittance. Admittance is the reciprocal of impedance and is calculated as follows:

$$\begin{aligned} Z &= \mathrm{Re}(Z) + \mathrm{Im}(Z)i \\ Y = Z^{-1} &= \frac{1}{\mathrm{Re}(Z) + \mathrm{Im}(Z)i} \\ &= \frac{1}{\mathrm{Re}(Z) + \mathrm{Im}(Z)i}\frac{\mathrm{Re}(Z) - \mathrm{Im}(Z)i}{\mathrm{Re}(Z) - \mathrm{Im}(Z)i} \\ &= \frac{\mathrm{Re}(Z) - \mathrm{Im}(Z)i}{\mathrm{Re}(Z)^2 + \mathrm{Im}(Z)^2} \\ &= \frac{\mathrm{Re}(Z)}{\mathrm{Re}(Z)^2 + \mathrm{Im}(Z)^2} + \frac{-\mathrm{Im}(Z)i}{\mathrm{Re}(Z)^2 + \mathrm{Im}(Z)^2} \\ &= \mathrm{Re}(Y) + \mathrm{Im}(Y)i \end{aligned} \tag{4.8}$$

4.2.5 Electrochemical Reduction of the β-$Ni(OH)_2$ Layer

Electropolishing is the preferred method of removing the β-$Ni(OH)_2$ layer (Section 2.4), however due to the nature of the high-temperature experiments an in-situ method of removing the β-$Ni(OH)_2$ layer was desired. It has been shown that sufficiently negative potential holds for a long enough duration can reduce β-$Ni(OH)_2$ to metallic nickel [107, 108].

By performing a potential hold at -0.2 V for 600 s followed by a hold at 0 V for 200 s the α-$Ni(OH)_2$ peak was observable (Fig. 4.6). This peak is smaller than the peak achieved by electropolishing the same electrode indicating that not all $Ni(OH)_2$

was reduced. However, subsequent tests show that this partial $Ni(OH)_2$ reduction is reproducible, making this a viable methodology for studying α-$Ni(OH)_2$ formation and its subsequent aging to β-$Ni(OH)_2$. All experiments performed on $Ni(OH)_2$ were preceded by this conditioning step.

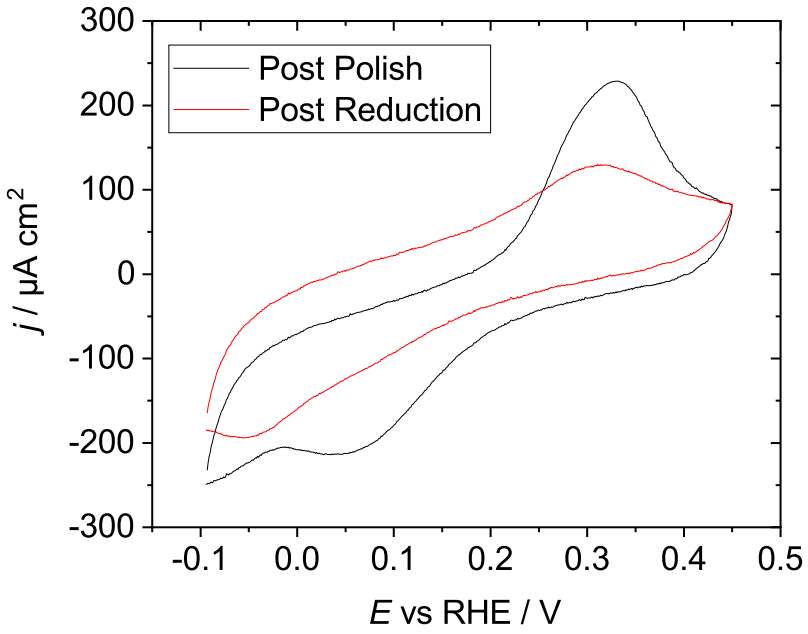

Figure 4.6: Comparison of electropolishing and reduction as a conditioning step for α-$Ni(OH)_2$ CVs. CVs were acquired by electropolishing, cycling through the α-$Ni(OH)_2$ region, cycling from 0 V through the NiOOH region until all α-$Ni(OH)_2$ features disappeared, performing the potential hold as described in this section, and finally cycling through the α-$Ni(OH)_2$ region again. Sweep rate is 50 mV s^{-1}.

4.2.6 Selectively Stabilizing β-NiOOH and γ-NiOOH Using Cyclic Voltammetry

Two separate schemes were developed wherein nickel wire was electropolished and immersed in 0.5 M KOH. After determining the surface area of the nickel wire (Section 2.4), CVs were run on the nickel wire until the nickel achieved steady state. One conditioning process was performed by cycling from 1.00 V to 1.484 V and the other cycling from 1.00 V to 1.526 V (Fig. 4.7). These will be called Scheme 1 and Scheme

2, respectively. The reason these voltage maximums were chosen is that the larger one incorporates some amount of oxygen evolution, whereas the smaller does not. In both schemes CVs were run until the electrode achieved a steady state.

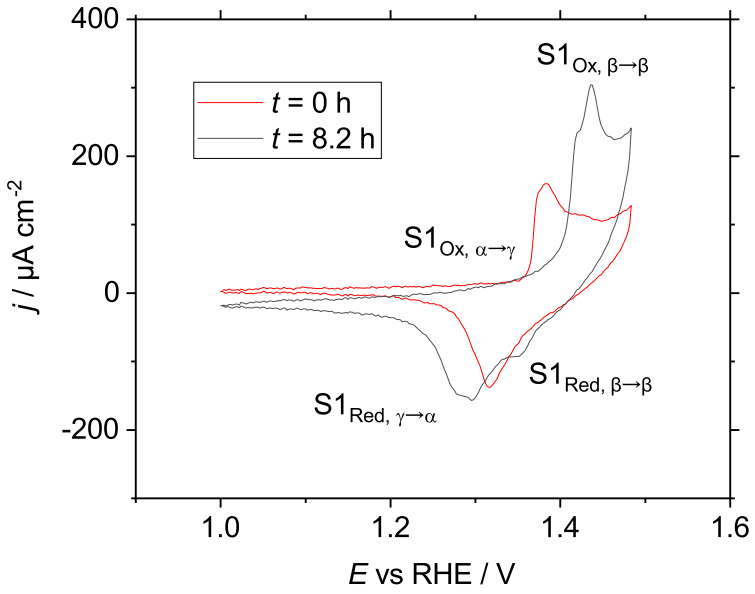

(a) 1.48 V vs RHE maximum potential, Scheme 1

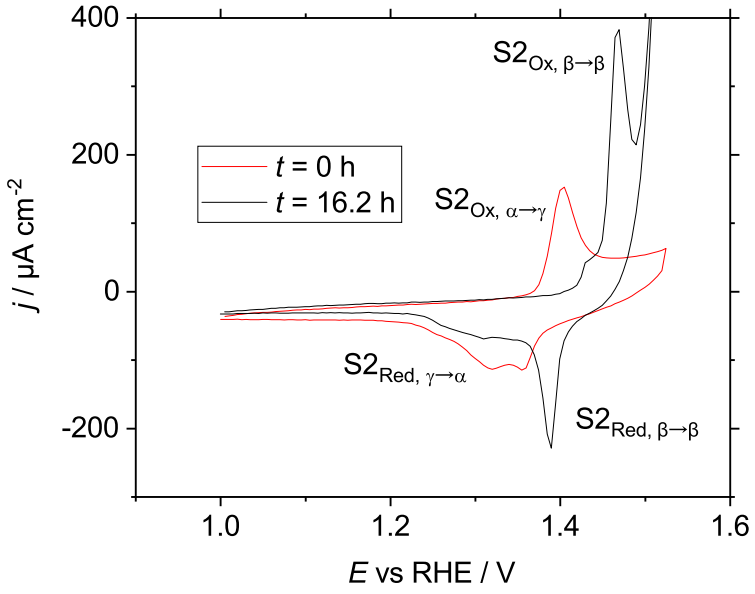

(b) 1.52 V vs RHE maximum potential, Scheme 2

Figure 4.7: CVs for the conditioning cycle of $Ni(OH)_2$ oxidation to steady state. While cycling according to Scheme 1 the electrode achieved steady state in 8.2 h, whereas while cycling according to Scheme 2 steady state was achieved in 16.2 h. Peaks have been labelled for easy reference. S1 refers to Scheme 1, and S2 refers to scheme 2. Whether the peak is an oxidation or reduction, and the oxide phases involved are noted in the subscript. Sweep rate 5 mV s^{-1}.

Based on literature [12, 14, 60, 68, 86, 126–128] Scheme 1 can be shown to preferentially stabilize γ-NiOOH and Scheme 2 can be shown to preferentially stabilize β-NiOOH.

4.3 Results and Discussion

4.3.1 Electrochemical Impedance Spectroscopy Validation

4.3.1.1 Kramers-Kronig Tests

pEIS was performed at 20 °C, 40 °C, 60 °C, 80 °C, 100 °C, 120 °C, and 140 °C at both 0.6 V and 1.2 V. Spectra collected contain very exotic features, and while some of these spectra failed the KK test many passed.

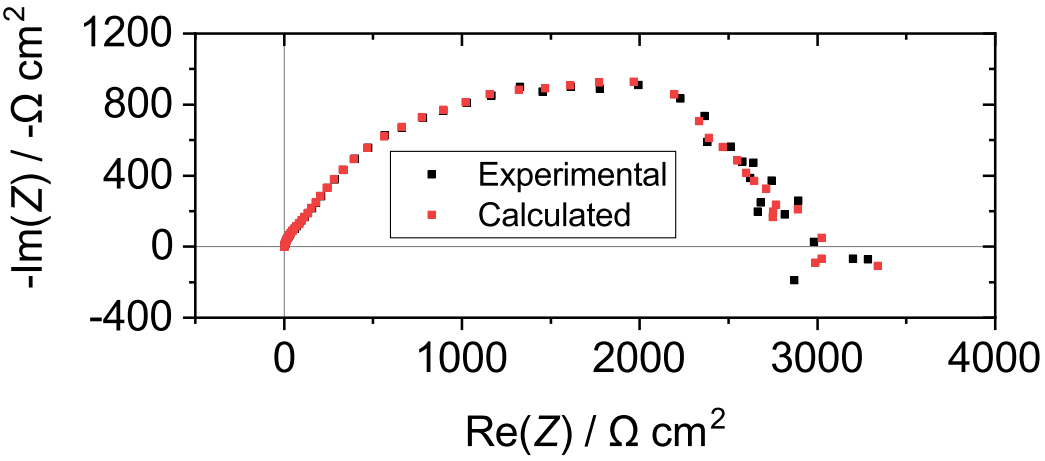

(a) Nyquist Result

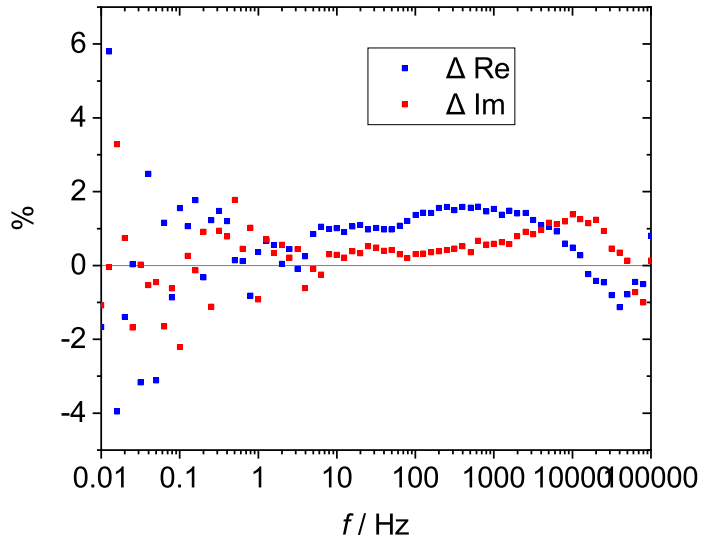

(b) Percent Error

Figure 4.8: KK test results for pEIS on $Ni(OH)_2$ performed at 0.6 V and 120 °C.

Due to the complexity of the pEIS spectra (Fig. 4.9), with many of them fitting as many as four time constants with statistical significance (Section 4.2.3), they have been left largely uninterpreted. Their sole purpose in this work is to show that at all temperatures and potentials tested there are very complex, slow processes occurring that are detectable by impedance spectroscopy.

The dEIS data passed the KK Test.

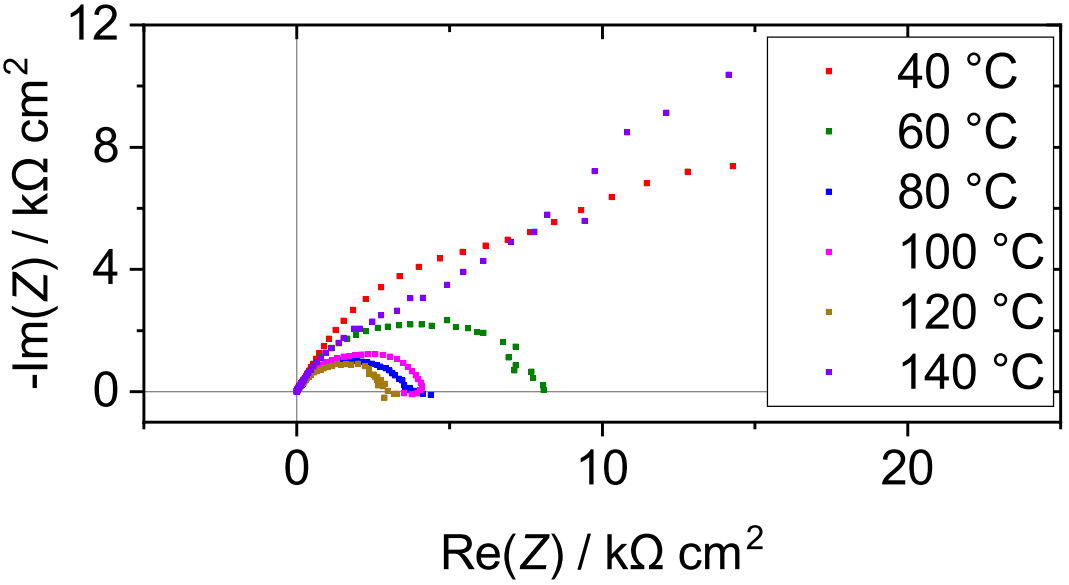

(a) 0.6 V

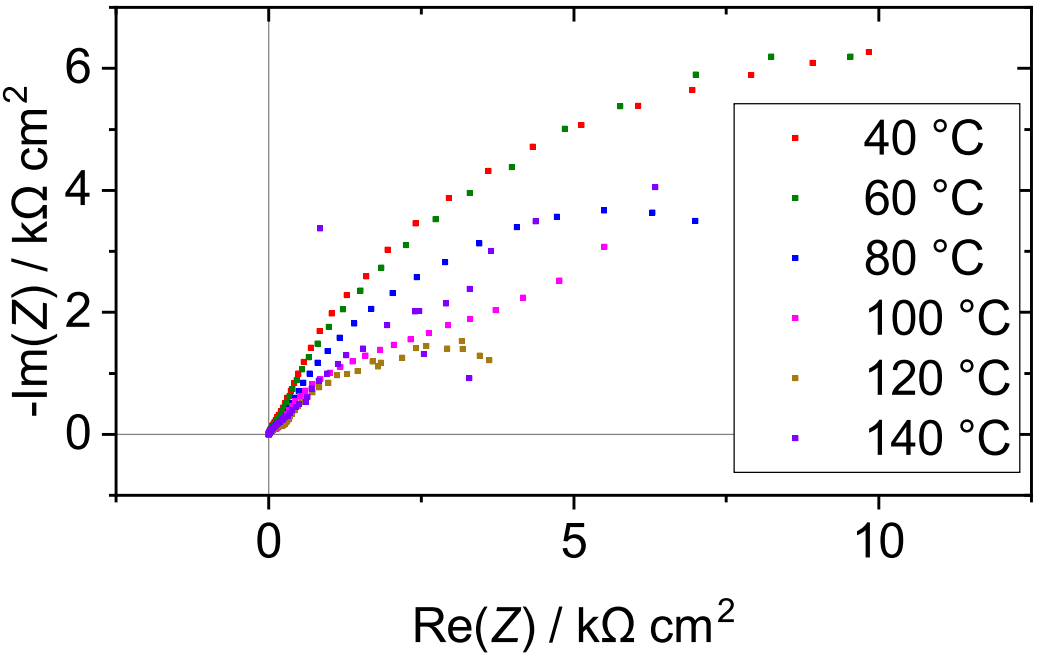

(b) 1.2 V

Figure 4.9: Nyquist plots for pEIS collected at 0.6 V and 1.2 V as a function of temperature. 20 °C not shown as they are off scale in this plot.

Temp / °C	Circuit	R_s / Ω cm^2	Q_{dl} / 10^{-6} cm^{-2}	α_{dl}	R_{ct} / Ω cm^2	Q_2 / 10^{-6} cm^{-2}	α_2	R_2 / Ω cm^2	C_3 / μF cm^{-2}	Q_3 / 10^{-6} cm^{-2}	α_3	R_3 / Ω cm^2	C_4 / μF cm^{-2}	R_4 / Ω cm^2
20	3	2.31	20.1	0.898	1719	19.2	0.931	53726						
40	4	1.99	14.9	0.878	669.4	32.2	0.758	12316	260.5			10042		
60	4	1.57	16.6	0.867	344.7	42.2	0.747	5647.1	572.1			1827.7		
80	8	1.36	10.8	0.932	274.8	55.6	0.766	2577.9		983.2	0.761	696.96	-1823.3	962.30
100	7	1.34	20.3	0.914	201.3	69.8	0.698	3087.6	498.4			861.63	-3643.2	-474.02
120	7	1.34	20.1	0.901	202.9	105	0.614	354.53	6.627			2463.9	-5651.5	647.94
140	8	1.22	42.3	0.800	1077	23.0	0.855	4859.6		126.6	0.954	7363.4	83.57	14444

Table 4.1: 0.6 V pEIS fitting parameters for circuits of best fit on $Ni(OH)_2$ interconversion. For more detailed data see Appendix A.1.

Temp / °C	Circuit	R_s / Ω cm^2	Q_{dl} / 10^{-6} cm^{-2}	α_{dl}	R_{ct} / Ω cm^2	C_2 / μF cm^{-2}	Q_2 / 10^{-6} cm^{-2}	α_2	R_2 / Ω cm^2	C_3 / μF cm^{-2}	Q_3 / 10^{-6} cm^{-2}	α_3	R_3 / Ω cm^2	C_4 / μF cm^{-2}	R_4 / Ω cm^2
20	3	2.38	182	0.829	15210		352	0.905	28001						
40	6	2.12	187	0.855	27.271		92.2	0.439	1036.2		111.9	0.884	20072		
60	5	1.70	208	0.841	427.71		277	0.819	11012	1199			4929.7		
80	8	1.43	77.9	0.868	231.14		129	0.901	233.48		278.3	0.847	5916.3	1269	3335
100	5	1.35	68.4	0.825	185.16		466	0.750	4652.6	3589			3124.1		
120	6	1.48	58.8	0.825	320.04		419	0.843	2349.3		2369	0.815	2252.6		
140	5	1.69	185	0.736	917.29	202			3399.1	1310			6366.4		

Table 4.2: 1.2 V pEIS fitting parameters for circuits of best fit on $Ni(OH)_2$ interconversion. For more detailed data see Appendix A.1.

4.3.1.2 Polarization Resistance Comparison

Comparing the polarization resistance acquired from both AC and DC techniques highlights some issues capturing slow processes involved in this system using dEIS (Fig. 4.10). All plots comparing polarization resistances have a significant discrepancy between values determined from AC and DC techniques. This indicates that not all processes present are being detected by the dEIS experiment. Values determined can still be used to determine some qualitative information about the system.

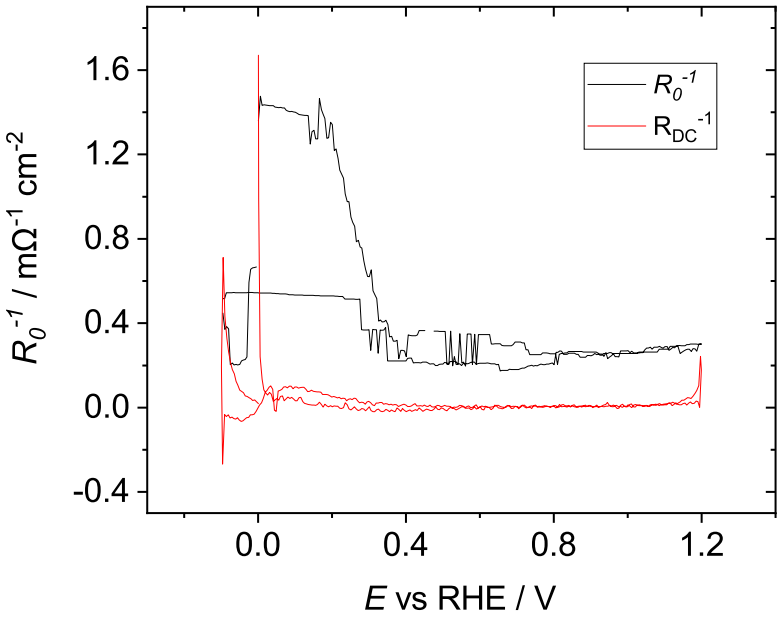

Figure 4.10: Comparison of polarization resistances acquired through AC and DC techniques at 140 °C on $Ni(OH)_2$. The sweep rate was 5 mV s^{-1}.

4.3.2 Effects of CV conditioning on $Ni(OH)_2$ oxidation

4.3.2.1 β-NiOOH and γ-NiOOH Aging Cyclic Voltammetry Analysis

It was previously explained in Section 1.2 that β-$Ni(OH)_2$ can oxidize to β-NiOOH, β-NiOOH can overcharge to γ-NiOOH, and γ-NiOOH can reduce to either β-$Ni(OH)_2$ or α-$Ni(OH)_2$. Additionally, there is a thin layer of NiO that appears to form beneath the various $Ni(OH)_2$ and NiOOH phases, next to the nickel metal itself [92, 93]. There

is some debate in the literature about the actual stoichiometry of the nickel oxide phases, as well as which phase of NiOOH is more active for oxygen evolution [14, 57, 63, 66, 68, 122, 127–129], but for simplicity of discussion they are acknowledged as being these discrete phases. This work seeks to develop a method for probing the potential dependence and oxygen evolution activity of these phases.

Long term conditioning experiments (Section 4.2.6) highlight the existence of the two phases of NiOOH. Both Schemes initially have a single anodic peak ($S1_{Ox,\alpha\rightarrow\gamma}$ and $S2_{Ox,\alpha\rightarrow\gamma}$) caused by the oxidation of α-$Ni(OH)_2$ to γ-NiOOH at approximately 1.4 V. As the cycling for each Scheme continues a second peak becomes visible caused by the formation of β-NiOOH ($S1_{Ox,\beta\rightarrow\beta}$ and $S2_{Ox,\beta\rightarrow\beta}$). In Scheme 1 at 8.2 h, $S1_{Ox,\beta\rightarrow\beta}$ appears as a small peak at approximately 1.43 V on top of $S1_{Ox,\alpha\rightarrow\gamma}$. In Scheme 2 at 16.2 h a large $S2_{Ox,\beta\rightarrow\beta}$ peak appears at 1.46 V as $S2_{Ox,\alpha\rightarrow\gamma}$ turns into a small shoulder to the left of the $S2_{Ox,\beta\rightarrow\beta}$ peak at 1.43 V.

The cathodic peaks show a similar trend. In Scheme 1 the initial CV has a single cathodic peak corresponding to the reduction of γ-NiOOH at approximately 1.3 V ($S1_{Red,\gamma\rightarrow\alpha}$). At 8.2 h a very small peak appears at approximately 1.35 V, corresponding to the reduction of β-NiOOH ($S1_{Red,\beta\rightarrow\beta}$). In Scheme 2 the initial CV has two cathodic peaks ($S2_{Red,\gamma\rightarrow\alpha}$) and ($S2_{Red,\beta\rightarrow\beta}$). By cycling according to Scheme 2 more β-NiOOH is stabilized on the electrode surface, agreeing with the Bode diagram of nickel oxidation (Fig. 1.2a)[91], as well as the rest of the literature [60, 68, 86, 126].

Correlating the oxidative and reductive peaks can be done by sweeping to various reversal potentials on the surfaces conditioned by Schemes 1 and 2 (Fig. 4.11). It is clearly seen that for both Schemes $\mathrm{Red}, \gamma \rightarrow \alpha$ corresponds to $\mathrm{Ox}, \alpha \rightarrow \gamma$, as $\mathrm{Red}, \beta \rightarrow \beta$ only appears when sweeping into $\mathrm{Ox}, \beta \rightarrow \beta$ found at approximately 1.4 V.

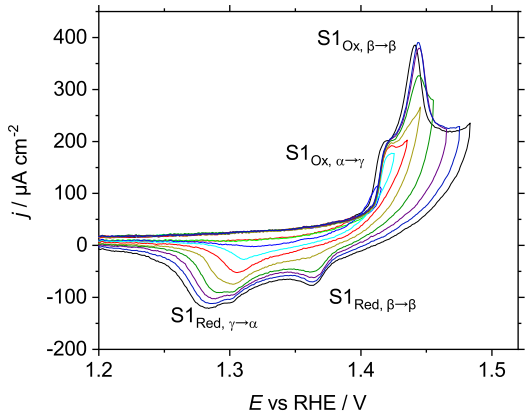

(a) Sweep reversals on a nickel surface conditioned by Scheme 1.

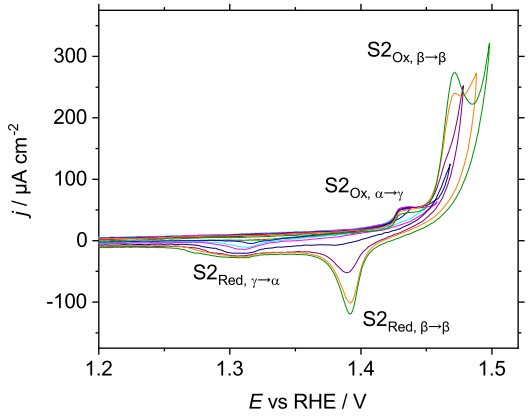

(b) Sweep reversals on a nickel surface conditioned by Scheme 2.

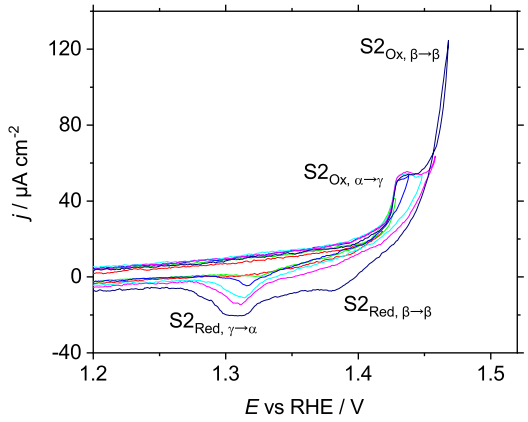

(c) Sweep reversals on a nickel surface conditioned by Scheme 2, focused on the β-NiOOH oxidation peak.

Figure 4.11: CVs for $Ni(OH)_2$ oxidation after conditioning Schemes 1 and 2, taken to various potentials. The sweep rate was 5 mV s^{-1}.

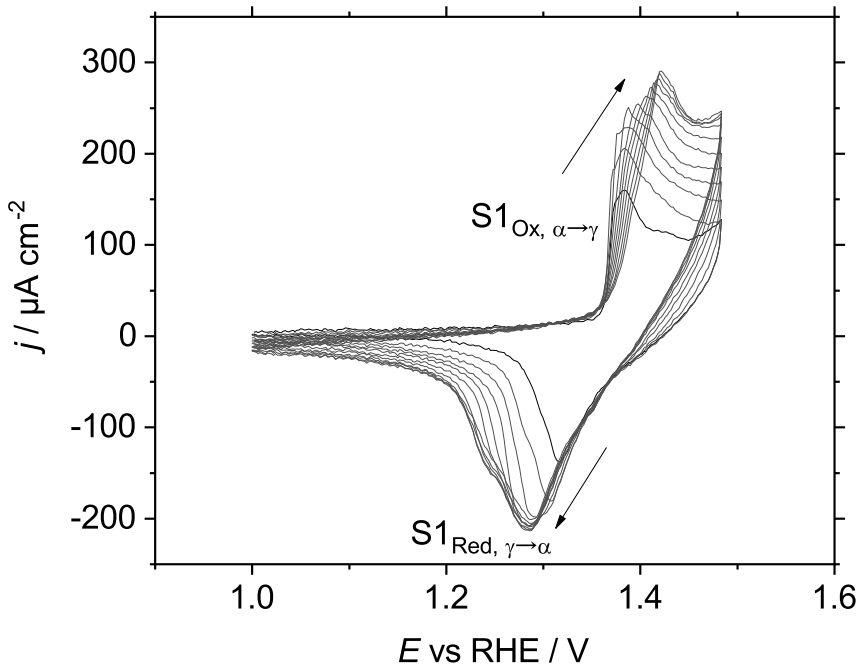

Figure 4.12: First 50 CV cycles of Scheme 1 long term conditioning. The sweep rate was 5 mV s^{-1}.

Of note is that while the oxidation and reduction for the β−β transitions appear to have a relatively fixed overpotential (Fig. 4.13), the oxidation and reduction of the $\alpha \rightarrow \gamma$ transition appear to become more irreversible with more γ-NiOOH formed, based on total charge density (Fig. 4.12). The $\gamma \rightarrow \alpha$ peaks are marked with asterisks to denote their non-linear growth (Fig. 4.13). In both Scheme 1 and Scheme 2 these peaks rapidly grow over the course of approximately 2.8 h, and then begin to become smaller over time. The decrease in this peak area coincides with an increase in both the oxidative and reductive $\beta \rightarrow \beta$ peak areas, indicating that some of the existing γ-NiOOH is being converted into β-NiOOH. As the $\gamma \rightarrow \alpha$ peaks decrease in size their overpotential also decreases. A possible explanation for this is that as more γ-NiOOH is formed it becomes significantly more difficult for the necessary intercalation of ions to occur in the formation of γ-NiOOH. This would be due to the amorphous nature of the γ-NiOOH phase.

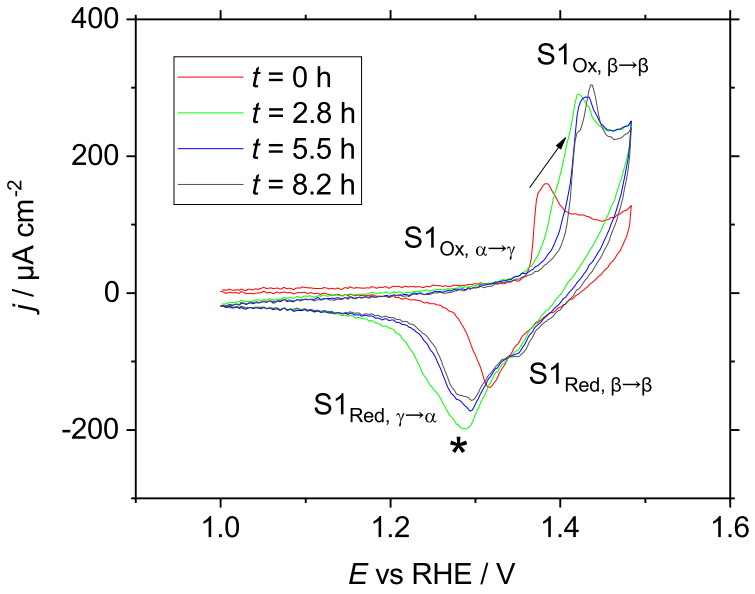

(a) 1.48 V vs RHE maximum potential, Scheme 1

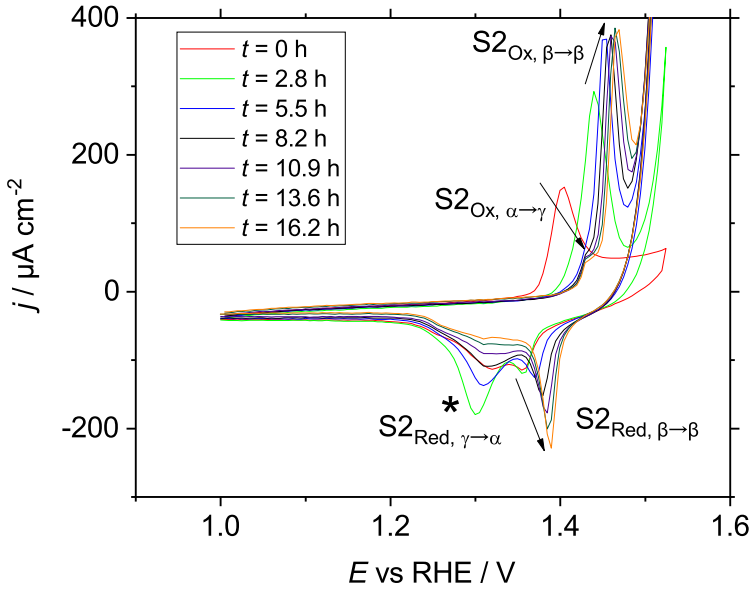

(b) 1.52 V vs RHE maximum potential, Scheme 2

Figure 4.13: CVs for the conditioning cycle of $Ni(OH)_2$ oxidation to steady state showing many cycles. Arrows have been added to indicate peak transformations over time. The sweep rate was 5 mV s^{-1}.

The oxidative and reductive $\beta \rightarrow \beta$ peaks in Figure 4.13 marked with arrows both

have a relatively linear and predictable anodic shift with time. This indicates that the reversible potential of the β → β transition appears to go higher as conditioning continues. Setting up the Nernst equation for the cell with the appropriate reactions shows

$$\begin{aligned} \mathrm{NiOOH} + \mathrm{H^+} + \mathrm{e^-} &\rightleftharpoons \mathrm{Ni(OH)_2} \\ \frac{1}{2}\,\mathrm{H_2} &\rightleftharpoons \mathrm{H^+} + \mathrm{e^-} \end{aligned} \tag{4.9}$$

$$\begin{aligned} E_r &= E^\circ - \frac{RT}{nF} \ln \frac{Products}{Reactants} \\ E_r &= E^\circ - \frac{RT}{F} \ln \frac{a(\beta\text{-Ni(OH)}_2)}{a(\beta\text{-NiOOH}) \cdot (f(\mathrm{H_2})/p^\circ)^{1/2}} = E^\circ \end{aligned} \tag{4.10}$$

assuming $f(\mathrm{H_2}) \approx p^\circ$ and $a(\beta\text{-Ni(OH)}_2) \approx a(\beta\text{-NiOOH})$. Given that

$$\Delta G^\circ = -nFE^\circ \tag{4.11}$$

and ΔG° is dependent on the stoichiometric composition of the solid compounds involved in the oxidation, this indicates that the stoichiometry of the β-NiOOH phase is changing as conditioning continues. Interestingly, the fixed E_r for the γ-NiOOH phase indicates that the stoichiometry of the γ-NiOOH phase is relatively consistent. Given that the γ-NiOOH phase is characterized by trapped intercalated ions, this is intuitive.

4.3.2.2 Oxygen Evolution Activity on β-NiOOH and γ-NiOOH

In the literature there is some debate as to whether β-NiOOH or γ-NiOOH is more active with regards to oxygen evolution [63, 66, 68, 122, 127–129]. The two separate conditioning Schemes discussed here offer a unique insight into this.

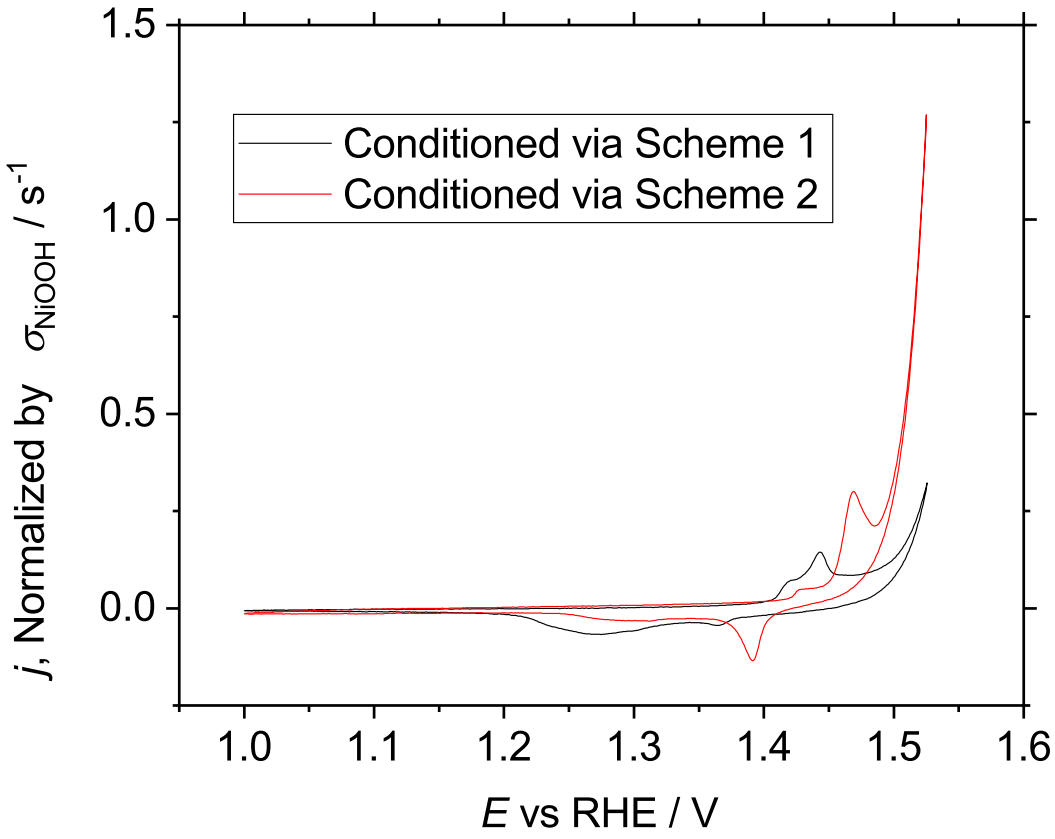

Figure 4.14: Cyclic voltammetry probing oxygen evolution for nickel electrodes conditioned by Schemes 1 and 2, normalized by NiOOH charge density. The sweep rate was 5 mV s^{-1}.

Schemes 1 and 2 have been shown to stabilize different phases of nickel oxyhydroxide. As previously mentioned, when a polycrystalline nickel electrode is conditioned by Scheme 1 it appears to preferentially stabilize the γ-NiOOH phase of nickel oxyhydroxide. When it is conditioned by Scheme 2 β-NiOOH appears to be the preferred oxide phase. By performing sweeps into the oxygen evolution region on these electrodes after conditioning, the phase with higher oxygen evolution activity can be determined (Fig. 4.14). In order to be able to draw direct comparison between the effects each conditioning Scheme has on oxygen evolution, the CVs must be normalized by the charge density of NiOOH formation, σ_{NiOOH}. σ_{NiOOH} was determined by using the integrate function in Gamry Echem Analyst and then normalizing by surface area. No baseline correction was applied. The lower limit of integration was the onset potential of NiOOH formation, defined here as the potential

at which the current density first exceeded 40 μA cm^{-2}. The upper limit of integration was the potential between the anodic NiOOH peak and oxygen evolution that had the lowest current density. The reason for this normalization is that NiOOH is a poorly defined, many layered phase. It is possible that even at steady state more or less NiOOH can exist on the surface depending on the conditioning Scheme. Based on these experiments it seems quite clear that the β-NiOOH phase has a higher oxygen evolution activity.

4.3.2.3 Sweep Hold Analysis

Sweep-hold protocols can be used to elucidate some mechanistic information for the oxidation. These experiments are similar to the ones shown in Figure 4.11, however instead of sweeping back after reaching the reversal potential the potential is held (Fig 4.15).

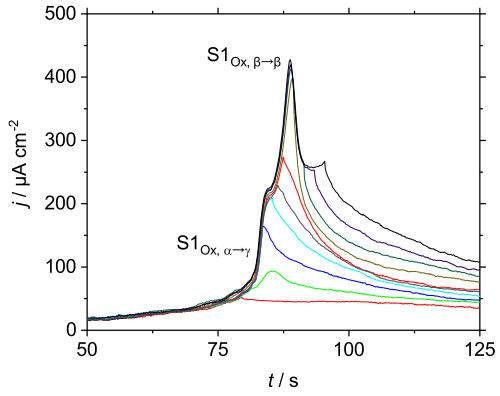

(a) Sweep holds on a nickel surface conditioned by Scheme 1.

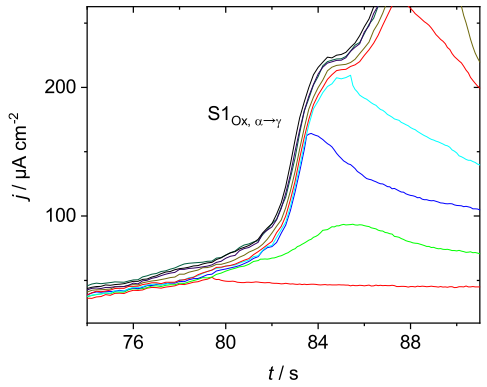

(b) Sweep holds on a nickel surface conditioned by Scheme 1, zoomed in on the β-NiOOH oxidation peak.

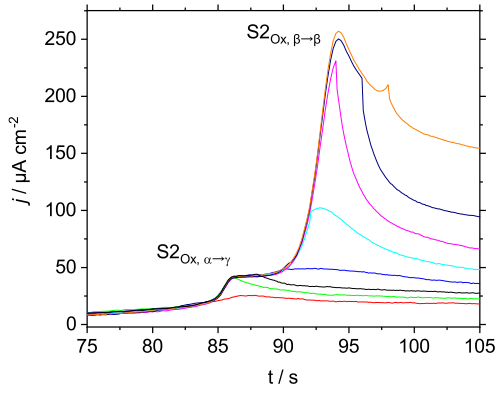

(c) Sweep holds on a nickel surface conditioned by Scheme 2.

Figure 4.15: Sweep hold experiments for $Ni(OH)_2$ oxidation after conditioning Schemes 1 and 2, taken to various potentials. The sweep rate was 5 mV s^{-1}.

During the initial stages of both Ox, $\alpha \rightarrow \gamma$ and Ox, $\beta \rightarrow \beta$ peaks conditioned by both Scheme 1 and Scheme 2 an increase in current can be seen after the potential hold has begun. This is evidence for a Nucleation Growth and Coalescence (NGC) mechanism [149] for the oxidation of $Ni(OH)_2$. It occurs because an NGC mechanism dictates that NiOOH starts as a small number of little spheres that gradually grow throughout the $NiOH_2$ layer. At these lower potentials within the peak the spheres have a small surface area, effectively limiting the rate of the sphere growth by offering fewer sites for oxidation. The crucial assumption that describes the NGC mechanism is that the RDS of the reaction is at the surface of the sphere. Therefore as the potential hold continues the spheres continue to grow, allowing for yet larger current densities to be passed. Eventually the reaction slows as the spheres merge, all available sites are taken, and the current decays to some steady state value.

4.3.2.4 NiO Investigation by Cyclic Voltammetry Integration and Sweep Hold Experiments

In the literature it is observed that the charge density of the NiOOH formation peaks is larger than the corresponding reductions [56]. By integrating the anodic and cathodic currents on the whole CV range over the course of the long term oxidation this was confirmed (Fig. 4.16).

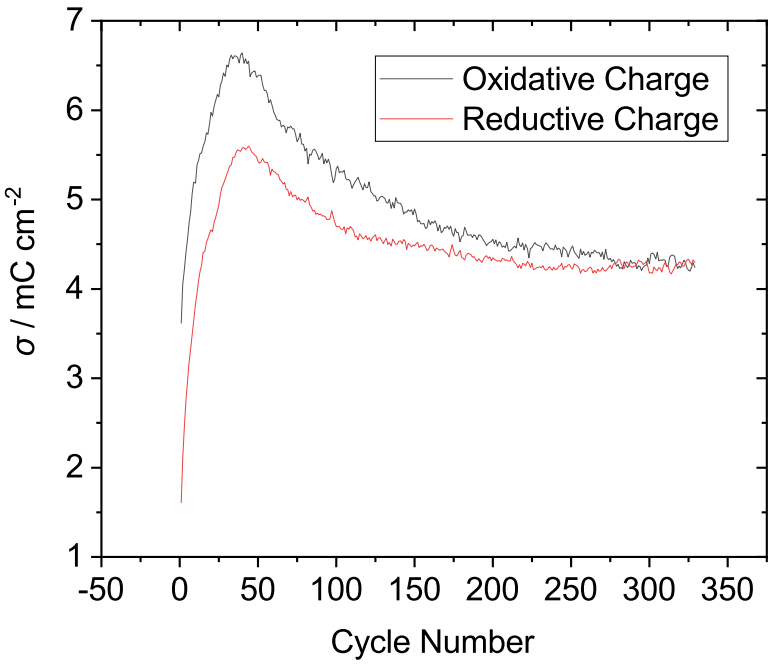

Figure 4.16: Integration of long term conditioning of Scheme 1 as a function of cycle number. No baseline correction has been made to these integrations, with the assumption being that all capacitive oxidative charge passed in the anodic sweep should be matched by capacitive reductive charge in the corresponding cathodic sweep.

The commonly accepted method by which $Ni(OH)_2$ oxidizes into NiOOH is the potential driven diffusion of protons through the oxide layer [19, 95, 103, 111–113, 115–118, 181–185]:

$$Ni(OH)_2 \rightleftharpoons NiOOH + H^+ + e^- \tag{4.12}$$

At sufficiently high potentials nickel metal can also oxidize directly to NiOOH [186]:

$$Ni + 3\,OH^- \rightleftharpoons NiOOH + H_2O + 3\,e^- \tag{4.13}$$

The second reaction here allows for the continuous growth of the oxide layer as hydroxide ions propagate through the oxide layer toward the nickel metal.

γ-NiOOH is a poor oxygen evolution catalyst and is the only significant NiOOH phase present for the first 50 CV cycles of Scheme 1 conditioning (Fig. 4.12). Oxidative charge passed with each cycle appears to continuously increase up to this point (Fig. 4.16). The first traces of β-NiOOH begin to appear shortly after this (Fig.

4.13), coinciding with the decrease in the oxidative charge passed with each cycle. It appears that as γ-NiOOH ages to β-NiOOH oxygen evolution begins and then the NiO layer growth accelerates. NiOOH continues to form at the boundary between the NiO and NiOOH layers, but the steady growth of the NiO phase eventually begins to inhibit NiOOH growth by reducing the total oxidative current passed during a sweep. NiO growth continues until the thickness of the resistive NiO layer begins to significantly slow the processes by which NiO can be formed [93, 96–100].

It is clear from the integrations of the CVs over the course of the Scheme 1 conditioning (Fig. 4.16) that the oxidative charge is larger than the reductive charge until approximately cycle 275. This excess oxidative charge is largely caused by the formation of new layers of NiOOH. After cycle 275 a steady state is achieved where the oxidative and reductive charges equalize. This steady state is likely caused by a combination of the NiO thickness and the diffusion limitation of H^+ ions moving into and out of the oxide layer [182]. At this point nearly all charge being passed goes to proton diffusion through the $Ni(OH)_2$/NiOOH matrix.

The shape of the integration of the reductive charge further validates the model above. If all the NiOOH formed in an anodic sweep were reduced in each subsequent cathodic sweep the reductive charge would be expected to grow until steady state were achieved through H^+ diffusion limitation. The actual reductive charge follows a trend similar to the oxidative charge, with a decrease beginning just after 50 cycles. This indicates that the factors inhibiting the oxidation processes are equally inhibiting the reduction processes. The increasing thickness of the highly resistive NiO layer describes this nicely as this layer is present for both processes due to its stability. Once the NiO layer is sufficiently thick the current passed through the $Ni(OH)_2$/NiOOH matrix will decrease to a point that some slower processes, such as NiO formation itself, occur very infrequently.

Further evidence of the NiO phase exists in the long term conditioning CVs for Schemes 1 and 2. They show an increase in a constant reductive current throughout the $Ni(OH)_2$ and NiO region (Fig. 4.13). This is likely caused by the build-up of the slow-to-reduce NiO phase. By performing some CVs, then a potential hold of 30 min at 0 V, followed immediately by more CVs, some interesting effects are observed (Fig. 4.17).

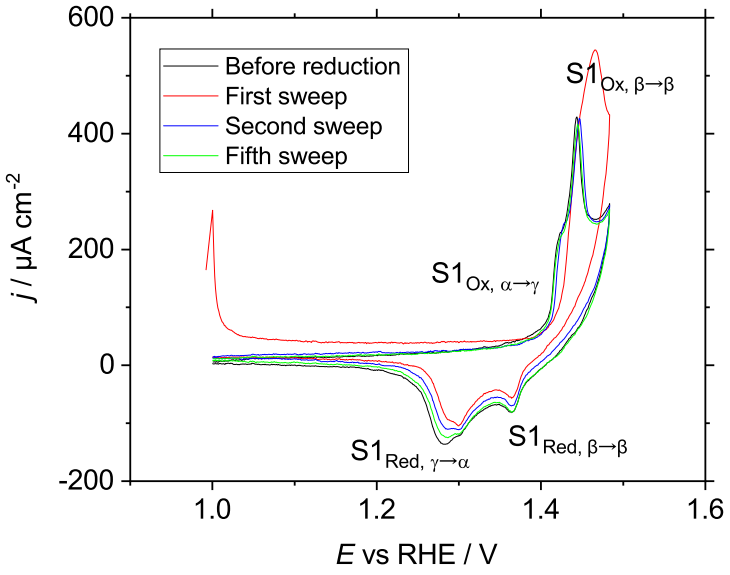

(a)

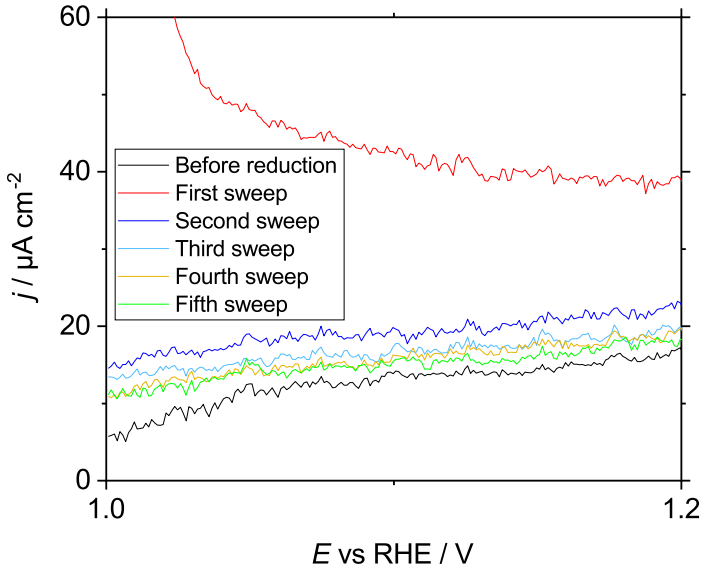

(b) Expanded view of (a), anodic sweeps only

Figure 4.17: CV of $Ni(OH)_2$ to NiOOH region before and after a 30 min potential hold at 0 V. The numbered sweeps occur after the potential hold. This experiment was performed on a sample conditioned by Scheme 1. The sweep rate was 5 mV s^{-1}.

The sweep-reduce-sweep experiment shows a typical CV on a nickel surface

that has achieved steady state by conditioning using Scheme 1. The initial sweep post-reduction has an anodic shift compared to the steady state CV. Additionally, this sweep appears to have a mildly delayed $S1_{Ox,\alpha\rightarrow\gamma}$ oxidation. The initial oxidation peak appears to belong to $S1_{Ox,\beta\rightarrow\beta}$ but in the following cathodic sweep both $S1_{Red,\beta\rightarrow\beta}$ and $S1_{Red,\gamma\rightarrow\alpha}$ are present. Subsequent sweeps appear to have retained the features from the long term conditioning process. The most interesting trend here is in the trend toward steady state after the reduction, with each cycle trending closer toward the steady state CV.

It appears that during the 30 min potential hold at 0 V much of the NiO layer was either reduced or converted to $Ni(OH)_2$. Without this layer the oxide has a lower resistance, causing a CV with a constant anodic shift compared to the steady state CV. Additionally, a thinner layer of NiO would have a larger capacitance [93]

$$C = \epsilon \frac{A}{d} \tag{4.14}$$

where C is the capacitance, A is the NiO surface area, ϵ is the permittivity of NiO, and d is the thickness of the NiO layer. This would result in a higher anodic current during sweeping experiments after conversion of NiO to $Ni(OH)_2$. The $Ni(OH)_2$/NiOOH oxidation region generates free reactive oxygen species in the $Ni(OH)_2$/NiOOH matrix, and the subsequent cathodic sweep appears similar to the steady state sweep due to the formation of more NiO. With each subsequent sweep the NiO layer continues to rebuild as more reactive oxygen species are trapped within the $Ni(OH)_2$/NiOOH matrix, moving the system closer to steady state. The process appears quite fast at first, with the difference between the first and second sweeps being quite significant. The difference between each subsequent sweep appears smaller (Fig. 4.17b).

The shape of the first anodic sweep after the reduction appears significantly different to the remaining sweeps with the onset of $Ni(OH)_2$ oxidation shifted to higher potentials (Fig. 4.17a). The change in onset potential of the first post-reduction sweep indicates that the 30 min hold at 0 V caused some structural changes to the oxide layer. The entire $Ni(OH)_2$ oxidation peak for the first post-reduction sweep appears as though it were a β-$Ni(OH)_2$ peak and regains the typical competitive α-$Ni(OH)_2$/β-$Ni(OH)_2$ behavior on the subsequent cathodic sweep. This could be caused by the NiO layers having been converted to a phase similar to β-$Ni(OH)_2$ during the 0 V hold. A thick enough layer of this oxide phase could prevent the

passing of current during a CV until the potential is reached at which proton diffusion can occur within it. This would make the entire $Ni(OH)_2$ CV peak appear as though it were β-$Ni(OH)_2$ as in Figure 4.17a.

The charge density of the entire $Ni(OH)_2$ oxidation peak on the steady state CV was determined by integrating all current from 1.380 V until the current became negative on the cathodic sweep. This was repeated on the first sweep after reduction after performing a constant horizontal baseline adjustment on this so that the capacitive region between 1.0 V and 1.2 V aligned with the steady state CV. It was found that the charge density of the steady state $Ni(OH)_2$ oxidation peak was 5.51 mC cm^{-2} and was 6.84 mC cm^{-2} for the first sweep after reduction. This likely relates to proton diffusion in the oxide layer as the mechanism of oxidation, and the issues that creates for utilization of the entire $Ni(OH)_2$/NiOOH matrix [110–112, 112, 113, 185]. Additionally, with much of the NiO layer converted to β-$Ni(OH)_2$ during the potential hold at 0 V, the resistance of the oxide layer would be much lower. As a result more current would be passed on the first sweep after reduction. Things would then return to a trend similar to steady state upon the first cathodic sweep and subsequent reformation of NiO.

The potential hold itself shows an interesting trend as well (Fig. 4.18). There is an initial large reductive current that decays quite rapidly, followed by a long slow decay to steady state.

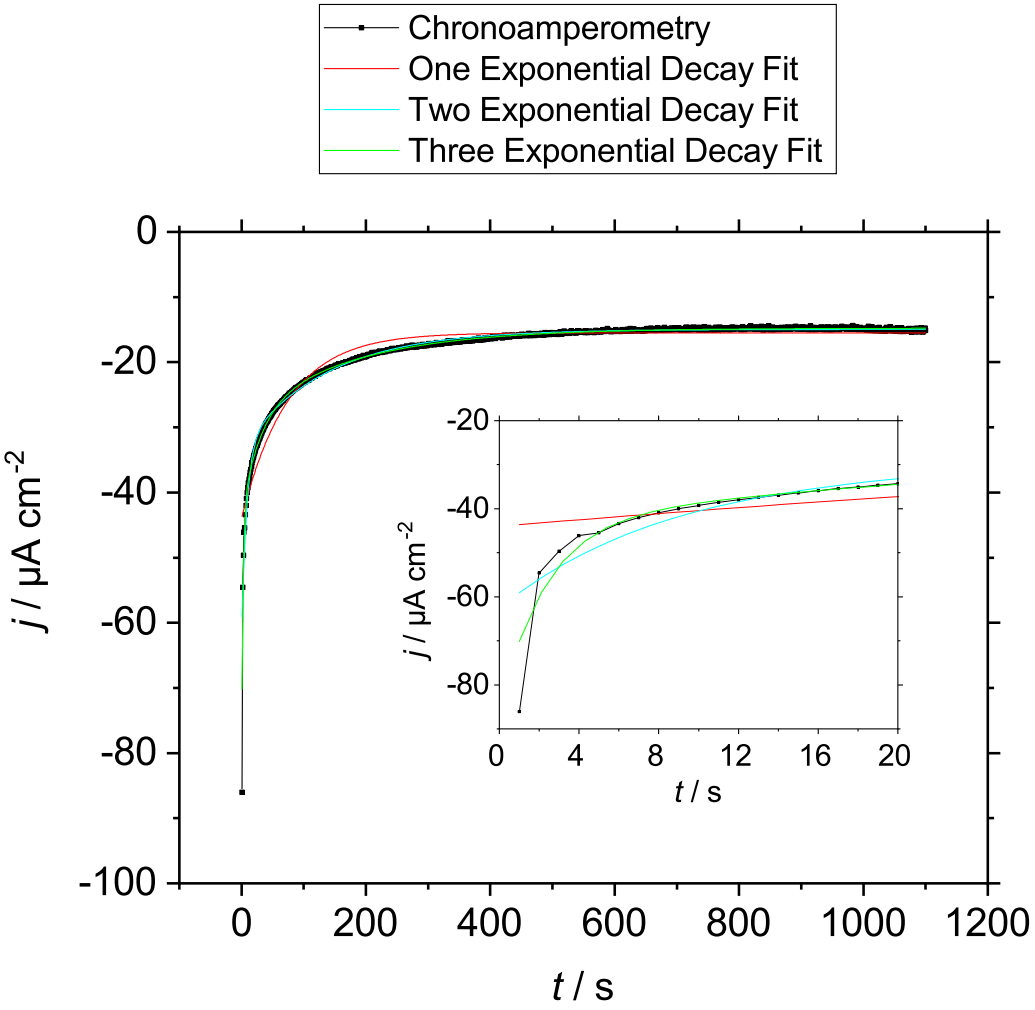

Figure 4.18: Chronoamperometry for the sweep-reduce-sweep experiment with exponential decay fits. The potential was held at 0 V for 30 min, however only 1100 seconds are shown here for clarity.

The chronoamperometry curve was fit in OriginPro 2018 using the exponential decay fitting function and the following equations:

$$
\begin{aligned}
j &= A1\,\exp\left(\frac{-t}{\tau_1}\right) + y0 \\
j &= A1\,\exp\left(\frac{-t}{\tau_1}\right) + A2\,\exp\left(\frac{-t}{\tau_2}\right) + y0 \\
j &= A1\,\exp\left(\frac{-t}{\tau_1}\right) + A2\,\exp\left(\frac{-t}{\tau_2}\right) + A3\,\exp\left(\frac{-t}{\tau_3}\right) + y0
\end{aligned}
\tag{4.15}
$$

The reduced chi-squared values of these fits were then compared using the F-Test sequentially, with a single decay being compared with two decays and two decays being compared with three. The requirement for acceptance was passing the F-Test at the 99% confidence level. This methodology, which has been used in literature [180], showed that the three time constant decay was an appropriate fit. A fit with four time constants was tested, but was unable to be fit. Given this, the following time constants were extracted from the fit:

$$
\begin{aligned}
\tau_1 &= 2.3\ \text{s} \\
\tau_2 &= 29.7\ \text{s} \\
\tau_3 &= 175.4\ \text{s}
\end{aligned}
\tag{4.16}
$$

Three time constants are found, but due to the variety of oxide phases present on the nickel surface and their non-stoichiometric nature it is not simple to determine what causes each time constant. It appears that the same ratio of β-NiOOH to γ-NiOOH existed on the surface after the second sweep post-reduction. This is indicated by the fact that the CV trace of the second sweep had the same shape as the steady state CV. This makes it unlikely that the $Ni(OH)_2$ was reduced at all. Other compounds that could be on the electrode at steady state include NiO, β-NiOOH, γ-NiOOH, and possibly some trapped oxygen species in the NiOOH matrix. It is unclear which time constants belong to which compounds, however both phases of NiOOH and any trapped oxygen species would be expected to get reduced quite quickly. The layer of NiO is then likely described by the 175 s time constant. It is also possible that the large time constant is describing some issue with NiOOH discharge caused by proton diffusion through the $Ni(OH)_2$/NiOOH matrix [110–112, 112, 113, 185]. Note that while a time constant for double-layer charging

may be expected here, 2.3 s is far too large a time constant for double layer charging as this is typically on the order of microseconds.

4.3.3 Determination of the source of the E_r shift of $Ni(OH)_2$ oxidation as a function of temperature

Cyclic voltammetry studies were performed on $Ni(OH)_2$ oxidation at various temperatures. For this study the working electrode was a piece of nickel wire allowed to sit in open air for many days. This allowed the formation of an air stabilized $Ni(OH)_2$ layer. This results in a $Ni(OH)_2$ to NiOOH oxidation peak that is very sharp and appears to be of one relatively consistent phase. Initial studies showed a significant decrease in the reversible potential, E_r, of the oxidation of β-$Ni(OH)_2$ as temperatures increased (Fig. 4.19). This effect has been documented previously in the literature [56, 146].

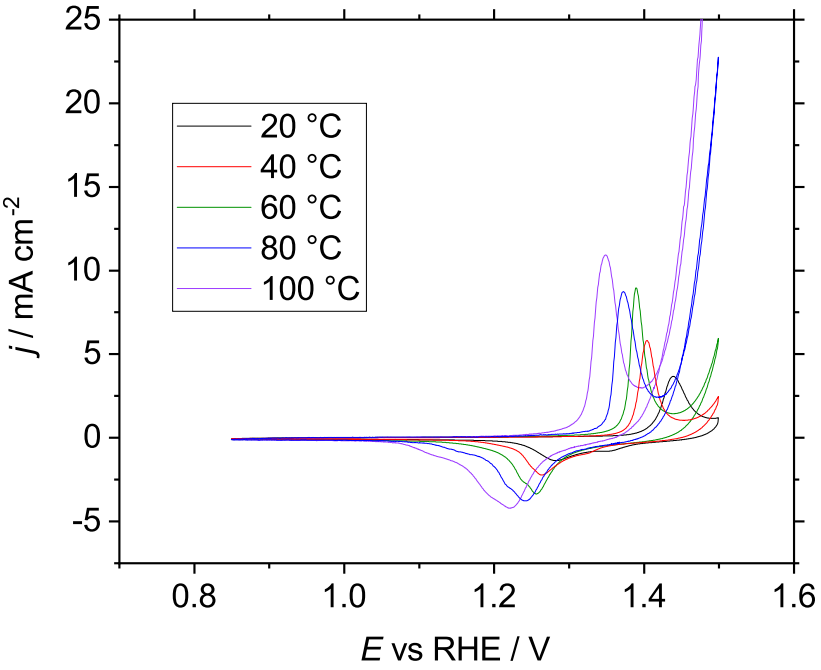

Figure 4.19: CVs for oxidation of β-$Ni(OH)_2$ as a function of temperature. The sweep rate was 50 mV s^{-1}.

The E_r of each β-$Ni(OH)_2$ oxidation CV can be determined by a variety of different methods. The open circuit potential of the electrode could be measured, however this requires a sacrifice of potential control and so was avoided. Additionally, it is difficult

to know whether or not the open circuit potential is stable and therefore a true reversible potential. The average of the anodic and cathodic peak potentials could be taken, however as discussed previously the oxide phases change in composition over time which can result in a substantial shift of the peak potentials while leaving the onset potentials relatively untouched. The Tafel regions of the anodic and cathodic peaks could be extrapolated to the x-axis and the point between their x-intercepts chosen. This method seems reasonable, however programmatically it is quite complex. Additionally, since the objective of the E_r measurements is to compare their shift as a function of temperature a high degree of accuracy is unnecessary so long as the method is self consistent. Any self consistent method should result in the observation of the same shift in E_r. For this reason the E_r of each β-$Ni(OH)_2$ oxidation CV was determined by adding the anodic and cathodic currents at each potential and selecting the potential between the anodic and cathodic peaks for which this sum is closest to 0. This resulted in a simple and robust means of consistently determining E_r. E_r can then be plotted against temperature (Fig. 4.20). This shows that the the E_r of each CV was decreased by approximately -1.14 mV K^{-1}. While not quantified in the literature, similar effects have been observed in lower temperature studies [56, 146]. It is difficult to estimate the effect from the literature studies without numerical data, however Alsabet et al. appear to observe a shift of about $-1.25\,\mathrm{mV\ K^{-1}}$ and Macdonald et al. appear to see a shift of about $-0.8\,\mathrm{mV\ K^{-1}}$.

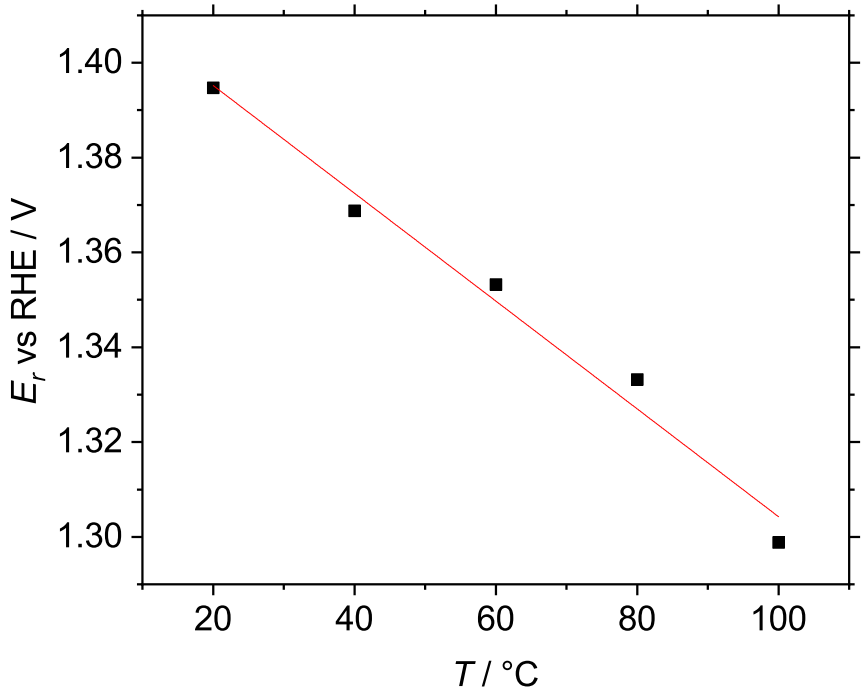

Figure 4.20: E_r of β-$Ni(OH)_2$ oxidation as a function of temperature. The formula for the line is $E_r = 1.418 \pm 0.006\,\mathrm{V} - 1.14 \pm 0.09\,\mathrm{mV\ °C^{-1}} \times T$ with $R^2 = 0.98$. This was determined using CVs collected at $50\,\mathrm{mVs^{-1}}$.

Ideally the source of the 1.14 mV K^{-1} change in reversible potential should be determined thermodynamically. If the half reactions that describe the β-$Ni(OH)_2$ oxidation are laid out vs the RHE reaction, with the reference reaction as an oxidation and the reaction of interest as a reduction (by convention),

$$\begin{aligned} \beta\text{−NiOOH} + \mathrm{H_2O} + \mathrm{e^-} &\rightleftharpoons \beta\text{−Ni(OH)}_2 + \mathrm{OH^-} \\ \frac{1}{2}\,\mathrm{H_2} + \mathrm{OH^-} &\rightleftharpoons \mathrm{H_2O} + \mathrm{e^-} \end{aligned} \tag{4.17}$$

and used alongside the Nernst equation:

$$\begin{aligned} \beta\text{−NiOOH} + \frac{1}{2}\,\mathrm{H_2} &\rightleftharpoons \beta\text{−Ni(OH)}_2 \\ E_r = E^\circ - \frac{RT}{nF} \ln \frac{Products}{Reactants} \\ E_r = E^\circ - \frac{RT}{F} \ln \frac{a(\beta\text{-Ni(OH)}_2)}{a(\beta\text{-NiOOH}) \cdot (f(\mathrm{H_2})/p^\circ)^{1/2}} \end{aligned} \tag{4.18}$$

where E_r is the reversible cell potential, E° is the standard cell potential, R is the universal gas constant, T is the absolute temperature, $n = 1$ is the number of electrons involved in the reaction, F is Faraday's constant, $a(\beta\text{-Ni(OH)}_2)$ is the activity of β-$Ni(OH)_2$, $a(\beta\text{-NiOOH})$ is the activity of β-NiOOH, $f(H_2)$ is the fugacity of hydrogen gas at the reference electrode, and p° is the standard state pressure.

β-$Ni(OH)_2$ and β-NiOOH are solids, so their activities can be approximated as 1 to simplify things. p° is a constant equal to 1 bar required in order to make the value inside the logarithm a dimensionless quantity. Fugacity can be separated into the fugacity coefficient, γ, and the partial pressure of hydrogen gas $p(H_2)$.

$$E_r = E^\circ + \frac{RT}{2F} \ln \gamma \cdot \frac{p(H_2)}{p^\circ} \tag{4.19}$$

This highlights the factors that might affect the reversible cell potential E_r as temperature changes. There appear to be three things that can change the cell potential: the standard cell potential E°, the fugacity coefficient γ, and hydrogen partial pressure $p(H_2)$. Here the effect each component has will be explored as a function of temperature.

Fugacity, γ, departs from 1 when the hydrogen molecules interact with themselves or other molecules they are contained with, decreasing for attractions. In this scenario, as the water in the solution below the hydrogen heats up, the vapor pressure of the water will increase. As the partial pressure of water vapor in the hydrogen bubble slowly increases the fugacity of the hydrogen will fall below 1, causing the fugacity term in equation 4.19 to become negative. This means that the fugacity contributes towards the 1.14 mV K^{-1} drop discussed initially. Considering the magnitude of the shift, however, the fugacity coefficient would have to be unrealistically small in order to mhave a significant effect. For example, if the fugacity coefficient were a very extreme 0.5 the total shift would be only -0.03 mV K^{-1}. The potential shift must be coming from another source.

The hydrogen partial pressure, $p(H_2)$, is not expected to change much throughout the experiment. Due to the autoclave being self-pressurized the partial pressure of hydrogen remained relatively constant at temperatures lower than approximately 100 °C. At higher temperatures, as hydrogen is dissolved the bubble decreases in volume but not pressure. Overall the potential shift caused by any change in the partial pressure of hydrogen is negligible as long as temperature is ramped slowly enough to prevent significant temperature gradients [1].

The effect that E° has on E_r can be determined using the following:

$$\begin{aligned} \Delta G^\circ &= -nFE^\circ \\ n &= 1 \\ \left(\frac{\partial \Delta G^\circ}{\partial T}\right)_p &= -F\left(\frac{\partial E^\circ}{\partial T}\right)_p \\ \left(\frac{\partial E^\circ}{\partial T}\right)_p &= \frac{-1}{F}\left(\frac{\partial \Delta G^\circ}{\partial T}\right)_p \end{aligned} \tag{4.20}$$

Where ΔG° is the change in the standard Gibbs' free energy of the reaction. Now using the relationships

$$\begin{aligned} \mathrm{d}\,G &= V\,\mathrm{d}\,p - S\,\mathrm{d}\,T \\ \mathrm{d}\,G &= \left(\frac{\partial G}{\partial p}\right)_T \mathrm{d}\,p + \left(\frac{\partial G}{\partial T}\right)_p \mathrm{d}\,T \\ \left(\frac{\partial G}{\partial T}\right)_p &= -S, \ \left(\frac{\partial G}{\partial p}\right)_T = V \end{aligned} \tag{4.21}$$

where G is Gibbs' free energy, V is volume, S is entropy, and p is pressure. If equation 4.21 is combined with the result from equation 4.20 it is follows that

$$\left(\frac{\partial E^\circ}{\partial T}\right)_p = \frac{-1}{F}\left(\frac{\partial \Delta G^\circ}{\partial T}\right)_p = \frac{\Delta S^\circ}{F} \tag{4.22}$$

This shows that the change in E° with respect to temperature can be determined as long as the ΔS° of the reaction remains relatively constant over the temperature range. This value is easy to calculate using table values.

Compound	Standard Molar Entropy S° / J mol^{-1}K^{-1}
β-Ni(OH)$_2$	88
β-NiOOH	66.98
H_2	130.680

Table 4.3: S° values for the oxidation of β-Ni(OH)$_2$ [187, 188]

Using these values shows

$$\Delta S^\circ = -44\,\mathrm{J\ mol^{-1}\ K^{-1}} \tag{4.23}$$

and therefore the change in E° as a function of potential per unit temperature given equation 4.22.

$$\frac{\mathrm{d}\,E^\circ}{\mathrm{d}\,T} = \frac{\Delta S^\circ}{F} = -0.46\,\mathrm{mV\ K^{-1}} \tag{4.24}$$

This does not match the empirically seen value of -1.14 mV K^{-1}.

The change in the S° of hydrogen as a function of temperature has been neglected. In order to rule it out as a major factor in the ΔS° of the reaction some calculations are done using the following data:

Temperature / K	Hydrogen Gas Standard Molar Entropy S° / J $\mathrm{mol^{-1}K^{-1}}$
298.15	130.680
400	131.818

Table 4.4: S° values for H_2 as a function of temperature [187].

Now with the data from tables 4.3 and 4.4, along with equation 4.22 the following is shown

$$\begin{aligned} \text{at } 298.15\text{ K}: \frac{dE^\circ}{dT} &= -0.46\,\mathrm{mV\ K^{-1}} \\ \text{at } 400\text{ K}: \frac{dE^\circ}{dT} &= -0.46\,\mathrm{mV\ K^{-1}} \end{aligned} \tag{4.25}$$

This shows that the effect due to the increase in the entropy of hydrogen as a function of temperature is not a significant enough result to create the effect seen in E° by itself.

A likely reason for this difference in $\Delta S^\circ F^{-1}$ value is that the oxidation process is more complex than the discrete phases often mentioned in literature. Recent Pourbaix diagrams of the aqueous nickel system published in literature [189] suggest that the regime in which this work was performed exists at a confluence of a variety of nickel oxide phases. In order to account for this all, likely possible phases in the Pourbaix diagram are considered for analysis. Additionally, two proposed non-stoichiometric oxidations found in the literature [14, 57] are considered (Table 4.5).

Possible Oxidation Processes	$\Delta S^\circ F^{-1}$ / mV K^{-1}	E_r / V
$NiO + OH^- \rightleftharpoons NiOOH + e^-$	-0.25	1.31
$3\,NiO + 2\,OH^- \rightleftharpoons Ni_3O_4 + H_2O + 2\,e^-$	-0.94	0.82
$2\,NiO + 2\,OH^- \rightleftharpoons Ni_2O_3 + H_2O + 2\,e^-$	-3.0	0.98
$NiO + 2\,OH^- \rightleftharpoons NiO_2 + H_2O + 2\,e^-$	-1.2	1.21
$Ni(OH)_2 + OH^- \rightleftharpoons NiOOH + H_2O + e^-$	-0.46	1.30
$3\,Ni(OH)_2 + 2\,OH^- \rightleftharpoons Ni_3O_4 + 4\,H_2O + 2\,e^-$	-1.56	0.81
$2\,Ni(OH)_2 + 2\,OH^- \rightleftharpoons Ni_2O_3 + 3\,H_2O + 2\,e^-$	-3.38	0.97
$Ni(OH)_2 + 2\,OH^- \rightleftharpoons NiO_2 + 2\,H_2O + 2\,e^-$	-1.41	1.20
$0.25\,NiOOH \cdot 0.75\,Ni(OH)_2 \cdot 0.25\,H_2O + 0.025\,K^+ + 0.525\,OH^- \rightleftharpoons 0.75\,NiOOH \cdot 0.25\,Ni(OH)_2 \cdot 0.22\,H_2O \cdot 0.025\,KOH\ ads + 0.53\,H_2O + 0.5\,e^-$	-0.23	1.42
$2\,[Ni(OH)_2 \cdot 1.28\,H_2O] + 0.14\,K^+ + 2.14\,OH^- \rightleftharpoons 2\,NiOOH \cdot 0.14\,KOH\ ads + 4.56\,H_2O + 2\,e^-$	-0.92	1.30

Table 4.5: Possible oxidation processes involved in the NiOOH oxidation peak. All values in the table were determined from the thermodynamic data listed in Table 4.6 using equations 4.22 and 4.20. While these processes are shown as oxidations the values were calculated with them set as reductions (by convention) balanced against the RHE reaction (Eq. 4.17) as an oxidation. The non-stoichiometric reactions are directly from the literature [14, 57]. Note that while these do contain K^+ ions where this work used Na^+, the thermodynamic behavior seen in either system is nearly indistinguishable suggesting they either behave very similarly or have very little effect.

Compound	S° / J mol^{-1}K^{-1}	ΔG_f° / kJ mol^{-1}	Reference
NiO	37.99	-211.10	[190]
$Ni(OH)_2$	88	-447.2	[187]
$Ni(OH)_3^-$	-133	-586.5	[190]
NiOOH	66.98	-321.7	[188]
Ni_3O_4	143.6[a]	-711.7	[191] [192]
Ni_2O_3	301.3[a]	-469.83	[187] [192]
NiO_2	93.2[a]	-215.1	[193] [110]
H_2O	70.0	-237.1	[187]
KOH	91.6	-440.50	[194]
OH^-	-10.75	-157.244	[194]
K^+	102.5	-283.27	[194]

Table 4.6: Thermodynamic data for the nickel-water system from literature.
[a]: Calculated using the ΔG_f° and ΔH_f° from the references listed to get ΔS_f°. From there S° was calculated using the definition of the formation reaction. Eg. $S_f^\circ(H_2O, 298.15K) = S^\circ(H_2O, 298.15K) - S^\circ(H_2, 298.15K) - S^\circ(\frac{1}{2}\,O_2, 298.15K)$

The data in table 4.5 appears to indicate that the reactions

$$\begin{aligned} NiO + 2\,OH^- &\rightleftharpoons NiO_2 + H_2O + 2\,e^- \\ Ni(OH)_2 + 2\,OH^- &\rightleftharpoons NiO_2 + 2\,H_2O + 2\,e^- \end{aligned} \tag{4.26}$$

could describe the experimental results, however the available thermodynamic data for the nickel-water system (Table 4.6) is insufficient to conclude that. The available sources neglect to take into account the various phases and stoichiometries that many of the nickel oxides have been shown to exist in [12–15, 57], and many sources have conflicting data. Table 4.6 represents the most reliable data, however some of these values had to be estimated from other available thermodynamic values. Given the unreliable nature of the current thermodynamic literature on the nickel-water system, it is likely that many of these reactions could describe the collected data to within a reasonable error.

4.3.4 $Ni(OH)_2$ Formation at High Temperatures

4.3.4.1 α-$Ni(OH)_2$ to β-$Ni(OH)_2$ Aging Mechanism

There are two mechanisms by which α-$Ni(OH)_2$ can age to β-$Ni(OH)_2$ at room temperature. The first is a dissolution, nucleation, and growth process [104, 195–199]. However, β-$Ni(OH)_2$ does not readily dissolve. The other is through a solid state transition by oxidation from α-$Ni(OH)_2$ to γ-$Ni(OH)_2$, followed by a transition through a poorly crystalline β-NiOOH phase resulting in properly crystalline β-NiOOH, and finally the reduction to β-$Ni(OH)_2$ [177, 200–202]. This pathway is unavailable at potentials where NiOOH is not formed.

It can be shown that a reduction peak corresponding to the reduction of γ-NiOOH to α-$Ni(OH)_2$, as determined by literature [12, 14, 60, 68, 86, 126–128], can be present on a nickel electrode while no features are present in the α-$Ni(OH)_2$ region (Fig. 4.21). This is because while the uppermost layer of α-$Ni(OH)_2$ has been allowed to dissolve and precipitate back into the β-$Ni(OH)_2$ state, the deeper layers of α-$Ni(OH)_2$ are not at the solution interface and so cannot undergo this transition easily. The result is that some of the outermost layers of $Ni(OH)_2$ are in the β-$Ni(OH)_2$ state after cycling. This in turn indicates that the features seen at room temperature between 0 V and 0.45 V attributed to α-$Ni(OH)_2$ only represent α-$Ni(OH)_2$ at the oxide/solution interface.

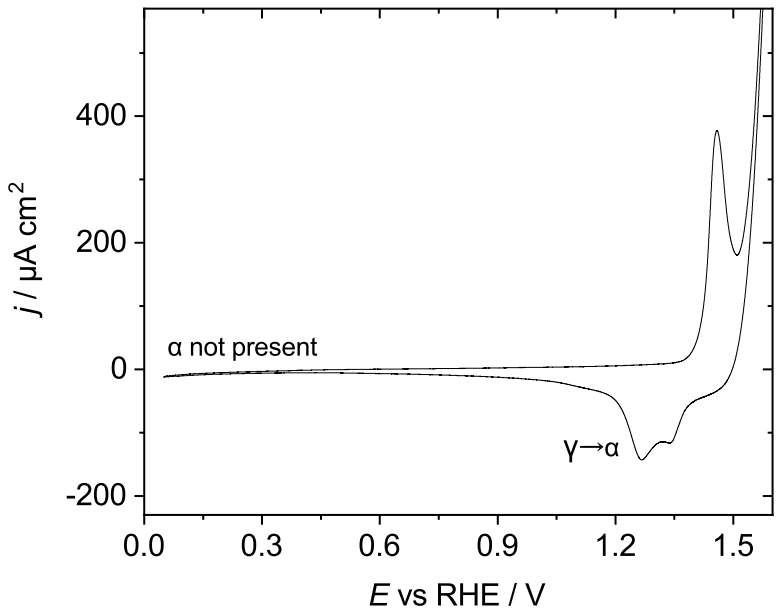

Figure 4.21: CV showing a reduction from γ to α with no activity in the α region. Very little conditioning is required to see this. It can be obtained by performing a CV through the NiOOH region, then sweeping down to the α region. The sweep rate was 100 mV s^{-1}.

4.3.4.2 AC and DC Voltammetry Analysis

The high temperature study of the region in which $Ni(OH)_2$ forms was performed in one continuous 71 hour experiment. This was done in an attempt to minimize variation between electrochemical experiments. The CVs shown here were collected simultaneously with the dEIS data. dEIS and AC voltammetry data for 20 °C, 100 °C, 120 °C, and 140 °C were collected.

The CVs collected for this experiment show very interesting features (Fig. 4.22). It was previously discussed (Section 2.4) that allowing the electrode potential to go beyond the α-$Ni(OH)_2$ region, above 0.5 V, would cause the α-$Ni(OH)_2$ features to be lost on any subsequent test. This is not true for sweeps performed at temperatures 100 °C and above.

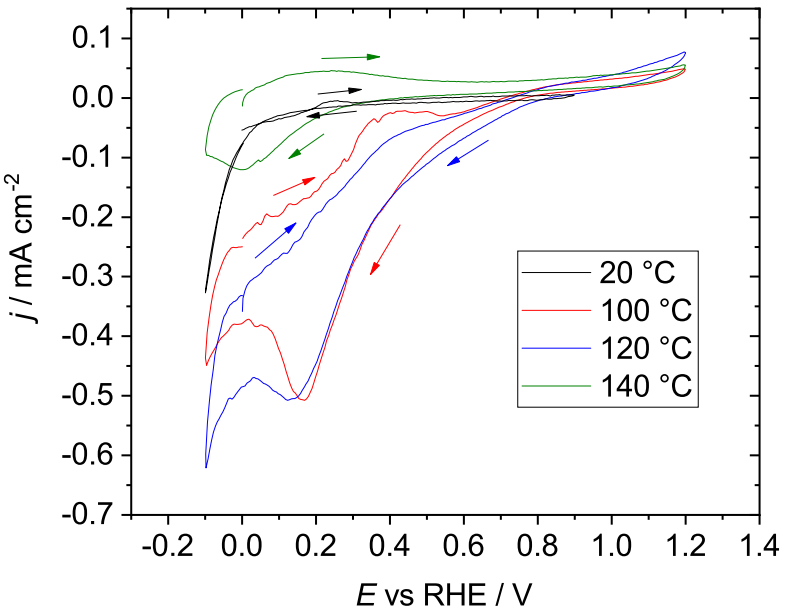

Figure 4.22: CVs for $Ni(OH)_2$ formation as a function of temperature. Sweeps were performed from 0 V to 1.2 V then back down to -0.1 V, with the exception of the 20 °C sweep that was performed from 0 V to 0.9 V then back down to -0.1 V. The sweep rate was 5 mV s^{-1}.

This behavior is confirmed in the AC voltammetry (Fig. 4.23), with increased admittance in both the imaginary and real components seen on the cathodic sweep starting between 0.4 V and 0.6 V for the experiments run at temperatures higher than 100 °C. This increase in admittance is not seen for the 20 °C trial. The only other noteworthy feature in the admittance plots is an increase in both real and imaginary components of the admittance. This starts at approximately 0.85 V on the 140 °C experiment and at 1.1 V on the 100 °C and 120 °C experiments.

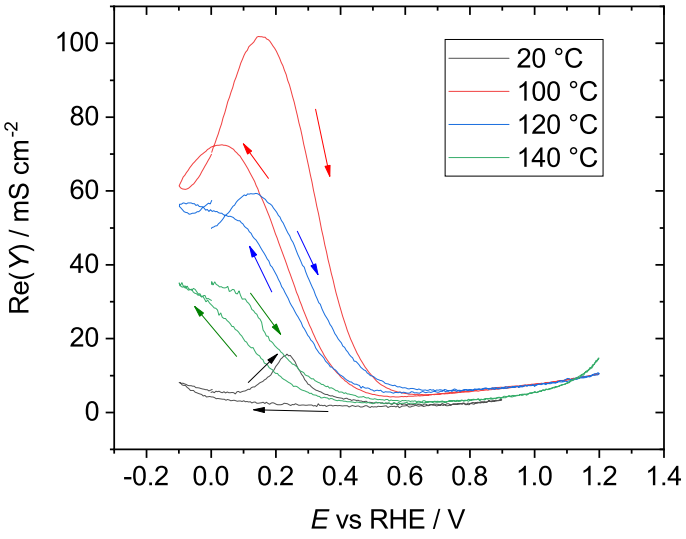

(a) Re(Y)

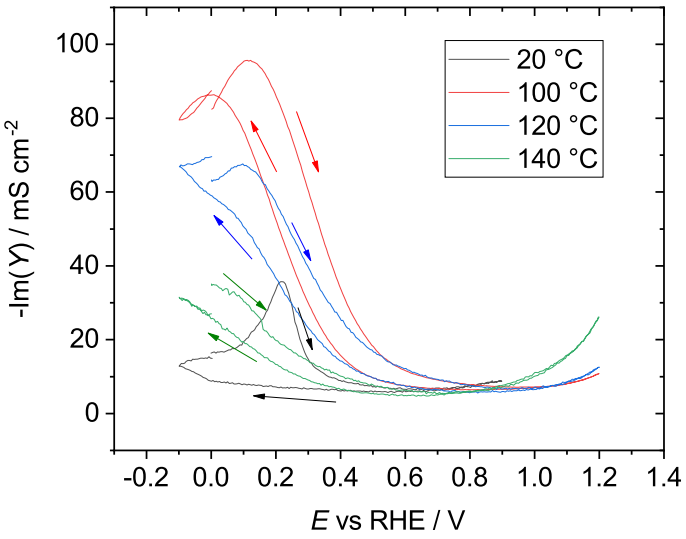

(b) Im(Y)

Figure 4.23: Admittance plots for $Ni(OH)_2$ formation as a function of temperature. Sweeps were performed from 0 V to 1.2 V then back down to -0.1 V, with the exception of the 20 °C sweep that was performed from from 0 V to 0.9 V then back down to -0.1 V. The sweep rate was 5 mV s^{-1}. Data for 100 Hz is shown.

Some cathodic current is seen below 0.8 V on the CVs performed at temperatures

100 °C and above. This is caused by oxygen reduction occurring on the $Ni(OH)_2$ surface [203, 204], as $Ni(OH)_2$ appears to be a reasonably efficient oxygen reduction catalyst with an onset potential around 0.8 V. Due to the long term experiment and single reaction vessel it appears that oxygen has been evolved at the counter electrode, dissolved in solution, and eventually made its way to be reduced at the working electrode. Interestingly, this indicates that the dominant oxide phase at the oxide/solution interface is NiOOH above this potential as this is still well below the oxygen reduction potential [205] and NiOOH does not appear to reduce oxygen gas [206]. It is possible that some amount of NiOOH can form at the topmost layer while the oxidation of other layers is inhibited by slow proton diffusion [110–113, 207] until higher potentials. Cathodic current for oxygen evolution is not seen at 140 °C likely due to the fact that the solubility of oxygen in aqueous solution decreases with temperature [187].

The fact that α features are visible between 0 V and 0.45 V at temperatures 100 °C and over indicates the β-$Ni(OH)_2$ phase is not crystallizing on the surface after the dissolution of α-$Ni(OH)_2$. It is possible that no recrystallization is occurring at all, but it is more likely that at these temperatures the recrystallization simply yields more α-$Ni(OH)_2$. This allows α-$Ni(OH)_2$ to remain the oxide phase at the oxide/solution interface resulting in the appearance of these features.

4.3.4.3 Electrochemical Impedance Spectroscopy Analysis

Fitting the impedance data collected using the method described previously (Section 4.2.3) resulted in complex data. Polarization resistances collected by dEIS were found to be consistently lower than those determined via the DC method (Section 4.3.1.2). This indicates that not all processes occurring on the electrode surface were detected by the dEIS experiment, and indeed by performing pEIS to much lower frequencies it appears that much more can be seen. Note that these two methods are not necessarily directly comparable, as pEIS data applies to the steady state condition and dEIS data applies to the slow sweep condition. Unfortunately due to the limitations of dEIS lower frequencies are not accessible.

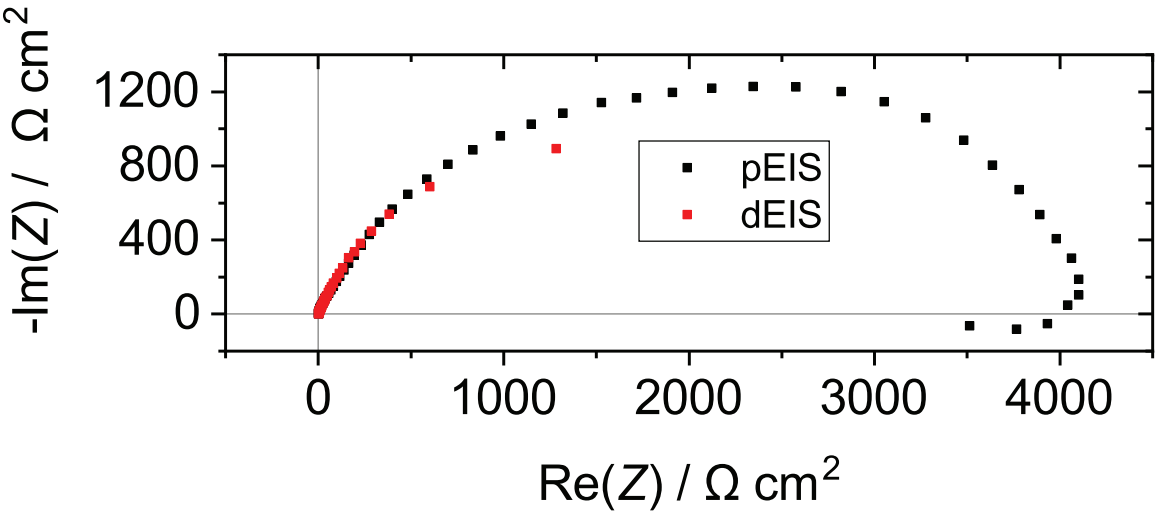

Figure 4.24: Nyquist plots for raw data of dEIS and pEIS at 0.6 V and 100 °C. dEIS was collected with a sweep rate of 5 mV s^{-1}.

The statistical methods used to determine the circuit of best fit indicated that circuit 3 was the best fit for many dEIS spectra (Fig. 4.5). When plotting the data from these fits, however, the results for the second time constant were very chaotic. This is likely due to a high degree of fitting error which can happen when frequencies probed are not low enough to capture a slow process accurately. In place of this, dEIS spectra that fit circuit 3 were analysed using circuit 2 (Fig. 4.25). The removal of one fitting parameter appears to simplify the fitting allowing for the emergence of trends to appear in the resulting fits. These trends may not be very quantitative, however for qualitative comparisons they should perform adequately. Some wiring artifacts appear above 4400 Hz in the 140 °C experiment so fitting was performed only on frequencies below that. Finally, viable fits were unable to be determined at potentials above 0.5 V for the 20 °C experiment, because at room temperature this potential region is where the top layer of α-$Ni(OH)_2$ ages into β-$Ni(OH)_2$ inhibiting further reactions.

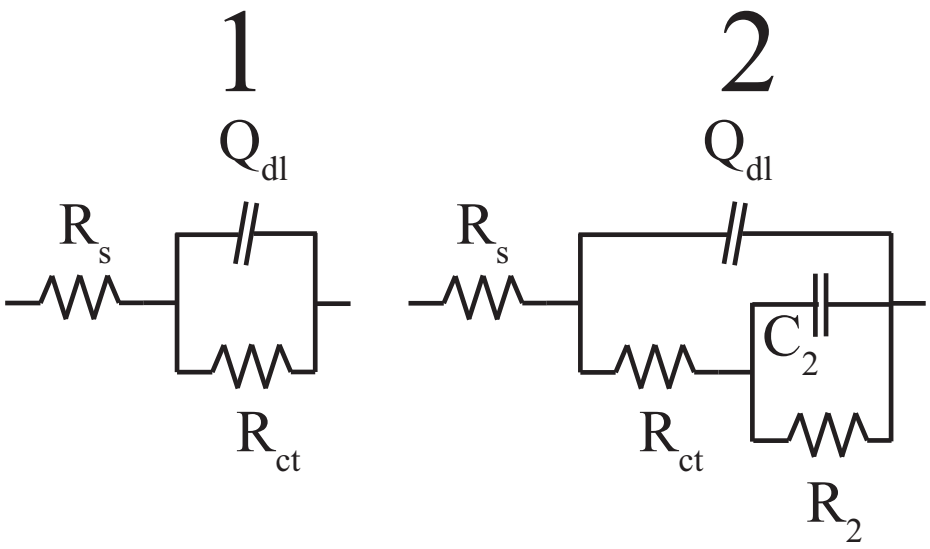

Figure 4.25: Circuits successfully fit to $Ni(OH)_2$ impedance data.

From the fits several values were determined. The effective double layer capacitance, $C_{dl,eff}$ was determined from CPE fitting parameters using the Brug formula [208, 209]:

$$C_{dl,eff} = Q^{\frac{1}{\alpha}} \left(\frac{R_s R_{ct}}{R_s + R_{ct}} \right)^{\frac{1-\alpha}{\alpha}} \tag{4.27}$$

where Q is the CPE coefficient, α is the CPE exponent, R_s is the solution resistance, and R_{ct} is the charge transfer resistance.

System time constants for the two-time-constant circuit were determined by converting the impedance formula for the circuit into its corresponding admittance form, which is the transfer function for a potential controlled experiment (Section 2.3.2.5). The time constants were determined to be:

$$\begin{aligned} \tau_1 &= \frac{2R_2 R_{ct} R_s C_2 C_{dl}}{\tau_{1,denominator}} \\ \tau_2 &= \frac{2R_2 R_{ct} R_s C_2 C_{dl}}{\tau_{2,denominator}} \end{aligned} \tag{4.28}$$

where

$$\begin{aligned}
\tau_{1,denominator} &= -R_2R_{ct}C_2 - R_2R_sC_2 - R_2R_sC_{dl} - R_{ct}R_sC_{dl} \\
&+ \sqrt{\begin{aligned}&R_2^2R_{ct}^2C_2^2 + 2R_2^2R_{ct}R_sC_2^2 - 2R_2^2R_{ct}R_sC_2C_{dl} + R_2^2R_s^2C_2^2 \\ &+ 2R_2^2R_s^2C_2C_{dl} + R_2^2R_s^2C_{dl}^2 - 2R_2R_{ct}^2R_sC_2C_{dl} \\ &- 2R_2R_{ct}R_s^2C_2C_{dl} + 2R_2R_{ct}R_s^2C_{dl}^2 + R_{ct}^2R_s^2C_{dl}^2\end{aligned}} \\
\tau_{2,denominator} &= R_2R_{ct}C_2 + R_2R_sC_2 + R_2R_sC_{dl} + R_{ct}R_sC_{dl} \\
&+ \sqrt{\begin{aligned}&R_2^2R_{ct}^2C_2^2 + 2R_2^2R_{ct}R_sC_2^2 - 2R_2^2R_{ct}R_sC_2C_{dl} + R_2^2R_s^2C_2^2 \\ &+ 2R_2^2R_s^2C_2C_{dl} + R_2^2R_s^2C_{dl}^2 - 2R_2R_{ct}^2R_sC_2C_{dl} \\ &- 2R_2R_{ct}R_s^2C_2C_{dl} + 2R_2R_{ct}R_s^2C_{dl}^2 + R_{ct}^2R_s^2C_{dl}^2\end{aligned}}
\end{aligned} \tag{4.29}$$

These values are clearly very complicated, and it is not clear how they describe the kinetics of the system measured. They do measure the rate of some processes happening on the electrode surface, however, and can be used to probe for processes as a function of potential as well as their relative rates.

Capacitance plots highlight that the dEIS data exists in two separate regimes (Figs. 4.26 and 4.27). By looking at plots of oxidative charge density from chronoamperometry experiments as a function of potential and temperature this is highlighted further (Fig. 4.28). The chronoamperometry data shows negative charge densities at potentials more negative than 0.8 V. The magnitudes of these charge densities is too large to be a process restricted to the electrode surface. They also appear to have exponential behavior as a function of potential. Finally, the steady state currents of the chronoamperometry experiments are all quite small. The largest steady state current, the one for 120 °C at 0.2 V, was -45 μA.

The logical conclusion is that this negative current is caused by the reduction of species in solution, and given the experimental setup this species is likely oxygen gas produced at the counter electrode. No reductive charge is seen for the 140 °C experiments. For this reason the 100 °C and 120 °C dEIS data should not be compared to the other dEIS trials, however comparison between 20 °C and 140 °C is acceptable. As no oxygen reduction appears to occur above 0.8 V, data at all temperatures can be compared in this potential region.

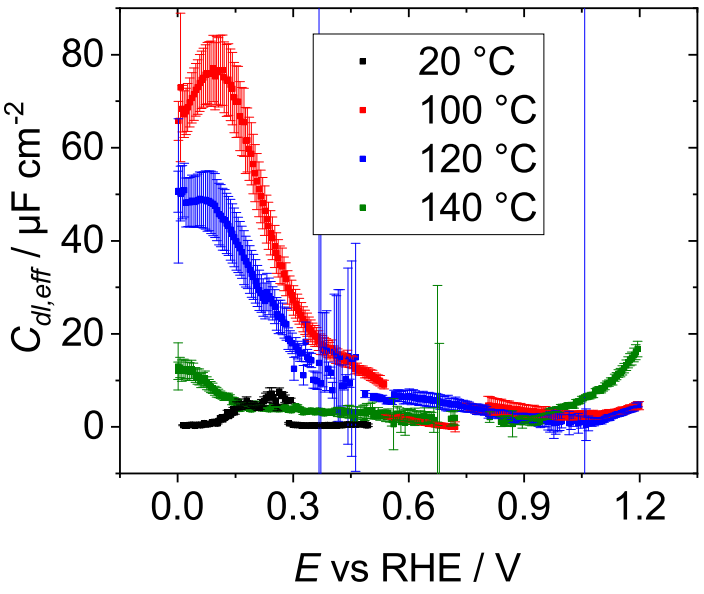

(a) Forward Sweep

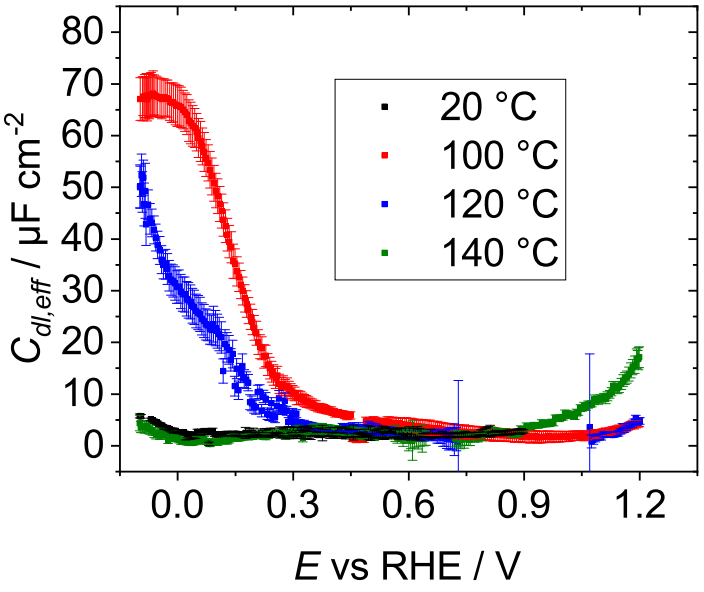

(b) Reverse Sweep

Figure 4.26: $C_{dl,eff}$ from $Ni(OH)_2$ dEIS data.The sweep rate was 5 mV s^{-1}.

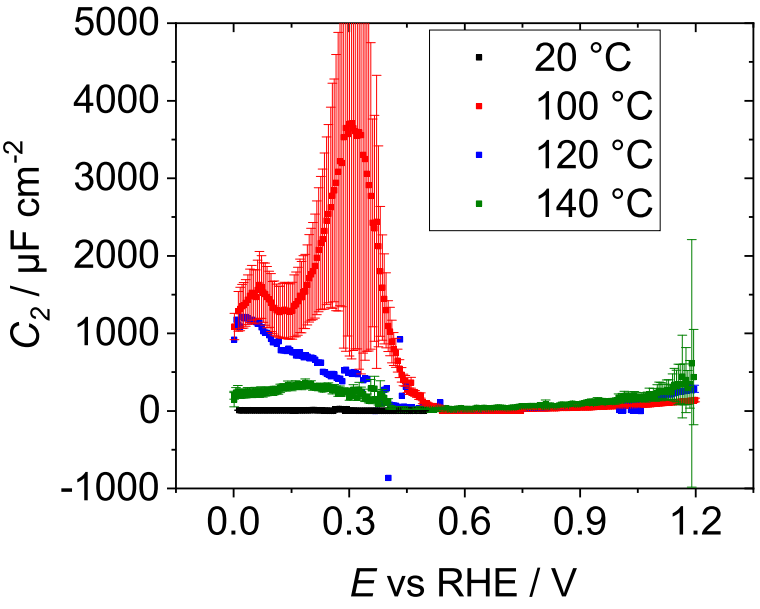

(a) Forward Sweep

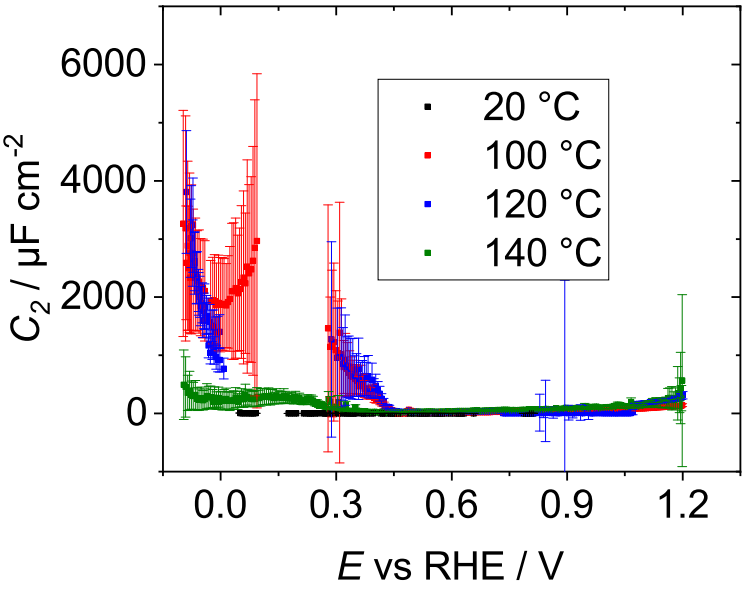

(b) Reverse Sweep

Figure 4.27: C_2 from $Ni(OH)_2$ dEIS data. The sweep rate was 5 mV s^{-1}.

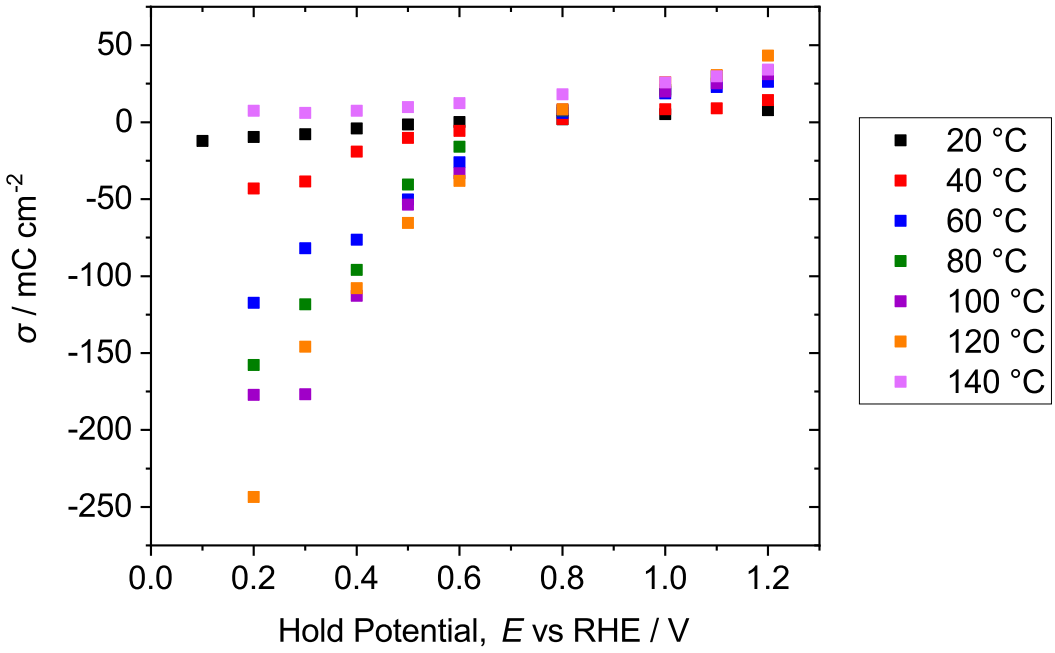

Figure 4.28: Charge density of $Ni(OH)_2$ formation as a function of potential and temperature. Holds are all 1000 s long, and preceded by a long reductive step as described previously (Section 4.2.5) No baseline correction has been made.

The plots of τ_1^{-1} on the forward sweep (Fig. 4.29a) clearly show α-$Ni(OH)_2$ formation between 0.1 V and 0.5 V at all temperatures. The data indicates that the formation is dramatically slower at room temperature. Also shown is an increase after 0.8 V. This is further evidence of some transformation of the β-$Ni(OH)_2$ layer occurring in this region.

The τ_1^{-1} reverse sweep (Fig. 4.29b) shows that the room temperature experiment has a relatively fast process occurring between 0.6 V and 0.3 V, relative to the data collected at other temperatures. It is also seen in the reverse sweep for τ_2^{-1}. This is associated with the β-$Ni(OH)_2$ being the oxide phase at the surface of the electrode on the room temperature run.

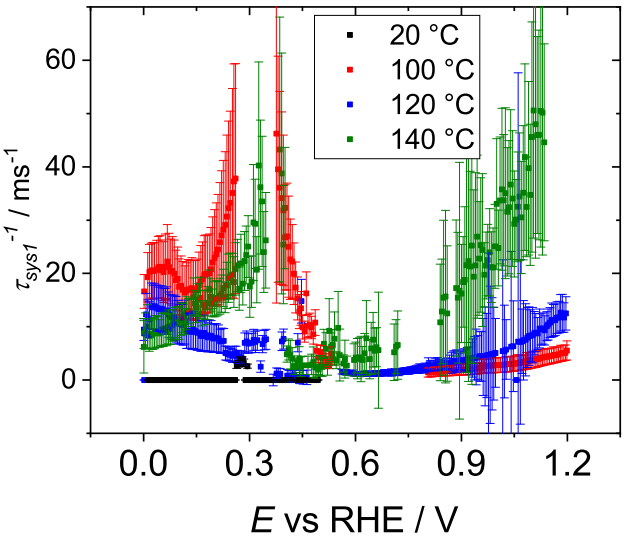

(a) Forward Sweep

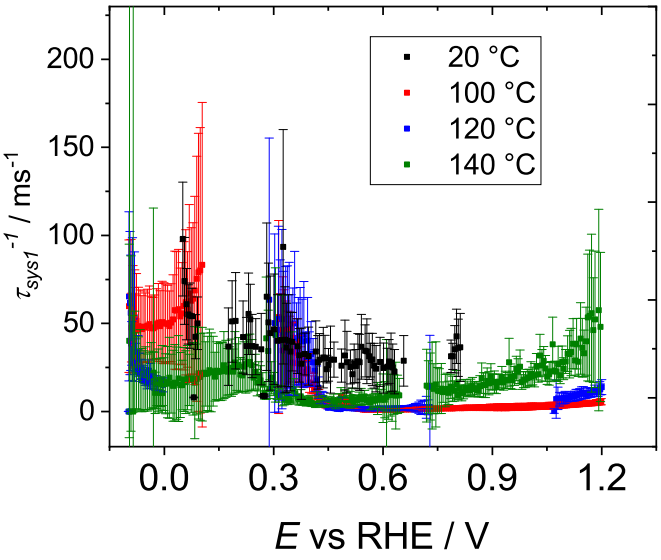

(b) Reverse Sweep

Figure 4.29: τ_1^{-1} from $Ni(OH)_2$ dEIS data. The sweep rate was 5 mV s^{-1}.

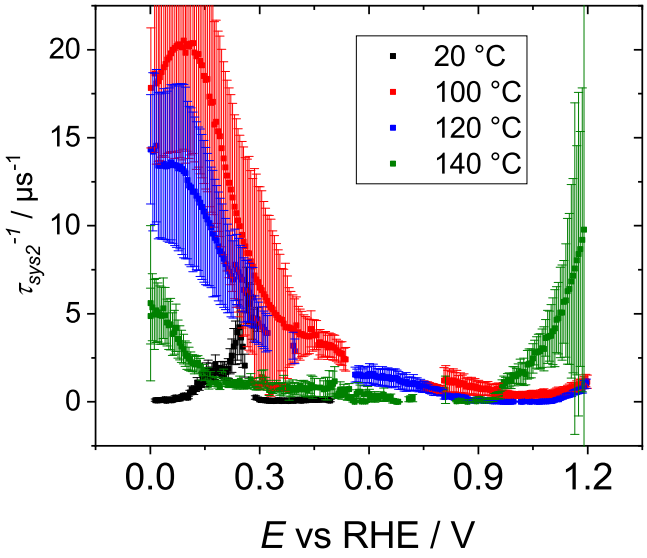

(a) Forward Sweep

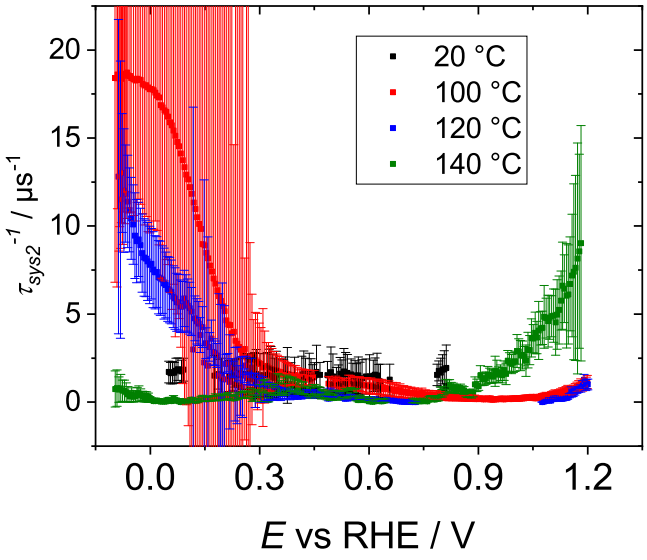

(b) Reverse Sweep

Figure 4.30: τ_2^{-1} from $Ni(OH)_2$ dEIS data. The sweep rate was 5 mV s^{-1}.

Ignoring the experiments at 100 °C and 120 °C due to the oxygen in solution, the comparison of 20 °C and 140 °C lends further confirmation to the presence of α-$Ni(OH)_2$ on the oxide surface at high temperatures. The resistance values are high at room temperature (Fig. 4.31) compared to 140 °C, which would contribute to an increased time constant. This indicates that the low time constant measured must

be largely an effect of capacitance.

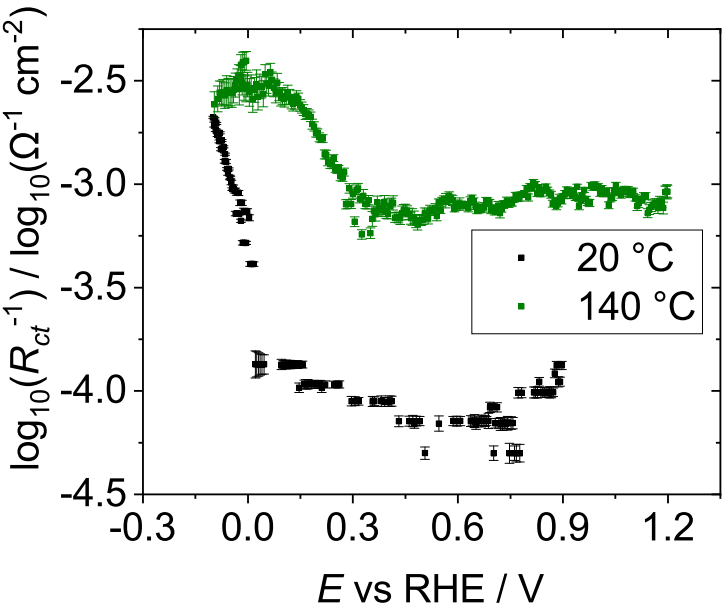

(a) R_{ct}

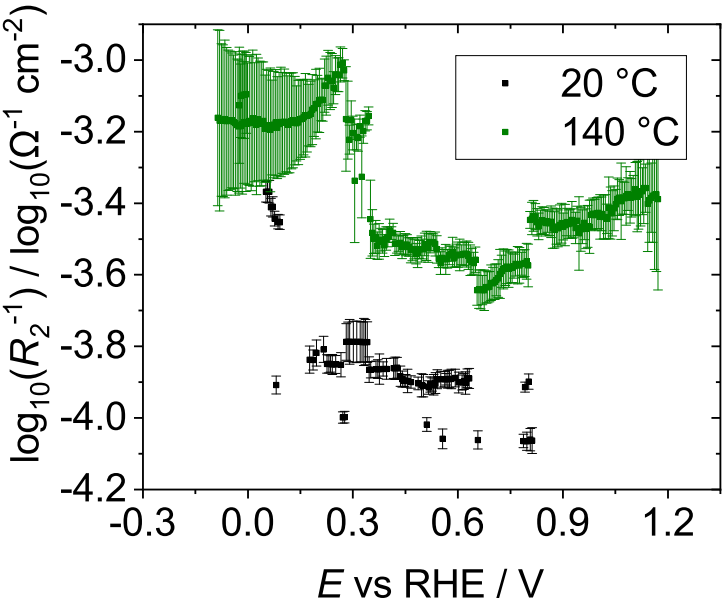

(b) R_2

Figure 4.31: Resistance values for the reverse sweep on $Ni(OH)_2$, determined by dEIS at 20 °C and 140 °C. The sweep rate was 5 mV s^{-1}.

By comparing the capacitance values for the reverse sweep at these two temperatures it is observed that while C_{dl} is comparable between the two experiments C_2 is much smaller at 20 °C (Fig. 4.32). This is likely due to the nature of β-$Ni(OH)_2$ as a well ordered crystalline structure, and its presence on the oxide surface at 20 °C. The amorphous and highly intercalated α-$Ni(OH)_2$ being on the oxide surface is then responsible for the drastically increased capacitance seen at 140 °C. The high capacitance at 140 °C on the reverse sweep is then responsible for increasing the corresponding time constants, making the process at 20 °C faster in comparison.

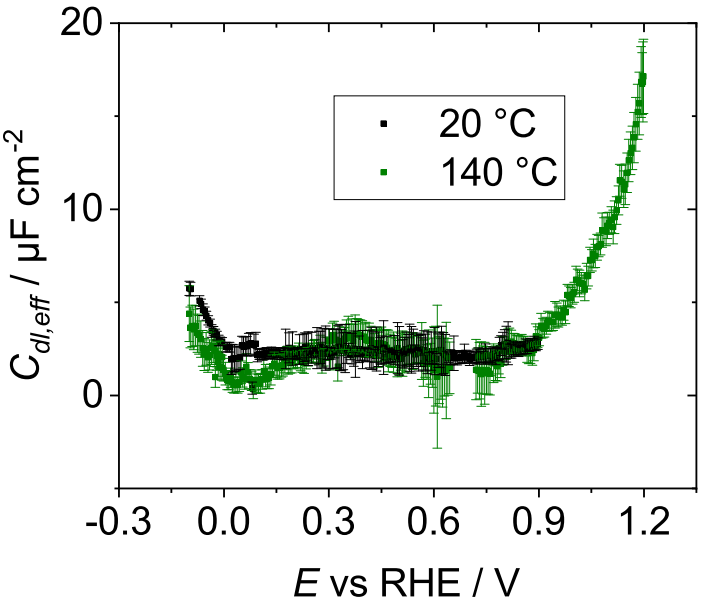

(a) C_{dl}

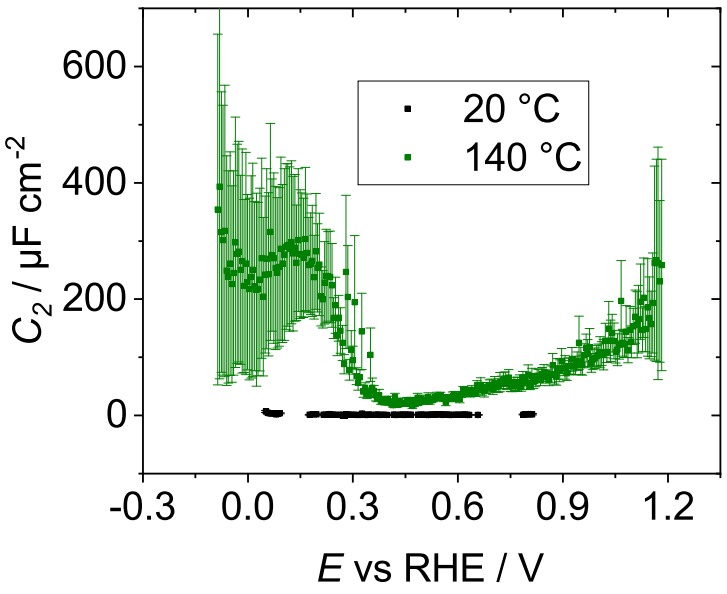

(b) C_2

Figure 4.32: Capacitance values for the reverse sweep on $Ni(OH)_2$, determined by dEIS at 20 °C and 140 °C. The sweep rate was 5 mV s^{-1}.

4.4 Conclusions

Using cyclic voltammetry a methodology was developed whereby β-NiOOH and γ-NiOOH could be preferentially stabilized on the nickel electrode surface. This allowed for the direct comparison of the activity of β-NiOOH and γ-NiOOH in oxygen evolution. The conditioning CVs were also used to investigate the NiOOH development process by analysing the charge density of each cycle.

Thermodynamic analysis was performed to determine the source of the potential shift in E_r for NiOOH as a function of temperature. This culminated in a comparison of various oxidation processes that could be responsible for the peak and how they should function as temperature increases. The state of the thermodynamic literature available for nickel and its various oxide phases is insufficient to conclusively indicate a particular reaction as responsible for the data observed. However, based on data available the following reactions appear most likely:

$$\begin{aligned} \mathrm{NiO} + 2\,\mathrm{OH^-} &\rightleftharpoons \mathrm{NiO_2} + \mathrm{H_2O} + 2\,\mathrm{e^-} \\ \mathrm{Ni(OH)_2} + 2\,\mathrm{OH^-} &\rightleftharpoons \mathrm{NiO_2} + 2\,\mathrm{H_2O} + 2\,\mathrm{e^-} \end{aligned} \tag{4.30}$$

CV and EIS were used to analyse the conversion of α-$\mathrm{Ni(OH)_2}$ to β-$\mathrm{Ni(OH)_2}$ as a function of temperature. The results indicate that the aging of α-$\mathrm{Ni(OH)_2}$ to β-$\mathrm{Ni(OH)_2}$ on the oxide surface does not occur at temperatures 100 °C and above. At room temperature this process occurs through a dissolution, nucleation, and growth process [104, 195–199]. At high temperatures it is likely that the recrystallization process simply returns α-$\mathrm{Ni(OH)_2}$ to the surface.

Chapter 5

Glycerol Oxidation on Nickel, Mechanistic and Activity Analysis as a Function of Temperature

5.1 Introduction

In this chapter electrochemical methods are used to explore kinetic and mechanistic effects of temperature on alkaline glycerol oxidation at nickel electrodes. Cyclic voltammetry is used to compare glycerol oxidation activities on air stabilized β-NiOOH as a function of temperature. A mechanistic analysis of glycerol oxidation on γ-NiOOH is also performed using Tafel analysis and EIS. This study results in the aging of the γ-NiOOH layer to β-NiOOH, highlighting some interesting glycerol adsorption behavior.

NiOOH is the active oxide phase for glycerol oxidation on nickel electrodes [59–68]. Glyceraldehyde has been shown to be one of the major electrochemical products of glycerol oxidation detectable at the oxide surface [20, 27, 28, 58]. Due to the alkaline solution in which these experiments are performed, immediate product speciation is expected through subsequent chemical reactions [10, 69, 70].

Since NiOOH is required on the oxide surface before glycerol oxidation can occur [14, 15, 56, 57] high potentials are required to initiate the process despite glycerol having a relatively low standard potential. The standard potential of glycerol oxidation can be determined with the following balanced reactions with the reaction

of interest as a reduction, by convention,

$$\begin{aligned} \mathrm{C_3H_6O_3 + 2\,H_2O + 2\,e^- &\rightleftharpoons C_3H_8O_3 + 2\,OH^-} \\ \frac{1}{2}\,\mathrm{H_2 + OH^- &\rightleftharpoons H_2O + e^-} \end{aligned} \tag{5.1}$$

to get

$$\mathrm{C_3H_6O_3 + H_2 \rightleftharpoons C_3H_8O_3} \tag{5.2}$$

and using the Joback method [210]:

$$\begin{aligned} E^\circ =& \frac{\Delta G^\circ}{-nF} \\ n =& \ 2 \\ \Delta G^\circ_{rxn} =& \Delta G^\circ_f\ \mathrm{C_3H_8O_3} - \ \Delta G^\circ_f\ \mathrm{H_2} - \Delta G^\circ_f\ \mathrm{C_3H_6O_3} \\ \Delta G^\circ_f\ \mathrm{C_3H_6O_3} =& -401.22\,\mathrm{kJ\ mol^{-1}} \\ \Delta G^\circ_f\ \mathrm{C_3H_8O_3} =& -438.52\,\mathrm{kJ\ mol^{-1}} \\ \Delta G^\circ_f\ \mathrm{H_2} =& \ 0\,\mathrm{kJ\ mol^{-1}} \\ E^\circ =& \ 0.193\ \mathrm{V} \end{aligned} \tag{5.3}$$

The process of converting $Ni(OH)_2$ to NiOOH relies on proton diffusion out of the oxide alongside simultaneous propagation of OH^- ions into the oxide through galleries within the oxide structure (Fig. 1.3) [19, 93, 115]. Note that while the propagation of OH^- is not shown in every figure it occurs at all potentials for which oxidation is occurring. This is necessary to complete the electrochemical circuit.

Mechanistic studies of the oxidation of organics on nickel have been performed previously [21, 22, 79] with some mechanisms having been proposed. These mechanisms are for the general oxidation of organics, and do not pertain specifically to glycerol.

Fleischmann Mechanism [21, 22]

$$\begin{aligned} \mathrm{Ni(OH)_2 + OH^- &\longrightarrow NiOOH + H_2O + e^-} \\ \mathrm{2\,NiOOH + RCH_2OH &\xrightarrow{RDS} 2\,Ni(OH)_2 + RCHO} \end{aligned} \tag{5.4}$$

Casella Scheme 1 (CS1) [79]

$$\begin{aligned}
\mathrm{Ni(OH)_2 + OH^- &\longrightarrow NiOOH + H_2O + e^-} \\
\mathrm{Ni(OH)_2 + RCH_2OH &\longrightarrow Ni(OH)_2(RCH_2OH)(ads)} \\
\mathrm{Ni(OH)_2(RCH_2OH)(ads) + NiOOH &\longrightarrow Ni(OH)_2(RCH_2O)(ads) + Ni(OH)_2} \\
\mathrm{Ni(OH)_2(RCH_2O)(ads) + NiOOH &\longrightarrow Ni(OH)_2(RCHO)(ads) + Ni(OH)_2} \\
\mathrm{Ni(OH)_2(RCHO)(ads) &\longrightarrow Ni(OH)_2 + RCHO}
\end{aligned} \tag{5.5}$$

Casella Scheme 2 (CS2) [79]

$$\begin{aligned}
\mathrm{Ni(OH)_2 + OH^- &\longrightarrow NiOOH + H_2O + e^-} \\
\mathrm{NiOOH + RCH_2OH &\longrightarrow NiOOH(RCH_2OH)(ads)} \\
\mathrm{NiOOH(RCH_2OH)(ads) + NiOOH &\longrightarrow NiOOH(RCH_2O)(ads) + Ni(OH)_2} \\
\mathrm{NiOOH(RCH_2O)(ads) + NiOOH &\longrightarrow NiOOH(RCHO)(ads) + Ni(OH)_2} \\
\mathrm{NiOOH(RCHO)(ads) &\longrightarrow NiOOH + RCHO}
\end{aligned} \tag{5.6}$$

Note that these mechanisms all involve the chemical reduction of NiOOH to $Ni(OH)_2$ as the means of oxidizing organic species on the oxide surface. Additionally, the Fleischmann mechanism explicitly suggests that there are no adsorbed intermediates involved in the oxidation of organics.

5.2 Experimental

5.2.1 Experimental Setup

The electronic dEIS equipment was setup as in Section 2.3.

Polycrystalline 99.999% nickel wire (Alfa Aesar, Puratronic) was sealed in heat-shrink teflon tubing for use as WE and CE in a teflon electrochemical cell. Experiments were performed using an RHE as the RE. Current densities are reported using the ECSA determined by the method described previously (Section 2.4). The cell was washed by soaking in 80 °C sulfuric acid (Sigma, ACS Reagent) for a minimum of 2 hours before being rinsed several times in Milli-Q water. The electrodes were rinsed in 80 °C sulfuric acid then Milli-Q water.

The glycerol oxidation CV peak has a tendency to blend in with the oxygen evolution reaction when using a nickel oxide electrode. This is caused by preferential stabilization of β-NiOOH on the surface, and can be exacerbated by the presence of Fe contaminants in solution [68, 126, 211–215]. By electropolishing immediately before addition of glycerol to solution, and selecting chemicals with assays proving

they are Fe-free the stabilization of β-NiOOH on the surface can be prevented. By doing this γ-NiOOH becomes the active Ni species on the surface for potentials at which glycerol oxidation occurs, and the glycerol oxidation peak can be seen.

A solution of 99.99% 0.5 M KOH (Sigma, Semiconductor Grade) and 0.2 M glycerol (Anachemia, ACS Grade) was made up in Milli-Q water and purged with Ar for 10 minutes, with slow continual bubbling continuing during initial experiments. In the event the autoclave was used, the autoclave was sealed immediately after the 10 minute Ar purge. Unless otherwise specified, all dynamic impedance experiments were carried out with a sweep rate of $5\,mV\,s^{-1}$ and frequencies ranging from 1 Hz to 13 kHz. Similarly, all potentiostatic impedance experiments were performed using frequencies ranging from 0.1 Hz to 100 kHz, taking approximately 3 minutes for acquisition to occur.

While ramping the temperature between experiments the potential was held at 0.9 V in an attempt to prevent the build-up of any excess nickel oxide on the electrode surface. This was done to keep the surface consistent between runs of the experiment.

Gas product analysis and ring disc electrode experiments were considered, however they were deemed to be impractical due to the necessity of the autoclave to achieve experimental conditions. Gas product analysis would require some means of separating gas phase products from water vapor, and subsequently returning the water vapor to the reaction vessel without significantly affecting the temperature. A ring disc electrode not used as it was determined glycerol would poison the ring, rendering the method unusable.

5.2.2 Impedance Data Validation

5.2.2.1 Kramers-Kronig Test

Because AC potential excitations are being applied and the AC current response is being measured, systems must be steady-state on the time scale of the measurement [154]. The method used for determining whether or not acquired data is valid with respect to this condition was described previously (Section 4.2.2).

5.2.2.2 Polarization Resistance Comparison

The polarization resistances determined by AC experiments were compared with the values determined by DC experiments. This was done using the method described

previously (Section 4.3).

5.2.3 Electrochemical Impedance Spectrum Fitting

EIS spectra were fitted to equivalent circuits using Maple software developed by the Harrington group [150]. The script uses a non-linear least squares fitting algorithm, fitting the theoretical expressions of the ECs to the empirically collected impedance data. All spectra were fitted to four separate circuits:

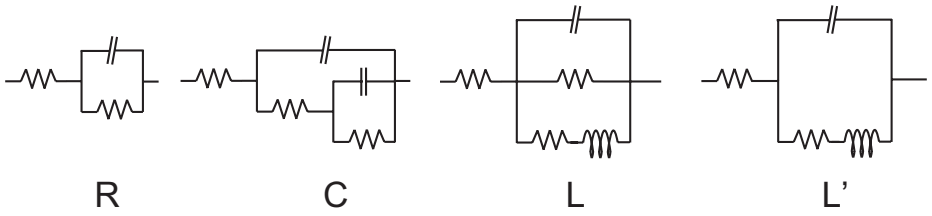

Figure 5.1: The four equivalent circuits tested. Circuit R contains one time constant, whereas circuits C and L contain two time constants. L' is a variant of L that was tested because the central resistor in L was found to have very large values at times.

The script also provides an Akaike Information Criterion (AIC) value for each fit, whose significance was described previously (Section 4.2.3).

5.2.4 AC Voltammetry

By applying an AC potential excitation and observing the current response the admittance of a system can be measured at a fixed frequency. This is performed by measuring the impedance (Section 2.3.1) and converting it to admittance. Admittance is the reciprocal of impedance and its calculation was discussed previously (Section 4.2.4).

5.2.5 High Temperature Experiment Order

Due to the nature of the growth for the different nickel oxide phases high temperature experiments were performed using two separate schemes for the glycerol oxidation mechanistic analysis. High Temperature Scheme 1 (HTS1) involved ramping the cell temperature in a simple temperature order: 20 °C, 40 °C, 60 °C, 80 °C, 110 °C. High Temperature Scheme 2 (HTS2) involved a more complex temperature order: 20 °C, 60 °C, 110 °C, 80 °C, 40 °C.

This was done in an attempt to deconvolute the effects caused by temperature from the effects caused by the duration of oxidation.

5.3 Results and Discussion

5.3.1 Electrochemical Impedance Spectroscopy Validation

5.3.1.1 Kramers-Kronig Tests

Initial impedance testing of glycerol oxidation on nickel was done using potentiostatic Electrochemical Impedance Spectroscopy (pEIS) at 1.59 V with frequencies from 0.1 Hz to 100 kHz. Between each of these pEIS spectra, the potential was held at 1.59 V. The results of these tests showed some interesting features. First, the impedance of the system changed significantly over time in a way that implied there may be some poisoning of the electrode due to the oxidation (Fig. 5.2a). The electrode can be considered poisoned when compounds in solution adsorb or bind to electrochemically available sites irreversibly given the present conditions. It is sometimes possible to remove these compounds given appropriate sweeps and holds, but without these interventions the electrochemical activity of the electrode will decline.

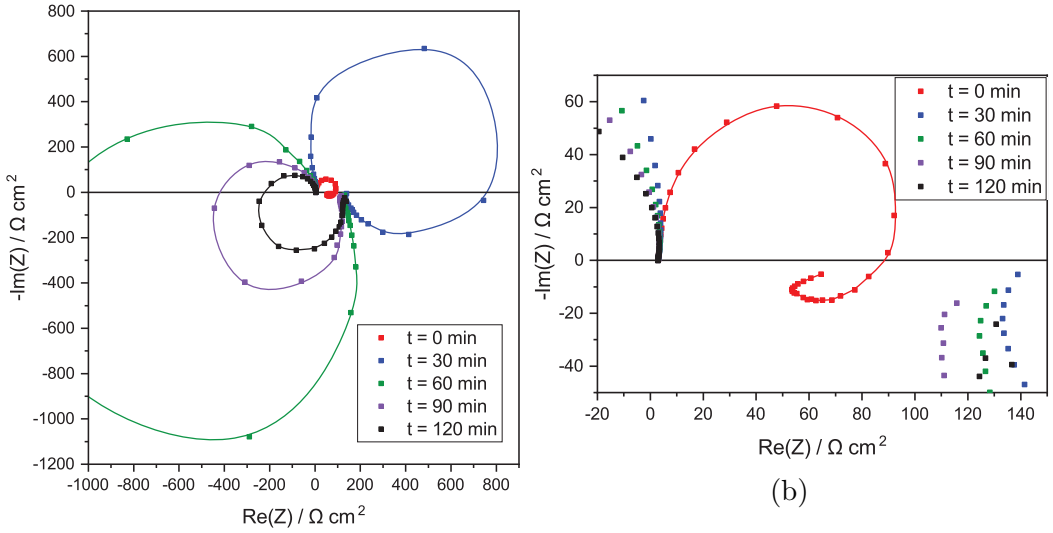

Figure 5.2: pEIS results for glycerol oxidation with 0.2 M glycerol and 0.5 M KOH at 1.59 V over time. Note that the lines here are not fits, but are merely illustrations to visualize the data. (a) shows all the impedance spectra on one plot (b) is an expanded portion of (a), highlighting the strange low frequency features in the t = 0 min plot.

Second, the data itself for $t = 0$ min contained some very odd features making a KK test impossible to pass (Figs. 5.2b and 5.3). It should be noted, that even the Nyquist plots that seem to have normal features still appear to have some trendlines in the KK test results.

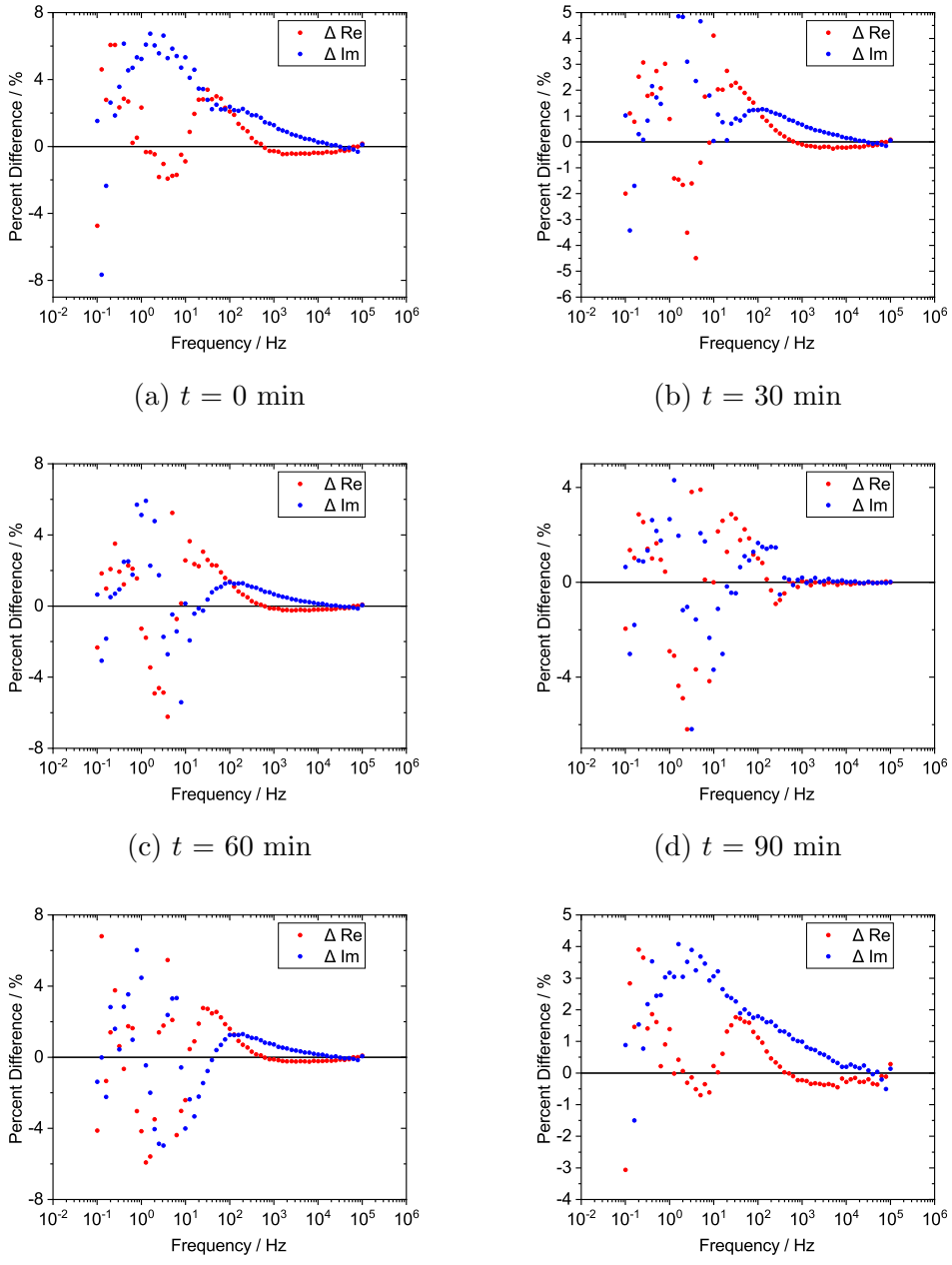

(a) $t = 0$ min

(b) $t = 30$ min

(c) $t = 60$ min

(d) $t = 90$ min

(e) $t = 120$ min

(f) $t = 0$ min, after reduction

Figure 5.3: KK test results for pEIS of glycerol on nickel with 0.2 M glycerol and 0.5 M KOH at 1.59 V.

It is known that, when using nickel as an electrode, there is an aging or curing element to the oxidation process. The conversion of α-$Ni(OH)_2$ to β-$Ni(OH)_2$ is not easily reversible [92, 102], and the oxidation from $Ni(OH)_2$ to NiOOH can cause

additional layers of NiOOH to form [56]. The oxidation and buildup of this NiOOH layer also appears to continue for several hours. Possibilities for the drift in the impedance data for the glycerol oxidation process include this NiOOH growth process, as well as a poisoning effect caused by the oxidation of the glycerol itself.

In order to determine which of these two likely processes was the cause of the drift, the same experiment was performed with no glycerol in solution.

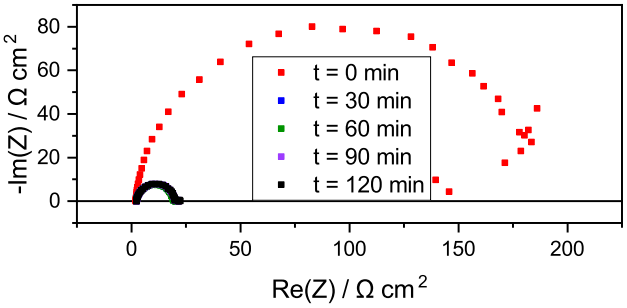

(a)

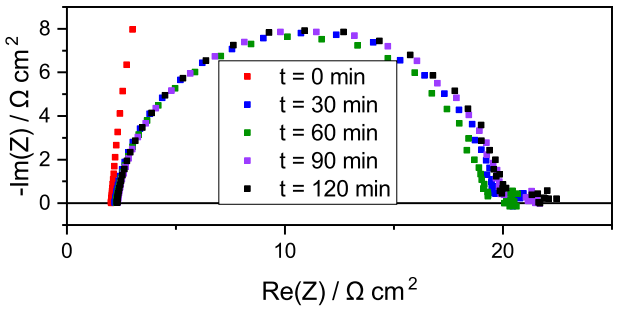

(b)

Figure 5.4: pEIS results for oxidation of nickel in 0.5 M KOH at 1.59 V over time. (a) shows all Nyquist plots at once (b) is an expanded view of (a) highlighting t = 30 min to 120 min. The drift in this system appears to be over within 30 min.

It can be seen from these Nyquist plots (Fig. 5.4) that while there is some drift in the system due to the oxidation of the nickel it appears to be completely finished after the first 30 min at 1.59 V. This is an interesting feature, as the aging continues to be seen on CVs for many hours. Regardless, the KK test results showed some significant systematic trends (Fig. 5.5).

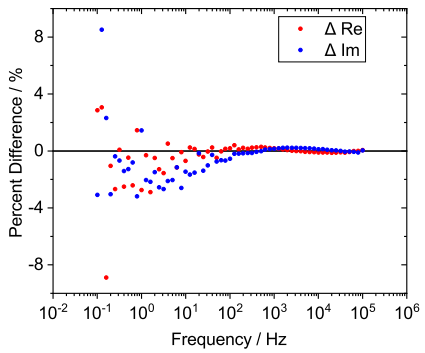

(a) $t = 0$ min

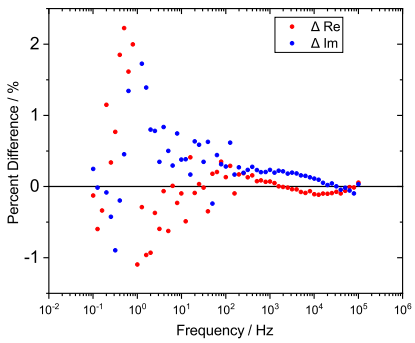

(b) $t = 30$ min

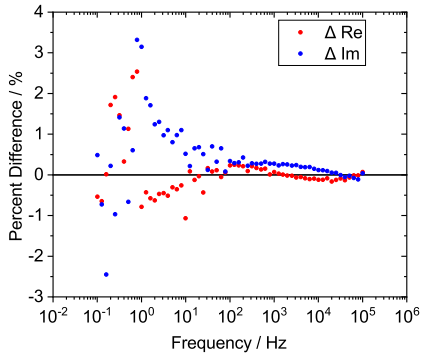

(c) $t = 60$ min

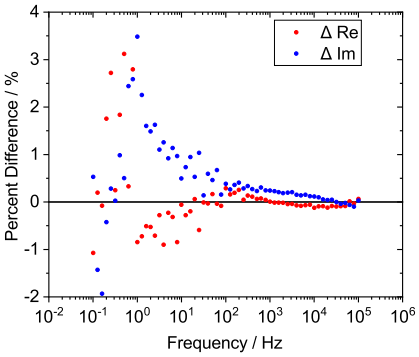

(d) $t = 90$ min

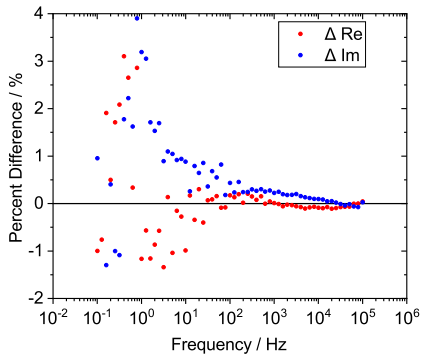

(e) $t = 120$ min

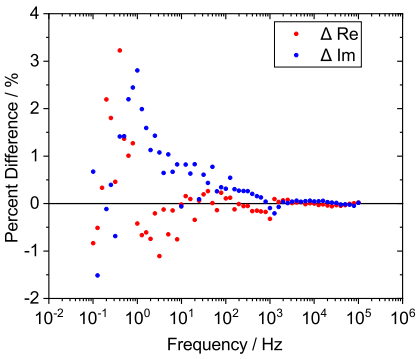

(f) $t = 0$ min, after reduction

Figure 5.5: KK test results for pEIS of oxidation of nickel in 0.5 M KOH at 1.59 V over time.

The KK tests for which there was no glycerol in solution show systematic trends quite similar to those seen in the glycerol experiments (Fig. 5.3).

Any systematic KK test trends caused by poisoning of the electrode, or by the

slow build-up of β-NiOOH, should be seen in the low frequency portion of the plots. These processes are slow, and witnessed on the timescale of seconds to minutes. Additionally, when performing pEIS excitations are performed one frequency at a time so lower frequencies naturally take longer to probe. Because of this there are gaps of up to 39 s between gathering data points, which allows a lot of drift to occur.

Some minor systematic trending in the low frequency KK tests for glycerol is observed (Fig. 5.3), particularly in the $t = 0$ plots. However, there is also systematic trending in the low frequencies of the KK tests for the experiments without glycerol (Fig. 5.5). The percent differences between the experiments with and without glycerol are definitely different, but within the same order of magnitude and not close enough that one could conclusively say whether or not the systematic trending and possible drift was caused by poisoning or β-NiOOH buildup.

Any systematic trends in the frequency portions greater than 10^2 Hz of the KK tests are likely caused by inductive effects due to the cabling of the device itself. On almost every KK test plot for the pEIS experiments some small amount of systematic trending can be seen at these frequencies, but they remain less than 1% in all KK test results. Due to the ease with which high frequencies can experience interference it is difficult to determine exactly where the interference might come from. Given the small magnitude of the residuals these trends are of little impact.

This data highlights the effectiveness of dEIS in gathering data that would otherwise contain some kind of drift if gathered using pEIS. Because dEIS uses a multisine approach, gathering data for all probed frequencies simultaneously, it is possible to acquire data fast enough that no drift is seen in the impedance data (Fig. 5.6), as illustrated by a lack of systematic trendlines. The speed of the data collection here creates the pseudo-steady state condition that allows for usable impedance data to be collected (Fig. 5.6).

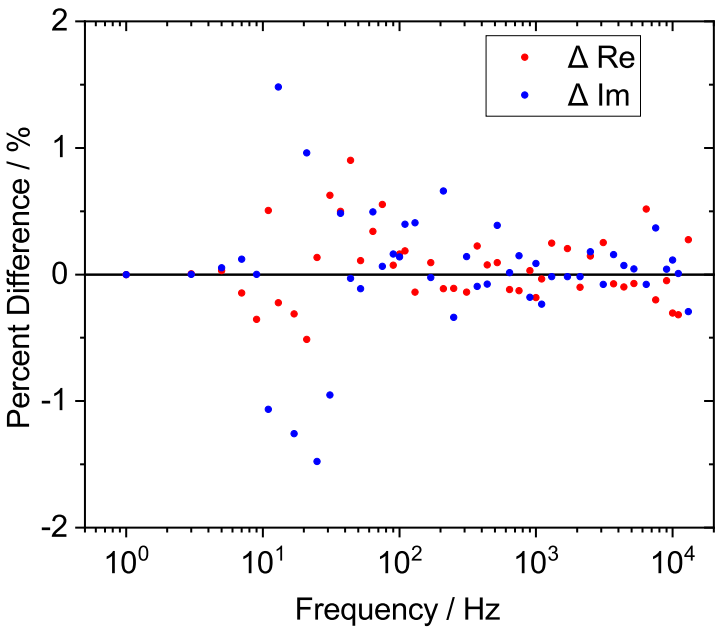

Figure 5.6: dEIS KK test results for glycerol oxidation with 0.2 M glycerol and 0.5 M KOH at 1.59 V and room temperature.

5.3.1.2 Polarization Resistance Comparison

Comparing the polarization resistances obtained from AC and DC experiments using the method described previously (Section 4.2.2.2) it can be seen that the obtained values are similar to within a reasonable degree (Figs. 5.7 and 5.8). Smoothing was performed on the DC traces collected from high temperature DC experiments. Bubble formation caused by oxygen evolution caused significant noise in these traces, but by smoothing the data it can be shown that the overall trend in the data agrees with the AC results quite nicely.

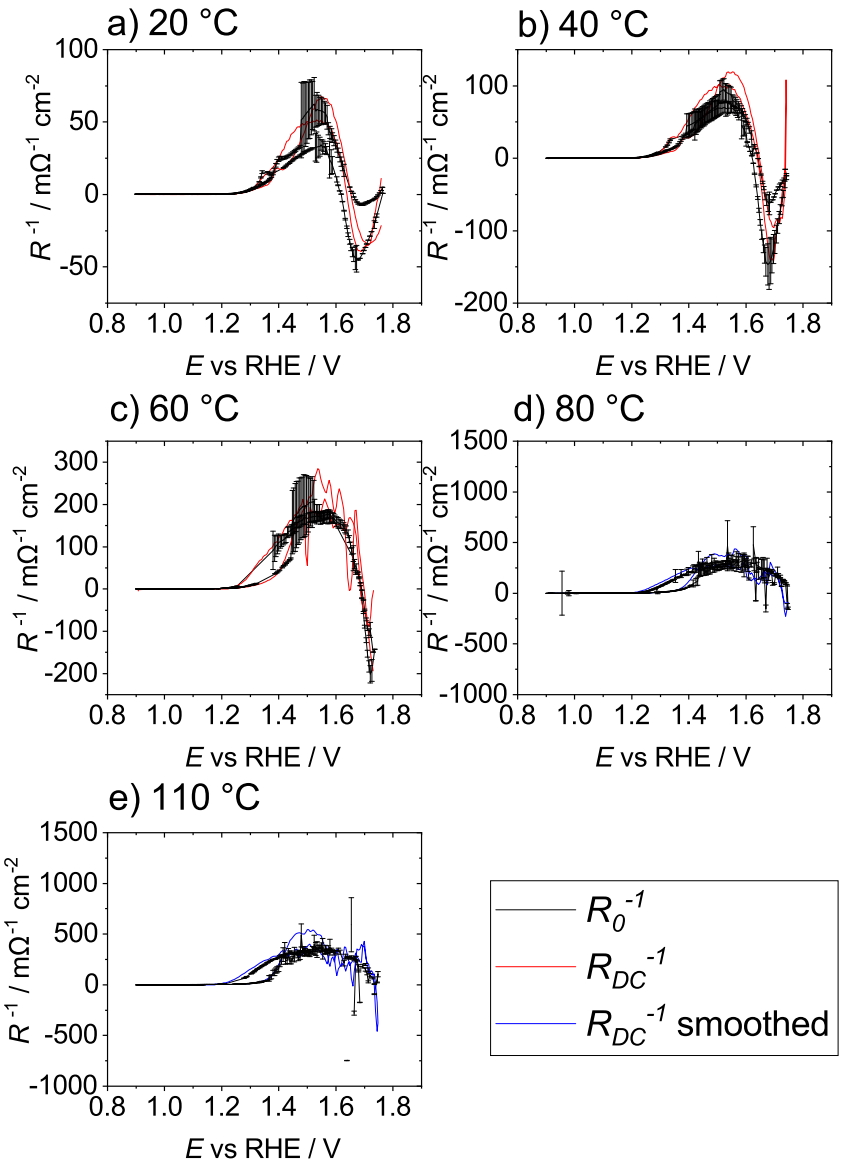

Figure 5.7: Differential resistance comparison for glycerol oxidation, HTS1 temperature order. Smoothing has been performed on some DC experiment results at high temperatures using Origin with the following settings: Savitsky-Golay method, 10 points of window, and polynomial order 1. After testing a variety of smoothing settings these were found to smooth out the noise optimally without introducing any significant visual artifacts.

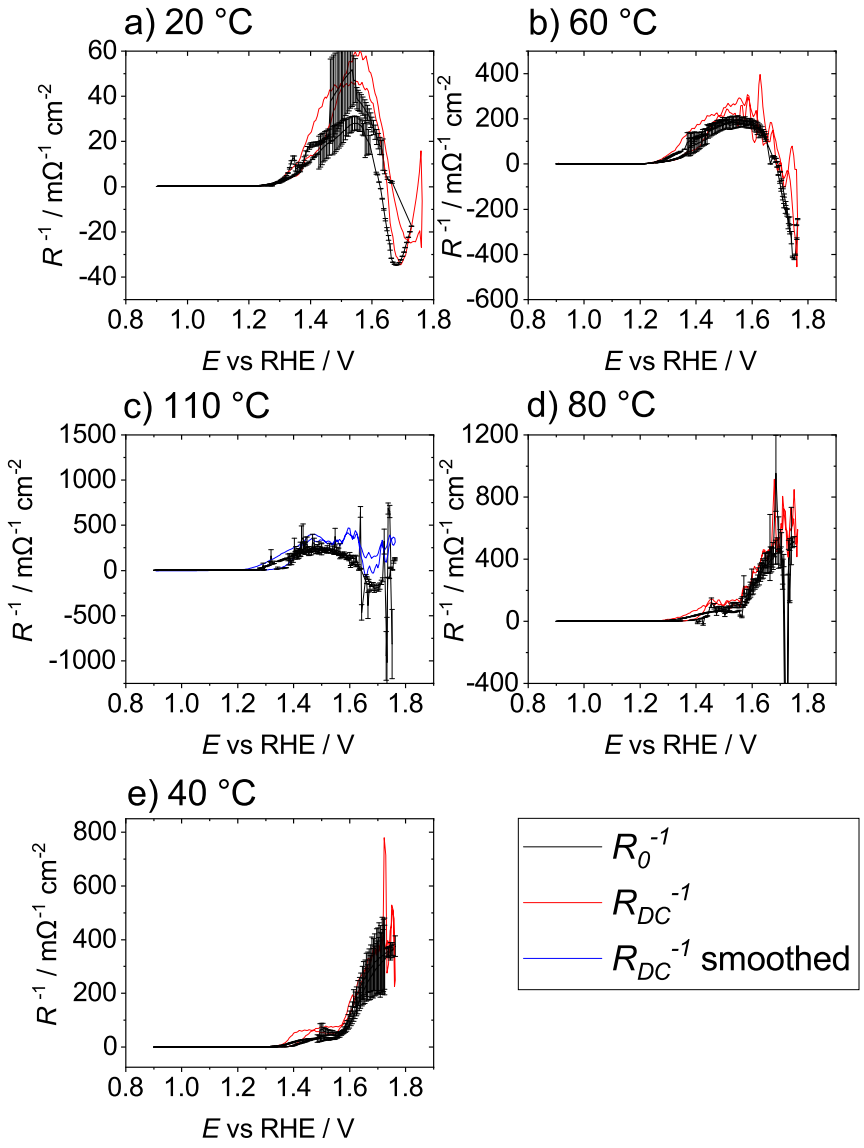

Figure 5.8: Differential resistance comparison for glycerol oxidation, HTS2 temperature order. Smoothing has been performed on some DC experiment results at high temperatures using Origin with the following settings: Savitsky-Golay method, 10 points of window, and polynomial order 1. After testing a variety of smoothing settings these were found to smooth out the noise optimally without introducing any significant visual artifacts.

The one exception is the large negative peak in R_0 for the 80 °C experiment from

the HTS2 temperature order session. This peak appears to occur on both the anodic and cathodic sweeps, making it unlikely that it is simply an error. This peak was seen in no other trials.

5.3.2 Effects of temperature on β-$Ni(OH)_2$ oxidation onset and glycerol oxidation activity

Cyclic voltammetry studies were performed on a nickel electrode where β-$Ni(OH)_2$ was air stabilized on the surface by leaving it in open atmosphere for several weeks. Experiments were performed at various temperatures both with and without glycerol in solution. Initial studies showed a significant decrease in the reversible potential, E_r, of the oxidation of β-$Ni(OH)_2$ as temperatures increased (Fig. 5.9a). The E_r is the point at which the net oxidative and reductive current is 0. This effect has been documented previously in the literature [56, 146]. A decrease in the onset potential of glycerol oxidation was also witnessed (Fig. 5.9b), however this coincides with the shift in the onset potential of oxidation of β-$Ni(OH)_2$ due to the decrease in the E_r. The literature establishes that NiOOH is the active catalyst oxide phase for various oxidation processes [59–64]. This data confirms that conclusion.

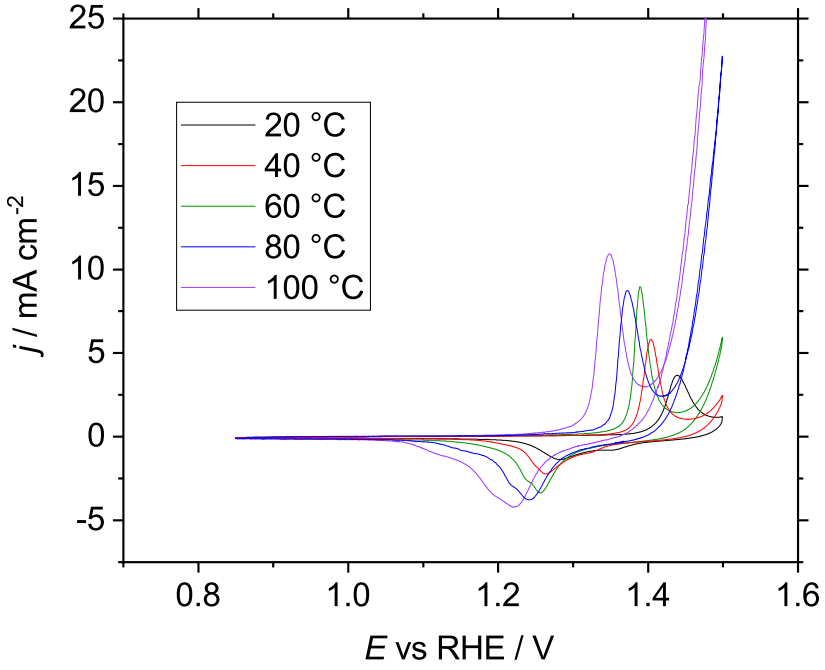

(a)

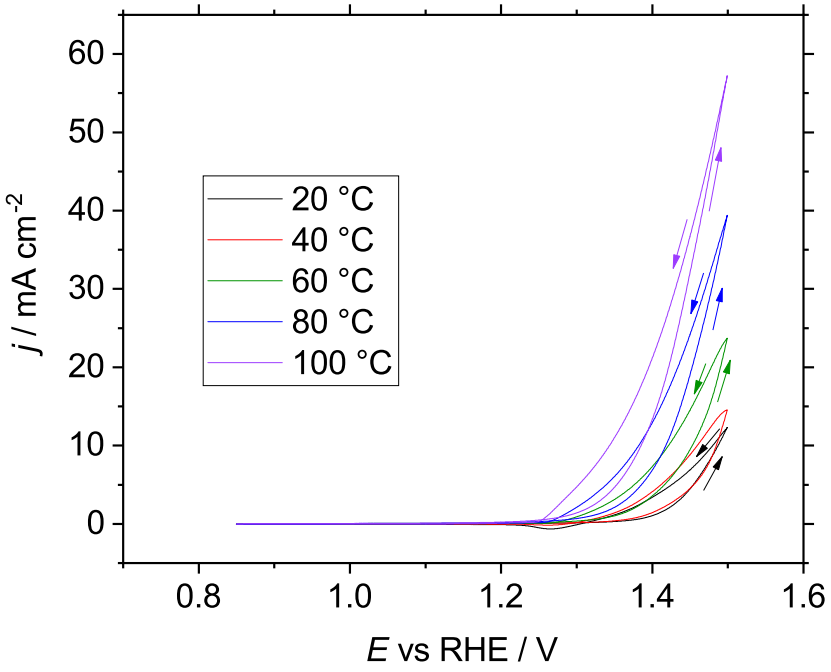

(b)

Figure 5.9: CVs for oxidation of (a) β-$Ni(OH)_2$ and (b) oxidation of glycerol as a function of temperature. The sweep rate was 50 mV s^{-1}.

Of note here is that the decrease in the perceived reversible potentials resulted in the increase of the activity of glycerol oxidation measured at a fixed potential by up to as much as 4×. Another thing of note, is that the increased area of the β-$Ni(OH)_2$ oxidation is not necessarily a function of temperature but also one of time. As the electrode spends time at more positive potentials it seems to undergo some irreversible process that allows for the β-NiOOH oxide to build more layers [56, 146]. In order to account for this oxidation time was kept consistent between the glycerol and glycerol-free trials.

The CVs of glycerol oxidation at various temperatures (Fig. 5.10) are all very similar. They show very little current until approximately 1.3 V. In these CVs there is no visible peak potential because the glycerol oxidation slowly blends into oxygen evolution. This occurs because β-$Ni(OH)_2$ has been allowed to stabilize on the electrode. For this reason only the initial portion of the peak has been analyzed here. In the cathodic portion of the sweep higher current is observed as the reversible potential E_r is approached, followed by a small reductive current at around 1.25 V.

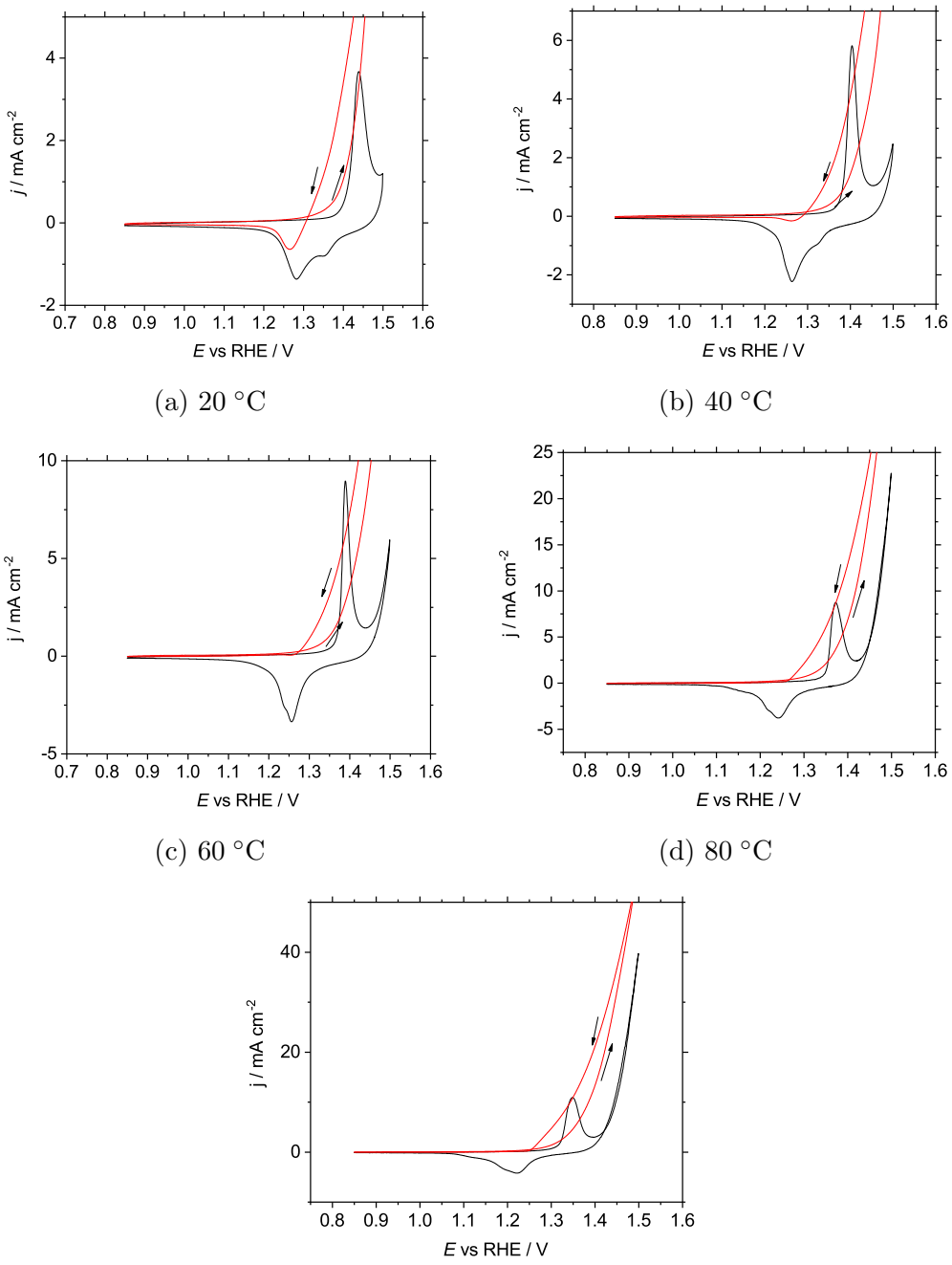

(a) 20 °C

(b) 40 °C

(c) 60 °C

(d) 80 °C

(e) 100 °C

Figure 5.10: CVs for oxidation of β-$Ni(OH)_2$ and oxidation of glycerol, temperatures overlaid. The sweep rate was 50 mV s^{-1}.

The likely reason for the increased current on the cathodic portion of the sweep is that on the anodic portion of the sweep the catalytically active oxide, some phase

of NiOOH [59–69], has yet to be formed in substantial quantities whereas on the cathodic portion a full layer of NiOOH already exists on the surface. The cause of the reductive current is likely the reduction of the NiOOH back to β-$Ni(OH)_2$.

The E_r of each β-$Ni(OH)_2$ oxidation CV can be determined by adding the anodic and cathodic currents at each potential and selecting the potential between the anodic and cathodic peaks for which this sum is closest to 0. The E_r can then be plotted vs temperature as discussed previously (Fig. 4.20).

By subtracting the E_r off each respective CV it can be shown that the glycerol onset potentials follow a predictable trend (Fig. 5.11).

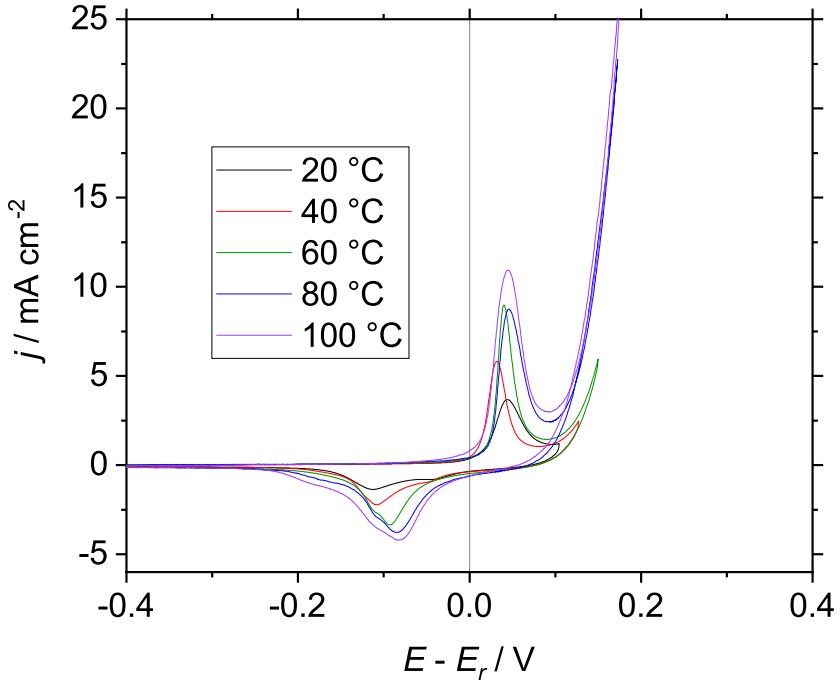

(a)

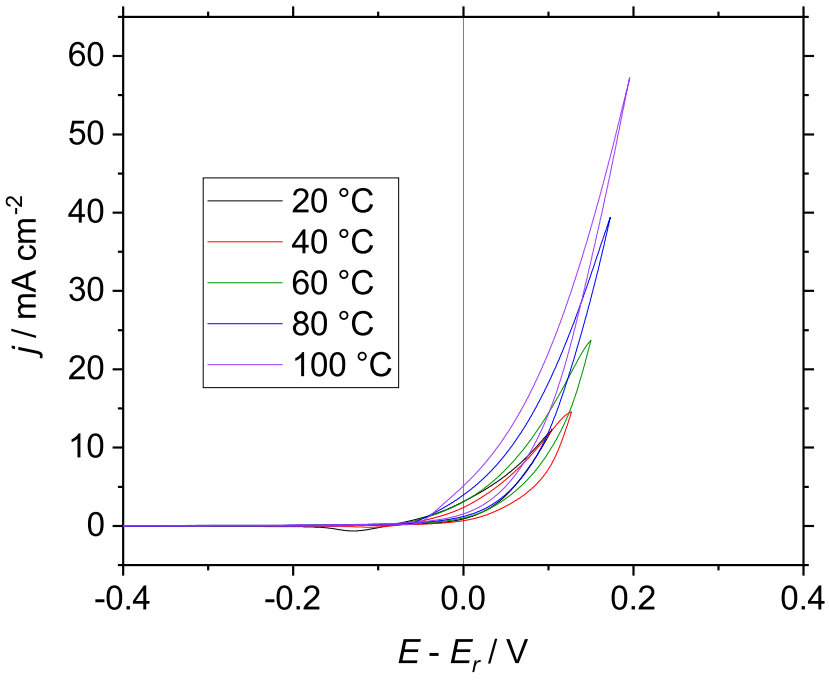

(b)

Figure 5.11: CVs for (a) oxidation of β-$Ni(OH)_2$ and (b) glycerol, centered around E_r of β-$Ni(OH)_2$ oxidation. The sweep rate was 50 mV s^{-1}.

These plots can be used to more easily compare the effects of temperature on the CVs while ignoring the effect on the reversible potential. For example, it becomes clear that while the oxidation peaks in figure 5.11a line up quite well the reduction peaks have a steadily decreasing overpotential as temperature increases. Whether this effect is due to the increase in temperature, or due to the time spent cycling is difficult to ascertain, however.

By normalizing the glycerol CVs (Fig. 5.11b) by the charge density of the β-$Ni(OH)_2$ oxidation of the respective temperature (Fig. 5.12) it shows that aside from the effect due to the change in E_r, the activity of the reaction is not increasing substantially as a function of temperature. The increase in current density observed after having removed the effect of the changing E_r (Fig. 5.11b) is due to the increased amount of β-NiOOH as a function of either time or temperature (Fig. 5.11a). This creates more sites for glycerol oxidation to occur, and therefore increases the current density.

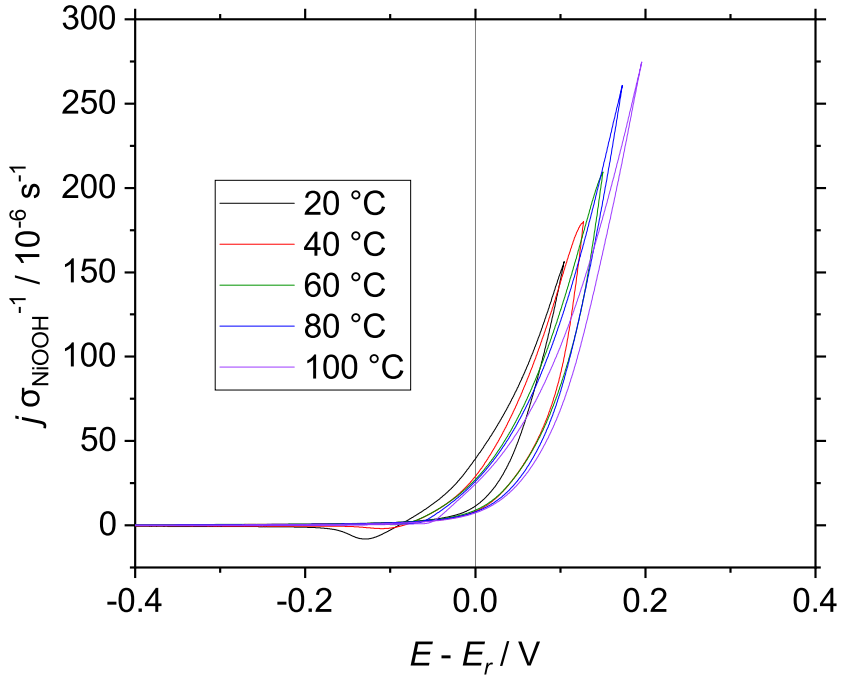

Figure 5.12: CVs for oxidation of glycerol, centered and normalized by charge density of oxidation of β-$Ni(OH)_2$. The sweep rate was 50 mV s^{-1}.

5.3.3 Mechanistic Analysis

For simplicity and because the literature has no conclusive evidence as to whether or no glycerol oxidizes at the solution/oxide interface or within the oxide galleries, glycerol will be considered to oxidize on the nickel oxide at the solution/oxide interface. Given this assumption, any growth of the oxide phase will have negligible effects on the total surface area during the course of a single Tafel sweep.

5.3.3.1 Comparison of literature mechanisms against collected data

Three of the mechanisms discussed in the literature by which glycerol oxidation can occur on nickel electrodes follow. For these mechanisms all nickel oxide phases mentioned refer only to sites at the solution/oxide interface. It is also important to note that the nickel oxide surface only becomes active for electrooxidation once the $Ni(OH)_2$ layer has been converted to NiOOH as shown in various EQCM studies [84, 128, 216]. This is due to the fact that oxidation of $Ni(OH)_2$ is mediated by proton diffusion through oxide layer galleries starting from near the nickel metal surface [85, 93, 110, 182]. Further evidence of this can be seen when performing CVs at a high sweep rate, where NiOOH formation can be seen even when glycerol is in solution and occurs before glycerol oxidation (Fig. 5.13). At slower sweep rates, the NiOOH formation should be complex at more negative potentials than the 1.5 V seen in Fig. 5.13, and is assumed to be complete by the early stage of the glycerol oxidation peak.

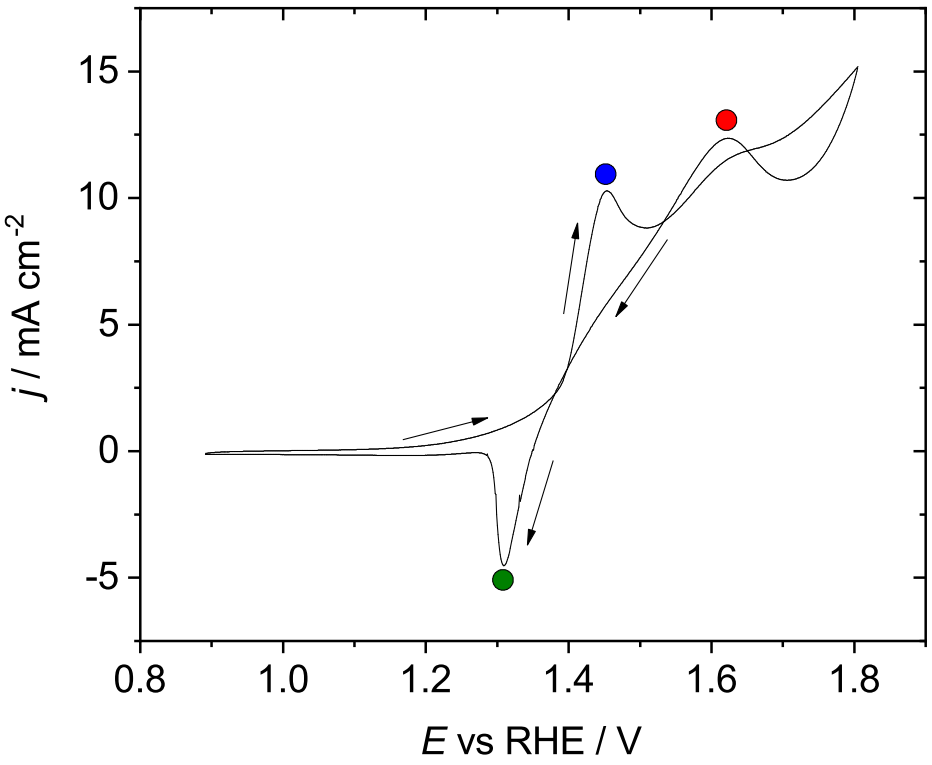

Figure 5.13: CV of nickel in 0.2 M Glycerol and 0.2 M NaOH solution at 1000 mV s^{-1} at room temperature. The blue circle indicates NiOOH formation, the red circle indicates the glycerol oxidation peak, and the green circle indicates NiOOH reduction.

The most commonly referred to is the Fleischmann mechanism [21, 22, 217]:

$$\begin{aligned} \mathrm{Ni(OH)_2 + OH^- \longrightarrow NiOOH + H_2O + e^-} \\ \mathrm{2\,NiOOH + RCH_2OH \xrightarrow{RDS} 2\,Ni(OH)_2 + RCHO} \end{aligned} \tag{5.7}$$

This mechanism starts with the oxidation of the $Ni(OH)_2$ phase to NiOOH. There is evidence that some form of NiOOH is the active phase for glycerol oxidation on nickel electrodes [59–68]. The Fleischmann mechanism is explicitly stated to involve no adsorbed species, however, and it is clear from impedance data that at least one adsorbate is present at potentials over 1.5 V on γ-NiOOH (Fig. 5.14) as shown by the presence of inductive semicircles in the Nyquist plot. These features are not present

in impedance experiments performed on nickel wire in glycerol-free KOH solution.

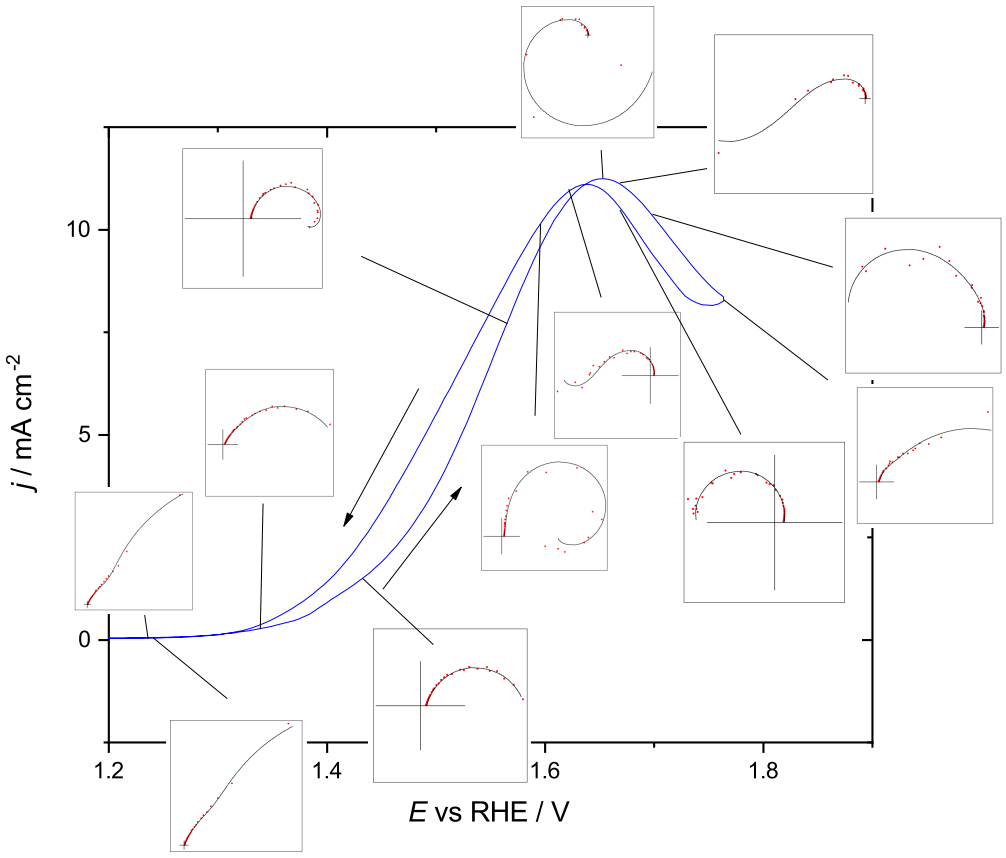

Figure 5.14: dEIS sweep of glycerol oxidation on γ-NiOOH at room temperature in 0.5 M glycerol and 0.2 M KOH solution. Insets show Nyquist plots and corresponding fits collected at the given potentials. The sweep rate was 5 mV s^{-1}.. Insets are at 1.24 V, 1.34 V, 1.44 V, 1.57 V, 1.65 V, 1.66 V, 1.69 V, 1.76 V, 1.68 V, 1.63 V, 1.59 V, 1.24 V.

The two less-discussed mechanisms are proposed by Casella et al [79]:

Casella Scheme 1 (CS1)

$$\begin{aligned}
\mathrm{Ni(OH)_2 + OH^- &\longrightarrow NiOOH + H_2O + e^-} \\
\mathrm{Ni(OH)_2 + RCH_2OH &\longrightarrow Ni(OH)_2(RCH_2OH)(ads)} \\
\mathrm{Ni(OH)_2(RCH_2OH)(ads) + NiOOH &\longrightarrow Ni(OH)_2(RCH_2O)(ads) + Ni(OH)_2} \\
\mathrm{Ni(OH)_2(RCH_2O)(ads) + NiOOH &\longrightarrow Ni(OH)_2(RCHO)(ads) + Ni(OH)_2} \\
\mathrm{Ni(OH)_2(RCHO)(ads) &\longrightarrow Ni(OH)_2 + RCHO}
\end{aligned} \tag{5.8}$$

Casella Scheme 2 (CS2)

$$
\begin{aligned}
Ni(OH)_2 + OH^- &\longrightarrow NiOOH + H_2O + e^- \\
NiOOH + RCH_2OH &\longrightarrow NiOOH(RCH_2OH)(ads) \\
NiOOH(RCH_2OH)(ads) + NiOOH &\longrightarrow NiOOH(RCH_2O)(ads) + Ni(OH)_2 \\
NiOOH(RCH_2O)(ads) + NiOOH &\longrightarrow NiOOH(RCHO)(ads) + Ni(OH)_2 \\
NiOOH(RCHO)(ads) &\longrightarrow NiOOH + RCHO
\end{aligned}
\tag{5.9}
$$

CS1 has glycerol adsorbing to $Ni(OH)_2$ in a step that is independent of potential. This means that in the potential region where NiOOH is expected to form it would be covered in a layer of glycerol. Given that $Ni(OH)_2$ oxidation is mediated by ion diffusion [111–113, 185], a process that would be drastically inhibited by adsorbed organics, and NiOOH is known to be the active oxide phase for oxidation of organics [59–68] this is unlikely to be the case. Based on these arguments Casella Scheme 2 (CS2) is taken to be the likely mechanism by which glycerol is oxidized on nickel electrodes in alkaline solution.

5.3.3.2 Comparison of Glycerol Oxidation on γ-NiOOH and β-NiOOH

It is known that when β-NiOOH is the dominant nickel oxide phase the glycerol oxidation does not show a distinct peak in CV, whereas when the dominant nickel oxide phase is γ-NiOOH the glycerol peak found between 1.6 V and 1.7 V is present (Fig. 5.15). The means by which different nickel oxides are stabilized on the nickel surface was discussed previously (Section 4.3.2).

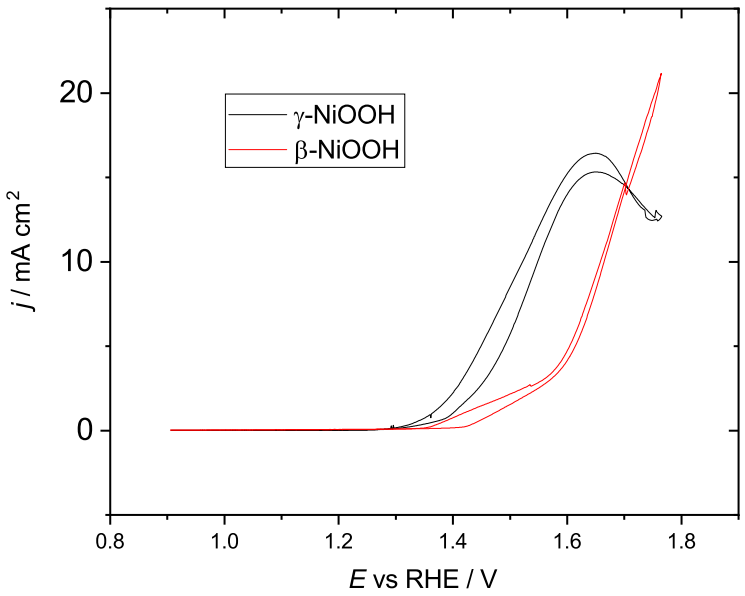

Figure 5.15: Comparison of glycerol oxidation CV on γ-NiOOH vs β-NiOOH. Solutions were 0.5 M KOH and 0.2 M glycerol. Sweep rate was 10 mV s^{-1} for the γ-NiOOH and 5 mV s^{-1} for the β-NiOOH.

It can also be shown that by cycling a γ-NiOOH electrode between 1 V and 1.52 V in 0.5 M KOH until steady state, β-NiOOH is stabilized at the surface (Fig. 5.16a). Steady state is achieved after approximately 16 h. When performing a similar experiment, cycling a γ-NiOOH electrode in a solution of 0.5 M KOH and 0.2 M glycerol for 16.2 h, the glycerol peak is retained (Fig. 5.16b). Since the glycerol peak only appears when γ-NiOOH is the dominant oxide phase on the electrode surface, this indicates that glycerol in solution inhibits the conversion of γ-NiOOH to β-NiOOH at room temperature.

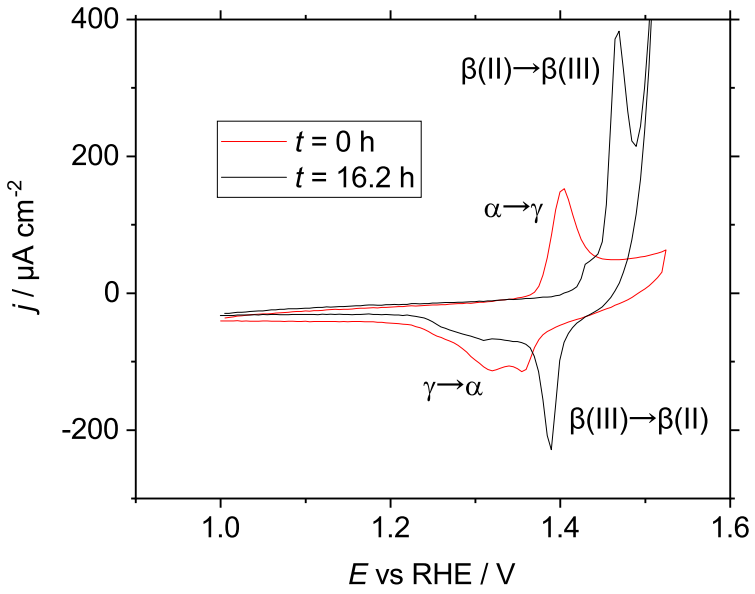

(a) Long term CV converting γ-NiOOH to β-NiOOH. Started with a freshly electropolished nickel electrode. CVs were performed in 0.5 M KOH for 16.2 h at 10 mV s^{-1}

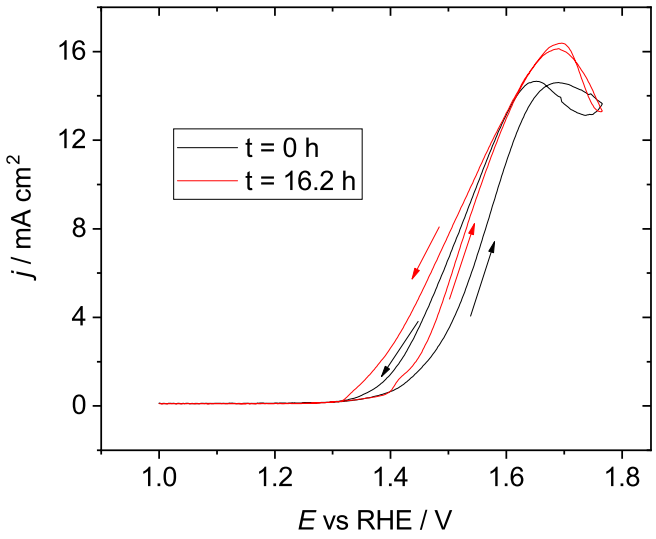

(b) Long term CV of nickel in glycerol solution. Nickel electrode was electropolished, then placed in 0.5 M KOH and 0.2 M glycerol solution. Cycling was performed for 16.2 h at 10 mV s^{-1}.

Figure 5.16: Comparison of the NiOOH aging process with and without glycerol

5.3.3.3 Tafel Analysis

More information can be gathered by looking at slow CVs and charge transfer coefficients of the glycerol system as a function of temperature. Experiments were performed in two separate, continuous sessions using temperature orders HTS1 and HTS2 (Figs. 5.17). All legends show the temperature order performed top to bottom for the relevant plot. Tafel slopes and charge transfer coefficients were extracted using the method described previously (Section 2.1).

Potential limits for linear fitting were determined using two separate methods, as the Tafel region for NiOOH formation and the Tafel region for glycerol oxidation blend into each other. As an approximation to simplify the mechanistic analysis, the entire Tafel region will be assumed to be due to glycerol oxidation with the $Ni(OH)_2$ phase having been substantially oxidized to NiOOH before glycerol oxidation occurs. For this method both upper and lower limits were determined visually and kept only when the R^2 value for the fit was greater than 0.99. These fits are shown in Figs. 5.18 and 5.19, and the resulting charge transfer coefficients are shown in Fig. 5.20.

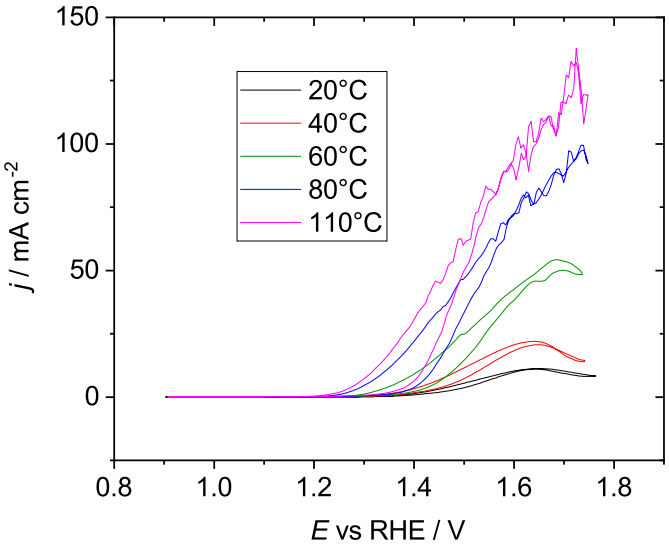

(a) CVs, HTS1

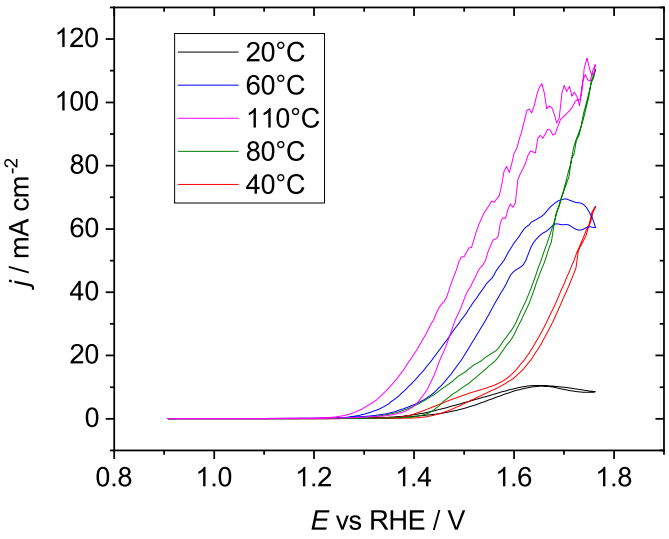

(b) CVs, HTS2

Figure 5.17: Glycerol oxidation CVs for HTS1 and HTS2 temperature orders on electropolished nickel. Solution was 0.5 M KOH and 0.2 M glycerol. Sweep rate for CV was 5 mV s^{-1}.

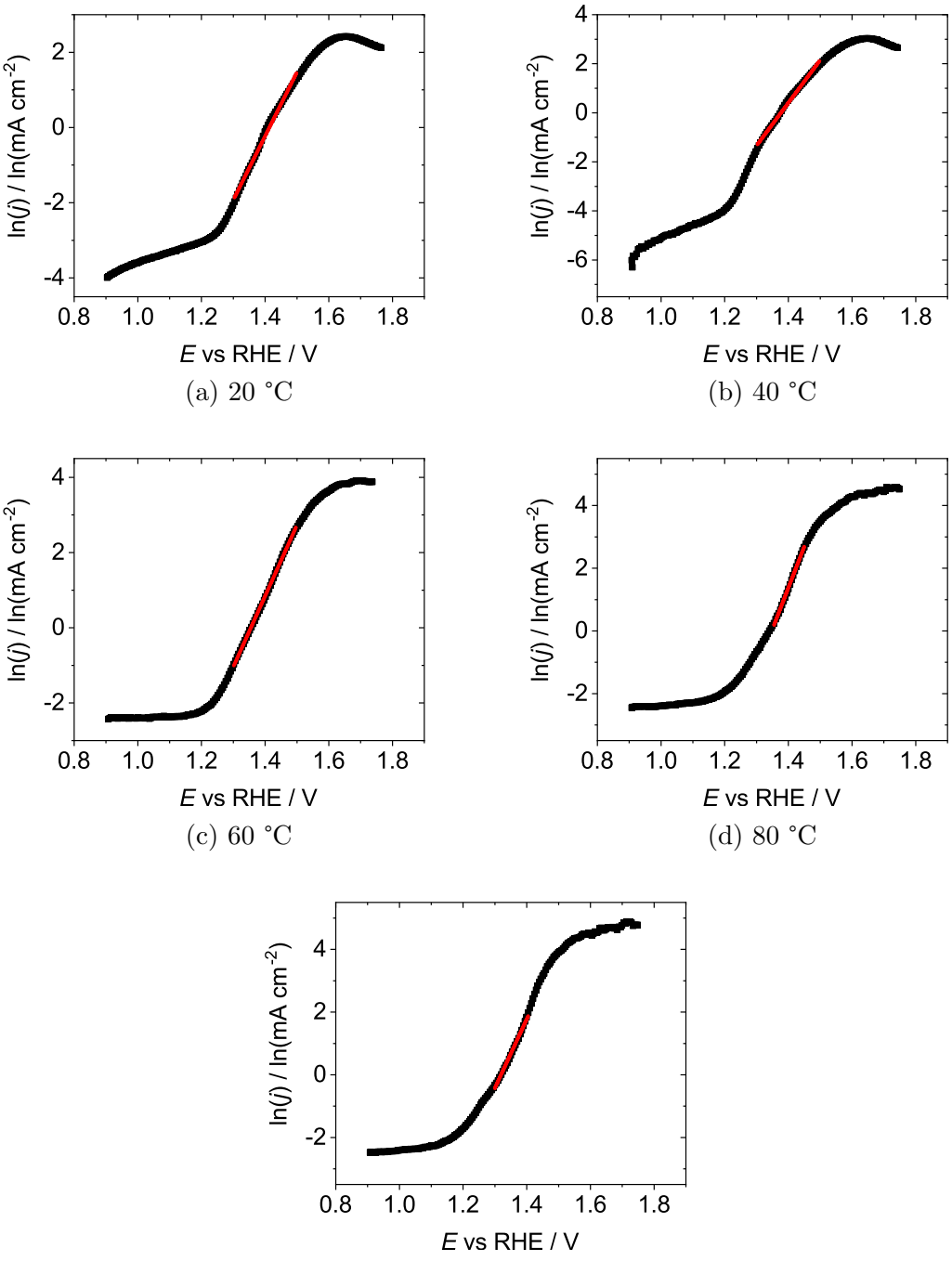

(a) 20 °C (b) 40 °C

(c) 60 °C (d) 80 °C

(e) 110 °C

Figure 5.18: HTS1 temperature order glycerol oxidation Tafel slopes. Potential limits were determined visually and accepted when a linear fit was performed with an R^2 value greater than 0.99. The presence of a second linear region starting at approximately 1.5 V is due to a transition to oxygen evolution as the dominant surface reaction. Sweep rate was 5 mV s^{-1}.

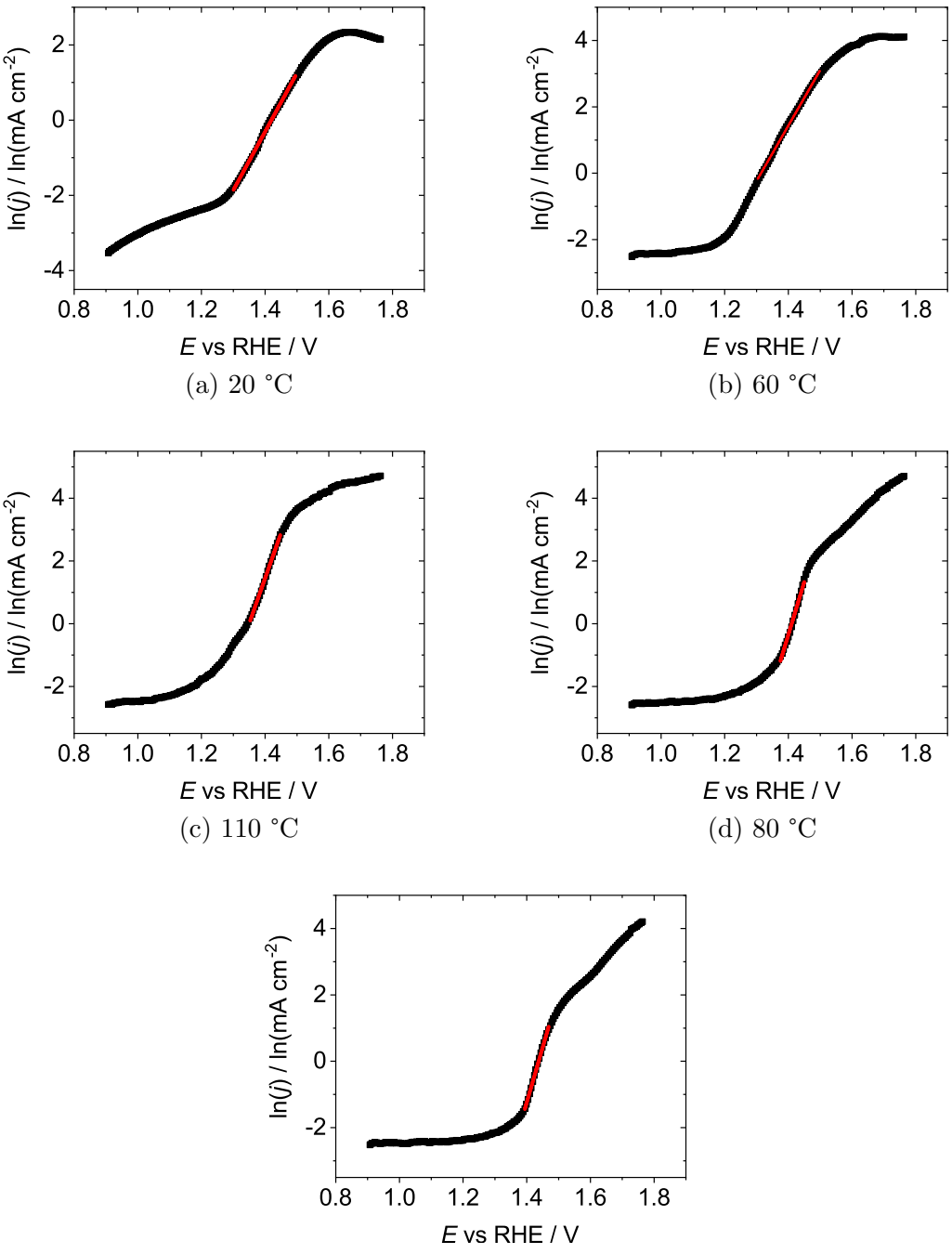

(a) 20 °C (b) 60 °C

(c) 110 °C (d) 80 °C

(e) 40 °C

Figure 5.19: HTS2 temperature order glycerol oxidation Tafel slopes. Potential limits were determined visually and accepted when a linear fit was performed with an R^2 value greater than 0.99. The presence of a second linear region starting at approximately 1.5 V is due to a transition to oxygen evolution as the dominant surface reaction. Sweep rate was 5 mV s^{-1}.

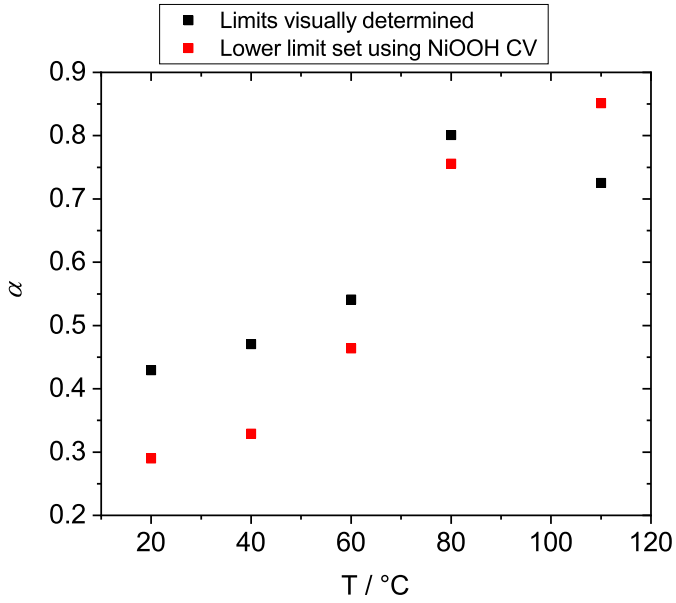

(a) Charge transfer coefficients, HTS1 temperature order

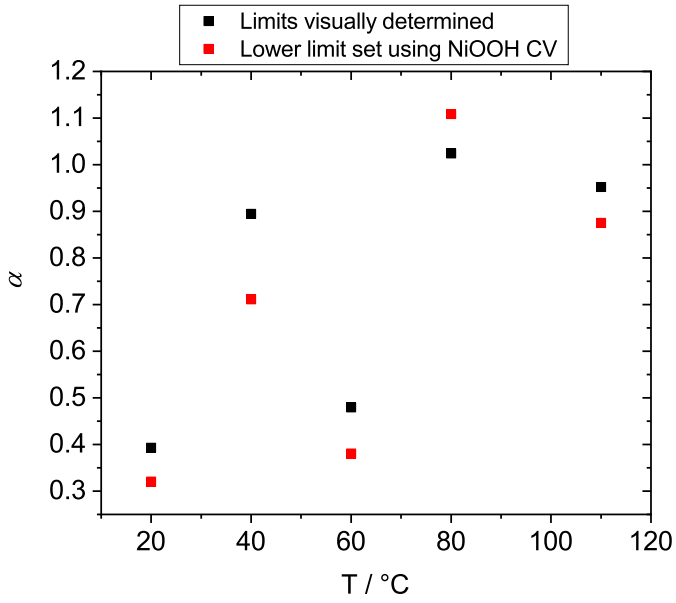

(b) Charge transfer coefficients, HTS2 temperature order

Figure 5.20: Charge transfer coefficients for glycerol oxidation as a function of temperature on electropolished nickel. Lower potential limits for fitting were determined using two different methods described previously: visual observation and analogous glycerol free experiments. The HTS2 temperature order is as follows: 20 °C, 60 °C, 110 °C, 80 °C, 40 °C.

The charge transfer coefficients collected as a function of temperature (Fig. 5.20) can give more mechanistic information. It appears that for the HTS1 temperature order the charge transfer coefficient is approximately 0.5 at temperatures up to and including 60 °C. This indicates that the first electron-transfer step in the mechanism is rate determining. Given the CS2 mechanism the following is consistent with this value:

$$\begin{aligned}
\mathrm{Ni(OH)_2 + OH^-} &\xrightarrow{\text{RDS}} \mathrm{NiOOH + H_2O + e^-} \\
\mathrm{NiOOH + RCH_2OH} &\longrightarrow \mathrm{NiOOH(RCH_2OH)(ads)} \\
\mathrm{NiOOH(RCH_2OH)(ads) + NiOOH} &\longrightarrow \mathrm{NiOOH(RCH_2O)(ads) + Ni(OH)_2} \\
\mathrm{NiOOH(RCH_2O)(ads) + NiOOH} &\longrightarrow \mathrm{NiOOH(RCHO)(ads) + Ni(OH)_2} \\
\mathrm{NiOOH(RCHO)(ads)} &\longrightarrow \mathrm{NiOOH + RCHO}
\end{aligned} \tag{5.10}$$

The mechanistic steps shown are for reactions occurring on the oxide surface. As discussed above, the oxide layer must be converted into NiOOH. At steady state, a cycle begins where a hydroxide ion deprotonates a $Ni(OH)_2$ site, glycerol adsorbs there, and then is oxidized. The oxidation causes the reduction of the site back to $Ni(OH)_2$ and the cycle continues. Note that the complete mechanism does require several NiOOH groups close together to fully complete the oxidation. Because the slow step is the deprotonation of the $Ni(OH)_2$ sites, the $Ni(OH)_2$ phase is near full coverage (Fig. 5.21). Full surface coverage of $Ni(OH)_2$ appears to inhibit the conversion of bulk layer α within the oxide matrix to its corresponding β phase at room temperature (Section 4.3.4.1). This is likely due to the galleries in the oxide being packed with protons in the $Ni(OH)_2$ phase, making it difficult for the deintercalation of the α and γ phases to occur.

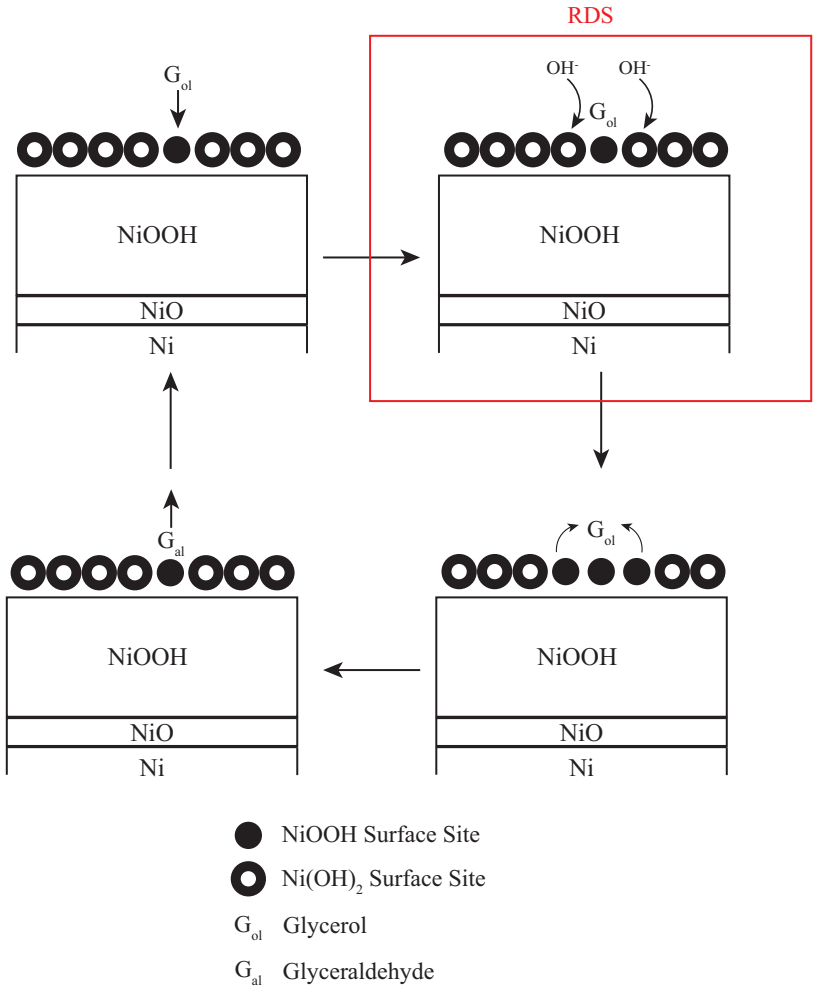

Figure 5.21: CS2 mechanism with step 1 as the RDS. The surface is largely composed of $Ni(OH)_2$ at all times. This figure shows only what happens once the system achieves steady state, as the oxide layer must be fully converted to the NiOOH phase before it becomes active for electrooxidation [84, 128, 216].

Because the rate of the RDS is potential dependent it explains the existence of the glycerol oxidation peak. The exponential dependence of the rate constant for step 1 is as follows

$$k = k^{eq} \exp\left(\frac{\beta F \eta}{RT}\right) \tag{5.11}$$

where k is the rate constant, k^{eq} is the equilibrium rate constant, β is the symmetry factor for this step, F is Faraday's constant, η is the overpotential, R is the universal gas constant in J K^{-1} mol^{-1}, and T is the absolute temperature. This leads to the rising edge of the peak.

The mechanisms have been simplified by writing the mechanisms as written in literature. For all electron transfers occurring at the solution/oxide interface a charge carrier is required in order to transport the electron from the interface to the nickel metal. This charge carrying process is included in the electron transfer step of the mechanism, as has been done in the literature [21, 22, 79]. Here the assumption is made that the transfer of the charge carrier through the film is fast compared to the oxidation event at the oxide surface.

Eventually the rate of this step exceeds the rate of some slower steps, which then become rate limiting (Fig. 5.22). At this point all NiOOH sites available become involved in adsorptions and are no longer available for oxidation. This causes a decay in the current density. Additionally, this adsorbed layer serves to continue blocking the deintercalation of the α and γ phases.

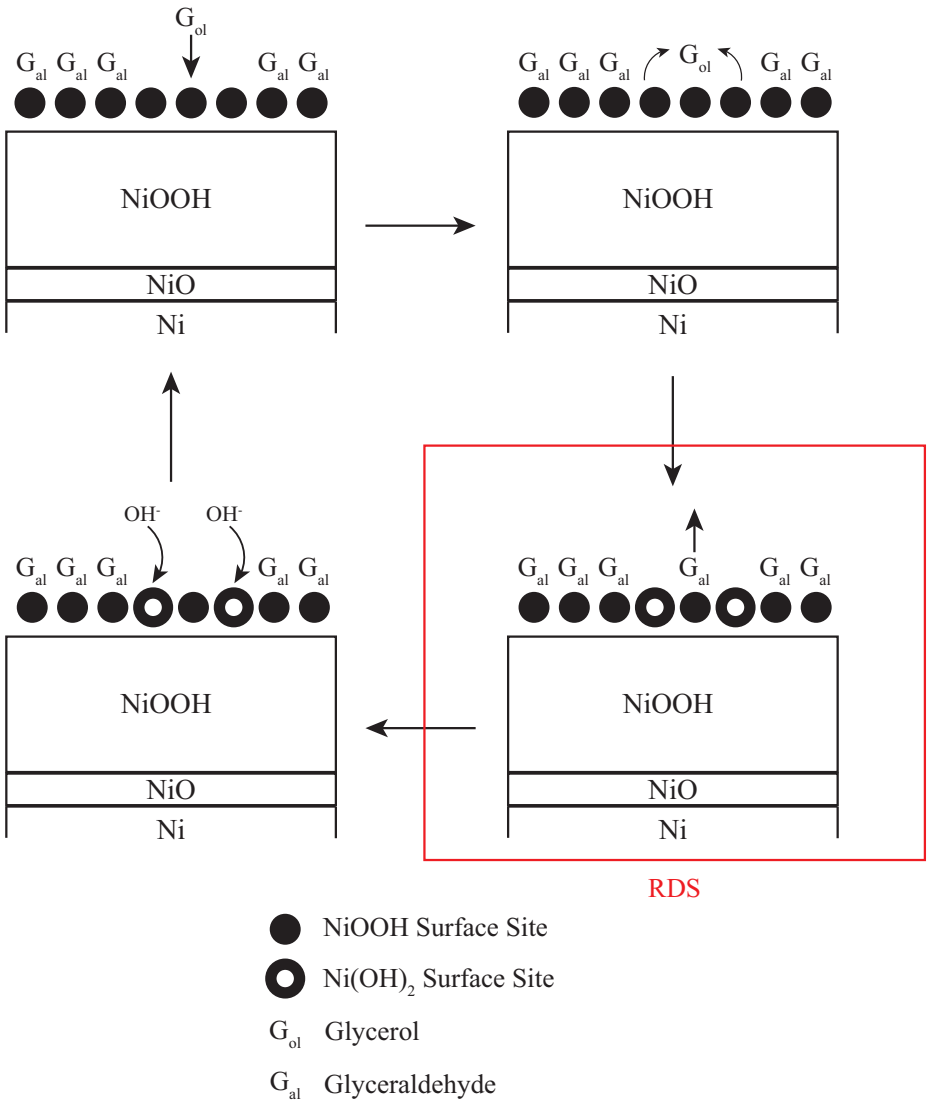

Figure 5.22: CS2 mechanism with step 3 as the RDS. This figure shows what is happening to cause decreasing current after the peak maximum. Adsorbed species begin to cover the surface due to the RDS being the release of the organic species from the NiOOH site. As this continues the condition required for oxidation, adjacent free NiOOH sites, becomes less likely due to the surface being covered in adsorbates.

As the temperature reaches and exceeds 80 °C in the HTS1 temperature order the charge transfer coefficient tends to unity. This indicates that the rate determining step involves no electron transfer, and has one electron transfer step somewhere before it. Any of the remaining mechanistic steps of CS2 satisfy this condition:

$$\begin{aligned}
\mathrm{Ni(OH)_2 + OH^- &\longrightarrow NiOOH + H_2O + e^-} \\
\mathrm{NiOOH + RCH_2OH &\xrightarrow{RDS?} NiOOH(RCH_2OH)(ads)} \\
\mathrm{NiOOH(RCH_2OH)(ads) + NiOOH &\xrightarrow{RDS?} NiOOH(RCH_2O)(ads) + Ni(OH)_2} \\
\mathrm{NiOOH(RCH_2O)(ads) + NiOOH &\xrightarrow{RDS?} NiOOH(RCHO)(ads) + Ni(OH)_2} \\
\mathrm{NiOOH(RCHO)(ads) &\xrightarrow{RDS?} NiOOH + RCHO}
\end{aligned} \tag{5.12}$$

Here the first step forming the NiOOH is quite fast, but one of the subsequent steps is quite slow. If any of steps 3 through 5 are rate determining, the adsorbed species on the surface would approach full coverage quite quickly. Because oxygen evolution can still be shown to occur (Fig. 5.17), and oxygen evolution requires free NiOOH sites [65] these steps are likely not rate determining. This leaves the second step as the likely rate determining step:

$$\begin{aligned}
\mathrm{Ni(OH)_2 + OH^- &\longrightarrow NiOOH + H_2O + e^-} \\
\mathrm{NiOOH + RCH_2OH &\xrightarrow{RDS} NiOOH(RCH_2OH)(ads)} \\
\mathrm{NiOOH(RCH_2OH)(ads) + NiOOH &\longrightarrow NiOOH(RCH_2O)(ads) + Ni(OH)_2} \\
\mathrm{NiOOH(RCH_2O)(ads) + NiOOH &\longrightarrow NiOOH(RCHO)(ads) + Ni(OH)_2} \\
\mathrm{NiOOH(RCHO)(ads) &\longrightarrow NiOOH + RCHO}
\end{aligned} \tag{5.13}$$

In turn, this describes why aging of the γ-NiOOH phase to β-NiOOH can occur at these temperatures. The high temperature has increased the rate at which hydroxide ions deprotonate $Ni(OH)_2$ sites, so the oxide surface is consistently in the NiOOH state at high potentials (Fig. 5.23). This NiOOH is exposed to solution, and allows for the deintercalation process of α and γ to their corresponding β phases due to having fewer protons packed into the galleries [93, 95, 184, 193]. This also explains why at high temperatures oxygen evolution appears to be the dominant process, as the surface contains no adsorbates and many free sites are available for the oxygen evolution reaction to occur on.

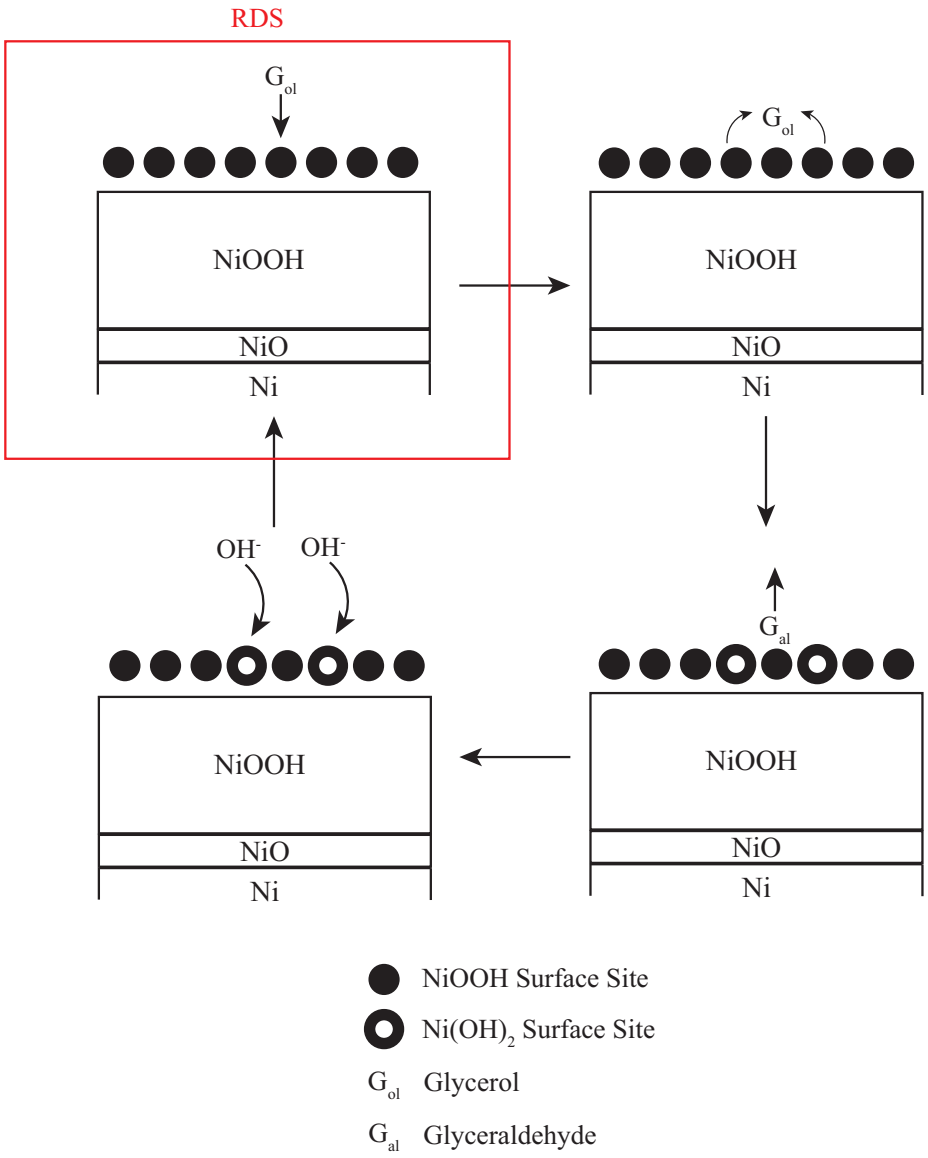

Figure 5.23: CS2 mechanism with step 2 as the RDS. The surface is largely composed of NiOOH at all times. This figure shows only what happens once the system achieves steady state, as the oxide layer must be fully converted to the NiOOH phase before it becomes active for electrooxidation [84, 128, 216].

Using the charge transfer coefficients from the HTS2 temperature order experiment (Fig. 5.20) it can be shown that this effect is not simply one of temperature, but that the electrode itself has been altered. Again the charge transfer coefficient is found to be approximately 0.5 up to 60 °C. The next temperature tested is 110 °C, and the charge transfer coefficient is found to be approximately 1. This

new charge transfer value is then retained as the system is cooled first to 80 °C, and finally to 40 °C. This indicates that whatever structural change has occurred to the nickel electrode is retained as the temperature is reduced, confirming the conversion of γ-NiOOH to β-NiOOH.

In summary, for γ-NiOOH at room temperature the RDS is the oxidation of $Ni(OH)_2$ to NiOOH (CS2-Step 1). Since the rate of this step is potential dependent, as the potential increases it ceases to be rate determining and the surface becomes fully covered in adsorbed organics. At higher temperatures glycerol adsorption is the RDS for the glycerol oxidation (CS2-Step 2). This allows for NiOOH to cover the surface at all potentials, leaving it exposed to solution and allowing for γ-NiOOH to age into β-NiOOH.

The approximation that the entire Tafel region is due to glycerol oxidation may not be particularly accurate, however, since the formation of NiOOH must be complete before the oxide surface is active for electrooxidation [84, 128, 216]. Additionally, not enough charge has passed by the start of the Tafel region (about 1.3 V) to form the NiOOH layer. A second method for determining the Tafel region was performed where the lower potential limit for the fit was determined using analogous experiments performed under the same reaction conditions with no glycerol in solution. The lower potential limit was selected as the potential of minimum current directly following the NiOOH peak. The upper potential limit for the second method is determined visually, and only accepted when the R^2 value for the fit was greater than 0.99. The resulting charge transfer coefficients gathered from each method are similar (Fig. 5.20), and result in the same mechanistic analysis.

The usage of Tafel analysis on nickel could be complicated by the fact that the nickel oxide phase continues to grow far beyond some small number of monolayers. Because the Tafel relation relies on coverage, and the reagent concentrations can be considered constant under these reaction conditions, it can be shown to be robust enough for use in this analysis. The changing surface area can be ignored so long as it does not increase significantly during the course of a single Tafel sweep. Based on literature studies this does not appear to be the case [93, 107], with significant cycling through high potentials required for substantial oxide thickening to occur.

The CS2 mechanism can be written out with appropriate variables for

concentration and coverage

$$
\begin{aligned}
\underset{1\text{-}\theta\text{-}\gamma\text{-}\sigma\text{-}\mu}{\mathrm{Ni(OH)_2}} + \underset{[\mathrm{OH^-}]}{\mathrm{OH^-}} &\underset{k_{-1}}{\overset{k_1}{\rightleftharpoons}} \underset{\theta}{\mathrm{NiOOH}} + \underset{[\mathrm{H_2O}]}{\mathrm{H_2O}} + \mathrm{e^-} \\
\underset{\theta}{\mathrm{NiOOH}} + \underset{[\mathrm{GlyOl}]}{\mathrm{RCH_2OH}} &\underset{k_{-2}}{\overset{k_2}{\rightleftharpoons}} \underset{\gamma}{\mathrm{NiOOH(RCH_2OH)(ads)}} \\
\underset{\gamma}{\mathrm{NiOOH(RCH_2OH)(ads)}} + \underset{\theta}{\mathrm{NiOOH}} &\underset{k_{-3}}{\overset{k_3}{\rightleftharpoons}} \underset{\sigma}{\mathrm{NiOOH(RCHOH)(ads)}} + \underset{1\text{-}\theta\text{-}\gamma\text{-}\sigma\text{-}\mu}{\mathrm{Ni(OH)_2}} \\
\underset{\sigma}{\mathrm{NiOOH(RCHOH)(ads)}} + \underset{\theta}{\mathrm{NiOOH}} &\underset{k_{-4}}{\overset{k_4}{\rightleftharpoons}} \underset{\mu}{\mathrm{NiOOH(RCHO)(ads)}} + \underset{1\text{-}\theta\text{-}\gamma\text{-}\sigma\text{-}\mu}{\mathrm{Ni(OH)_2}} \\
\underset{\mu}{\mathrm{NiOOH(RCHO)(ads)}} &\underset{k_{-5}}{\overset{k_5}{\rightleftharpoons}} \underset{\theta}{\mathrm{NiOOH}} + \underset{[\mathrm{GlyAl}]}{\mathrm{RCHO}}
\end{aligned}
\tag{5.14}
$$

Here, θ is the coverage of NiOOH, γ is the coverage of adsorbed glycerol, σ is the coverage of adsorbed intermediate, and μ is the coverage of adsorbed glyceraldehyde. These are all normalized together as a percentage, so that $\theta + \gamma + \sigma + \mu \leq 1$.

Given the previous mechanism, the rates of each step follow:

$$
\begin{aligned}
v_1 &= k_1(1-\theta-\gamma-\sigma-\mu)[\mathrm{OH^-}] - k_{-1}\theta[\mathrm{H_2O}] \\
v_2 &= k_2\theta - k_{-2}\gamma \\
v_3 &= k_3\theta\gamma - k_{-3}(1-\theta-\gamma-\sigma-\mu)\sigma \\
v_4 &= k_4\theta\sigma - k_{-4}(1-\theta-\gamma-\sigma-\mu)\mu \\
v_5 &= k_5\mu - k_{-5}\theta[\mathrm{GlyAl}]
\end{aligned}
\tag{5.15}
$$

Assuming step 1 as the RDS all coverages are small, and the back reaction is neglected. The observed rate, v_{obs}, can be shown to be

$$
v_{obs} = \frac{j}{F} = v_1 = k_1[\mathrm{OH^-}] \tag{5.16}
$$

Now by taking into account the potential dependence of k_1, the rate constant of step 1

$$
k_1 = k_1^{eq} \exp\left(\frac{\beta_1 F\eta}{RT}\right) \tag{5.17}
$$

where β_1 is the symmetry factor of the reaction step (≈ 0.5), the potential dependence

of the current is

$$j = Fk_1[\mathrm{OH}^-] = Fk_1^{eq}[\mathrm{OH}^-]\exp\left(\frac{\beta_1 F\eta}{RT}\right) \tag{5.18}$$

Taking the natural logarithm to put things in the Tafel form gives the following result

$$\ln(j) = \ln(Fk_1^{eq}[\mathrm{OH}^-]) + \left(\frac{\beta_1 F\eta}{RT}\right) \tag{5.19}$$

where it is shown that the slope of this plot is $\frac{\beta_1 F}{RT}$. Since the slope of this plot, based on Tafel relations, is known to be $\frac{\alpha F}{RT}$ and $\beta_1 = 0.5$ an experimental α of 0.5 should be expected for this mechanism.

5.3.3.4 Cyclic Voltammetry Sweep Rate Analysis

Varying the sweep rate of CVs performed on this system highlights some interesting features (Fig. 5.24). The experiments performed at 20 °C in the HTS1 temperature order show that there is some small dependence of the current density on the scan rate. At this temperature glycerol oxidation is the only expected reaction at these potentials, so this behavior is attributed to glycerol oxidation. The experiments performed at 110 °C in the HTS1 temperature order show little to no dependence of the current density on scan rate. After 1.6 V there does appear to be some difference between current densities as a function of sweep rate, however this is likely due to oxygen bubbles disturbing the reaction at the electrode surface. Under these conditions oxygen evolution is expected to be the dominant reaction, therefore a total lack of correlation between sweep rate and current density is attributed to oxygen evolution. This reaction is known to be quite fast on nickel [126, 218], allowing the system to remain at pseudosteady state for all sweep rates tested.

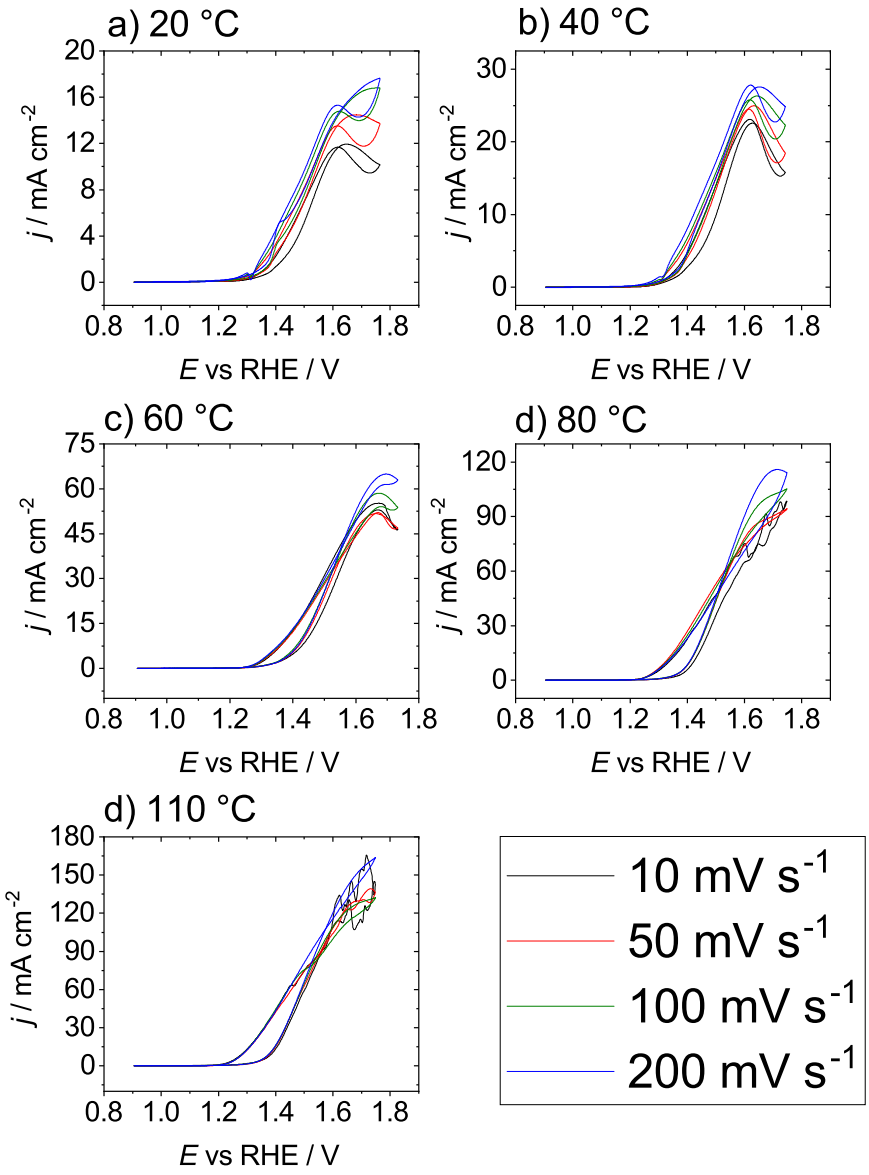

Figure 5.24: CV of glycerol on nickel at various sweep rates, as a function of temperature in HTS1 order. Solution was 0.5 M KOH and 0.2 M glycerol.

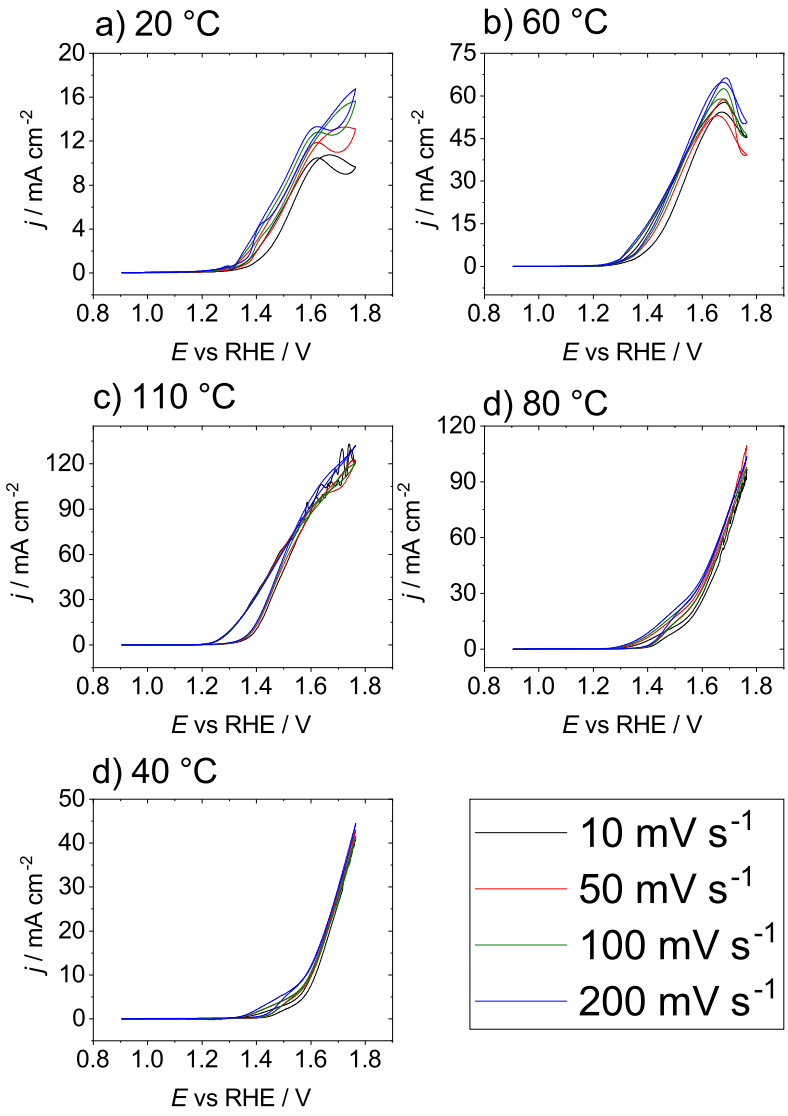

Figure 5.25: CV of glycerol on nickel at various sweep rates, as a function of temperature in HTS2 order. Solution was 0.5 M KOH and 0.2 M glycerol.

Similarly, CVs performed at or after the 110 °C experiment from the HTS2 temperature order experiments show little correlation between sweep rate and current density (Fig. 5.25). The exception is a brief potential window between 1.3 V and 1.6

V on the 80 °C and 40 °C trials (Fig. 5.26). For this potential region it appears that glycerol oxidation dominates. It is expected that CS2-Step 2 is the rate determining step here, making the surface covered in NiOOH available for oxidation. The RDS of the glycerol oxidation reaction is not potential dependent, however the RDS for the oxygen evolution reaction is [66, 218–220]. As the potential increases the oxygen evolution reaction begins to dominate.

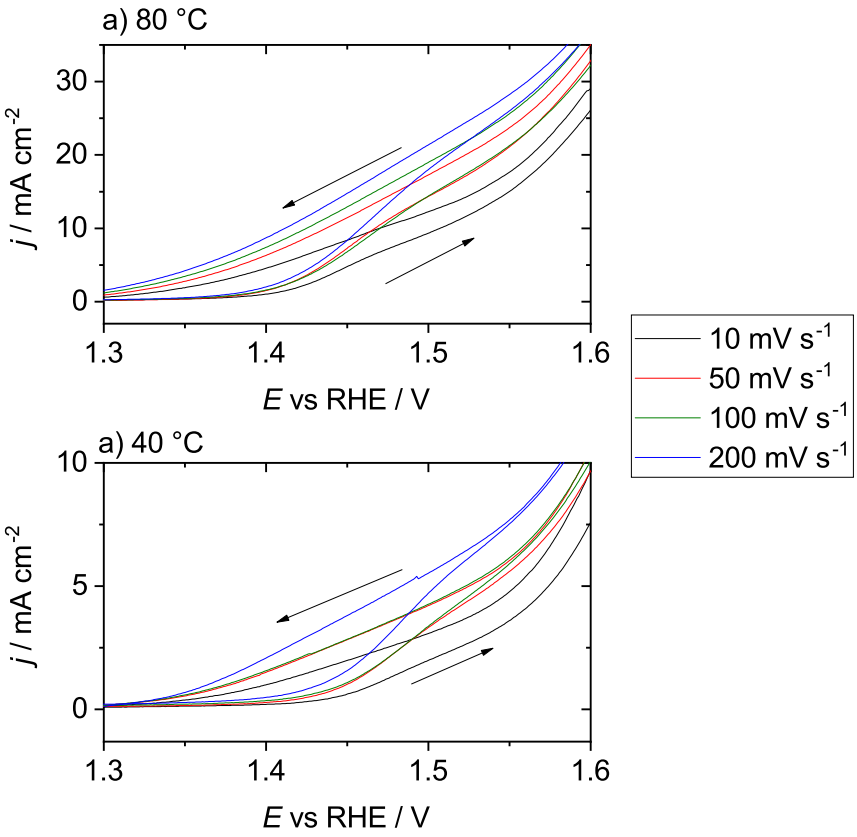

Figure 5.26: CV of glycerol on nickel at various sweep rates. 80 °C and 40 °C enhanced view. HTS2 temperature order. Solution was 0.5 M KOH and 0.2 M glycerol. For all CVs here the lower trace is the anodic sweep and the upper trace is the cathodic sweep.

5.3.3.5 AC Voltammetry Analysis

The AC voltammetry of this system gives additional support for the sweep rate studies, and reveals some interesting information regarding the surface processes of the nickel electrode. It further highlights which phase of NiOOH is present on the

nickel surface for a given combination of temperature and potential. It does this by conveying whether glycerol oxidation or oxygen evolution is the dominant reaction based on trends in the real and imaginary components of the admittance.

When performing AC voltammetry at 100 Hz during the HTS1 temperature order experiments (Fig. 5.27), peaks are seen corresponding to the oxidation of $Ni(OH)_2$ to NiOOH in both the real and imaginary plots. These peaks are labelled in the plots. Interestingly, these peaks are seen at every temperature in the imaginary plot but are only seen at 20 °C and 40 °C in the real plot.

The real component of the admittance on the anodic sweep becomes negative at approximately 1.6 V for 20 °C and 40 °C but stays positive until approximately 1.7 V for the 60 °C experiment. This highlights the competing oxygen evolution and glycerol oxidation reactions, as the real component becomes negative as the glycerol oxidation current begins to decline. This indicates that the real component likely becomes negative when the glycerol adsorption mechanistic step begins to take over as the RDS, instead of the $Ni(OH)_2$ oxidation step. For 80 °C and 110 °C the real component of the anodic sweep remains positive throughout the sweep indicating that the adsorption of glycerol is never a kinetically dominant reaction.

It is noteworthy that the potential regions where the real component of the admittance is increasing coincide quite well with the potential regions where current density was found to be entirely independent of sweep rate (Section 5.3.3.4). Both of these features appear to indicate oxygen evolution as the dominant reaction on the NiOOH surface.

The imaginary component of the admittance at 100 Hz portrays trends similar to the real component, in that it appears to have two discrete behaviors depending on whether glycerol oxidation or oxygen evolution is the dominant electrochemical reaction. The oxidation of $Ni(OH)_2$ to NiOOH is clearly present at all temperatures. The imaginary component of the 60 °C experiment highlights the competing oxygen evolution and glycerol oxidation. It appears that at this temperature oxygen evolution has become competitive with glycerol oxidation at most potentials, indicated by the low imaginary component value that occurs in experiments at 80 °C and 110 °C. This value abruptly increases at approximately 1.7 V matching the point at which CS2-Step 1 stops being the RDS for the glycerol oxidation and the surface becomes covered in organic adsorbates.

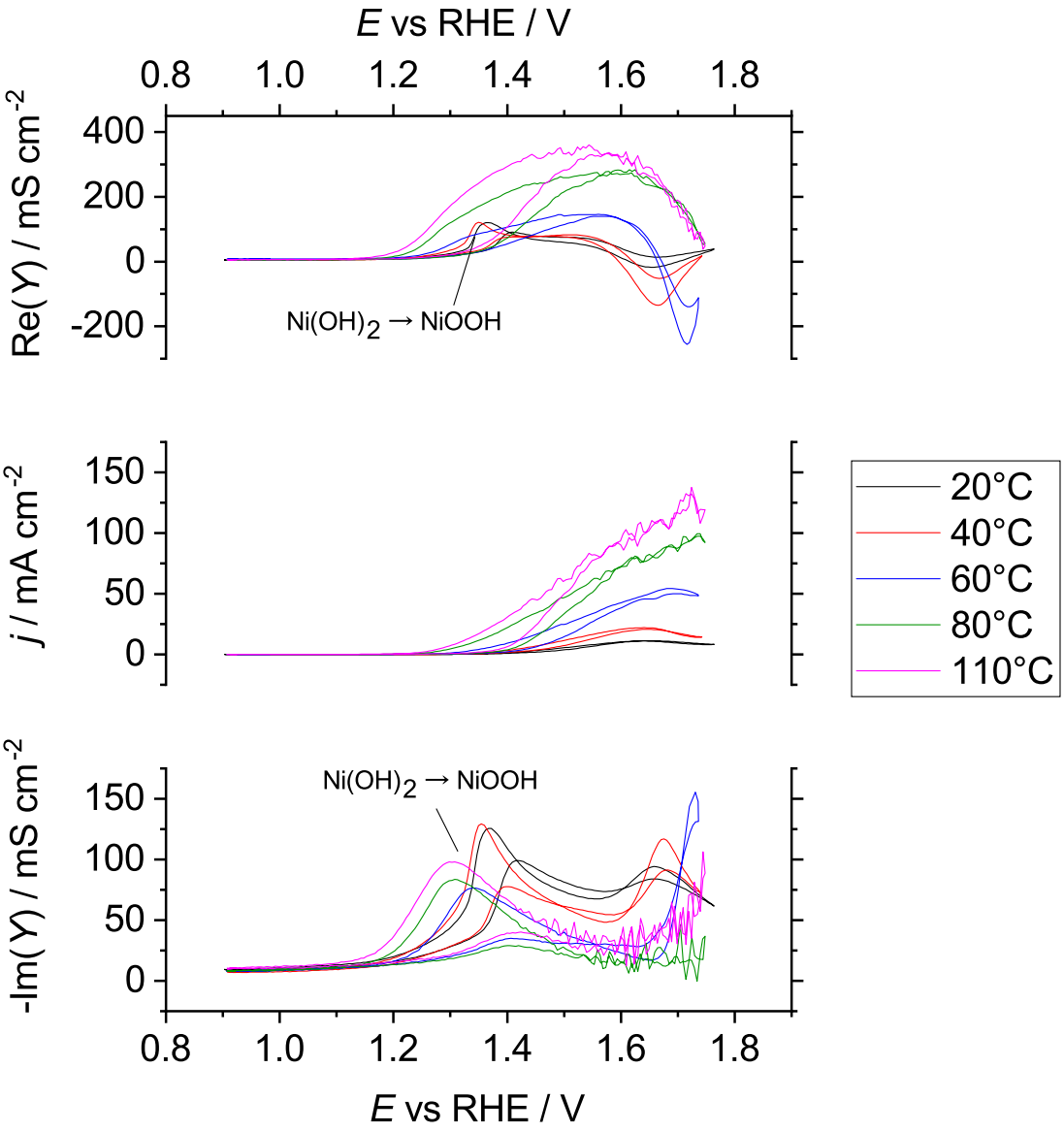

Figure 5.27: AC voltammetry of glycerol on nickel, in HTS1 temperature order. The solution is 0.5 M KOH and 0.2 M glycerol. The frequency was 100 Hz and the sweep rate was 5 mV s^{-1}. For all experiments the anodic trace is the one that starts low.

Performing the same experiment in HTS2 temperature order highlights a few things that would have otherwise gone unnoticed. First, both the real and imaginary components of the 110 °C experiment show trends similar to the 60 °C experiment

performed in HTS1 temperature order. This indicates that at 110 °C glycerol adsorption is still occurring, and confirms the importance of oxidation duration in the transformation of the γ-NiOOH phase to the β-NiOOH phase. It appears that having the surface stripped of glycerol at high temperatures does not cause the transition to occur immediately, and that a significant amount of time spent at high potentials while maintaining high temperature is required. Additionally, the trends found in both the real and imaginary components for the 80 °C and 40 °C experiments coincide with the conclusions reached from the sweep rate analysis. The potential region between 1.3 V and 1.6 V correlates with glycerol oxidation, and the region above 1.6 V correlates with oxygen evolution.

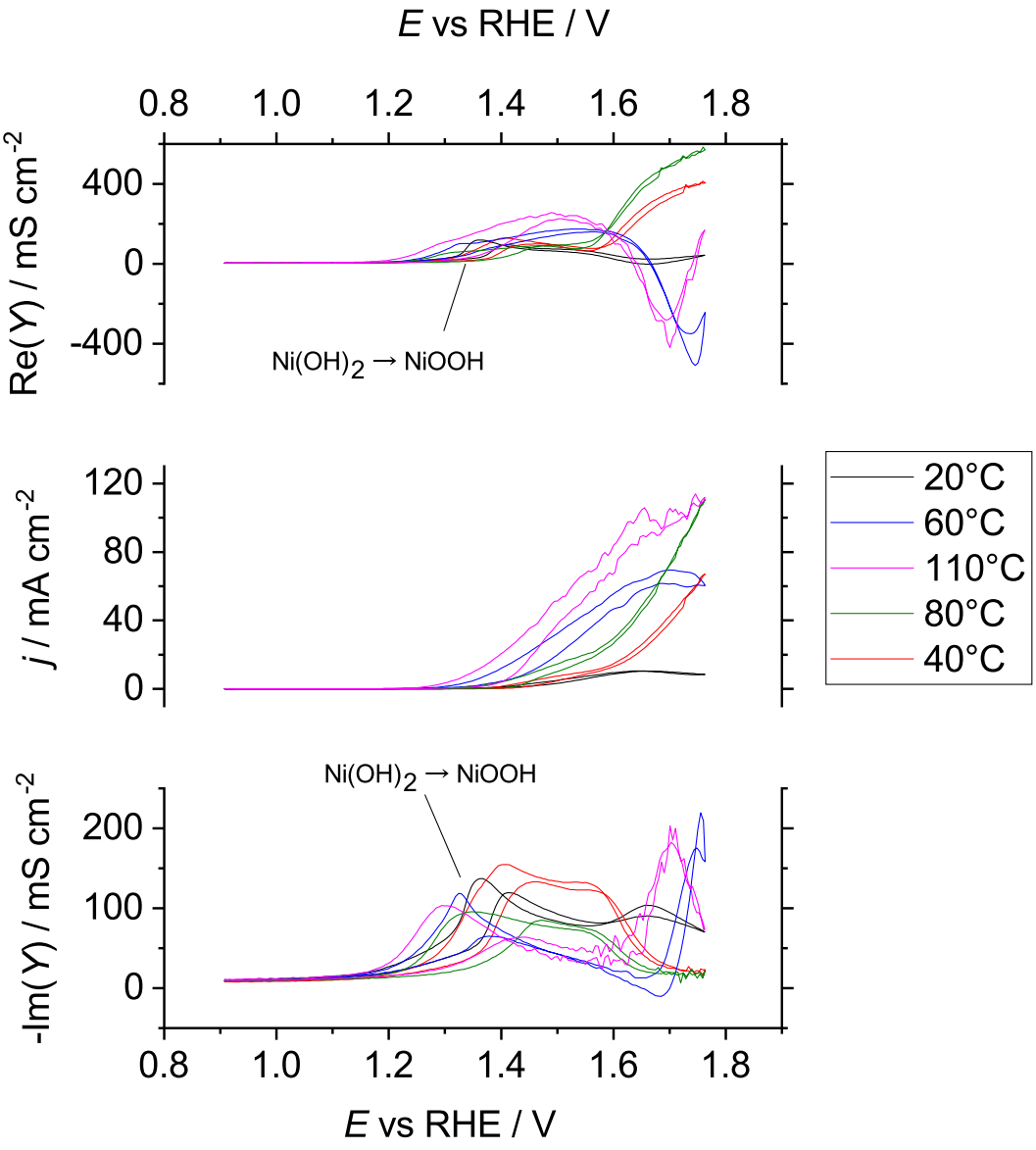

Figure 5.28: AC voltammetry of glycerol on nickel, in HTS2 temperature order. The solution is 0.5 M KOH and 0.2 M glycerol. The frequency tested was 100 Hz and the sweep rate was 5 mV s^{-1}. For all experiments the anodic trace is the lower one and the cathodic trace is the upper one.

5.3.3.6 Impedance Spectroscopy Analysis

Upon fitting the impedance data to circuits using the method described previously (Section 5.2.3) it was found that the L circuit was a superior fit to the C circuit in all cases. L' was found to be superior to L under certain conditions where R_{ct} drastically increased.

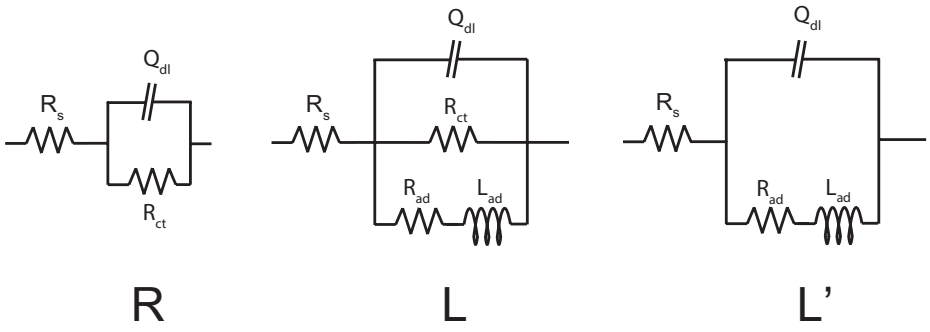

Figure 5.29: The three equivalent circuits successfully fit. R_s is the solution resistance, R_{ct} is the charge transfer resistance, R_{ad} is the resistance associated with an adsorption process, Q_{dl} is the double layer constant phase element, and L_{ad} is the inductance associated with an adsorption process.

From the fits several values were determined. The effective double layer capacitance, $C_{dl,eff}$ was determined from CPE fitting parameters using the Brug formula [208, 209]:

$$C_{dl,eff} = Q^{\frac{1}{\alpha}} \left(\frac{R_s R_{ct}}{R_s + R_{ct}} \right)^{\frac{1-\alpha}{\alpha}} \tag{5.20}$$

and when R_{ct} becomes infinitely large

$$C_{dl,eff} = Q^{\frac{1}{\alpha}} R_s^{\frac{1-\alpha}{\alpha}} \tag{5.21}$$

where Q is the CPE coefficient, α is the CPE exponent, R_s is the solution resistance, and R_{ct} is the charge transfer resistance.

The time constant of the double layer charging was determined as

$$\tau_{dl} = R_{ct} C_{dl,eff} \tag{5.22}$$

and similarly the time constant for the adsorption was determined as (Section 2.3.2.5)

$$\tau_{ad} = \frac{L_{ad}}{R_{ad}} \tag{5.23}$$

Fit results for this particular experiment are quite noisy in some regions. For the case of the lower potential region between 0.9 V and 1.2 V this is because impedance data collected represents a small portion of a semicircle in the Nyquist plot, resulting in a high degree of error in fitting the R_{ct} value. Additionally, experiments performed at 80 °C experience some noise caused by the competing oxygen evolution reaction. This noise can be seen in some of the lower temperature experiments at potentials higher than 1.6 V. Lastly, there are some interesting features around 1.4 V in many of the experiments. This is likely due to the initial formation of NiOOH at the electrode surface. In short, the competition of three separate processes on the electrode leads to complex features in the fitted dEIS spectra.

The $\log_{10}(R_{ct}^{-1})$ plots (Fig. 5.30) for both forward and reverse sweeps show the presence of two large negative peaks, one at approximately 1.6 V and one at just over 1.7 V. The existence of these two peaks indicates that at some temperatures, and for some ratios of γ-NiOOH to β-NiOOH there may exist a second kinetically significant adsorbate.

The first negative peak coincides with the onset of organic coverage on the NiOOH surface, and shows a significant trend as a function of oxidation time. For the HTS1 temperature order it appears to be linear as a function of temperature, with the peak appearing at higher potentials given higher temperatures. The HTS2 temperature order shows that the 110 °C peak appears at a lower potential than the 60 °C peak, indicating that the potential of the peak is not strictly linear with temperature. It appears that high temperatures cause the peak to shift to lower potentials, but the conversion of γ-NiOOH to β-NiOOH causes it to shift to higher potentials.

Comparing $\log_{10}(R_{ct}^{-1})$ for the forward sweeps on both the room temperature dEIS experiments (Figs. 5.30a and 5.30c) highlights something quite interesting. A large negative spike is observed just above 1.6 V, coinciding with the peak potential in the corresponding CV. In the HTS1 temperature order data this negative spike recovers and for this entire region circuit L is found to be the best fit, however in the HTS2 temperature order data the R_{ct} value spikes to infinity and circuit L' is found to be the circuit of best fit. For this reason no value of R_{ct} is observed in the corresponding $\log_{10}(R_{ct}^{-1})$ plot. What makes this so significant is that these features are found on

the first dEIS experiment performed in each sequence, and experimental protocol has kept all variables identical up to this point. Additionally, it appears that the standard behavior returns for the reverse sweep (Figs. 5.30d).

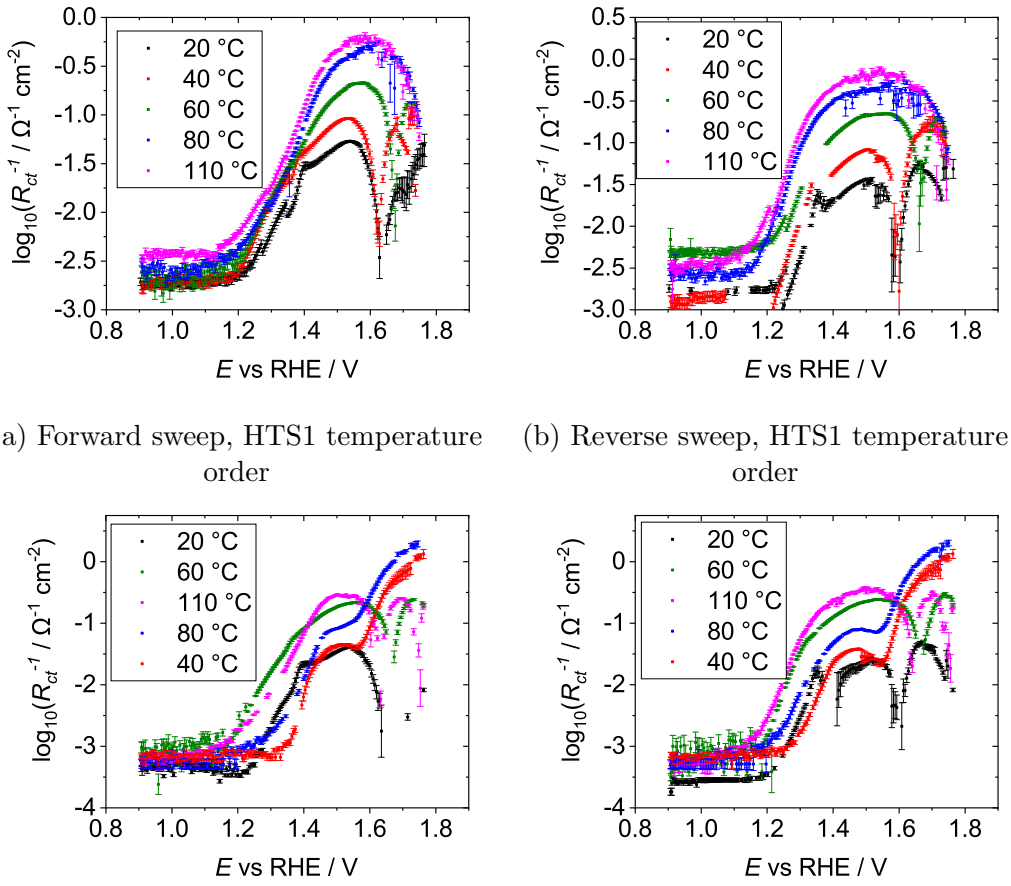

(a) Forward sweep, HTS1 temperature order

(b) Reverse sweep, HTS1 temperature order

(c) Forward sweep, HTS2 temperature order

(d) Reverse sweep, HTS2 temperature order

Figure 5.30: Tafel plots of R_{ct}^{-1} for glycerol oxidation, HTS1 and HTS2 temperature orders. The sweep rate was 5 mV s^{-1}.

By examining the Nyquist plots for these potential regions (Figs. 5.31 and 5.32) the reason for this behavior becomes apparent. The Nyquist plots make it clear that for the HTS1 temperature order experiment there is a potential region where C_{dl} is positive and R_{ct} is negative. This results in a negative time constant which is a feature associated with instability in an electrochemical system. This particular type of instability is called a Hopf bifurcation [221–223], characterized by a negative real component in the impedance with an imaginary component going from negative to

positive as a function of frequency. In the Nyquist plot this appears as a semicircle that goes from quadrant 2 to quadrant 3. The Hopf bifurcation suggests that by using an external resistor of the appropriate value, the negative R_{ct} determined for the frequency at which the Nyquist plot crosses the real axis, the system could be made to oscillate between two separate states. No such feature exists for the HTS2 temperature order experiment in this region.

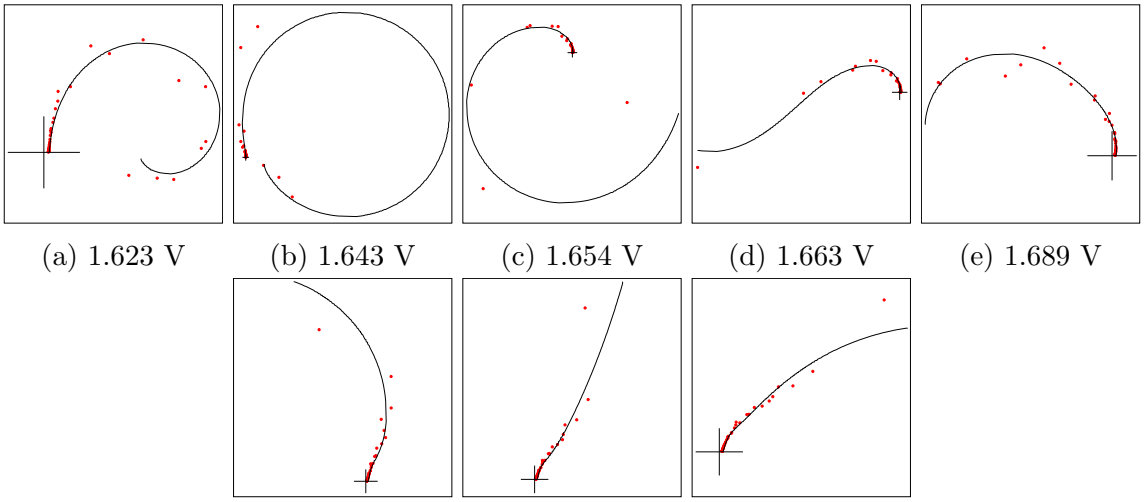

(a) 1.623 V (b) 1.643 V (c) 1.654 V (d) 1.663 V (e) 1.689 V

(f) 1.738 V (g) 1.748 V (h) 1.758 V

Figure 5.31: Nyquist plots of glycerol oxidation, room temperature, HTS1 temperature order. Potentials shown highlight the interesting features found at high potentials on the forward sweep. Red dots are experimental data, and black line is the corresponding fit. Black axis lines shown for scale; they are -100 to 100 on both axes in every figure.

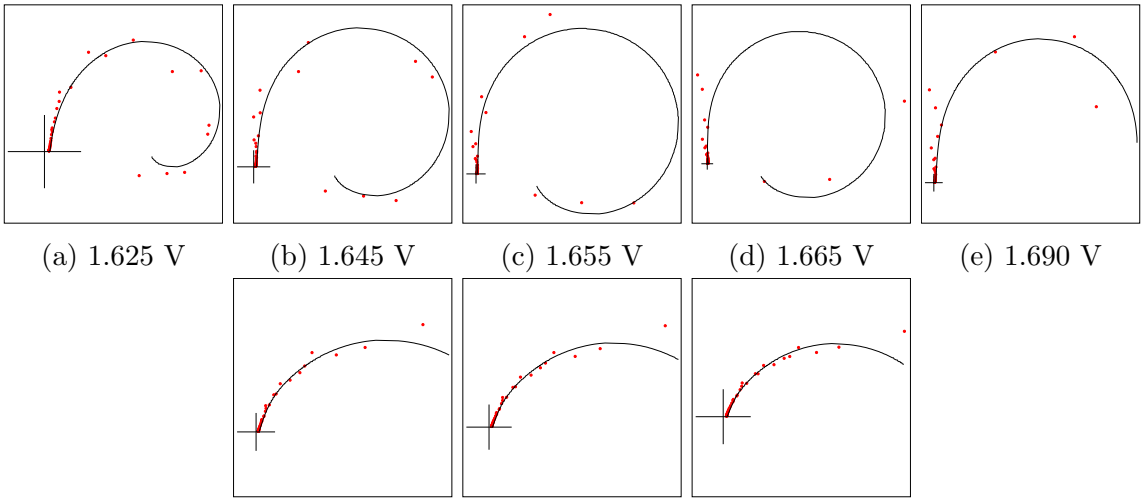

(a) 1.625 V (b) 1.645 V (c) 1.655 V (d) 1.665 V (e) 1.690 V

(f) 1.740 V (g) 1.750 V (h) 1.760 V

Figure 5.32: Nyquist plots of glycerol oxidation, room temperature, HTS2 temperature order. Potentials shown highlight the interesting features found at high potentials on the forward sweep. Red dots are experimental data, and black line is the corresponding fit. Black axis lines shown for scale; they are -100 to 100 on both axes in every figure.

A plot of the double layer time constants (Fig. 5.33) reveals that there are many temperatures and potentials at which they become negative. The transition from positive to negative time constants appear to coincide with the potential at which the slope of the corresponding CV stops being constant and begins to decrease to form the glycerol peak. This indicates that the adsorption of organics is involved in the instability in the system.

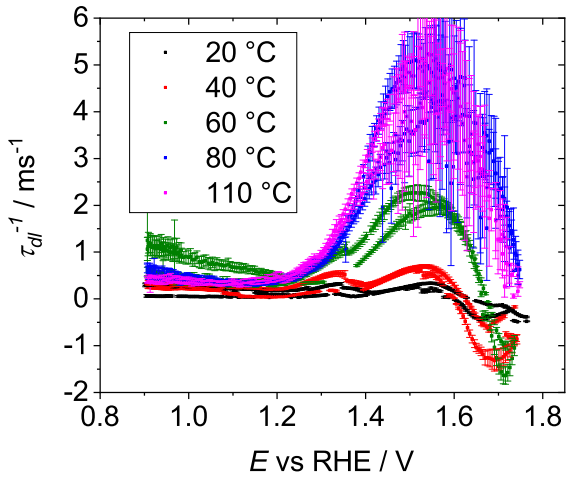

(a) HTS1 temperature order

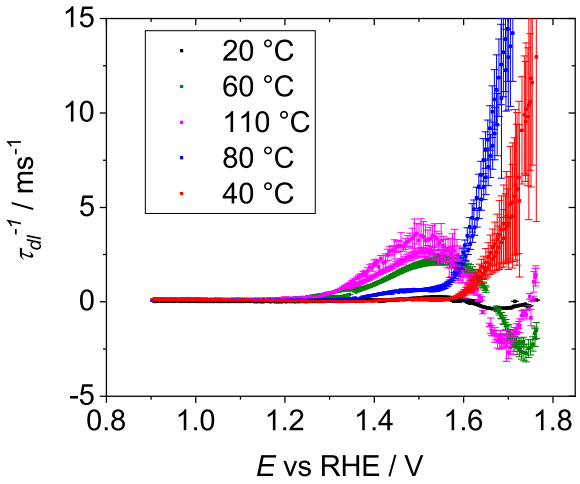

(b) HTS2 temperature order

Figure 5.33: Time constants for double layer charging, HTS1 and HTS2 temperature order. The sweep rate was 5 mV s^{-1}.

The system appears to exist on a knife edge between two separate states on the forward sweep (Fig. 5.34). In one state the R_{ct} becomes negative and R_{ad} remains small, staying less than 120 Ω cm^2. In the other state R_{ct} trends toward infinity and R_{ad} increases substantially, reaching as high as 390 Ω cm^2. The resulting R_0 is similar between the two states, but their existence indicates that there may be two separate mechanisms by which this oxidation can occur.

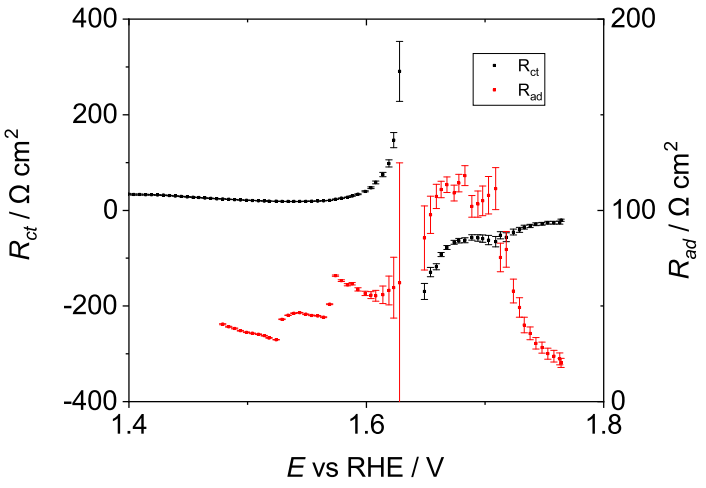

(a) HTS1 temperature order

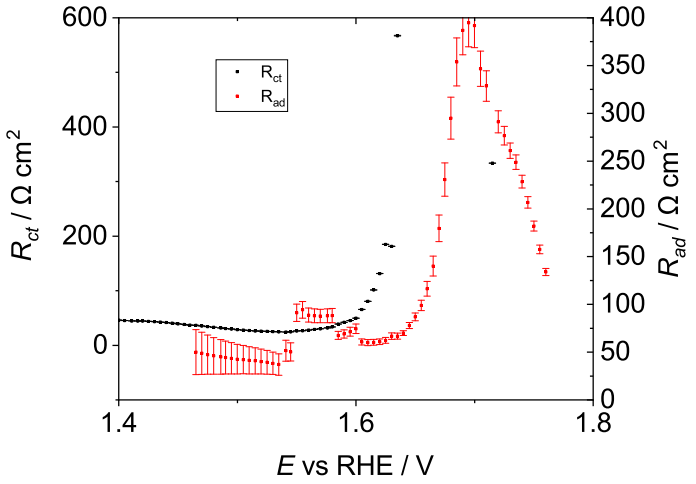

(b) HTS2 temperature order

Figure 5.34: R_{ct} and R_{ad} for room temperature experiments, forward sweep. The sweep rate was 5 mV s^{-1}.

The effective double layer capacitance $C_{dl,eff}$ (Fig. 5.35) determined from the CPE parameter (Section 5.3.3.6) shows that the capacitance decreases significantly as a function of temperature. It does appear that the capacitance increases as a function of oxidation time when comparing the HTS1 and HTS2 temperature order experiments. However, this is expected to some degree as the number of layers of NiOOH are expected to increase as a function of oxidation time. Given that the

NiOOH is a large, porous, three dimensional structure and the data has only been normalized to a two dimensional surface area it follows that the capacitance would appear to increase. The peak seen at approximately 1.4 V coincides with the potential at which NiOOH is expected to begin forming. What is interesting is the existence of a second peak on many of these traces, fairly consistently seen on experiments performed at 40 °C or less. It appears to occur at just over 1.6 V, but in some situations appears as high as 1.7 V. The peak appears to be absent at temperatures 60 °C and above.

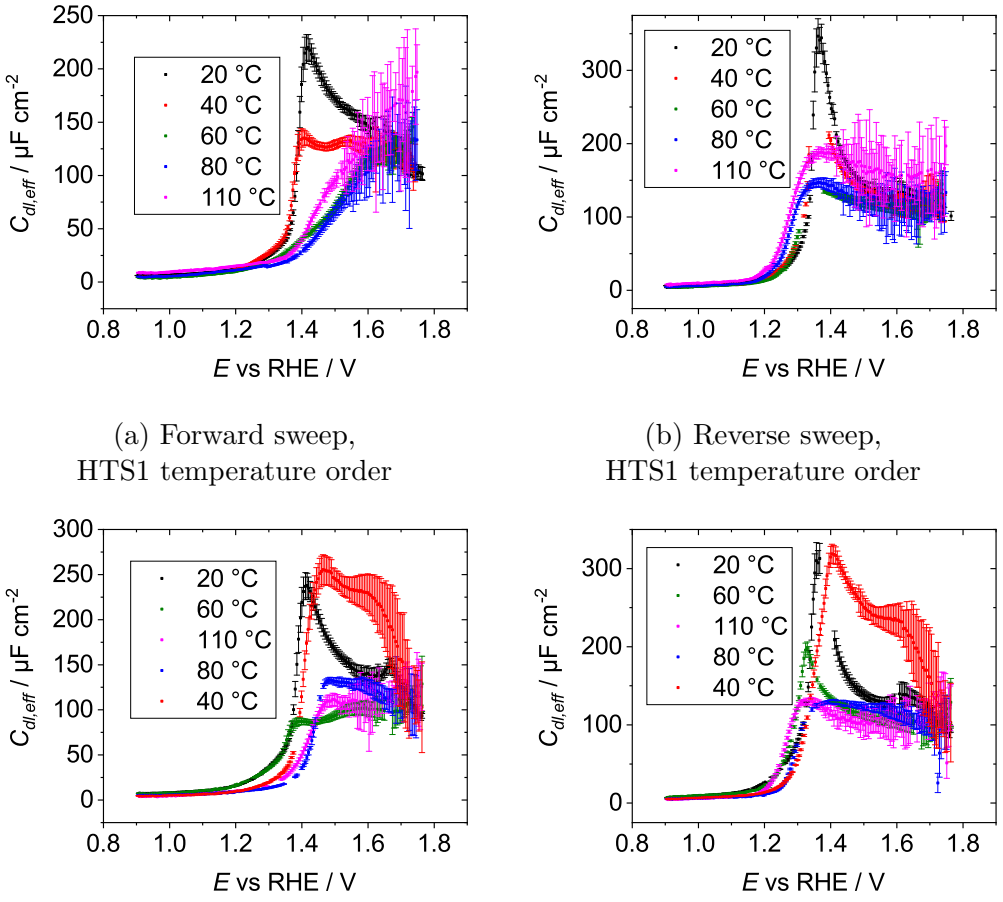

(a) Forward sweep, HTS1 temperature order

(b) Reverse sweep, HTS1 temperature order

(c) Forward sweep, HTS2 temperature order

(d) Reverse sweep, HTS2 temperature order

Figure 5.35: Plots of C_{dl} for glycerol oxidation, HTS1 and HTS2 temperature orders. The sweep rate was 5 mV s^{-1}.

5.4 Conclusions

Cyclic voltammetry was used to determine the effect of temperature on glycerol oxidation onset potential and activity when using a nickel electrode. The effects seen in the CV study were determined to be caused by changes in the electrochemistry of the active phase of nickel oxide, NiOOH. By adjusting CV potentials by the E_r of NiOOH formation, and normalizing by the NiOOH charge density of a corresponding glycerol-free experiment, it can be shown that temperature has very little effect on both the onset potential and activity of glycerol oxidation on nickel.

A mechanistic analysis of glycerol oxidation on nickel was performed as a function of temperature using Tafel analysis, cyclic voltammetry, AC voltammetry, and EIS. The collected data was compared to mechanisms from literature and it was determined that the mechanism of best fit was that proposed by Casella et al [79].

It appears that glycerol oxidation behavior differs between γ-NiOOH and β-NiOOH. Deprotonation of α-$Ni(OH)_2$ to form γ-NiOOH at the oxide surface is slow and as a result the formation of NiOOH on the oxide surface is rate determining at room temperature. As temperature increases this process speeds up, making glycerol adsorption the rate determining step. This exposes γ-NiOOH to the surface and allows it to age to the more crystalline β-NiOOH [177, 186]. When the temperature is subsequently reduced glycerol adsorption remains the rate determining step due to the increased speed of deprotonation of β-NiOOH and the retention of β-NiOOH on the surface.

Chapter 6

Final Remarks

6.1 Conclusions

Product analysis of glycerol electro-oxidation on nickel in alkaline solutions was performed at various temperatures using HPLC. This was achieved using a two-electrode electrochemical cell built within an autoclave, allowing for the heating of solutions beyond their normal boiling point. Through this and literature comparison a reaction pathway for the organic products was determined. Additionally, the effect of temperature on this reaction pathway was studied. At sufficiently high temperatures a polymer was found to form. This polymer product was analysed using DLS, DSC, NMR, and ATR-IR. These tests indicated that the polymer is large and thoroughly cross-linked. Additionally, it appears that the polymer exists in three distinct structures as indicated by the three separate peaks in the DSC traces. This is supported by the DLS evidence, which also shows three distinct groups of peaks. Since DSC pertains to structural composition and DLS pertains to size it appears that the three separate polymeric structures exist in three distinct size regimes, perhaps indicating something about their relative stabilities and reactivities in alkaline solution. ATR-IR and NMR studies indicate a significant presence of ether bonds in the overall polymer structure, as well as some small amount of alkenes. A subsequent analysis of available reactivity in solution suggests that the polymer is to likely be a pseudo-polysaccharide. A pseudo-polysaccharide describes the ATR-IR and NMR results, as well as the overall stability of the polymer product.

An electrochemical study was performed on the various phases of nickel oxide in alkaline solution as a function of temperature. Using a three-electrode electrochemical

cell, cyclic voltammetry, EIS, and various potential holds were used to explore the interconversion between the various nickel oxide phases. Using this methodology it was determined that β-NiOOH is a more active oxygen evolution catalyst than γ-NiOOH. Thermodynamic analysis was performed on the $Ni(OH)_2$/NiOOH oxidation process. This involved experimentally determining the shift in E_r of the reaction as a function of temperature, which had a value of -1.14 mV K^{-1}. This experimentally determined value was then subsequently described using values calculated from Gibb's energies and standard entropies for the possible compounds involved. Pourbaix diagrams from the literature were used to determine these possible oxide phases [189, 190], and reaction candidates were selected. It was determined that while the nickel oxide literature leaves much to be desired, based on current knowledge the following two reactions appear to best match the observed data:

$$\begin{aligned} NiO + 2\,OH^- &\rightleftharpoons NiO_2 + H_2O + 2\,e^- \\ Ni(OH)_2 + 2\,OH^- &\rightleftharpoons NiO_2 + 2\,H_2O + 2\,e^- \end{aligned} \tag{6.1}$$

The aging process of α-$Ni(OH)_2$ to β-$Ni(OH)_2$ was studied as a function of temperature using cyclic voltammetry and EIS. This lead to the observation that β-$Ni(OH)_2$ does not appear to form on the oxide surface at sufficiently high temperatures below 1.2 V.

Temperature dependent kinetic and mechanistic studies were performed on the alkaline glycerol nickel electro-oxidation system. In a cyclic voltammetry study it was determined that temperature has very little effect on the activity of glycerol oxidation on nickel. In order to determine this the shift in E_r as a function of temperature and the charge density of NiOOH had to be accounted for. Mechanistic analysis was performed using a combination of Tafel analysis, cyclic voltammetry, AC voltammetry, and EIS. This study indicates that glycerol oxidation behaves differently on γ-NiOOH and β-NiOOH due to the differing rates of deprotonation of the two oxide phases. It also describes how glycerol can prevent the conversion of γ-NiOOH to β-NiOOH at room temperature and why this behavior is no longer seen as temperature increases. Ultimately, it was determined that the commonly accepted Fleischmann mechanism [21, 22] does not fit the observed data as well as the less commonly referred to Casella mechanism [79].

The results of these projects indicate that this field is heading in a useful, industrially relevant direction. The discovery of a new polymer product represents

a promising path to a commercially viable product. Additionally, the understanding that γ-NiOOH and β-NiOOH have significant effects on the oxidation of glycerol, and likely alcohols in general, is a significant one. These discoveries indicate that this area of research still has much to be discovered and understood. In the future I hope to see significant use of this technology in general, with large glycerol fuel cell reactor plants generating high value products from glycerol alongside hydrogen for use in fuel cells. Currently it is difficult to imagine what the polymer product itself may be used for given the difficulty in manipulating it. However, at the very least once it is scaled up it could be used as a green and possibly biodegradable alternative for packing material.

6.2 Future Work

6.2.1 Product Analysis of High Temperature Electrochemical Oxidation of Glycerol on Nickel

The solution state glycerol oxidation product analysis needs no further study, however the polymer product is still of interest. Some avenues of further exploration include:

(1) Scaling up the polymer synthesis should be the highest priority, though this has proven difficult so far. The understanding of the likely polymer product provided in this document may make this process easier. Workups can be tested on the reaction mixture in an attempt to cause further polymer precipitation. These may include various pH adjustments along with subsequent liquid-liquid extraction with various organic solvents. Protonating the alcohol groups in the pseudo-polysaccharide could result in different solubility behavior.

(2) Many alkaline exchange membranes were tested for use separating the working and counter electrodes but none were found to be stable for the required duration given the experimental conditions necessary for polymer synthesis to occur. For this reason a glass frit was used in the cell. A viable membrane could be less resistive than the frit, allowing for higher current densities to be passed.

(3) The reversible hydrogen electrode used in the three-electrode experiments was often found to become unstable when raised to high temperatures for long periods of time. Determining a viable reference electrode for use at high temperatures on long term experiments would allow for much more electrochemical characterization of the polymer synthesis process.

(4) The autoclave design works quite well for kinetic and mechanistic analysis of various systems, but it is not the optimal setup for maximizing the output of electro-oxidation products. A redesign of the cell with a heavy focus on maximizing polymer product could be worthwhile. This may involve increasing the total volume of the reaction chamber, as well as increasing electrode surface area. A more robust current source may be required to drive the electrochemistry.

6.2.2 A Study of the Phases of Nickel Oxide as a Function of Temperature

The aging process of α-$Ni(OH)_2$ to β-$Ni(OH)_2$ at high temperatures could benefit from a study involving tandem electrochemistry and surface X-ray diffraction. This would allow for structural information on the top few layers of the nickel oxide layer to be collected during the electrochemical studies. The best initial course of action for this would be to re-perform the experiments described in this dissertation exactly as written alongside the X-ray experiment. This would require a full redesign of the cell in order to accommodate X-ray penetration of this cell and would be very non-trivial.

Another useful experiment would involve tandem high temperature EQCM and probe beam diffraction. EQCM experiments can be performed to measure minute changes in the electrode mass during the charging process, and probe beam diffraction experiments can be performed to detect specific species moving in or out of the electrode surface. Combining these experiments could provide significant evidence to further support the claims of this work. Incorporating them into the high-temperature apparatus could prove to be quite challenging, however.

6.2.3 Glycerol Oxidation on Nickel, Mechanistic and Activity Analysis as a Function of Temperature

The high temperature activity and mechanistic studies should be performed using the established methodology to explore the effect of pH on the process. The nickel oxide phases are quite sensitive to both pH and potential, especially in the regime in which these studies were performed [189, 190]. Altering the pH of the reaction could reveal substantially different behavior than what has been explored here.

A study of the effects of glycerol concentration on oxidation currents as a function of temperature should be performed. The oxidation current is related to reagent

concentration according to the Tafel equation.

$$j = nFKC^m \exp\left(\alpha F \frac{\eta}{RT}\right) \tag{6.2}$$

Here j is current density, n is the number of electrons transferred in the reactions, F is Faraday's constant, K is the rate constant of the reaction in s^{-1}, C is reactant concentration, m is an exponent representing the order of the reaction effect of concentration, α is the charge transfer coefficient, η is overpotential, R is the gas constant, and T is absolute temperature. By performing this experiment at various glycerol concentrations the conditions under which glycerol oxidation and oxygen evolution respectively dominate can be further confirmed.

Appendix A

A.1 Detailed fitting data for pEIS data from Section 4.3.1.1

Temp / °C	Circuit	R_s / Ω cm^2	Q_{dl} / 10^{-6} cm^{-2}	α_{dl}	R_{ct} / Ω cm^2	Q_2 / 10^{-6} cm^{-2}	α_2	R_2 / Ω cm^2	C_3 / μF cm^{-2}	Q_3 / 10^{-6} cm^{-2}	α_3	R_3 / Ω cm^2	C_4 / μF cm^{-2}	R_4 / Ω cm^2
20	3	2.31	20.1	0.898	1719	19.2	0.931	53726						
40	4	1.99	14.9	0.878	669.4	32.2	0.758	12316	260.5			10042		
60	4	1.57	16.6	0.867	344.7	42.2	0.747	5647.1	572.1			1827.7		
80	8	1.36	10.8	0.932	274.8	55.6	0.766	2577.9		983.2	0.761	696.96	-1823.3	962.30
100	7	1.34	20.3	0.914	201.3	69.8	0.698	3087.6	498.4			861.63	-3643.2	-474.02
120	7	1.34	20.1	0.901	202.9	105	0.614	354.53	6.627			2463.9	-5651.5	647.94
140	8	1.22	42.3	0.800	1077	23.0	0.855	4859.6		126.6	0.954	7363.4	83.57	14444

Table A.1: 0.6 V pEIS fitting parameters for circuits of best fit on $Ni(OH)_2$ interconversion.

Temp / °C	Circuit	R_s / %	Q_{dl} / %	α_{dl} / %	R_{ct} / %	Q_2 / %	α_2 / %	R_2 / %	C_3 / %	Q_3 / %	α_3 / %	R_3 / %	C_4 / %	R_4 / %
20	3	2.03	5.31	0.694	11.1	6.80	2.14	2.38						
40	4	0.550	1.64	0.193	3.25	2.36	0.906	1.87	3.01			1.82		
60	4	0.917	2.90	0.330	4.80	4.09	1.36	2.67	11.5			6.81		
80	8	0.445	1.57	0.167	2.32	4.57	1.35	4.12		24.4	6.85	17.7	5.50	5.70
100	7	0.683	3.37	0.366	7.49	6.30	2.13	4.85	18.1			12.6	19.7	12.1
120	7	0.885	4.56	0.490	11.4	2.41	3.00	49.5	22.5			6.61	11.7	24.0
140	8	2.35	5.25	0.679	22.2	48.9	15.4	33.9		15.0	21.5	36.5	13.8	7.54

Table A.2: Relative standard errors corresponding to 0.6 V pEIS fitting parameters for circuits of best fit on $Ni(OH)_2$ interconversion.

Temp / °C	Circuit	R_s / Ω cm^2	Q_{dl} / 10^{-6} cm^{-2}	α_{dl}	R_{ct} / Ω cm^2	C_2 / μF cm^{-2}	Q_2 / 10^{-6} cm^{-2}	α_2	R_2 / Ω cm^2	C_3 / μF cm^{-2}	Q_3 / 10^{-6} cm^{-2}	α_3	R_3 / Ω cm^2	C_4 / μF cm^{-2}	R_4 / Ω cm^2
20	3	2.38	182	0.829	15210		352	0.905	28001						
40	6	2.12	187	0.855	27.271		92.2	0.439	1036.2		111.9	0.884	20072		
60	5	1.70	208	0.841	427.71		277	0.819	11012	1199			4929.7		
80	8	1.43	77.9	0.868	231.14		129	0.901	233.48		278.3	0.847	5916.3	1269	3335
100	5	1.35	68.4	0.825	185.16		466	0.750	4652.6	3589			3124.1		
120	6	1.48	58.8	0.825	320.04		419	0.843	2349.3		2369	0.815	2252.6		
140	5	1.69	185	0.736	917.29	202			3399.1	1310			6366.4		

Table A.3: 1.2 V pEIS fitting parameters for circuits of best fit on $Ni(OH)_2$ interconversion.

Temp / °C	Circuit	R_s / %	Q_{dl} / %	α_{dl} / %	R_{ct} / %	C_2 / %	Q_2 / %	α_2 / %	R_2 / %	C_3 / %	Q_3 / %	α_3 / %	R_3 / %	C_4 / %	R_4 / %
20	3	1.07	1.55	0.323	9.36		27.9	11.6	20.6						
40	6	0.321	6.14	0.700	969		30.3	23.6	30.6		4.81	10.6	10.6		
60	5	0.447	1.71	0.272	4.21		2.57	1.71	8.47	21.3			14.4		
80	8	0.604	3.68	0.457	12.3		5.76	37.2	9.57		5.72	11.5	8.78	14.3	11.3
100	5	1.38	4.11	0.557	3.41		2.73	1.77	6.72	14.9			10.0		
120	6	0.832	2.08	0.288	1.83		4.31	2.25	10.1		31.4	11.2	18.2		
140	5	4.00	7.39	1.30	12.1	11.2			10.9	16.6			13.2		

Table A.4: Relative standard errors corresponding to 1.2 V pEIS fitting parameters for circuits of best fit on $Ni(OH)_2$ interconversion.

References

[1] T. Holm, P. K. Dahlstrom, S. Sunde, D. A. Harrington, F. Seland, Method for studying high temperature aqueous electrochemical systems: A self pressurized autoclave, ECS Transactions 75 (14) (2016) 1055–1061. doi:10.1149/07514.1055ecst.

[2] W. M. Flarsheim, Y. M. Tsou, I. Trachtenberg, K. P. Johnston, A. J. Bard, Electrochemistry in near-critical and supercritical fluids. 3. studies of bromide, iodide, and hydroquinone in aqueous solutions, The Journal of Physical Chemistry 90 (16) (1986) 3857–3862. doi:10.1021/j100407a066.

[3] A. C. Mcdonald, F. R. F. Fan, A. J. Bard, Electrochemistry in near-critical and supercritical fluids. 2. water. experimental techniques and the copper(II) system, The Journal of Physical Chemistry 90 (1) (1986) 196–202. doi:10.1021/j100273a044.

[4] A. J. Bard, W. M. Flarsheim, K. P. Johnston, High-pressure electrochemical oxidation of benzene at a lead dioxide electrode in aqueous bisulfate solutions at 25° to 250°c, Journal of The Electrochemical Society 135 (8) (1988) 1939–1944. doi:10.1149/1.2096184.

[5] P. Kritzer, Corrosion in high-temperature and supercritical water and aqueous solutions: A review, The Journal of Supercritical Fluids 29 (1-2) (2004) 1–29. doi:10.1016/s0896-8446(03)00031-7.

[6] I. Perissi, U. Bardi, S. Caporali, A. Lavacchi, High temperature corrosion properties of ionic liquids, Corrosion Science 48 (9) (2006) 2349–2362. doi:10.1016/j.corsci.2006.06.010.

[7] C. A. C. Sequeira, High Temperature Corrosion: Fundamentals and Engineering, WILEY, 2019.

URL https://www.ebook.de/de/product/34644294/cesar_a_c_sequeira_high_temperature_corrosion_fundamentals_and_engineering.html

[8] T. Holm, P. K. Dahlstrøm, O. S. Burheim, S. Sunde, D. A. Harrington, F. Seland, Method for studying high temperature aqueous electrochemical systems: Methanol and glycerol oxidation, Electrochimica Acta 222 (2016) 1792–1799. doi:10.1016/j.electacta.2016.11.130.

[9] G. Wildgoose, D. Giovanelli, N. Lawrence, R. Compton, High-temperature electrochemistry: A review, Electroanalysis 16 (6) (2004) 421–433. doi:10.1002/elan.200302875.

[10] V. Oliveira, C. Morais, K. Servat, T. Napporn, G. Tremiliosi-filho, K. Kokoh, Glycerol oxidation on nickel based nanocatalysts in alkaline medium – identification of the reaction products, Journal of Electroanalytical Chemistry 703 (2013) 56–62. doi:10.1016/j.jelechem.2013.05.021.

[11] J. C. B. Prieto, J. Pecha, V. Kašpárková, K. Kolomazník, Development of an HPLC method for the determination of glycerol oxidation products, Journal of Liquid Chromatography & Related Technologies 36 (19) (2013) 2758–2773. arXiv:https://www.tandfonline.com/doi/pdf/10.1080/10826076.2012.725695, doi:10.1080/10826076.2012.725695.
URL https://www.tandfonline.com/doi/abs/10.1080/10826076.2012.725695

[12] R. Barnard, C. F. Randell, Studies concerning charged nickel hydroxide electrodes. VI. voltammetric behaviour for pre-cycled electrodes, Journal of Applied Electrochemistry 13 (1) (1983) 27–38. doi:10.1007/bf00615885.

[13] R. Barnard, C. Randell, F. Tye, Studies concerning charged nickel hydroxide electrodes, Journal of Electroanalytical Chemistry and Interfacial Electrochemistry 119 (1) (1981) 17–24. doi:10.1016/s0022-0728(81)80120-9.

[14] R. Barnard, C. F. Randell, F. L. Tye, Studies concerning charged nickel hydroxide electrodes i. measurement of reversible potentials, Journal of Applied Electrochemistry 10 (1) (1980) 109–125. doi:10.1007/bf00937345.

[15] R. Barnard, C. F. Randell, F. L. Tye, Studies concerning charged nickel hydroxide electrodes. II. thermodynamic considerations of the reversible potentials, Journal of Applied Electrochemistry 10 (1) (1980) 127–141. doi:10.1007/bf00937346.

[16] G. W. D. Briggs, M. Fleischmann, Oxidation and reduction of nickel hydroxide at constant potential, Transactions of the Faraday Society 67 (1971) 2397. doi:10.1039/tf9716702397.

[17] G. W. D. Briggs, W. F. K. W. Jones, The nickel oxide electrode. part 3, Transactions of the Faraday Society 52 (1956) 1272. doi:10.1039/tf9565201272.

[18] G. W. D. Briggs, E. Jones, W. F. K. W. Jones, The nickel oxide electrode. part 1., Transactions of the Faraday Society 51 (1955) 1433. doi:10.1039/tf9555101433.

[19] H. M. French, M. J. Henderson, A. Hillman, E. Vieil, Ion and solvent transfer discrimination at a nickel hydroxide film exposed to LiOH by combined electrochemical quartz crystal microbalance (EQCM) and probe beam deflection (PBD) techniques, Journal of Electroanalytical Chemistry 500 (1-2) (2001) 192–207. doi:10.1016/s0022-0728(00)00373-9.

[20] M. S. Houache, E. Cossar, S. Ntais, E. A. Baranova, Electrochemical modification of nickel surfaces for efficient glycerol electrooxidation, Journal of Power Sources 375 (2018) 310–319. doi:10.1016/j.jpowsour.2017.08.089.

[21] M. Fleischmann, K. Korinek, D. Pletcher, The kinetics and mechanism of the oxidation of amines and alcohols at oxide-covered nickel, silver, copper, and cobalt electrodes, Journal of the Chemical Society, Perkin Transactions 2 1 (10) (1972) 1396. doi:10.1039/p29720001396.

[22] M. Fleischmann, K. Korinek, D. Pletcher, The oxidation of organic compounds at a nickel anode in alkaline solution, Journal of Electroanalytical Chemistry and Interfacial Electrochemistry 31 (1) (1971) 39–49. doi:10.1016/s0022-0728(71)80040-2.

[23] D. T. Johnson, K. A. Taconi, The glycerin glut: Options for the value-added conversion of crude glycerol resulting from biodiesel production, Environmental Progress 26 (4) (2007) 338–348. doi:10.1002/ep.10225.

[24] EPA, Final renewable fuel standards for 2020, https://www.epa.gov/renewable-fuel-standard-program/final-renewable-fuel-standards-2020-and-biomass-based-diesel-volume, accessed November 19th 2020 (2020).

[25] H. Tan, A. A. Aziz, M. Aroua, Glycerol production and its applications as a raw material: A review, Renewable and Sustainable Energy Reviews 27 (2013) 118–127. doi:10.1016/j.rser.2013.06.035.

[26] J. I. García, H. G. Marín, E. Pires, Glycerol based solvents: Synthesis, properties and applications, Green Chem. 16 (3) (2014) 1007–1033. doi:10.1039/c3gc41857j.

[27] M. S. E. Houache, K. Hughes, A. Ahmed, R. Safari, H. Liu, G. A. Botton, E. A. Baranova, Electrochemical valorization of glycerol on Ni-rich bimetallic NiPd nanoparticles: Insight into product selectivity using in situ polarization modulation infrared-reflection absorption spectroscopy, ACS Sustainable Chemistry & Engineering 7 (17) (2019) 14425–14434. doi:10.1021/acssuschemeng.9b01070.

[28] M. S. E. Houache, K. Hughes, E. A. Baranova, Study on catalyst selection for electrochemical valorization of glycerol, Sustainable Energy & Fuels 3 (8) (2019) 1892–1915. doi:10.1039/c9se00108e.

[29] Z. Xiu, H. Wang, C. Cai, C. Li, L. Yan, C. Wang, W. Li, H. Xin, C. Zhu, Q. Zhang, Q. Liu, L. Ma, Ultrafast glycerol conversion to lactic acid over magnetically recoverable Ni–NiOx@C catalysts, Industrial & Engineering Chemistry Research 59 (21) (2020) 9912–9925. doi:10.1021/acs.iecr.0c01145.

[30] X. Fan, R. Burton, Y. Zhou, Glycerol (byproduct of biodiesel production) as a source for fuels and chemicals - mini review, The Open Fuels & Energy Science Journal 3 (1) (2010) 17–22. doi:10.2174/1876973x01003010017.

[31] Y. Mu, H. Teng, D. J. Zhang, W. Wang, Z. L. Xiu, Microbial production of 1,3-propanediol by klebsiella pneumoniae using crude glycerol from biodiesel preparations, Biotechnology Letters 28 (21) (2006) 1755–1759. doi:10.1007/s10529-006-9154-z.

[32] M. Watanabe, T. Iida, Y. Aizawa, T. M. Aida, H. Inomata, Acrolein synthesis from glycerol in hot-compressed water, Bioresource Technology 98 (6) (2007) 1285–1290. doi:10.1016/j.biortech.2006.05.007.

[33] N. Benipal, J. Qi, J. C. Gentile, W. Li, Direct glycerol fuel cell with polytetrafluoroethylene (PTFE) thin film separator, Renewable Energy 105 (2017) 647–655. doi:10.1016/j.renene.2016.12.028.

[34] P. Sangkheaw, S. Therdthianwong, A. Therdthianwong, N. Wongyao, S. Yongprapat, Enhancement of anode performance for alkaline-acid direct glycerol fuel cells, Renewable Energy 161 (2020) 395–407. doi:10.1016/j.renene.2020.07.069.

[35] A. C. Garcia, M. J. Kolb, C. V. N. Y. Sanchez, J. Vos, Y. Y. Birdja, Y. Kwon, G. T. Filho, M. T. M. Koper, Strong impact of platinum surface structure on primary and secondary alcohol oxidation during electro-oxidation of glycerol, ACS Catalysis 6 (7) (2016) 4491–4500. doi:10.1021/acscatal.6b00709.

[36] J. R. Mcmanus, E. Martono, J. M. Vohs, Reaction of glyceraldehyde and glucose on zn-modified pt(111) surfaces, Catalysis Today 237 (2014) 157–165. doi:10.1016/j.cattod.2013.11.010.

[37] I. Takigawa, K. I. Shimizu, K. Tsuda, S. Takakusagi, Machine-learning prediction of the d-band center for metals and bimetals, RSC Advances 6 (58) (2016) 52587–52595. doi:10.1039/c6ra04345c.

[38] Y. Kwon, S. C. S. Lai, P. Rodriguez, M. T. M. Koper, Electrocatalytic oxidation of alcohols on gold in alkaline media: Base or gold catalysis?, Journal of the American Chemical Society 133 (18) (2011) 6914–6917. doi:10.1021/ja200976j.

[39] C. S. Lee, M. K. Aroua, W. A. W. Daud, P. Cognet, Y. Pérès, M. A. Ajeel, Selective electrochemical conversion of glycerol to glycolic acid and lactic acid on a mixed carbon-black activated carbon electrode in a single

compartment electrochemical cell, Frontiers in Chemistry 7 (Mar. 2019). doi:10.3389/fchem.2019.00110.

[40] C. Coutanceau, S. Baranton, Electrochemical conversion of alcohols for hydrogen production: A short overview, Wiley Interdisciplinary Reviews: Energy and Environment 5 (4) (2016) 388–400. doi:10.1002/wene.193.

[41] K. I. Ozoemena, Nanostructured platinum-free electrocatalysts in alkaline direct alcohol fuel cells: Catalyst design, principles and applications, RSC Advances 6 (92) (2016) 89523–89550. doi:10.1039/c6ra15057h.

[42] L. S. Ribeiro, E. G. Rodrigues, J. J. Delgado, X. Chen, M. F. R. Pereira, J. J. M. Órfão, Pd, pt, and pt–cu catalysts supported on carbon nanotube (CNT) for the selective oxidation of glycerol in alkaline and base-free conditions, Industrial & Engineering Chemistry Research 55 (31) (2016) 8548–8556. doi:10.1021/acs.iecr.6b01732.

[43] O. Muneeb, J. Estrada, L. Tran, K. Nguyen, J. Flores, S. Hu, A. M. F. Petit, L. Scudiero, S. Ha, J. L. Haan, Electrochemical oxidation of polyalcohols in alkaline media on palladium catalysts promoted by the addition of copper, Electrochimica Acta 218 (2016) 133–139. doi:10.1016/j.electacta.2016.09.105.

[44] E. Habibi, H. Razmi, Glycerol electrooxidation on pd, pt and au nanoparticles supported on carbon ceramic electrode in alkaline media, International Journal of Hydrogen Energy 37 (22) (2012) 16800–16809. doi:10.1016/j.ijhydene.2012.08.127.

[45] B. Wang, L. Tao, Y. Cheng, F. Yang, Y. Jin, C. Zhou, H. Yu, Y. Yang, Electrocatalytic oxidation of small molecule alcohols over pt, pd, and au catalysts: The effect of alcohol's hydrogen bond donation ability and molecular structure properties, Catalysts 9 (4) (2019) 387. doi:10.3390/catal9040387.

[46] C. Bianchini, P. K. Shen, Palladium-based electrocatalysts for alcohol oxidation in half cells and in direct alcohol fuel cells, Chemical Reviews 109 (9) (2009) 4183–4206. doi:10.1021/cr9000995.

[47] A. Zalineeva, S. Baranton, C. Coutanceau, How do bi-modified palladium nanoparticles work towards glycerol electrooxidation? an in situ FTIR study,

Electrochimica Acta 176 (2015) 705–717. doi:10.1016/j.electacta.2015.07.073.

[48] X. Shi, D. E. Simpson, D. Roy, The role of chemisorbed hydroxyl species in alkaline electrocatalysis of glycerol on gold, Physical Chemistry Chemical Physics 17 (17) (2015) 11432–11444. doi:10.1039/c5cp00313j.

[49] Y. Chen, L. Zhuang, J. Lu, Non-pt anode catalysts for alkaline direct alcohol fuel cells, Chinese Journal of Catalysis 28 (10) (2007) 870–874. doi:10.1016/s1872-2067(07)60073-4.

[50] B. N. Zope, D. D. Hibbitts, M. Neurock, R. J. Davis, Reactivity of the gold/water interface during selective oxidation catalysis, Science 330 (6000) (2010) 74–78. doi:10.1126/science.1195055.

[51] R. Kannan, A. R. Kim, D. J. Yoo, Enhanced electrooxidation of methanol, ethylene glycol, glycerol, and xylitol over a polypyrrole/manganese oxyhydroxide/palladium nanocomposite electrode, Journal of Applied Electrochemistry 44 (8) (2014) 893–902. doi:10.1007/s10800-014-0706-y.

[52] C. A. Ottoni, S. G. D. Silva, R. F. B. D. Souza, A. O. Neto, Glycerol oxidation reaction using PdAu/c electrocatalysts, Ionics 22 (7) (2016) 1167–1175. doi:10.1007/s11581-015-1631-8.

[53] Z. Zhang, L. Xin, W. Li, Supported gold nanoparticles as anode catalyst for anion-exchange membrane-direct glycerol fuel cell (AEM-DGFC), International Journal of Hydrogen Energy 37 (11) (2012) 9393–9401. doi:10.1016/j.ijhydene.2012.03.019.

[54] J. L. B. Neto, A. C. Garcia, V. L. Oliveira, N. E. D. Souza, G. T. Filho, Au/c catalysts prepared by a green method towards c3 alcohol electrooxidation: A cyclic voltammetry and in situ FTIR spectroscopy study, Journal of Electroanalytical Chemistry 735 (2014) 57–62. doi:10.1016/j.jelechem.2014.10.010.

[55] P. Sivasakthi, M. V. Sangaranarayanan, Pulse electrodeposited nickel with structure directing agents as an electrocatalyst for oxidation of glycerol, New Journal of Chemistry 43 (21) (2019) 8352–8362. doi:10.1039/c9nj01351b.

[56] M. Alsabet, M. Grdeń, G. Jerkiewicz, Electrochemical growth of surface oxides on nickel. part 3: Formation of β-NiOOH in relation to the polarization potential, polarization time, and temperature, Electrocatalysis 6 (1) (2014) 60–71. doi:10.1007/s12678-014-0214-1.

[57] P. L. Bourgault, B. E. Conway, The electrochemical behavior of the nickel oxide electrode: Part ii. quasi-equilibrium behavior, Canadian Journal of Chemistry 38 (9) (1960) 1557–1575. doi:10.1139/v60-216.

[58] M. S. E. Houache, K. Hughes, R. Safari, G. A. Botton, E. A. Baranova, Modification of nickel surfaces by bismuth: Effect on electrochemical activity and selectivity toward glycerol, ACS Applied Materials & Interfaces 12 (13) (2020) 15095–15107. doi:10.1021/acsami.9b22378.

[59] Kinoshita, Oxygen Technology, John Wiley & Sons, 1992.
URL https://www.ebook.de/de/product/4245318/kinoshita_oxygen_technology.html

[60] M. E. G. Lyons, M. P. Brandon, The oxygen evolution reaction on passive oxide covered transition metal electrodes in aqueous alkaline solution. part 1-nickel, Int. J. Electrochem. Sci. (2008) 1386–1424.

[61] A. J. Tkalych, J. M. P. Martirez, E. A. Carter, Effect of transition-metal-ion dopants on the oxygen evolution reaction on NiOOH(0001), Physical Chemistry Chemical Physics 20 (29) (2018) 19525–19531. doi:10.1039/c8cp02849d.

[62] A. J. Tkalych, K. Yu, E. A. Carter, Structural and electronic features of β-$Ni(OH)_2$ and β-NiOOH from first principles, The Journal of Physical Chemistry C 119 (43) (2015) 24315–24322. doi:10.1021/acs.jpcc.5b08481.

[63] Y. F. Li, A. Selloni, Mechanism and activity of water oxidation on selected surfaces of pure and Fe-doped NiOx, ACS Catalysis 4 (4) (2014) 1148–1153. doi:10.1021/cs401245q.

[64] S. R. Mellsop, A. Gardiner, B. Johannessen, A. T. Marshall, Structure and transformation of oxy-hydroxide films on ni anodes below and above the oxygen evolution potential in alkaline electrolytes, Electrochimica Acta 168 (2015) 356–364. doi:10.1016/j.electacta.2015.04.020.

[65] L. F. Li, Y. F. Li, Z. P. Liu, Oxygen evolution activity on NiOOH catalysts: Four-coordinated Ni cation as the active site and the hydroperoxide mechanism, ACS Catalysis 10 (4) (2020) 2581–2590. doi:10.1021/acscatal.9b04975.

[66] D. K. Bediako, Y. Surendranath, D. G. Nocera, Mechanistic studies of the oxygen evolution reaction mediated by a nickel–borate thin film electrocatalyst, Journal of the American Chemical Society 135 (9) (2013) 3662–3674. doi:10.1021/ja3126432.

[67] D. K. Bediako, B. L. Kaiser, Y. Surendranath, J. Yano, V. K. Yachandra, D. G. Nocera, Structure–activity correlations in a nickel–borate oxygen evolution catalyst, Journal of the American Chemical Society 134 (15) (2012) 6801–6809. doi:10.1021/ja301018q.

[68] L. Trotochaud, S. L. Young, J. K. Ranney, S. W. Boettcher, Nickel–iron oxyhydroxide oxygen-evolution electrocatalysts: The role of intentional and incidental iron incorporation, Journal of the American Chemical Society 136 (18) (2014) 6744–6753. doi:10.1021/ja502379c.

[69] V. Oliveira, C. Morais, K. Servat, T. Napporn, G. T. Filho, K. Kokoh, Studies of the reaction products resulted from glycerol electrooxidation on Ni-based materials in alkaline medium, Electrochimica Acta 117 (2014) 255–262. doi:10.1016/j.electacta.2013.11.127.

[70] V. L. Oliveira, C. Morais, K. Servat, T. W. Napporn, P. Olivi, K. B. Kokoh, G. T. Filho, Kinetic investigations of glycerol oxidation reaction on Ni/C, Electrocatalysis 6 (5) (2015) 447–454. doi:10.1007/s12678-015-0261-2.

[71] X. Liang, M. Xiao, M. Xu, D. Yang, Y. Yan, Y. Tian, Y. Miao, Simultaneous in situ formation of ni-based catalysts at the anode for glycerol oxidation and at the cathode for hydrogen evolution, Journal of Applied Electrochemistry 46 (1) (2015) 1–8. doi:10.1007/s10800-015-0888-y.

[72] C. Dai, L. Sun, H. Liao, B. Khezri, R. D. Webster, A. C. Fisher, Z. J. Xu, Electrochemical production of lactic acid from glycerol oxidation catalyzed by AuPt nanoparticles, Journal of Catalysis 356 (2017) 14–21. doi:10.1016/j.jcat.2017.10.010.

[73] F. Auneau, S. Noël, G. Aubert, M. Besson, L. Djakovitch, C. Pinel, On the role of the atmosphere in the catalytic glycerol transformation over iridium-based catalysts, Catalysis Communications 16 (1) (2011) 144–149. doi:10.1016/j.catcom.2011.09.011.

[74] D. Roy, B. Subramaniam, R. V. Chaudhari, Cu-based catalysts show low temperature activity for glycerol conversion to lactic acid, ACS Catalysis 1 (5) (2011) 548–551. doi:10.1021/cs200080j.

[75] L. S. Sharninghausen, J. Campos, M. G. Manas, R. H. Crabtree, Efficient selective and atom economic catalytic conversion of glycerol to lactic acid, Nature Communications 5 (1) (2014). doi:10.1038/ncomms6084.

[76] J. G. Chang, H. T. Chen, S. Xu, M. C. Lin, Computational study on the kinetics and mechanisms for the unimolecular decomposition of formic and oxalic acids, The Journal of Physical Chemistry A 111 (29) (2007) 6789–6797. doi:10.1021/jp069036p.

[77] F. D. Chattaway, XX.—interaction of glycerol and oxalic acid, J. Chem. Soc., Trans. 105 (0) (1914) 151–156. doi:10.1039/ct9140500151.

[78] S. Berchmans, H. Gomathi, G. Rao, Electrooxidation of alcohols and sugars catalysed on a nickel oxide modified glassy carbon electrode, Journal of Electroanalytical Chemistry 394 (1-2) (1995) 267–270. doi:10.1016/0022-0728(95)04099-a.

[79] I. G. Casella, T. R. I. Cataldi, A. M. Salvi, E. Desimoni, Electrocatalytic oxidation and liquid chromatographic detection of aliphatic alcohols at a nickel-based glassy carbon modified electrode, Analytical Chemistry 65 (21) (1993) 3143–3150. doi:10.1021/ac00069a032.

[80] G. Vértes, G. Horányi, Some problems of the kinetics of the oxidation of organic compounds at oxide-covered nickel electrodes, Journal of Electroanalytical Chemistry and Interfacial Electrochemistry 52 (1) (1974) 47–53. doi:10.1016/s0022-0728(74)80100-2.

[81] A. E. Shafei, Electrocatalytic oxidation of methanol at a nickel hydroxide/glassy carbon modified electrode in alkaline medium, Journal of Electroanalytical Chemistry 471 (2) (1999) 89–95. doi:10.1016/s0022-0728(99)00235-1.

[82] P. Robertson, On the oxidation of alcohols and amines at nickel oxide electrodes: Mechanistic aspects, Journal of Electroanalytical Chemistry and Interfacial Electrochemistry 111 (1) (1980) 97–104. doi:10.1016/s0022-0728(80)80079-9.

[83] J. Taraszewska, G. Rosłonek, Electrocatalytic oxidation of methanol on a glassy carbon electrode modified by nickel hydroxide formed by ex situ chemical precipitation, Journal of Electroanalytical Chemistry 364 (1-2) (1994) 209–213. doi:10.1016/0022-0728(93)02919-9.

[84] M. S. Kim, T. S. Hwang, K. B. Kim, A study of the electrochemical redox behavior of electrochemically precipitated nickel hydroxides using electrochemical quartz crystal microbalance, Journal of The Electrochemical Society 144 (5) (1997) 1537–1543. doi:10.1149/1.1837637.

[85] D. S. Hall, D. J. Lockwood, C. Bock, B. R. Macdougall, Nickel hydroxides and related materials: A review of their structures, synthesis and properties, Proceedings of the Royal Society A: Mathematical, Physical and Engineering Sciences 471 (2174) (2015) 20140792. doi:10.1098/rspa.2014.0792.

[86] Besenhard, Handbook of Battery Materials, Wiley-VCH, Weinheim New York, 1999.

[87] C. S. Yudha, S. U. Muzayanha, H. Widiyandari, F. Iskandar, W. Sutopo, A. Purwanto, Synthesis of LiNi0.85Co0.14Al0.01O2 cathode material and its performance in an NCA/graphite full-battery, Energies 12 (10) (2019) 1886. doi:10.3390/en12101886.

[88] R. A. Huggins, Advanced Batteries, Springer US, 2009. doi:10.1007/978-0-387-76424-5.

[89] M. Kiani, M. Mousavi, S. Ghasemi, Size effect investigation on battery performance: Comparison between micro- and nano-particles of β-$Ni(OH)_2$ as nickel battery cathode material, Journal of Power Sources 195 (17) (2010) 5794–5800. doi:10.1016/j.jpowsour.2010.03.080.

[90] B. Battke, T. S. Schmidt, D. Grosspietsch, V. H. Hoffmann, A review and probabilistic model of lifecycle costs of stationary batteries in multiple

applications, Renewable and Sustainable Energy Reviews 25 (2013) 240–250. doi:10.1016/j.rser.2013.04.023.

[91] H. Bode, K. Dehmelt, J. Witte, Zur kenntnis der nickelhydroxidelektrode—i.Über das nickel (II)-hydroxidhydrat, Electrochimica Acta 11 (8) (1966) 1079–1087. doi:10.1016/0013-4686(66)80045-2.

[92] M. Alsabet, M. Grden, G. Jerkiewicz, Electrochemical growth of surface oxides on nickel. part 2: Formation of β-$Ni(OH)_2$ and NiO in relation to the polarization potential, polarization time, and temperature, Electrocatalysis 5 (2) (2013) 136–147. doi:10.1007/s12678-013-0172-z.

[93] S. Medway, C. Lucas, A. Kowal, R. Nichols, D. Johnson, In situ studies of the oxidation of nickel electrodes in alkaline solution, Journal of Electroanalytical Chemistry 587 (1) (2006) 172–181. doi:10.1016/j.jelechem.2005.11.013.

[94] N. F. Mott, The basis of the electron theory of metals, with special reference to the transition metals, Proceedings of the Physical Society. Section A 62 (7) (1949) 416–422. doi:10.1088/0370-1298/62/7/303.

[95] L. Burke, T. Twomey, Voltammetric behaviour of nickel in base with particular reference to thick oxide growth, Journal of Electroanalytical Chemistry and Interfacial Electrochemistry 162 (1-2) (1984) 101–119. doi:10.1016/s0022-0728(84)80158-8.

[96] P. Häring, R. Kötz, Nanoscale thickness changes of nickel hydroxide films during electrochemical oxidation/reduction monitored by in situ atomic force microscopy, Journal of Electroanalytical Chemistry 385 (2) (1995) 273–277. doi:10.1016/0022-0728(94)03869-5.

[97] G. Barral, F. N. Eyoke, S. Maximovitch, Characterisation of the passive layer and of hydroxide deposits of nickel by impedance spectroscopy, Electrochimica Acta 40 (17) (1995) 2815–2828. doi:10.1016/0013-4686(95)00274-i.

[98] G. Barral, S. Maximovitch, F. N. Eyoke, Study of electrochemically formed $Ni(OH)_2$ layers by EIS, Electrochimica Acta 41 (7-8) (1996) 1305–1311. doi:10.1016/0013-4686(95)00451-3.

[99] A. Kowal, R. Niewiara, B. Perończyk, J. Haber, In situ atomic force microscopy observation of change in thickness of nickel hydroxide layer on ni electrode, Langmuir 12 (10) (1996) 2332–2333. doi:10.1021/la9515229.

[100] R. S. S. Guzmán, J. R. Vilche, A. J. Arvía, Rate processes related to the hydrated nickel hydroxide electrode in alkaline solutions, Journal of The Electrochemical Society 125 (10) (1978) 1578–1587. doi:10.1149/1.2131247.

[101] P. Oliva, J. Leonardi, J. Laurent, C. Delmas, J. Braconnier, M. Figlarz, F. Fievet, A. Guibert, Review of the structure and the electrochemistry of nickel hydroxides and oxy-hydroxides, Journal of Power Sources 8 (2) (1982) 229–255. doi:10.1016/0378-7753(82)80057-8.

[102] M. Alsabet, M. Grden, G. Jerkiewicz, Electrochemical growth of surface oxides on nickel. part 1: Formation of α-Ni$(OH)_2$ in relation to the polarization potential, polarization time, and temperature, Electrocatalysis 2 (4) (2011) 317–330. doi:10.1007/s12678-011-0067-9.

[103] B. Beden, D. Floner, J. Léger, C. Lamy, A voltammetric study of the formation on hydroxides and oxyhydroxides on nickel single crystal electrodes in contact with an alkaline solution, Surface Science 162 (1-3) (1985) 822–829. doi:10.1016/0039-6028(85)90985-9.

[104] M. Danczuk, C. V. Nunes, K. Araki, F. J. Anaissi, Influence of alkaline cation on the electrochemical behavior of stabilized α-Ni$(OH)_2$, Journal of Solid State Electrochemistry 18 (8) (2014) 2279–2287. doi:10.1007/s10008-014-2478-z.

[105] F. Flevet, Preparation and study by electron microscopy of the development of texture with temperature of a porous exhydroxide nickel oxide, Journal of Catalysis 39 (3) (1975) 350–356. doi:10.1016/0021-9517(75)90300-0.

[106] S. C. Jung, S. L. Sim, Y. W. Soon, C. M. Lim, P. Hing, J. R. Jennings, Synthesis of nanostructuredβ-ni(OH)2by electrochemical dissolution–precipitation and its application as a water oxidation catalyst, Nanotechnology 27 (27) (2016) 275401. doi:10.1088/0957-4484/27/27/275401.

[107] L. D. Souza, F. Kong, F. Mclarnon, R. Muller, Spectroscopic ellipsometry study of nickel oxidation in alkaline solution, Electrochimica Acta 42 (8) (1997) 1253–1267. doi:10.1016/s0013-4686(96)00298-8.

[108] Z. I. Kudryavtseva, L. A. Burkal'tseva, A. G. Pshenichnikov, Surface properties of nickel electrodes in an alkaline electrolyte: An ellipsometry study, Russian Journal of Electrochemistry 40 (11) (2004) 1208–1213. doi:10.1023/b:ruel.0000048656.31084.12.

[109] B. Habibi, N. Delnavaz, Electrooxidation of glycerol on nickel and nickel alloy (ni–cu and ni–co) nanoparticles in alkaline media, RSC Advances 6 (38) (2016) 31797–31806. doi:10.1039/c5ra26006j.

[110] R. Huggins, H. Prinz, M. Wohlfahrtmehrens, L. Jorissen, W. Witschel, Proton insertion reactions in layered transition metal oxides, Solid State Ionics 70-71 (1994) 417–424. doi:10.1016/0167-2738(94)90347-6.

[111] D. M. Macarthur, The proton diffusion coefficient for the nickel hydroxide electrode, Journal of The Electrochemical Society 117 (6) (1970) 729. doi:10.1149/1.2407618.

[112] S. Motupally, C. C. Streinz, J. W. Weidner, Proton diffusion in nickel hydroxide: Prediction of active material utilization, Journal of The Electrochemical Society 145 (1) (1998) 29–34. doi:10.1149/1.1838205.

[113] J. W. Weidner, P. Timmerman, Effect of proton diffusion, electron conductivity, and charge-transfer resistance on nickel hydroxide discharge curves, Journal of The Electrochemical Society 141 (2) (1994) 346–351. doi:10.1149/1.2054729.

[114] Y. Mo, E. Hwang, D. A. Scherson, In situ quartz crystal microbalance studies of nickel hydrous oxide films in alkaline electrolytes, Journal of The Electrochemical Society 143 (1) (1996) 37–43. doi:10.1149/1.1836384.

[115] H. French, Temporal resolution of ion and solvent transfers at nickel hydroxide films exposed to LiOH, Solid State Ionics 150 (1-2) (2002) 27–37. doi:10.1016/s0167-2738(02)00261-8.

[116] P. Bernard, C. Gabrielli, M. Keddam, H. Takenouti, J. Leonardi, P. Blanchard, AC quartz crystal microbalance applied to the studies of the nickel hydroxide behaviour in alkaline solutions, Electrochimica Acta 36 (3-4) (1991) 743–746. doi:10.1016/0013-4686(91)85166-5.

[117] G. T. Cheek, W. E. O'grady, Redox behavior of the nickel oxide electrode system: Quartz crystal microbalance studies, Journal of Electroanalytical Chemistry 421 (1-2) (1997) 173–177. doi:10.1016/s0022-0728(96)04821-8.

[118] R. R. Chen, Y. Mo, D. A. Scherson, In situ atomic force microscopy imaging of electroprecipitated nickel hydrous oxide films in alkaline electrolytes, Langmuir 10 (11) (1994) 3933–3936. doi:10.1021/la00023a005.

[119] R. Carbonio, V. Macagno, A. Arvía, The electrochemical response of thin, chemically precipitated nickel hydroxide layers containing inserted hydroxide ions, Journal of Electroanalytical Chemistry and Interfacial Electrochemistry 177 (1-2) (1984) 217–228. doi:10.1016/0022-0728(84)80224-7.

[120] J. A. Bau, E. J. Luber, J. M. Buriak, Oxygen evolution catalyzed by nickel–iron oxide nanocrystals with a nonequilibrium phase, ACS Applied Materials & Interfaces 7 (35) (2015) 19755–19763. doi:10.1021/acsami.5b05594.

[121] S. Carenco, C. Boissiere, L. Nicole, C. Sanchez, P. L. Floch, N. Mezailles, Controlled design of size-tunable monodisperse nickel nanoparticles, Chemistry of Materials 22 (4) (2010) 1340–1349. doi:10.1021/cm902007g.

[122] M. Gao, W. Sheng, Z. Zhuang, Q. Fang, S. Gu, J. Jiang, Y. Yan, Efficient water oxidation using nanostructured α-nickel-hydroxide as an electrocatalyst, Journal of the American Chemical Society 136 (19) (2014) 7077–7084. doi:10.1021/ja502128j.

[123] E. Kaniukov, A. Shumskaya, M. Kutuzau, V. Bundyukova, D. Yakimchuk, D. Borgekov, M. Ibragimova, I. Korolkov, S. Giniyatova, A. Kozlovskiy, M. Zdorovets, Degradation mechanism and way of surface protection of nickel nanostructures, Materials Chemistry and Physics 223 (2019) 88–97. doi:10.1016/j.matchemphys.2018.09.010.

[124] Y. Qiu, L. Xin, W. Li, Electrocatalytic oxygen evolution over supported small amorphous ni–fe nanoparticles in alkaline electrolyte, Langmuir 30 (26) (2014) 7893–7901. doi:10.1021/la501246e.

[125] M. Hao, S. Garbarino, S. Prabhudev, T. B. Hanson, G. A. Botton, D. A. Harrington, D. Guay, Vertically aligned ni nanowires as a platform for

kinetically limited water-splitting electrocatalysis, The Journal of Physical Chemistry C 123 (2) (2018) 1082–1093. doi:10.1021/acs.jpcc.8b10414.

[126] S. Klaus, Y. Cai, M. W. Louie, L. Trotochaud, A. T. Bell, Effects of Fe electrolyte impurities on $Ni(OH)_2$/NiOOH structure and oxygen evolution activity, The Journal of Physical Chemistry C 119 (13) (2015) 7243–7254. doi:10.1021/acs.jpcc.5b00105.

[127] P. W. T. Lu, Electrochemical-ellipsometric studies of oxide film formed on nickel during oxygen evolution, Journal of The Electrochemical Society 125 (9) (1978) 1416. doi:10.1149/1.2131689.

[128] M. W. Dijksma, P. Notten, Electrochemical quartz microbalance characterization of $Ni(OH)_2$-based thin film electrodes, Electrochimica Acta 51 (18) (2006) 3609–3621. doi:10.1016/j.electacta.2005.10.022.

[129] I. Godwin, M. Lyons, Enhanced oxygen evolution at hydrous nickel oxide electrodes via electrochemical ageing in alkaline solution, Electrochemistry Communications 32 (2013) 39–42. doi:10.1016/j.elecom.2013.03.040.

[130] L. N. Trevani, E. Calvo, H. R. Corti, Diffusion coefficients of iodide in high temperature aqueous solutions, Electrochemistry Communications 2 (5) (2000) 312–316. doi:10.1016/s1388-2481(00)00023-0.

[131] B. Conway, D. Wilkinson, Non-isothermal cell potentials and evaluation of entropies of ions and of activation for single electrode processes in non-aqueous media, Electrochimica Acta 38 (7) (1993) 997–1013. doi:10.1016/0013-4686(93)87020-e.

[132] S. Hettiarachchi, D. D. Macdonald, A solid polymer electrolyte internal reference electrode for high temperature aqueous systems, Journal of The Electrochemical Society 134 (5) (1987) 1307–1308. doi:10.1149/1.2100663.

[133] D. L. Goldfarb, H. R. Corti, Electrochemistry in supercritical trifluoromethane, Electrochemistry Communications 2 (9) (2000) 663–670. doi:10.1016/s1388-2481(00)00099-0.

[134] J. Barthel, R. Wachter, H. j. Gores, Temperature dependence of conductance of electrolytes in nonaqueous solutions, in: Modern Aspects of Electrochemistry, Springer US, 1979, pp. 1–79. doi:10.1007/978-1-4615-7455-2_1.

[135] J. Barthel, H. J. Gores, G. Schmeer, The temperature dependence of the properties of electrolyte solutions. III. conductance of various salts at high concentrations in propylene carbonate at temperatures from - 45 °C to plus 25 °C, Berichte der Bunsengesellschaft für physikalische Chemie 83 (9) (1979) 911–920. doi:10.1002/bbpc.19790830908.

[136] M. J. Moorcroft, N. S. Lawrence, B. a Coles, R. G. Compton, L. N. Trevani, High temperature electrochemical studies using a channel flow cell heated by radio frequency radiation, Journal of Electroanalytical Chemistry 506 (1) (2001) 28–33. doi:10.1016/s0022-0728(01)00468-5.

[137] B. A. Coles, M. J. Moorcroft, R. G. Compton, Non-aqueous electrochemical studies at a high temperature channel flow cell heated by radio frequency radiation, Journal of Electroanalytical Chemistry 513 (2) (2001) 87–93. doi:10.1016/s0022-0728(01)00606-4.

[138] F. Qiu, R. G. Compton, B. A. Coles, F. Marken, Thermal activation of electrochemical processes in a Rf-heated channel flow cell: Experiment and finite element simulation, Journal of Electroanalytical Chemistry 492 (2) (2000) 150–155. doi:10.1016/s0022-0728(00)00222-9.

[139] S. S. Kumar, V. Himabindu, Hydrogen production by PEM water electrolysis – a review, Materials Science for Energy Technologies 2 (3) (2019) 442–454. doi:10.1016/j.mset.2019.03.002.

[140] G. Schiller, A. Ansar, M. Lang, O. Patz, High temperature water electrolysis using metal supported solid oxide electrolyser cells (SOEC), Journal of Applied Electrochemistry 39 (2) (2008) 293–301. doi:10.1007/s10800-008-9672-6.

[141] A. Brisse, J. Schefold, M. Zahid, High temperature water electrolysis in solid oxide cells, International Journal of Hydrogen Energy 33 (20) (2008) 5375–5382. doi:10.1016/j.ijhydene.2008.07.120.

[142] M. Schalenbach, M. Carmo, D. L. Fritz, J. Mergel, D. Stolten, Pressurized PEM water electrolysis: Efficiency and gas crossover, International Journal of Hydrogen Energy 38 (35) (2013) 14921–14933. doi:10.1016/j.ijhydene.2013.09.013.

[143] Y. Shin, W. Park, J. Chang, J. Park, Evaluation of the high temperature electrolysis of steam to produce hydrogen, International Journal of Hydrogen Energy 32 (10-11) (2007) 1486–1491. doi:10.1016/j.ijhydene.2006.10.028.

[144] W. Doenitz, R. Schmidberger, E. Steinheil, R. Streicher, Hydrogen production by high temperature electrolysis of water vapour, International Journal of Hydrogen Energy 5 (1) (1980) 55–63. doi:10.1016/0360-3199(80)90114-7.

[145] A. Hauch, S. D. Ebbesen, S. H. Jensen, M. Mogensen, Highly efficient high temperature electrolysis, Journal of Materials Chemistry 18 (20) (2008) 2331. doi:10.1039/b718822f.

[146] D. Macdonald, B. Pound, S. Lenhart, The application of electrochemical impedance spectroscopy for characterizing the degradation of Ni(OH)2/NiOOH electrodes, Journal of Power Sources 29 (3-4) (1990) 477–502. doi:10.1016/0378-7753(90)85020-d.

[147] R. Haugsrud, On the high-temperature oxidation of nickel, Corrosion Science 45 (1) (2003) 211–235. doi:10.1016/s0010-938x(02)00085-9.

[148] T. Holm, P. K. Dahlstrøm, S. Sunde, F. Seland, D. A. Harrington, Dynamic electrochemical impedance study of methanol oxidation at Pt at elevated temperatures, Electrochimica Acta 295 (2019) 139–147. doi:10.1016/j.electacta.2018.10.071.

[149] F. Seland, R. Tunold, D. A. Harrington, Impedance study of methanol oxidation on platinum electrodes, Electrochimica Acta 51 (18) (2006) 3827–3840. doi:10.1016/j.electacta.2005.10.050.

[150] M. Ingdal, R. Johnsen, D. A. Harrington, The akaike information criterion in weighted regression of immittance data, Electrochimica Acta 317 (2019) 648–653. doi:10.1016/j.electacta.2019.06.030.

[151] D. A. Harrington, P. V. D. Driessche, Mechanism and equivalent circuits in electrochemical impedance spectroscopy, Electrochimica Acta 56 (23) (2011) 8005–8013. doi:10.1016/j.electacta.2011.01.067.

[152] G. Popkirov, Fast time-resolved electrochemical impedance spectroscopy for investigations under nonstationary conditions, Electrochimica Acta 41 (7-8) (1996) 1023–1027. doi:10.1016/0013-4686(95)00434-3.

[153] G. S. Popkirov, R. N. Schindler, Optimization of the perturbation signal for electrochemical impedance spectroscopy in the time domain, Review of Scientific Instruments 64 (11) (1993) 3111–3115. doi:10.1063/1.1144316.

[154] R. L. Sacci, D. Harrington, Dynamic electrochemical impedance spectroscopy, ECS Transactions 19 (20) (2009) 31–42. doi:10.1149/1.3247564.

[155] D. Harrington, B. Conway, Ac impedance of faradaic reactions involving electrosorbed intermediates—i. kinetic theory, Electrochimica Acta 32 (12) (1987) 1703–1712. doi:10.1016/0013-4686(87)80005-1.

[156] B. E. Conway, L. Bai, Determination of the adsorption behaviour of 'overpotential-deposited' hydrogen-atom species in the cathodic hydrogen-evolution reaction by analysis of potential-relaxation transients, Journal of the Chemical Society, Faraday Transactions 1: Physical Chemistry in Condensed Phases 81 (8) (1985) 1841. doi:10.1039/f19858101841.

[157] S. Machado, L. Avaca, The hydrogen evolution reaction on nickel surfaces stabilized by h-absorption, Electrochimica Acta 39 (10) (1994) 1385–1391. doi:10.1016/0013-4686(94)e0003-i.

[158] M. Besson, P. Gallezot, Selective oxidation of alcohols and aldehydes on metal catalysts, Catalysis Today 57 (1-2) (2000) 127–141.

[159] S. Carrettin, P. Mcmorn, P. Johnston, K. Griffin, C. J. Kiely, G. J. Hutchings, Oxidation of glycerol using supported Pt, Pd and Au catalysts, Physical Chemistry Chemical Physics 5 (6) (2003) 1329–1336.

[160] R. Garcia, M. Besson, P. Gallezot, Chemoselective catalytic oxidation of glycerol with air on platinum metals, Applied Catalysis A: General 127 (1-2) (1995) 165–176. doi:10.1016/0926-860x(95)00048-8.

[161] R. K. P. Purushothaman, J. V. Haveren, D. V. Es, I. M. Cabrera, J. Meeldijk, H. Heeres, An efficient one pot conversion of glycerol to lactic acid using bimetallic gold-platinum catalysts on a nanocrystalline CeO_2 support, Applied Catalysis B: Environmental 147 (2014) 92–100. doi:10.1016/j.apcatb.2013.07.068.

[162] M. Sun, Y. Zhang, S. Y. Kong, L. F. Zhai, S. Wang, Excellent performance of electro-assisted catalytic wet air oxidation of refractory organic pollutants, Water Research 158 (2019) 313–321. doi:10.1016/j.watres.2019.04.040.

[163] Y. Huang, M. Luo, Z. Xu, D. Zhang, L. Li, Catalytic ozonation of organic contaminants in petrochemical wastewater with iron-nickel foam as catalyst, Separation and Purification Technology 211 (2019) 269–278. doi:10.1016/j.seppur.2018.09.080.

[164] J. M. Grill, J. W. Ogle, S. A. Miller, An efficient and practical system for the catalytic oxidation of alcohols, aldehydes, and α,β-unsaturated carboxylic acids, The Journal of Organic Chemistry 71 (25) (2006) 9291–9296. doi:10.1021/jo0612574.

[165] E. Jolimaitre, D. Delcroix, N. Essayem, C. Pinel, M. Besson, Dihydroxyacetone conversion into lactic acid in an aqueous medium in the presence of metal salts: Influence of the ionic thermodynamic equilibrium on the reaction performance, Catalysis Science & Technology 8 (5) (2018) 1349–1356. doi:10.1039/c7cy02385e.

[166] S. Lux, Catalytic conversion of dihydroxyacetone to lactic acid with brønsted acids and multivalent metal ions, Chemical and Biochemical Engineering Quarterly 29 (4) (2016) 575–585. doi:10.15255/cabeq.2014.2110.

[167] T. Kakumoto, K. Saito, A. Imamura, Unimolecular decomposition of oxalic acid, The Journal of Physical Chemistry 91 (9) (1987) 2366–2371. doi:10.1021/j100293a034.

[168] S. Ramakrishnan, Condensation polymerization, Resonance 22 (4) (2017) 355–368. doi:10.1007/s12045-017-0475-0.

[169] D. E. Koppel, Analysis of macromolecular polydispersity in intensity correlation spectroscopy: The method of cumulants, The Journal of Chemical Physics 57 (11) (1972) 4814–4820. doi:10.1063/1.1678153.

[170] M. A. Sharaf, J. E. Mark, The effects of cross-linking and strain on the glass transition temperature of a polymer network, Rubber Chemistry and Technology 53 (4) (1980) 982–987. doi:10.5254/1.3535073.

[171] H. Stutz, K. Illers, J. Mertes, A generalized theory for the glass transition temperature of crosslinked and uncrosslinked polymers, Journal of Polymer Science Part B: Polymer Physics 28 (9) (1990) 1483–1498. doi:10.1002/polb.1990.090280906.

[172] G. W. H. Höhne, W. F. Hemminger, H. j. Flammersheim, Differential Scanning Calorimetry, Springer Berlin Heidelberg, 2003. doi:10.1007/978-3-662-06710-9.

[173] A. B. Northrup, Two-step synthesis of carbohydrates by selective aldol reactions, Science 305 (5691) (2004) 1752–1755. doi:10.1126/science.1101710.

[174] A. Córdova, I. Ibrahem, J. Casas, H. Sundén, M. Engqvist, E. Reyes, Amino acid catalyzed neogenesis of carbohydrates: A plausible ancient transformation, Chemistry - A European Journal 11 (16) (2005) 4772–4784. doi:10.1002/chem.200500139.

[175] J. Kofoed, J. L. Reymond, T. Darbre, Prebiotic carbohydrate synthesis: Zinc–proline catalyzes direct aqueous aldol reactions of α-hydroxy aldehydes and ketones, Organic & Biomolecular Chemistry 3 (10) (2005) 1850. doi:10.1039/b501512j.

[176] R. Xiao, M. W. Grinstaff, Chemical synthesis of polysaccharides and polysaccharide mimetics, Progress in Polymer Science 74 (2017) 78–116. doi:10.1016/j.progpolymsci.2017.07.009.

[177] R. S. Jayashree, P. V. Kamath, G. N. Subbanna, The effect of crystallinity on the reversible discharge capacity of nickel hydroxide, Journal of The Electrochemical Society 147 (6) (2000) 2029. doi:10.1149/1.1393480.

[178] M. Merrill, M. Worsley, A. Wittstock, J. Biener, M. Stadermann, Determination of the "NiOOH" charge and discharge mechanisms at ideal activity, Journal of Electroanalytical Chemistry 717-718 (2014) 177–188. doi:10.1016/j.jelechem.2014.01.022.

[179] B. A. Boukamp, A linear kronig-kramers transform test for immittance data validation, Journal of The Electrochemical Society 142 (6) (1995) 1885. doi:10.1149/1.2044210.

[180] M. E. V. D. Geest, N. J. Dangerfield, D. A. Harrington, An AC voltammetry study of Pt oxide growth, Journal of Electroanalytical Chemistry 420 (1-2) (1997) 89–100. doi:10.1016/s0022-0728(96)04812-7.

[181] J. L. Bantignies, S. Deabate, A. Righi, S. Rols, P. Hermet, J. L. Sauvajol, F. Henn, New insight into the vibrational behavior of nickel hydroxide and oxyhydroxide using inelastic neutron scattering, far/mid-infrared and raman spectroscopies, The Journal of Physical Chemistry C 112 (6) (2008) 2193–2201. doi:10.1021/jp075819e.

[182] D. S. Hall, C. Bock, B. R. Macdougall, The electrochemistry of metallic nickel: Oxides, hydroxides, hydrides and alkaline hydrogen evolution, Journal of The Electrochemical Society 160 (3) (2013) F235–F243. doi:10.1149/2.026303jes.

[183] B. Paxton, J. Newman, Variable diffusivity in intercalation materials: A theoretical approach, Journal of The Electrochemical Society 143 (4) (1996) 1287–1292. doi:10.1149/1.1836631.

[184] G. Barral, F. N. Eyoke, S. Maximovitch, Growth of a nickel oxide layer on a rotating nickel electrode in a non-buffered solution of sodium sulfate, Electrochimica Acta 40 (6) (1995) 709–718. doi:10.1016/0013-4686(94)00331-t.

[185] Y. Elbaz, D. Furman, M. C. Toroker, Hydrogen transfer through different crystal phases of nickel oxy/hydroxide, Physical Chemistry Chemical Physics 20 (39) (2018) 25169–25178. doi:10.1039/c8cp01930d.

[186] J. L. Weininger, M. W. Breiter, Effect of crystal structure on the anodic oxidation of nickel, Journal of The Electrochemical Society 110 (6) (1963) 484. doi:10.1149/1.2425798.

[187] J. Rumble, Crc Handbook of Chemistry and Physics, 100$^{\text{th}}$ Edition, Thermodynamic Properties As a Function of Temperature, Taylor and Francis Ltd., 2019.
URL https://www.ebook.de/de/product/36589507/crc_handbook_of_chemistry_and_physics_100th_edition.html

[188] D. D. Macdonald, Thermodynamics of nickel-cadmium and nickel-hydrogen batteries, Journal of The Electrochemical Society 140 (3) (1993) 606. doi:10.1149/1.2056129.

[189] L. f. Huang, M. J. Hutchison, R. J. Santucci, J. R. Scully, J. M. Rondinelli, Improved electrochemical phase diagrams from theory and experiment: The Ni–water system and its complex compounds, The Journal of Physical Chemistry C 121 (18) (2017) 9782–9789. doi:10.1021/acs.jpcc.7b02771.

[190] B. Beverskog, I. Puigdomenech, Revised pourbaix diagrams for nickel at 25–300 °C, Corrosion Science 39 (5) (1997) 969–980. doi:10.1016/s0010-938x(97)00002-4.

[191] L. Duro, M. Grive, E. Cera, C. Domenech, J. Bruno, Update of a thermodynamic database for radionuclides to assist solubility limits calculation for performance assessment (Dec. 2006).

[192] Cebelcor, Enthalpies libres de formation standard, a 25 °C, Rapports Techniques RT.87 (1960).

[193] J. Balej, J. Divisek, On the thermodynamics of higher solid nickel oxocompounds, Berichte der Bunsengesellschaft für physikalische Chemie 97 (7) (1993) 933–939. doi:10.1002/bbpc.19930970715.

[194] J. J. Reed, The nbs tables of chemical thermodynamic properties: Selected values for inorganic and C1 and C2 organic substances in si units, glycerol, organic (2020). doi:10.18434/M32124.

[195] S. L. Bihan, M. Figlarz, Croissance de l'hydroxyde de nickel $Ni(OH)_2$ à partir d'un hydroxyde de nickel turbostratique, Journal of Crystal Growth 13-14 (1972) 458–461. doi:10.1016/0022-0248(72)90280-1.

[196] A. D. Vidal, B. Beaudoin, M. Figlarz, Textural and structural studies on nickel hydroxide electrodes, Reactivity of Solids 2 (3) (1986) 223–233. doi:10.1016/0168-7336(86)80085-7.

[197] A. D. Vidal, M. Figlarz, Textural and structural studies on nickel hydroxide electrodes. II. turbostratic nickel (II) hydroxide submitted to electrochemical redox cycling, Journal of Applied Electrochemistry 17 (3) (1987) 589–599. doi:10.1007/bf01084134.

[198] A. Nadeema, V. M. Dhavale, S. Kurungot, NiZn double hydroxide nanosheet-anchored nitrogen-doped graphene enriched with the γ-NiOOH phase as an activity modulated water oxidation electrocatalyst, Nanoscale 9 (34) (2017) 12590–12600. doi:10.1039/c7nr02225e.

[199] V. Kotok, V. Kovalenko, Definition of the aging process parameters for nickel hydroxide in the alkaline medium, Eastern-European Journal of Enterprise Technologies 2 (12 (92)) (2018) 54–60. doi:10.15587/1729-4061.2018.127764.

[200] R. Jayashree, P. V. Kamath, Suppression of the alpha to beta-nickel hydroxide transformation in concentrated alkali: Role of dissolved cations, Journal of Applied Electrochemistry 31 (12) (2001) 1315–1320. doi:10.1023/a:1013876006707.

[201] C. Tessier, C. Faure, L. G. Demourgues, C. Denage, G. Nabias, C. Delmas, Electrochemical study of zinc-substituted nickel hydroxide, Journal of The Electrochemical Society 149 (9) (2002) A1136. doi:10.1149/1.1495496.

[202] M. Morishita, T. Kakeya, S. Ochiai, T. Ozaki, Y. Kawabe, M. Watada, T. Sakai, Structural analysis by synchrotron x-ray diffraction, x-ray absorption fine structure and transmission electron microscopy for aluminum-substituted α-type nickel hydroxide electrode, Journal of Power Sources 193 (2) (2009) 871–877. doi:10.1016/j.jpowsour.2009.03.065.

[203] S. Dresp, P. Strasser, Non-noble metal oxides and their application as bifunctional catalyst in reversible fuel cells and rechargeable air batteries, ChemCatChem 10 (18) (2018) 4162–4171. doi:10.1002/cctc.201800660.

[204] Z. X. Liu, Z. P. Li, H. Y. Qin, B. H. Liu, Oxygen reduction reaction via the 4-electron transfer pathway on transition metal hydroxides, Journal of Power Sources 196 (11) (2011) 4972–4979. doi:10.1016/j.jpowsour.2011.01.102.

[205] A. B. Anderson, R. Jinnouchi, J. Uddin, Effective reversible potentials and onset potentials for O_2 electroreduction on transition metal electrodes: Theoretical analysis, The Journal of Physical Chemistry C 117 (1) (2012) 41–48. doi:10.1021/jp307367m.

[206] V. Vij, S. Sultan, A. M. Harzandi, A. Meena, J. N. Tiwari, W. G. Lee, T. Yoon, K. S. Kim, Nickel-based electrocatalysts for energy-related applications: Oxygen reduction, oxygen evolution, and hydrogen evolution reactions, ACS Catalysis 7 (10) (2017) 7196–7225. doi:10.1021/acscatal.7b01800.

[207] R. Bock, H. Karoliussen, F. Seland, B. G. Pollet, M. S. Thomassen, S. Holdcroft, O. S. Burheim, Measuring the thermal conductivity of membrane and porous transport layer in proton and anion exchange membrane water electrolyzers for temperature distribution modeling, International Journal of Hydrogen Energy (2019). doi:10.1016/j.ijhydene.2019.01.013.

[208] G. Brug, A. V. D. Eeden, M. S. Rehbach, J. Sluyters, The analysis of electrode impedances complicated by the presence of a constant phase element, Journal of Electroanalytical Chemistry and Interfacial Electrochemistry 176 (1-2) (1984) 275–295. doi:10.1016/s0022-0728(84)80324-1.

[209] B. Hirschorn, M. E. Orazem, B. Tribollet, V. Vivier, I. Frateur, M. Musiani, Determination of effective capacitance and film thickness from constant-phase-element parameters, Electrochimica Acta 55 (21) (2010) 6218–6227. doi:10.1016/j.electacta.2009.10.065.

[210] K. Joback, R. Reid, Estimation of pure-component properties from group-contributions, Chemical Engineering Communications 57 (1-6) (1987) 233–243. doi:10.1080/00986448708960487.

[211] Y. Wu, M. J. Zhao, F. Li, J. Xie, Y. Li, J. B. He, Trace Fe incorporation into Ni-(oxy)hydroxide stabilizes Ni^{3+} sites for anodic oxygen evolution: A double thin-layer study, Langmuir 36 (19) (2020) 5126–5133. doi:10.1021/acs.langmuir.0c00264.

[212] C. Mahala, M. Devi sharma, M. Basu, Fe-doped nickel hydroxide/nickel oxyhydroxide function as an efficient catalyst for the oxygen evolution reaction, ChemElectroChem 6 (13) (2019) 3488–3498. doi:10.1002/celc.201900857.

[213] A. C. Garcia, T. Touzalin, C. Nieuwland, N. Perini, M. T. M. Koper, Enhancement of oxygen evolution activity of nickel oxyhydroxide by electrolyte alkali cations, Angewandte Chemie International Edition 58 (37) (2019) 12999–13003. doi:10.1002/anie.201905501.

[214] M. Görlin, P. Chernev, P. Paciok, C. W. Tai, J. F. D. Araújo, T. Reier, M. Heggen, R. D. Borkowski, P. Strasser, H. Dau, Formation of unexpectedly active Ni–Fe oxygen evolution electrocatalysts by physically mixing Ni and Fe oxyhydroxides, Chemical Communications 55 (6) (2019) 818–821. doi:10.1039/c8cc06410e.

[215] H. Xiao, H. Shin, W. A. Goddard, Synergy between Fe and Ni in the optimal performance of (Ni,Fe)OOH catalysts for the oxygen evolution reaction, Proceedings of the National Academy of Sciences 115 (23) (2018) 5872–5877. doi:10.1073/pnas.1722034115.

[216] S. I. C. Torresi, C. Gabrielli, A. H. L. Goff, R. Torresi, Electrochromic behavior of nickel oxide electrodes: I . identification of the colored state using quartz crystal microbalance, Journal of The Electrochemical Society 138 (6) (1991) 1548–1553. doi:10.1149/1.2085830.

[217] D. Pletcher, M. Fleischmann, K. Korinek, The oxidation of organic compounds at a cobalt electrode in alkaline media, Journal of Electroanalytical Chemistry and Interfacial Electrochemistry 33 (2) (1971) 478–479. doi:10.1016/s0022-0728(71)80131-6.

[218] B. Pierozynski, T. Mikolajczyk, M. Luba, A. Zolfaghari, Kinetics of oxygen evolution reaction on nickel foam and platinum-modified nickel foam materials in alkaline solution, Journal of Electroanalytical Chemistry 847 (2019) 113194. doi:10.1016/j.jelechem.2019.113194.

[219] K. Juodkazis, J. Juodkazytė, R. Vilkauskaitė, V. Jasulaitienė, Nickel surface anodic oxidation and electrocatalysis of oxygen evolution, Journal of Solid State Electrochemistry 12 (11) (2008) 1469–1479. doi:10.1007/s10008-007-0484-0.

[220] A. J. Tkalych, H. L. Zhuang, E. A. Carter, A density functional U assessment of oxygen evolution reaction mechanisms on β-NiOOH, ACS Catalysis 7 (8) (2017) 5329–5339. doi:10.1021/acscatal.7b00999.

[221] M. M. J. E. Marsden, The Hopf Bifurcation and Its Applications, Springer New York, 1976.
URL https://www.ebook.de/de/product/8046332/j_e_marsden_m_mccracken_the_hopf_bifurcation_and_its_applications.html

[222] V. V. Pototskaya, O. I. Gichan, Dynamic instabilities of model electrochemical system with electrocatalytic oxidation and preceding chemical reaction, Russian Journal of Electrochemistry 47 (3) (2011) 336–344. doi:10.1134/s1023193511030116.

[223] M. Orlik, Application of impedance spectroscopy to electrochemical instabilities, in: Monographs in Electrochemistry, Springer Berlin Heidelberg, 2012, pp. 111–195. doi:10.1007/978-3-642-27673-6_3.